The formation and evolution of galaxies as a function of environment

Yara Lorena Jaffé Ribbi

The University of Nottingham

Thesis submitted to the University of Nottingham
for the degree of Doctor of Philosophy

July 2012

Supervisor:	Prof. Alfonso Aragón-Salamanca (*University of Nottingham*)
Examiners:	Prof. Bodo Ziegler (*University of Vienna*) Dr. Frazer Pearce (*University of Nottingham*)

Submitted:	2 February 2011
Examined:	8 April 2011
Final version:	15 November 2011

Dijo Tennyson que si pudiéramos comprender una sola flor
sabríamos quiénes somos y qué es el mundo

Jorge Luis Borges

Abstract

This thesis investigates the rôle of environment on galaxy formation and evolution, giving particular focus to the transformation of star forming spirals into passive S0s. The data utilised for this study comes from photometric and spectroscopic observations of galaxies at $0 < z < 1$ in different environments from the ESO Distant Cluster Survey. We first study the formation history of (172) cluster ellipticals (Es) and S0s, the oldest types of galaxies in the local universe. We examine their colour-magnitude relation (CMR), and find a very small intrinsic colour scatter. Only 7% of the galaxies are significantly bluer than the CMR. The scarcity of blue S0s indicates that, if they are the descendants of spirals, these were already red when they became S0s. We observe no dependence of the CMR scatter with z or cluster velocity dispersion. This implies that by the time cluster E/S0s achieve their morphology, the vast majority have already joined the red sequence. We estimate the galaxy formation redshift $z_{\rm F}$ for each cluster and find that while it does not depend on the cluster velocity dispersion, it increases weakly with cluster redshift. This suggests that, at any given z, in order to have a population of fully-formed E and S0s they needed to have formed most of their stars $\simeq$ 2–4 Gyr prior to observation. In other words, the galaxies that already have early-type morphologies also have reasonably-old stellar populations. This is partly a manifestation of the "progenitor bias", but also a consequence of the fact that the vast majority of the E/S0s in clusters (in particular the massive ones) were already red by the time they achieved their morphology. Moreover, E and S0 galaxies exhibit very similar colour scatter, implying similar stellar population ages. We also find that fainter E/S0s finished forming their stars later, consistent with the cluster red sequence being built over time and the brightest galaxies reaching the red sequence earlier than fainter ones. Finally, we find that the E/S0s cluster galaxies must have had their star

formation truncated over an extended period $\Delta t \gtrsim 1\,\mathrm{Gyr}$.

We then move our focus to the evolution of star-forming galaxies. We investigate the effect of the environment on the transformation of star-forming spirals into passive S0s by studying the properties of the gas and the stars in a sample of 422 emission-line galaxies in different environments. We identify galaxies with kinematical disturbances (in their gas disks), and find that they are more frequent in clusters than in the field. The fraction of kinematically-disturbed galaxies increases with cluster velocity dispersion and decreases with distance from the cluster centre, but remains constant with projected galaxy density. We also studied morphological disturbances in the stellar light, finding that the fraction of morphologically disturbed galaxies is independent of environment. Moreover, there is little correlation between the presence of kinematically-disturbed gas and morphological distortions. For the kinematically-undisturbed galaxies, we find that the cluster and field B-band Tully-Fisher relations are remarkably similar. Additionally, we find that the kinematically-disturbed galaxies show a suppressed specific star formation rate. There is also evidence indicating that the gas disks in cluster galaxies have been truncated, and therefore their star formation is more concentrated than in low-density environments. If spirals are the progenitors of cluster S0s, our findings imply that the physical mechanism transforming cluster galaxies efficiently disturbs the star-forming gas and reduces their specific star formation rate. This star-forming gas is either removed more efficiently from the outskirts of the galaxies or it is driven towards the centre (or both). In any case, this makes any remaining star formation more centrally concentrated, helping to build the bulges of S0s. All this evidence, together with the fact that the transformation mechanism does not seem to induce strong morphological disturbances on the galaxies, suggests that the physical processes involved are related to the intracluster medium, with galaxy-galaxy interactions playing only a limited role in clusters. Interestingly, in analogy with the "blue" early-type galaxies found in the CMR study in clusters, we have also found several emission-line E/S0 galaxies with extended rotating star-forming gas disks.

Acknowledgements

First of all I thank my parents for the huge amount of support and love that they always have given me, visiting me, and always receiving me with open arms in Caracas. I also thank my *brüderchen* Rodolfo, for always being the supporting brother that he is, regardless of the distance.

A huge thanks to my academic father, Alfonso , for the invaluable support, motivation, and advice throughout my PhD. I always felt lucky to have him as a supervisor. I also thank my academic mother, Kathy, for the huge support and encouragement to do my PhD, and for always keeping in touch, making me feel that I have a home at CIDA. I would also like to thank my ESO advisor Harald Kuntschner, for his great advice and supervision during the year I spent in München (and after), as well as the support in my job applications. I'm also greatly indebted to Gustavo Bruzual for his support in every step of my career. Thanks to my second supervisor in Nottingham, Meghan Grey, as well as Omar Almaini, and June McCombie for their support, advice and kindness. I also thank "my" post-docs Steven Bamford and Carlos Hoyos for their time, input, and patience, as well as my second ESO advisor, Piero Rosati, and of course, the EDisCS collaboration. I want to thank Bianca Poggianti for giving me a great motivation to submit: a job, which I'm looking forward to start. I thank my examinors Frazer Pearce and Bodo Ziegler for making my VIVA a survivable experience and for the really useful comments and ideas.

I'm greatly indebted to ESO for the generous Studentship, without which I would probably not have been able to finish my PhD. I also want to give a special thanks to the *Academia de Ciencias Físicas Matemáticas y Naturales de Venezuela* for the financial support given throughout my PhD, that has been of enormous help, and to The University of Nottingham and its international office for their support and help.

Acknowledgements

I would also like to thank the Royal Astronomical Society. Furthermore, the work presented in this thesis is based on observations collected at the European Southern Observatory, Chile, as part of programme 166.A-0161.

Nearly 4 years have passed since I landed in Nottingham for the first time. I have spent this time in 3 different locations and met incredible people along the way. I thank them here in chronological and geographical order: In Nottingham, my first friends were Arianna, Alkistula and Alessandra, three girls that I know will always be in my life. Thank you for teaching me so many things, from inflation and Greek communism, to natural medicine, hippiness in the 21^{st} century, chemistry and witchcraft. Thanks to all my astro and non-astro mates that made Nottingham a missable place. In particular I would like to mention (in random order) a few of them: Mark & (his) Amanda, the old and grumpy Riccardo, Olivia, Lady Amanda (thanks for sharing SEA, and so many other things with me), Ruth, without whom a full night out was never achieved, Jesus, for guiding our way, Asa and his discussions on ekpyrosis and other drugs, Rob for saving the world for us, Fernandito, for reminding me we were once a ESpanish colony, Magda & (her) Mark, Karimakia and Vanesa for always being up for salsa, Roberto & Begoña for bringing Venezuela to Lenton and always welcoming me in it, Markus, Gustavo, Frank, Boris, Keith, Chrati, Will, Dan, Alice, and all the copper nanotubes that I'm forgetting. Thanks to my house mates, Mando, Mey and Daniele, for making the house-sharing a never-boring experience. Guys thanks for the daily political discussions, the Bang, the dinners, the smoking-under-the-rain conversations, the movies, the poo coffee, the extra-extra-extra virgin olive oil, the malako-magnetism, the yoghurt experiments, the raki, but most of all thanks for the good company! I would also like to thank our landlady Maria, for being so wonderful.

From my year in München, le doy unas gracias especiales a mi querida tia y abuela tante Ilse, por brindarme un hogar tanto en Neustadt como en München, y a Carito por compartir conmigo un año tan fino (sabes que sin ti no hubiese sido lo mismo!). I would like to thank my girls, Audrey, Gina and Fatme for being so wonderful and rarely speak about science, especially Audrey for all the good times in Asia, and for visiting me twice in the UK! Thanks to Mecha & Carlitos for all the good BBQs, bolero-afternoons and *zeitung mit der maus*, as well as Okuary for being "el primo",

Acknowledgements

Andy & his gang for the music, Simon, Iva, and the loyal members of ESO's "female" football team (Camilla, Alma, Andre, Diego, and Nuno).

I am also greatly indebted to the astrophysics group of Exeter University, for giving me an office and accepting me as a visitor, even if I don't know anything about planet atmospheres or star-forming regions. In particular to Mathew Bates, Isabelle Baraffe, Susie, Al, Catia, Rob1, Rob2, Wolfgang, Maxime, and Arthur.

Agradezco a mi abuelita Sol por el cariño y todas las polvorosas que sobrevivieron el transatlántico. También a todos mis (desperdigados) primos y tios, por estar siempre "cerca". Gracias a mis panas en Venezuela (y a los expatriados) por siempre compartir y recordarme de ese denominador común que nos une: el hogar. Especialmente a Pedrito Lola Derak (a quien dedico el epígrafe), Alejandra, Alessandra, Isa, Kiki, Andrés, Ir^n, Julian, Nestor E. M. G., Raúl, Alecia, Fúlvio, Bárbara & Pablo, Mertio, Jisus, Michi, Laura, Fer, Isaac, Juana, la familia KQT, "los cidosos", y tantos otros.

Last but not least, I thank my loving boyfriend Gra-e-mi-to for believing in me, helping me survive the winter, and always making me laugh (even during the writing of this thesis), but mostly for teaching me how to swear politely.

I would like to dedicate this thesis to my cousin Javier and my friend Carlitos, two loved colleagues who are no longer with us.

Published Work

The work contained in this thesis reflects the work presented in the following papers:

I Jaffé Y. L.,Aragón-Salamanca A., De Lucia G., Jablonka P., Rudnick G., Saglia R., Zaritsky D., 2011, "The colour-magnitude relation of Elliptical and Lenticular galaxies in the ESO Distant Cluster Survey", MNRAS, 410, 280

II Jaffé Y. L., Aragón-Salamanca A., Kuntschner H., Bamford S., Carlos Hoyos C., De Lucia G., Halliday C., Milvang-Jensen B., Poggianti B., Rudnick G., Saglia R., Sanchez-Blazquez P.,Zaritsky D., 2011, "The effect of environment on the gas kinematics and the stellar structure of distant galaxies", MNRAS, 417, 1996.

III Jaffé Y. L., "The effect of the environment on the gas kinematics and morphologies of distant galaxies", Proceedings from JENAM 2010, Symposium 2 (Environment and the Formation of Galaxies), 2010arXiv1011.6525J

IV Jaffé Y. L., Aragón-Salamanca A., Kuntschner H., & the EDisCS collaboration, 2011, "On the origin of elliptical and S0 galaxies with extended gas disks", in preparation.

V Rhodes R., Jaffé Y. L., Aragón-Salamanca A., Pearce F., et al., & the EDisCS collaboration, 2011 "Identifying backsplash galaxies in EDisCS: understanding the clustering history of distant galaxies through simulations", in preparation.

All papers are based on the observations described in chapter 2. Paper I contains much of the work described in chapter 3, whilst Paper II has been presented in this thesis as two chapters, 4 and 5. Paper III is a short summary of some of the results presented in paper II, prepared for a conference proceedings.

Additionally, two other papers are being prepared for publication. These are Papers IV and V, which are projects that have resulted from the study of Paper II and, although do not form part of the results presented in this thesis, they are discussed in chapter 6.

Although the data was taken by many of my collaborators listed above (and not by the author), the vast majority of the work presented here was prepared by the author.

Contents

List of Figures

List of Tables

The formation and evolution of galaxies as a function of environment

Chapter 1

Introduction

In 2011, we are proud to say that we understand $\sim 4\%$ of the universe that we live in. It will become evident throughout this thesis however, that this 4% is far from being fully understood. This little fraction of the universe most familiar to us, includes atoms, stars, and galaxies. We can see, and study these objects because they interact with radiation. The remaining 96% of the universe is not visible and poorly understood, hence it is distinguished with the adjective "dark". Dark energy for instance, is the mysterious driver of the accelerated expansion of the universe, while dark matter, is believed to be responsible for the formation of structure in the universe and is present in galaxies and clusters of galaxies. Although we have some understanding of how they affect the evolution of the universe, we do not understand the essence of their nature.

This thesis focuses mainly in the 4% of the universe that we can see, but it also refers to dark energy and dark matter, as they are greatly responsible for the shaping of our universe, and thus directly affect the visible 4%. In particular, this thesis investigates the formation and evolution of galaxies as a function of cosmic time. We study these topics by analysing observational data of galaxies in different environments in a wide range of cosmic time.

1.1 Us and the universe

For thousands of years we have looked up at the sky and tried to build models to explain the behaviour of the sun, the moon and the other light sources in the night sky. The (most accepted) model of the universe that we have today has been built over the history of humanity by many great thinkers. The modern basis of this model however, is not as ancient. It was not until the 16^{th} century that Giordano Bruno suggested that stars were actually other suns, and may have other planets in orbit around them. And, although many ancient observers described the Milky Way as a collection of stars, it was not until Galileo Galilei's time (17^{th} century), when actual proof came, from observations made with his telescope. A century later, these ideas were further polished. In 1750, Thomas Wright speculated that the Milky Way was a flattened disk of stars, and that some of the nebulae visible in the night sky might be objects similar to the Milky Way. In 1755, Immanuel Kant introduced the term *island universes* to describe these distant nebulae. These ideas have been confirmed by observations, after causing much debate. Evidently, since the telescope was first used for astronomical observations, our understanding of the universe has improved immensely[1]. Since then, technology has advanced with unprecedented rapidity, accelerating knowledge growth. Figure 1.1 illustrates the advances in astronomical observations over a period of 160

[1]This was such an important step in astronomy, that in 2009 the whole world celebrated the "international year of astronomy", marking 400 years after Galileo's first pointing at the sky with a telescope.

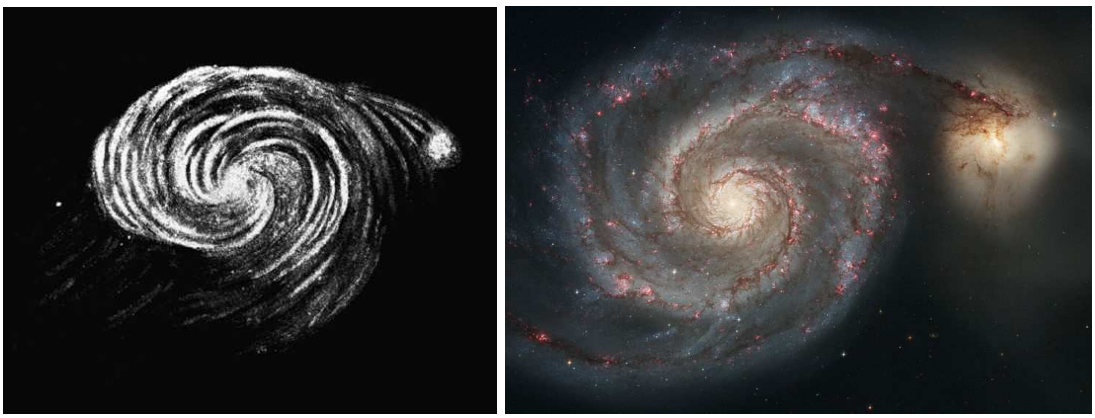

Figure 1.1: M51: before and after. *Left:* Sketch of the Whirlpool Galaxy (also known as M51) made by Lord Rosse in 1845 from observations made with a (183 cm) telescope he built himself. *Right:* Composite image of M51 taken in 2005 with the Advanced Camera for Surveys, on board of the Hubble Space Telescope.

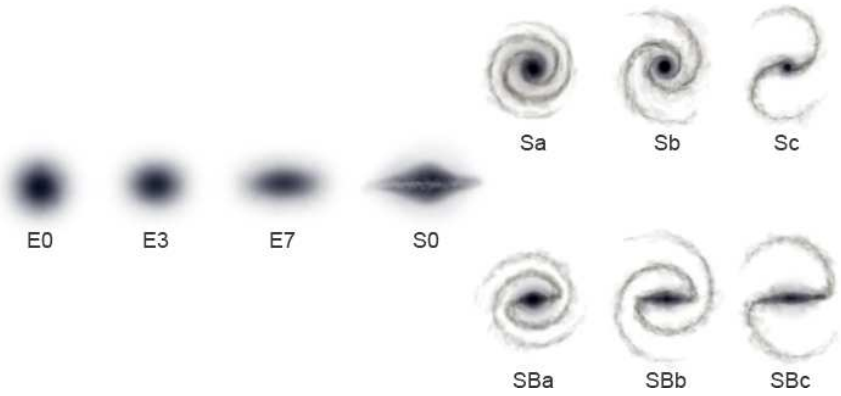

Figure 1.2: Figure showing the morphological classification scheme introduced by Hubble (1926). In this scheme galaxies are classified (according to their appearance) as ellipticals (Es), spirals(S, and SB if a bar is present), irregulars (Irr) and lenticulars (S0s), a transitional class of galaxy between the ellipticals and spirals.

years. There is no doubt that the fast technological growth of the past few decades has extended our horizons enormously.

Observations of galaxies through the years led to a classification scheme, first proposed by Hubble (1926), where galaxies are divided by morphology into 3 distinct classes: ellipticals (E), lenticulars (S0), and spirals (S). Further improvements to this scheme have defined a fork that splits barred (SB) from non-barred spirals, and included an additional class of galaxies with peculiar or irregular morphologies (Irr). Hubble's classification (schematically shown in figure 1.2) is still used today and it is known as the "Hubble sequence". The name hints at an evolutionary link between the different types of galaxies[2], where S0s mark a transition between ellipticals and spirals. Indeed, after Hubble's paper, many referred to the ellipticals and S0s as "early-type" galaxies. More recent studies, that have considered other galaxy properties (e.g. spectral features) have confirmed the presence of evolution, but have proved that, actually, "early-type" galaxies have older stellar populations than the "later" spirals. However, remaining loyal to history, astronomers nowadays still use the term "early-type" when referring to E/S0 galaxies. We also know that spirals tend to have circular motions, bluer colours, and more gas and dust content than elliptical galaxies. But why are there such differences? How did the different galaxies form? How did they acquire the shape, size, and colours we observe?

[2] Although Hubble himself did not imply any evolutionary link.

1.2 Galaxy formation

To understand galaxy formation we must start from the beginning: the origin of the universe. The Big Bang is the most accepted model of the universe that we have nowadays. Although it requires particular initial conditions (not fully understood yet), this model successfully describes the observed expansion of the universe, the origin of the Cosmic Microwave Background (CMB) Radiation, the synthesis of light elements, and the formation of large-scale structure. From CMB observations, we know that after the Big Bang, the universe, for a time, was remarkably homogeneous (see figure 1.3). The small CMB anisotropies, which represent small changes in the primordial universe's density (dominated by dark matter), then grew. As the universe cooled due to the expansion, clumps of dark matter began to condense (into what are generally referred to as "haloes"), channelling material into these increasingly dense areas. At this point the visible universe was almost exclusively composed of hydrogen and helium. Along with the dark matter, the hydrogen and helium gas within these dense regions began to condense, making the first stars. Eventually, the first proto-galaxies were also formed. The structures kept growing as the universe aged, reaching the levels of clumpiness seen in the matter distribution of today's universe (galaxies, galaxy clusters, galaxy filaments, etc). This is a consequence of the fact that baryonic (visible) matter will generally follow the dark matter, as they interact gravitationally. The detailed baryon distribution however, will differ from that of the dark matter within an individual halo

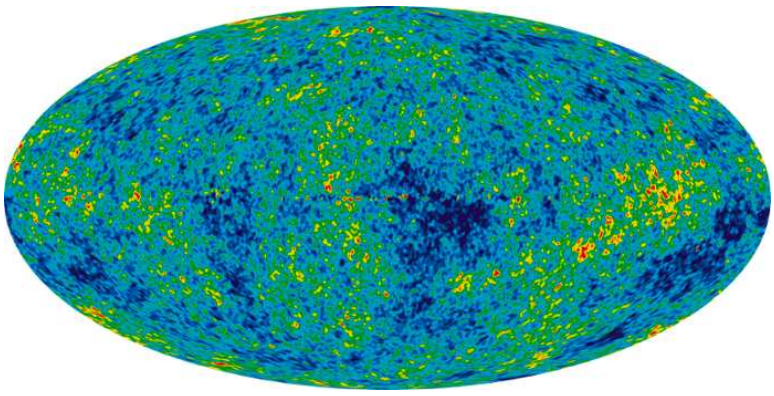

Figure 1.3: The Cosmic Microwave Background (CMB) is the radiation left over from the early stages of the universe. This map shows the CMB temperature fluctuations from the 7-year Wilkinson Microwave Anisotropy Probe data (Jarosik *et al.*, 2011) seen over the full sky. The average temperature is 2.725 K, and the colours represent the tiny temperature fluctuations. Red regions are warmer and blue regions are colder by about 0.0002 degrees. Credits: NASA / WMAP Science Team.

due to hydrodynamic effects. In other words, the structure of the gas and the stars within a galaxy does not follow the same distribution as the dark matter in it.

This cosmological model has been built from analytical and numerical work. The analytical approach is based on the derivation of the overall mass function of dark matter haloes as a function of cosmic time (Press & Schechter, 1974). More recently, advances in computer technology have led to the development of a large number of numerical cosmological simulations (e.g. Springel *et al.*, 2005). These simulations agree with the analytical results but have the advantage that the histories of individual haloes can be tracked, and their internal structure examined. Figure 1.4 shows the predicted distribution of dark matter from 10^{10} particle simulations, contrasted with the

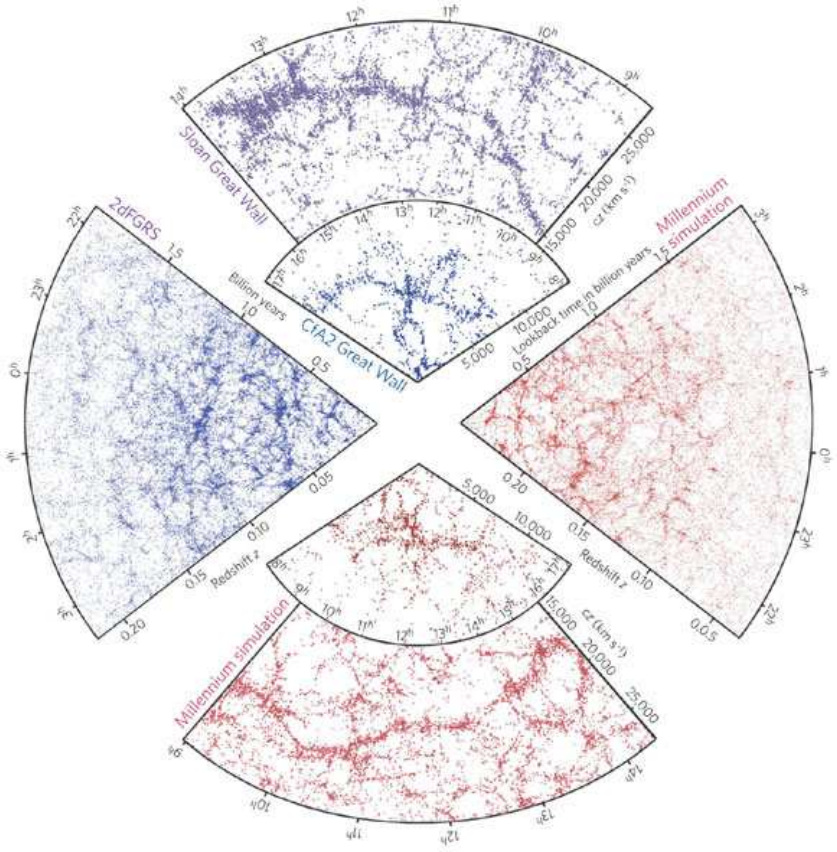

Figure 1.4: Observations and simulations of large-scale structure in the universe. The top and left slices (blue and purple) show the distribution of galaxies in the universe as seen by SDSS (around the Coma cluster) and 2dFGRS (in the southern sky) respectively. The 2dFGRS determined distances to more than 220,000 galaxies in the southern sky out to a depth of 2 billion light years. The SDSS has a similar depth but a larger solid angle and currently includes over 650,000 observed redshifts in the northern sky. At the bottom and on the right (in red), mock galaxy surveys constructed using semi-analytic techniques to simulate the formation and evolution of galaxies within the evolving dark matter distribution of the 'Millennium' simulation are shown, selected with matching survey geometries and magnitude limits. From Springel, Frenk & White (2006).

observed distribution of galaxies. The resemblance between the observations and the simulated distribution of matter in the universe is so remarkable that without a caption in the figure, it would be impossible to distinguish one from the other. The success of dark matter simulations in reproducing observations strongly supports the hierarchical picture of galaxy formation. Observations of galaxy mergers and accretion also support this model. A crucial piece of evidence is the discovery of stellar streams in the halo of the Milky Way and M31, that imply that accretion is still taking place (e.g. Ibata, Gilmore & Irwin, 1994; Vivas *et al.*, 2001, 2008, and many others). Moreover, galaxy mergers have been observed in the local universe and at high redshifts, and they are thought to be able to transform spiral galaxies into ellipticals (Toomre & Toomre, 1972; Mihos, 2003).

The hierarchical picture described above is, however, not the only galaxy formation model proposed. A competing scenario proposes that galaxies formed through the monolithic collapse of a single, massive over-dense region, without gaining significant mass thereafter (e.g. Eggen, Lynden-Bell & Sandage, 1962). Despite all the supporting evidence for the hierarchical picture of galaxy formation, there are a few unresolved problems. One of them arises from the old ages found in massive elliptical galaxies. Ellipticals are known to be the oldest galaxies in the universe, and dominate clusters at $z = 0$, whilst spiral galaxies are younger (and typically have ongoing star formation) and are more frequently found in less dense environments. Studies of the passive, red galaxies that dominate local clusters show that the bulk of their stars formed at $z > 2$ (Bower, Lucey & Ellis, 1992; Aragón-Salamanca *et al.*, 1993) and indicate that the cluster population has evolved passively in the last ~ 8 Gyr. These results favour the collapse model over the current paradigm of hierarchical assembly, that predicts that clusters continue to grow by accreting galaxies. In this picture, the stellar disks are the first galactic components to form, with elliptical galaxies and bulges of spiral galaxies forming later through the merging of pre-existing galaxy disks (e.g. Kauffmann, White & Guiderdoni, 1993).

Additionally, many observations indicate that the main epoch of star-formation activity was earlier for massive galaxies. This problem, known as "downsizing" (Cowie *et al.*, 1997), troubles the hierarchical picture for galaxy formation unless there is a mecha-

nism delaying star-formation in less massive galaxies and quenching it in the massive ones. A great deal of simulation work has been done to reconcile these observations with the hierarchical picture, and recent results are suggesting it is possible. The answer seems to come from one magic word: "feedback". Feedback from the supernovae of the first stars is a good candidate for delaying star formation in low-mass galaxies[3], while feedback from AGN in the centre of massive galaxies could efficiently stop the star formation in these systems.

Although there is progress still to be done in polishing the details of the hierarchical galaxy formation picture, it seems to be an excellent framework to study galaxy evolution in a ΛCDM universe[4].

1.3 Galaxy evolution

Evolution can be defined as "a process of gradual change occurring in a system, institution, subject, artefact, product, etc., from a simpler to a more complex or advanced state"[5]. Galaxy evolution is thus the process changing galaxies through cosmic time. Because galaxies have such long lifetimes (as compared to a human lifetime, or even the history of humanity), we cannot see the same galaxies being born, and ageing until their death. However, we can model such evolution by making physical assumptions that can successfully reproduce the observable universe. It is thus extremely important to study galaxy properties through observations at different cosmic epochs that can help constrain these models.

One of the most fundamental properties of galaxies subject to change or evolution is galaxy morphology, which represents the underlying structure of the stars. In figure 1.2 it was hinted that S0s represent a transition between spiral galaxies and elliptical galaxies. Supporting evidence for transformation of galaxy morphology from spiral to S0 and elliptical includes the following: The fraction of spiral galaxies in clusters rises from the local universe to $z \sim 0.5$, while the S0 fraction decreases comparatively

[3]The first stars formed in the early universe, known as Population III stars, are thought to have been extraordinarily massive, hence likely ended their live as powerful supernovae.

[4]ΛCDM refers to a universe dominated by dark energy (Λ) and cold dark matter (CDM).

[5]Definition taken from the *Oxford English Dictionary* (http://www.oed.com)

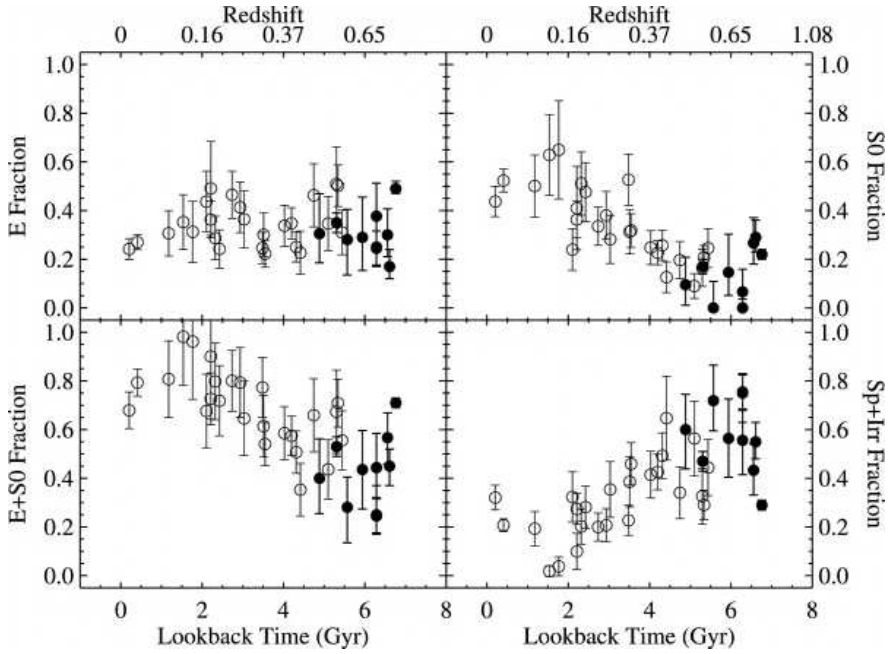

Figure 1.5: Evolution of the E, S0, E+S0, and Sp+Irr fractions as traced by EDisCS clusters (filled circles) and F00 clusters (open circles). All fractions were computed within a radius of 600 kpc, using the standard cosmology. The lookback times were calculated with the WMAP cosmology. From Desai *et al.* (2007).

(Couch *et al.*, 1994; Dressler *et al.*, 1997; van Dokkum *et al.*, 1998; Fasano *et al.*, 2000; Desai *et al.*, 2007)[6]. In contrast, the elliptical fraction appears to remain constant, as shown in figure 1.5. Moreover, it has been well established that galaxy morphology is tightly correlated with environment: dense environments such as cluster cores predominantly contain galaxies with elliptical or S0 morphology (~ 80 per cent; Dressler, 1980; Postman & Geller, 1984), while the field contains a smaller fraction of galaxies of early-type morphology. This is known as the morphology-density relation, shown in figure 1.6. These observations have been interpreted as evidence for transformation of star-forming spiral galaxies into passive S0s by the effect of the environment. Such hypothesis is consistent with the structure formation scenario of ΛCDM (discussed in section 1.2), that predicts that many field galaxies have been accreted by clusters since $z \lesssim 1$ (De Lucia *et al.*, 2004).

In addition to the morphology evolution, much has been learned from the study of other galaxy properties that are also subject to evolution. One of the most important is galaxy colour, as it is easily measured, and reflects the state of the stellar population's

[6]See Desai *et al.* (2007) for a detailed discussion on the classification of S0 galaxies and associated uncertainties.

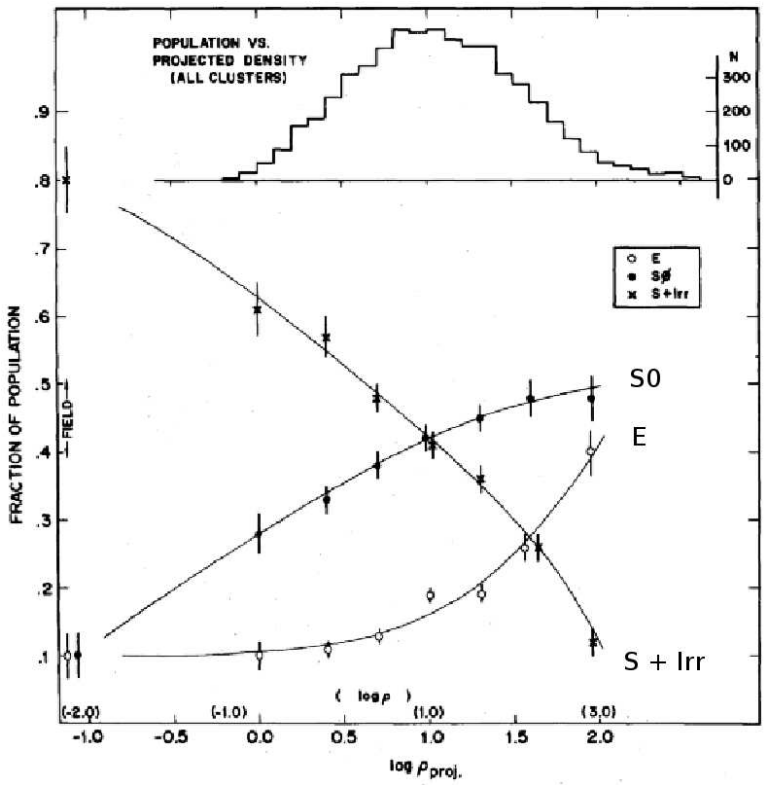

Figure 1.6: The morphology-density relation, from Dressler (1980). This plot first showed that, in the local universe, the fraction of S0 galaxies increases with density, whilst the spiral galaxy fraction decreases comparatively. This is considered to be strong observational evidence of transformation of spirals into S0 by the influence of cluster environment.

age and metallicity, the gas and dust content within galaxies, and the star formation activity. The gas is the reservoir of material from which stars are formed, while the stars themselves can give important clues about the age and metal content of the system. It is well known that spiral galaxies tend to have rich gas reservoirs and young stellar populations (hence their blue colours), while early-type galaxies (E/S0s) are known to have older stellar populations on average. A direct consequence of this is the colour bimodality found in cluster galaxies, composed of a tight red concentration of galaxies known as the "red sequence" and a more diffuse cloud of blue galaxies called the "blue cloud". This colour bimodality is thus well correlated with morphology (e.g. see recent work by Conselice, 2006; Wang *et al.*, 2007), implying that morphology correlates at some level with the stellar population content. Much work has been done in understanding the origin and evolution of the bimodality and the current picture is that the red sequence is built from bluer galaxies over cosmic time. On one hand, red sequence galaxies exhibit *redder* colours at lower redshift (Aragón-Salamanca *et al.*, 1993). The systematic trend in the infrared colours of cluster ellipticals up to $z \sim 1$,

supports a monotonic evolution with redshift, where red galaxies formed at $z > 2$ and aged passively since then. On the other hand, there is evidence for an increasing fraction of blue, star-forming galaxies in clusters at higher redshifts (Butcher & Oemler, 1984; Couch & Sharples, 1987; Ellingson *et al.*, 2001; Poggianti *et al.*, 2006). This effect, known as the "Butcher-Oemler effect", has triggered a significant amount of work in understanding the link between the evolving cluster population at intermediate redshifts with the predominantly quiescent ones at $z \sim 0$. A possible explanation is that the effect may be partially the result of galaxy-galaxy mergers (Dressler *et al.*, 1994; Couch *et al.*, 1994). Complementary studies of the star-formation activity in distant galaxies have confirmed that, in general, galaxies were producing far more stars at intermediate redshifts than they are at $z = 0$. However, from observations at $z \sim 0.7$, Bell *et al.* (2005) found that about half of these star-forming galaxies have undisturbed spiral morphology. They imply from these results that the rapid evolution of the cosmic star formation is not driven by a higher incidence of major mergers at these redshifts. Instead, it has been proposed that the star-formation can be effectively reduced by the influence of cluster environment (e.g. Poggianti *et al.*, 2006, 2008). Even fairly low-density environments (galaxy groups) have shown great effect on their star-formation activity (Poggianti *et al.*, 2006) and it has been proposed that galaxy pre-processing might occur in groups that are later accreted into more massive clusters (e.g. Zabludoff & Mulchaey, 1998; McGee *et al.*, 2009).

Although the effect of environment on galaxy evolution is unquestionable, galaxies have been caught in the act of transforming outside clusters, making the emerging galaxy evolution picture even more complex. Observations have discovered a class of galaxy with strong Balmer absorption lines but no optical emission lines (the so-called k+a or 'post-starburst' galaxies, Dressler & Gunn, 1983). The absence of emission lines suggest that there is no ongoing star formation, whilst the strong Balmer absorption is indicative of the presence of A stars and hence a recent (and rapid) truncation of star formation (within the past ~ 1 Gyr, Couch & Sharples, 1987; Poggianti *et al.*, 1999, 2009). These galaxies are understood to mark the transition from a star-forming disk galaxy into a quiescent spheroidal (Caldwell *et al.*, 1996; Zabludoff *et al.*, 1996; Yang *et al.*, 2004, 2008). Interestingly, k+a galaxies exist in clusters but are also found in the field (Zabludoff *et al.*, 1996). Cluster k+a galaxies however, are observed in a

transition phase, at the moment they are rather massive S0 and Sa galaxies, evolving to passive cluster early-types (Poggianti *et al.*, 2009).

So far, we have discussed the evolution of galaxy morphology, colour and star formation properties, but in order to build a complete picture of galaxy evolution, another important property must be included: galaxy mass. The mass of a galaxy is one of its most fundamental characteristics, and it is generally related to its total luminosity. Bundy *et al.* (2006) suggested that there is a threshold stellar mass above which star formation is somehow quenched. These results imply that galaxy evolution might be at some level, a consequence of intrinsic properties of galaxies ("nature", rather than "nurture").

The distribution of galaxy stellar mass at the present day and in the past is key in understanding the assembly of galaxies over cosmic time. Studies of the evolution of the stellar mass function indicate that blue galaxies do not show much evolution, even though these galaxies host the majority of the star formation. In contrast, the growth of the total stellar mass density is dominated by red sequence galaxies (Borch *et al.*, 2006). Moreover, Rudnick *et al.* (2009) studied the luminosity function of distant cluster galaxies and found that, while the bright end of the luminosity function is consistent with passive evolution, there is a significant build-up of the faint end of the red sequence toward lower redshift.

The debate between the "nature" and "nurture" scenarios for galaxy evolution has been arduous. On one hand, several studies (e.g. Bundy, Ellis & Conselice, 2005; Vergani *et al.*, 2008) have shown that mass plays a crucial rôle in determining galaxy properties and in driving their evolution. On the other hand, the stellar mass function of galaxies depends on environment (Baldry *et al.*, 2006; Bolzonella *et al.*, 2010). Evidently, mass and environment are linked, and it is thus important to study them with caution. Recently, Peng *et al.* (2010) have claimed that the effect of environment and mass are separable up to $z \sim 1$. From a large galaxy sample at low and high redshift (SDSS and zCOSMOS respectively), they propose an empirical law in which the quenching rate is related to the star formation rate and the local density. Although their empirical description works surprisingly well, it still doesn not provide a clear physical interpretation.

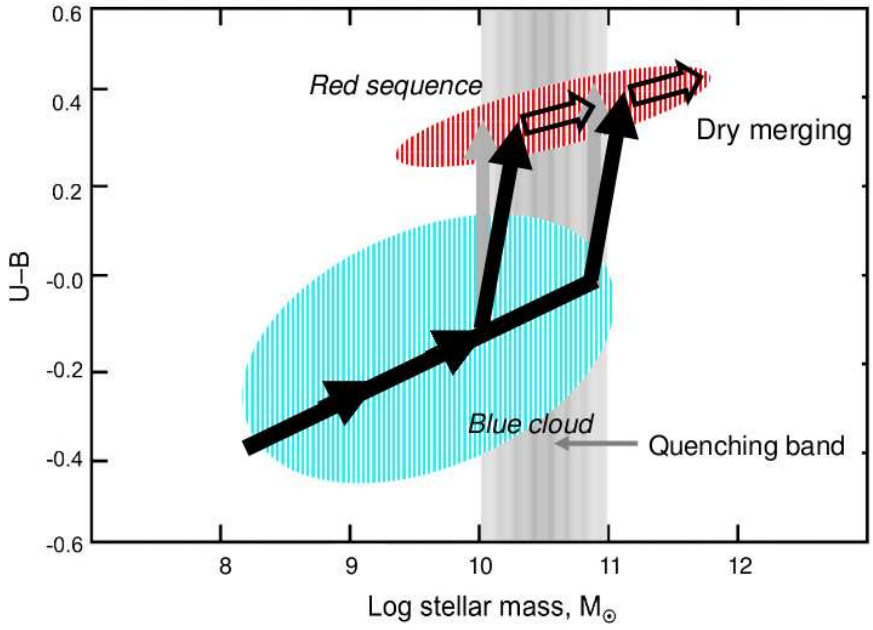

Figure 1.7: Schematic arrows showing galaxies migrating to the red sequence under a "mixed" merging hypothesis. Evolutionary tracks are plotted in the colour-mass diagram. Quenching tracks are shown by the nearly vertical black arrows. The mergers would be gas-rich ("wet") because the progenitor galaxies are blue objects making stars and hence contain gas. Once a galaxy arrives on the red sequence, it may evolve more slowly along it through a series of gas-poor, or "dry", mergers (open black arrows). They are tilted upward to reflect the ageing of the stellar populations during the more gradual dry merging. A major variable is the time of mass assembly vs. the time of quenching. Wet mergers are not the only way to transform blue galaxies into red ones. The gas supply of some disks may simply be choked off or stripped out without mergers (by the effect of cluster environment), to produce disky S0s. In this case, the evolutionary tracks would be vertical (see grey arrows), but aside from this their histories are similar. Adapted from Faber *et al.* (2007)

It is possible that there are various physical processes responsible for the transformation of galaxies, or that different mechanisms act in different environments, but this is still unclear. A number of plausible mechanisms have been proposed for spiral-to-S0 galaxies in clusters (discussed in depth in chapters 4 and 5). These include ram-pressure stripping by the intracluster medium (Gunn & Gott, 1972), numerous high speed encounters between galaxies or "harassment" (Moore *et al.*, 1999), and tidal interactions between galaxies and the gravitational potential of the cluster (Larson, Tinsley & Caldwell, 1980; Balogh, Navarro & Morris, 2000).

In summary, observations have shown that galaxies change their morphologies, stellar population, colours and masses through cosmic time, possibly transforming from blue, star-forming spirals into red and dead early-types. In doing that, they migrate from the blue cloud to the red sequence as shown schematically in figure 1.7. If we assume mergers as a transformation driver in this model, blue galaxies can either (i) populate

the lower-mass end of the red sequence[7] with cosmic time via "wet" (gas-rich) mergers, and once in the red sequence, galaxies grow in mass via "dry" (gas-poor) mergers, or (ii) populate the higher-mass end of the red sequence by having maximally late quenching, in which case they assemble most of their mass while still blue and then merge to become red with no or little further dry merging. In clusters however, galaxy mergers are rare due to the high velocities of the galaxies. In this case, the gas supply of some disks may simply be choked off or stripped out without mergers (by the effect of the environment), to produce disky S0s. Such evolutionary tracks would be vertical, as the galaxy migrates from the blue cloud to the red sequence without gaining mass (see vertical grey arrows in the diagram).

Although we have constructed a general galaxy evolution picture, the details of the mechanisms driving the evolution are still debated.

1.4 Motivation and thesis outline

With the aim of understanding the physical mechanisms driving massive galaxy formation and evolution, we study galaxy properties in a broad range of environments up to redshift of ~ 1. We use photometric and spectroscopic data from the ESO Distant Cluster Survey, which is described in chapter 2.

In chapter 3, we constrain the formation history of early-type galaxies, the oldest type of galaxies in the local universe. We do this by examining the colour-magnitude relation of morphologically selected elliptical and S0 galaxies in clusters of different masses and redshifts.

In chapters 4 and 5 we move our focus to the evolution of young (star-forming) galaxies. We investigate the effect of the environment on the transformation of star-forming spirals into passive S0s by studying the state of the gas and the stars in galaxies in different environments (chapter 4), as well as correlations between the star formation and scaling relations with environment (chapter 5).

Finally, the conclusions of this thesis are summarised in chapter 6, where future prospects

[7] Likely galaxies of S0 morphology, as S0s dominate on the red sequence below L^*, while ellipticals are common above that luminosity (Marinoni *et al.*, 1999).

are also described.

Throughout this thesis, we use Vega magnitudes and adopt the "concordance" ΛCDM cosmology with $\Omega_{\rm M} = 0.3$, $\Omega_{\Lambda} = 0.7$, and $H_0 = 70$ km s^{-1} Mpc^{-1} is assumed, unless otherwise stated.

Chapter 2

The Data

Throughout this thesis, different sub-samples of galaxies from the ESO Distant Cluster Survey (EDisCS) dataset are used.

The survey details are presented in this chapter, and in each of the following chapters the sub-set of galaxies utilized will be further described.

2.1 EDisCS

EDisCS is a multi-wavelength survey designed to study cluster structure and cluster galaxy evolution over a large fraction of cosmic time. The complete dataset is focused on 20 fields containing galaxy clusters at redshifts between 0.4 and 1. The cluster sample was selected to be among 30 of the highest surface brightness candidates in the Las Campanas Distant Cluster Survey (Gonzalez *et al.*, 2001), after confirming the presence of an apparent cluster and a possible red sequence with Very Large Telescope (VLT) 20-min exposures in two filters. From these candidates, 10 of the highest surface brightness clusters were followed up in each of two bins at estimated redshifts $0.45 < z_{est} < 0.55$ and $0.75 < z_{est} < 0.85$, where z_{est} was based on the magnitude of the putative brightest cluster galaxy.

For the 20 fields with confirmed cluster candidates, matched optical photometry was taken using FORS2 at the VLT (see White *et al.*, 2005, for a detailed description). In brief, the optical photometry consists of B, V and I imaging for the 10 intermediate-

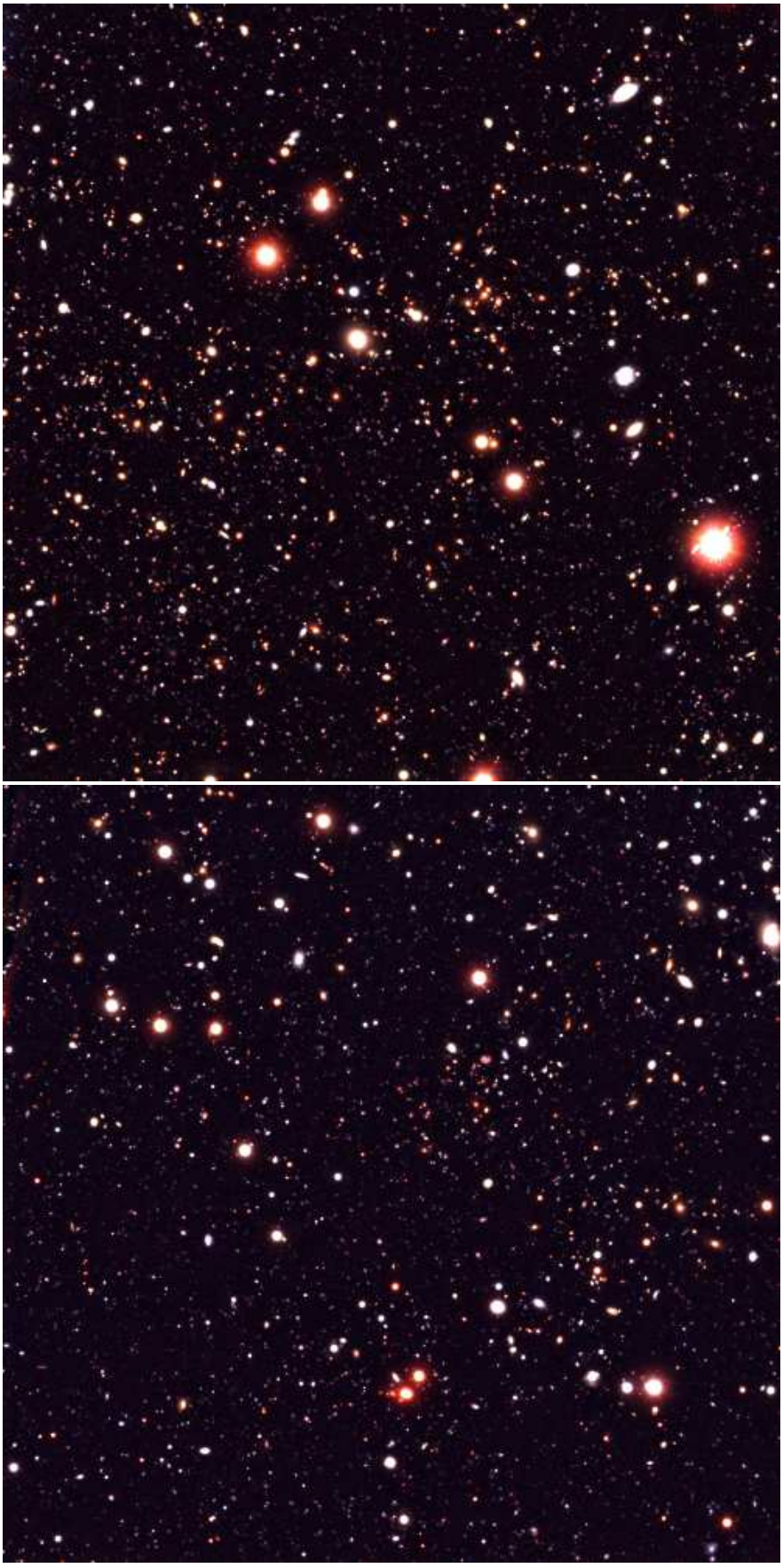

Figure 2.1: Two (VRI) colour composite images of EDisCS clusters are shown as examples. Top: CL 1054.4−1146 (z =0.70, cluster velocity dispersion $\sigma_{\rm cl} = 589$ km/s). Botom: CL 1103.7−1245 (z =0.96, 0.70, 0.63, $\sigma_{\rm cl} = 534, 252, 336$ km/s).

redshift ($z_{est} \backsimeq 0.5$) cluster candidates and V, R and I imaging for the 10 high-redshift ($z_{est} \backsimeq 0.75$) cluster candidates. Typically, the integration times were 45 min for the intermediate-redshift sample and 2 h for the high-redshift sample. Figure 2.1 shows two example composite images. In addition, near-IR J and K photometry was obtained for most clusters using SOFI at the New Technology Telescope (NTT) (Aragón-Salamanca et al., in preparation). Deep multi-slit spectroscopy with FORS2/VLT (Halliday *et al.*, 2004; Milvang-Jensen *et al.*, 2008) showed that several of the confirmed fields contained multiple clusters at different redshifts (cf. also Gonzalez *et al.*, 2002; White *et al.*, 2005).

The spectroscopic targets were selected from I-band catalogues (Halliday *et al.*, 2004). Conservative rejection criteria based on photometric redshifts (Pelló *et al.*, 2009), I-band magnitudes, star-galaxy separation parameters, and FWHM (or ellipticity) were used in the selection of spectroscopic targets to reject a significant fraction of non-members, while retaining a spectroscopic sample of cluster galaxies equivalent to a purely I-band selected one. Halliday *et al.* (2004) and Milvang-Jensen *et al.* (2008) verified that these criteria excluded at most 1.3% of cluster galaxies.

The extensive spectroscopic observations were taken with the MXU multi-object mask facility of the FORS2 spectrograph mounted on the VLT Yepun UT4 telescope, ESO Paranal. The field of view of the FORS2 instrument is $6.8' \times 6.8'$. The observations consist of high signal-to-noise data for $\sim 30 - 50$ members per cluster and a comparable number of field galaxies in each field down to $I \sim 22$. The wavelength ranged typically from 5300 Å to 8000 Å for two of the runs and 5120 Å to 8450 Å for the other two, although the exact wavelength range for each galaxy depends on its exact position on the mask. The mask design gave priority to target galaxies, but included non-targeted objects when there was free space in the masks. The exposure times were typically 4 hours for the high-z sample and 1 or 2 hours for the mid-z one. Given the long exposure times, the success rate for the spectroscopic redshifts is 97% above the magnitude limit. The completeness of the spectroscopic catalogues, which depends on galaxy magnitude and distance from the cluster centre, was computed for each cluster in Poggianti *et al.* (2006). Typically, the spectroscopy samples a region out to a cluster-centric radius equal to R_{200}[1] (see Poggianti *et al.*, 2009, and references therein).

[1] R_{200} is the radius delimiting a sphere that has mean density in the interior equal to 200 times the

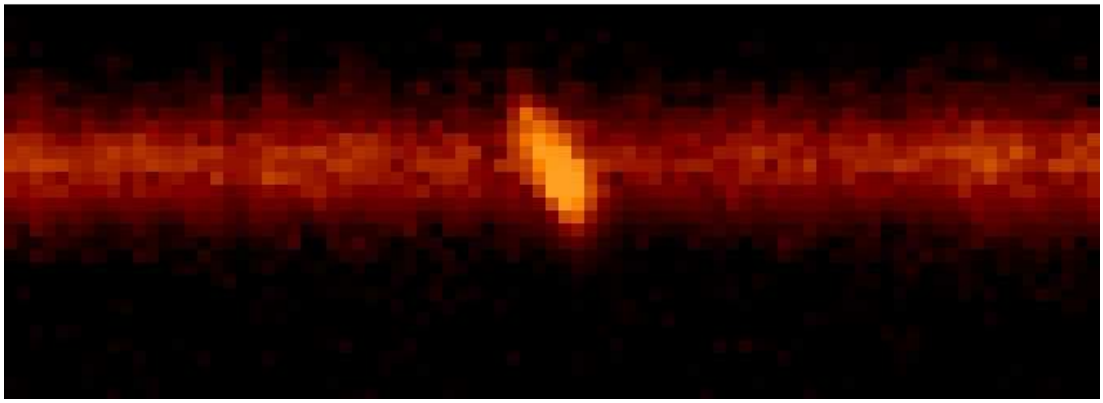

Figure 2.2: Example of a 2-dimensional emission-line spectrum of a galaxy at $z = 0.47$. In this spectrum, the dispersion direction is horizontal, and the spacial direction is vertical. The prominent emission line seen is the [OII]3727 Å doublet. Although the doublet is not resolved, the emission feature is clearly tilted due to rotation.

The slit size used for the spectroscopic observations was 10×1 arcseconds, and the spectra have a dispersion of 1.32 Å pix^{-1} or 1.66 Å pix^{-1}, depending on the observing run. The masks were designed using the I-band images, since they best correspond to the wavelength range chosen for the spectroscopy. The slits were aligned with the major axis of the targeted object if the tilting of the slit did not exceed $\pm 45°$. In the second run however, this was only done for objects identified as late-types by the photometric redshift code (we refer to Halliday *et al.* (2004); Milvang-Jensen *et al.* (2008) for full details on the mask design).

The FWHM resolution of the spectroscopy is ~ 6 Å, corresponding to rest-frame 3.8Å at $z = 0.6$. This translates into a rest-frame 1σ velocity resolution of ~ 70 km/s at 6780 Å (central wavelength of grism 600RI+19). For the typical signal-to-noise ratio in the emission lines, this means that reliable rotation velocities can be measured down to ~ 20 km/s. An example two-dimensional spectrum is shown in figure 2.2.

Spectroscopic redshifts were measured using emission lines where possible, in particular the [OII]λ3727 line, or the most prominent absorption lines (see Milvang-Jensen *et al.* (2008)). Figure 2.3 shows the redshift distribution of the galaxies with spectroscopy.

critical density.

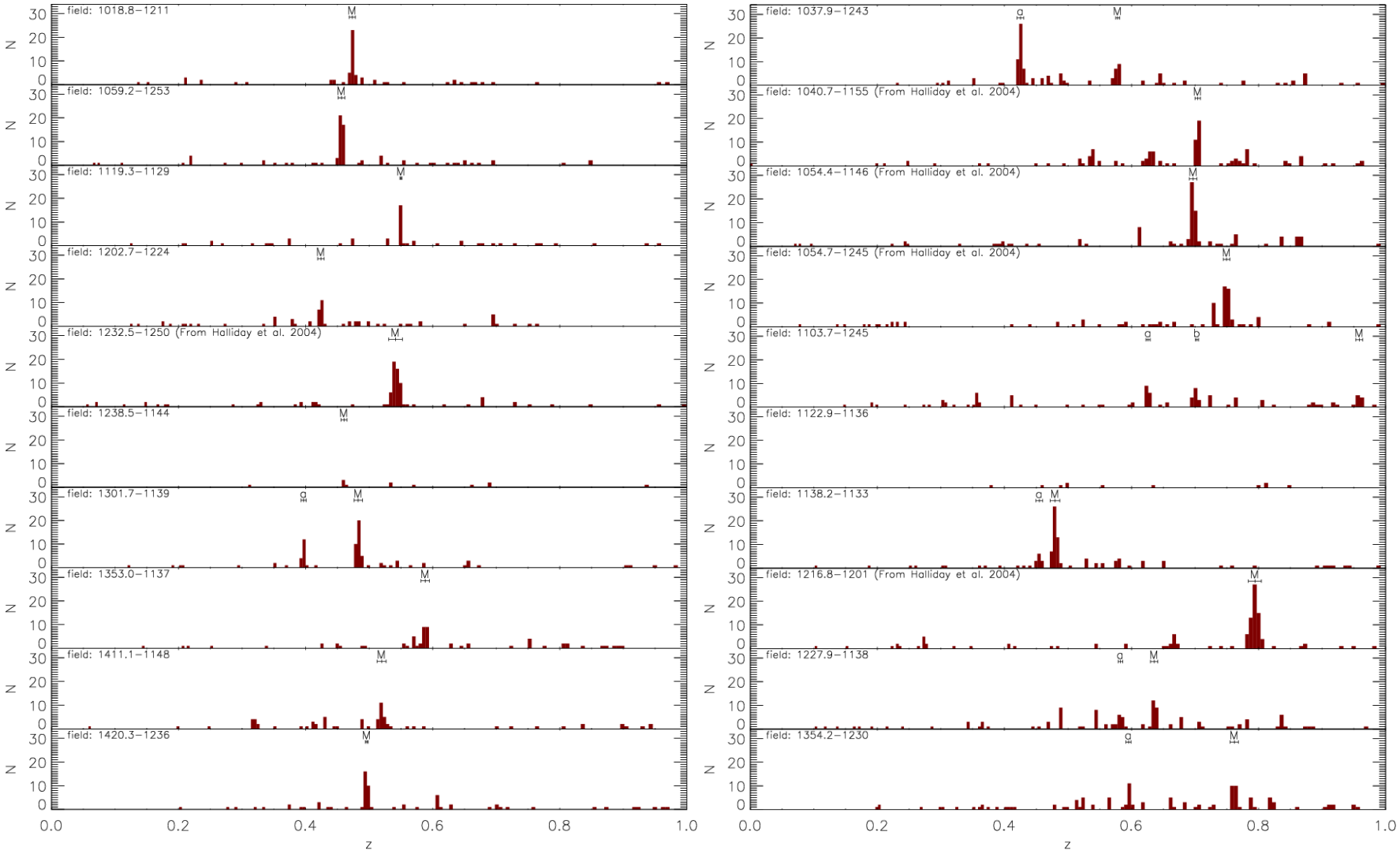

Figure 2.3: Redshift histograms for the 20 EDisCS fields, from Milvang-Jensen *et al.* (2008). The labels are "M" for the main cluster and "a" or "b" for secondary clusters. The binsize in z, Δz, varies with z in such a way that the binsize in rest-frame velocity, $\Delta v_{\rm rest} = c\Delta z/(1+z)$, is kept constant at 1000 km s-1. This is achieved binning in $\log\ (1+z)$ space with a constant binsize of $\log\ (\Delta v_{\rm rest}/c + 1)$.

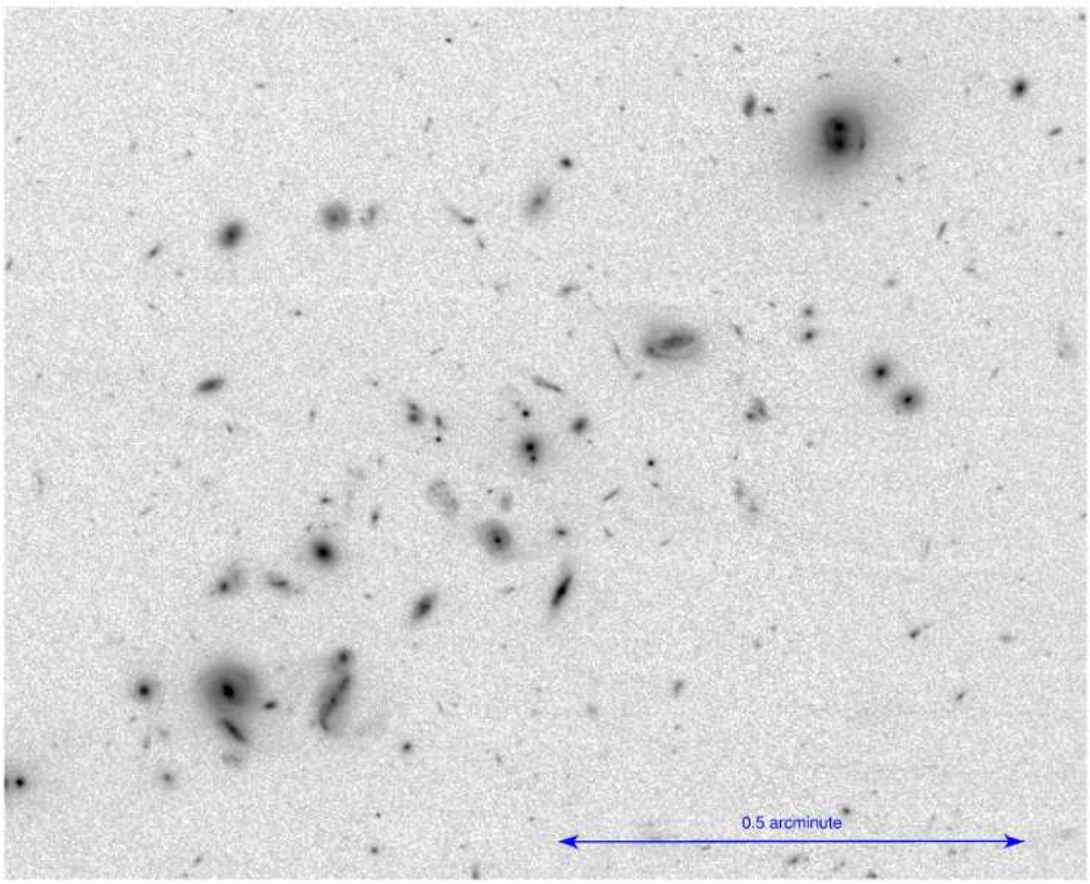

[!b]

Figure 2.4: An HST view of cluster 1037. Galaxies of different morphologies can be easily spotted in the image. The arrow indicates the size of 0.5 arcminutes, which at the cluster redshift ($z \cong 0.4$) is equivalent to $\sim$165 kpc.

In addition to this, ten of the highest redshift clusters from the database were enriched with Hubble Space Telescope (HST) mosaic imaging in the F814W filter with the Advanced Camera for Surveys Wide Field Camera (Desai *et al.*, 2007). This allowed us to perform a visual morphological classification of the galaxies in these fields. An example HST image is shown in figure 2.4. The morphological classification was done visually, by a team of expert classifiers (see Desai *et al.*, 2007, for details).

Additional follow-up of EDisCS fields includes narrow-band Hα imaging (Finn *et al.*, 2005) and XMM X-ray observations (Johnson *et al.*, 2006) for a subset of the clusters.

One of the key advantages of EDisCS is its ability to probe a large range of environments, as it contains a large and homogeneous sample of galaxies in clusters, groups, and the field. Cluster and field galaxies were distinguished using spectroscopic redshift information. Galaxies whose spectroscopic redshift places them within $\pm 3\sigma_{cluster}$ of the $z_{cluster}$ in rest-frame peculiar velocity were considered cluster mem-

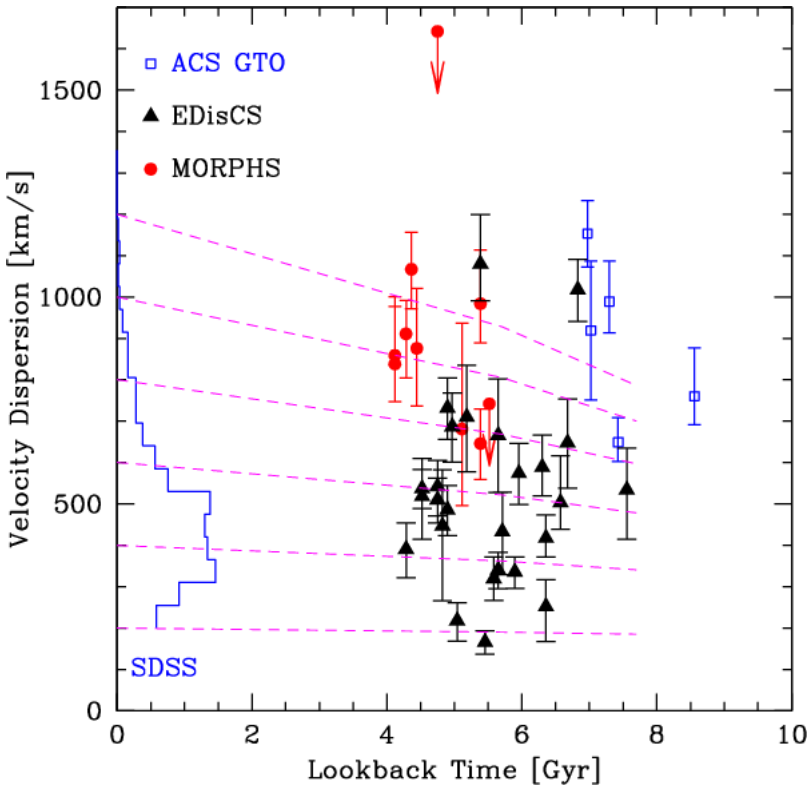

Figure 2.5: The distribution of velocity dispersion vs. lookback time for EDisCS (black points) and for two other well-studied cluster samples at similar redshifts (red and blue points), as well as for a well-studied local sample (histogram). Dashed lines show how the velocity dispersion is expected to evolve with time. From Milvang-Jensen *et al.* (2008).

bers. Galaxies with z outside this range were flagged as field population (see Halliday *et al.*, 2004; Milvang-Jensen *et al.*, 2008). EDisCS clusters have velocity dispersion in the range $400 < \sigma_v < 1100$ km/s. Galaxy groups with velocity dispersion of $160 < \sigma_v < 400$km/s are also present (See Poggianti *et al.*, 2009, for further details). Unless stated otherwise, the group and cluster population will be studied together.

The EDisCS dataset is larger than all previous (similar) studies at high redshift and not only has the advantage of spanning a broad range in cluster properties but also contains a significant field sample to match the cluster galaxies (see figure 2.3). Figure 2.5 illustrates the wide velocity dispersion range of EDisCS clusters. From this plot it is apparent that EDisCS clusters span a wide range of velocity dispersions (and hence masses), and that the majority of EDisCS clusters can be progenitors of typical low redshift clusters.

Chapter 3

Formation of early-type cluster galaxies

3.1 Introduction

Galaxy clusters have proven to be very useful laboratories for the study of galaxy formation and evolution. They can provide large and diverse galaxy samples across practically small areas of sky. Although the relative importance of nature and nurture in shaping galaxy evolution remains debated, it is well established that many galaxy properties in the nearby Universe correlate strongly with their environment. In this chapter, we will study the properties of E/S0 galaxies in clusters in order to better understand galaxy formation and evolution.

In section 1.3, we mentioned observational evidence for a colour bimodality present in cluster galaxies (e.g. Conselice, 2006; Wang *et al.*, 2007, and references therein). From this bimodality, we are able to divide galaxies into three distinct groups: (i) the "blue cloud", dominated by spirals and irregular galaxies, (ii) the "red sequence", the prominent ridge of red galaxies (mainly passive E/S0), and (iii) a less distinct group of presumably transition objects in the so-called "green valley".

The existence of a red sequence of cluster ellipticals in the local Universe was established by the works of Baum (1959), Faber (1973) and Caldwell (1983). They showed that these galaxies have systematically redder colours with increasing luminosity. Vis-

vanathan & Sandage (1977) and Sandage & Visvanathan (1978a,b) later found that this colour-magnitude relation (hereafter CMR) is universal. The detailed study of the UVK colours of local cluster early-type galaxies carried out by Bower, Lucey & Ellis (1992) confirmed Sandage & Visvanathan's anticipation that both S0s and ellipticals follow the same relation. Furthermore, they also showed that the observed scatter about the CMR is very small (~ 0.04 mag in $U - V$ for their sample).

In the past decade, a number of studies have shown that the CMR of elliptical galaxies holds at progressively higher redshifts, at least up to $z = 1.4$ (e.g. Ellis *et al.*, 1997; Stanford, Eisenhardt & Dickinson, 1998; van Dokkum *et al.*, 2000, 2001; Blakeslee *et al.*, 2003; Mei *et al.*, 2006; Lidman *et al.*, 2008). As a consequence, the CMR is, arguably, one of the most powerful scaling relations obeyed by the early-type galaxy population at the cores of clusters, encoding important information about their formation history.

The slope of the CMR has traditionally been interpreted as the direct consequence of a mass-metallicity relation (e.g. Faber, 1973; Larson, 1974; Gallazzi *et al.*, 2006). The classical explanation of this mass-metallicity sequence is based on the idea that star-formation-induced galactic outflows would be more efficient at expelling metal-enriched gas in low-mass galaxies than in massive ones (e.g. Larson, 1974; Dekel & Silk, 1986; Tremonti *et al.*, 2004; De Lucia, Kauffmann & White, 2004; Kobayashi, Springel & White, 2007; Finlator & Davé, 2008; Arimoto & Yoshii, 1987). An alternative interpretation in which the CMR is predominantly an age sequence would imply that the relation changes significantly with redshift as less massive galaxies approach their formation epochs. The possibility that age is the main driver for the CMR was ruled out by observations of clusters at intermediate redshift that showed that the slope of the CMR evolves little with redshift (Kodama & Arimoto, 1997; Kodama *et al.*, 1998). Nevertheless, weak age trends along the CMR have been claimed (e.g. Ferreras, Charlot & Silk, 1999; Poggianti *et al.*, 2001; Nelan *et al.*, 2005), even though it seems clear that they are not the main physical driver.

Bower, Lucey & Ellis (1992) interpreted the small scatter about the CMR as the result of small age differences at a given galaxy mass. The tightness of the relation then implies very synchronized star-formation histories for these galaxies. Larger colour

scatter would imply later episodes of star-formation, or a wider range in galaxy formation redshifts. These results are not only indicative of the passive evolution of elliptical galaxies but also of an early formation epoch ($z > 2$–3; e.g. Bower, Lucey & Ellis, 1992; Blakeslee *et al.*, 2003; Mei *et al.*, 2009). Studies of absorption-line indices in the spectra of early-type galaxies also imply old ages (e.g. Trager *et al.*, 1998). Furthermore, combined evidence from studies of the Faber-Jackson, Mgb-σ and Fundamental Plane, and line strengths, also agree with passive evolution of cluster early-type galaxies (see e.g. Ziegler *et al.*, 2001; Fritz, Böhm & Ziegler, 2009, and references therein). Some evidence has been found that the mean stellar ages of early-type galaxies may depend on their stellar mass in the sense that lower-mass galaxies appear to have formed their stars at later epochs than the more massive ones (e.g. Thomas *et al.*, 2005), although Trager, Faber & Dressler (2008) find no such trend in their study of the Coma cluster.

The above interpretation of the nature of the CMR, although traditionally accepted, has an important problem: it assumes that all red-sequence galaxies that we see today can be identified as red-sequence members of high redshift galaxy clusters. As noted by van Dokkum & Franx (1996), this assumption is probably wrong because of the so-called *progenitor bias*: if the progenitors of some early-type galaxies were spirals at higher redshift, they would not be included in the higher redshift samples, which biases the studied population towards older ages. This effect has been corroborated by recent studies of the CMR evolution. De Lucia *et al.* (2007) found a significant deficit of faint red cluster galaxies at $0.4 \lesssim z \lesssim 0.8$ compared to galaxy clusters in the local Universe. They conclude that the red sequence population of high redshift clusters does not contain all the progenitors of nearby red sequence cluster galaxies (see also De Lucia *et al.*, 2009, and references therein). Tanaka *et al.* (2008) also find such deficit in a galaxy cluster at $z = 1.1$. We will come back to this issue in sections 3.4 and 3.7.

In this chapter, we present a study of the CMR for a total sample of 174 morphologically-selected elliptical and S0 galaxies contained in 13 galaxy clusters and groups at $0.4 \lesssim z \lesssim 0.8$ from the ESO Distant Cluster Survey (White *et al.*, 2005, EDisCS), taking advantage of the availability of extensive Hubble Space Telescope (HST) imaging

obtained with the Advanced Camera for Surveys (ACS) and extensive ground-based imaging and spectroscopy (see chapter 2). We interpret the scatter about the CMR as a proxy for age (or formation time t_F), and study its dependence on intrinsic galaxy properties such as their luminosities and morphologies, and the role of the environment as quantified by the mass/velocity dispersion of the clusters. We complement the scatter analysis with information derived from the zeropoint of each cluster's CMR to constrain not only the formation epoch of early-type galaxies but also the duration of their formation phase.

It is important to point out that, even though there is much evidence suggesting that the CMR scatter is principally driven by galaxy age (e.g. Kodama & Arimoto, 1997; Kauffmann & Charlot, 1998; Bernardi *et al.*, 2005), metallicity variations could also contribute to it (Nelan *et al.*, 2005). If that is the case, the stellar ages we derive here would be lower limits since the colour scatter we measure would contain both an age component and a metallicity one. Taking the results of Nelan *et al.* (2005) at face value, the maximum scatter in metallicity at a given velocity dispersion (luminosity) is ~ 0.1dex, implying that at most we could be systematically underestimating the stellar ages by ~ 0.15dex, where we have assumed Worthey (1994) $3/2$ age-metallicity degeneracy law. Notwithstanding this caveat, even if the absolute ages were affected at this level, it is not unreasonable to expect that the effect on relative ages (the main focus of this chapter) would be smaller.

3.2 The sample of cluster early-type galaxies

This chapter focuses on a sub-sample of galaxies from the EDisCS dataset (fully described in chapter 2). The selection yielded 174 E/S0 galaxies in 13 clusters/groups and was based on the following criteria:

1. The galaxies must be spectroscopically-confirmed cluster/group members (Halliday *et al.*, 2004; Milvang-Jensen *et al.*, 2008). This ensures a very clean sample, avoiding the uncertainties introduced by other cluster membership criteria such as photometric redshifts (Rudnick *et al.*, 2009; Pelló *et al.*, 2009). The penalty is, of course, a significant reduction in the sample size.

2. They must have early-type morphology (E or S0), based on visual classification from HST images (Desai *et al.*, 2007). We note that by imposing this, the sample reduces to galaxies within the 10 fields observed with HST.

3. The galaxies should belong to clusters/groups with at least 4 early-type members in order to measure the CMR scatter with reasonable accuracy. This allows us to detect the presence of an intrinsic colour scatter with $> 3\sigma$ confidence in all cases.

Since all spectroscopically-confirmed members in the HST-covered area have been morphologically classified, the selection function of our sample is the same as that of the spectroscopic sample (with a magnitude limit of $I \sim 22$). This means that for all practical purposes our early-type galaxy sample behaves like the original I-band selected spectroscopic sample (Milvang-Jensen *et al.*, 2008), and therefore as a rest-frame B-band selected sample. On average we typically reach $M_B < -18.5$, with some cluster-to-cluster variation. Although all our analysis has been carried out using this empirically-defined I-band selected sample, thus maximizing the sample size, we have checked that using a rest-frame B-band luminosity selected sample would not have altered any of our conclusions. We have also checked that the spectroscopic selection function does not affect our conclusions. We produced Monte Carlo realizations of the colour-magnitude diagram of our sample taking into account the empirical selection function determined by Milvang-Jensen *et al.* (2008) and found that the simulated colour scatter agrees very well with the measured one.

To test the robustness of the morphologies for the galaxies in our sample, we re-examined visually their HST images (see figure 3.1). It turned out that only two galaxies had been misclassified as early-types in Desai *et al.* (2007). The first one, EDCSNJ1138096−1135223, is clearly not an elliptical and shows a very perturbed morphology. The second one, EDCSNJ1138127−1134190, is in a dense group of (probably) interacting galaxies and there is a bright elliptical very close to the position of this object. It is obvious that the wrong galaxy was classified. The last two lines of table 3.4 show some of the properties of these two galaxies and their HST F814W images are shown in the bottom row of figure 3.1. It is not surprising that both galaxies are substantially bluer than the red-sequence. They are also quite faint, where

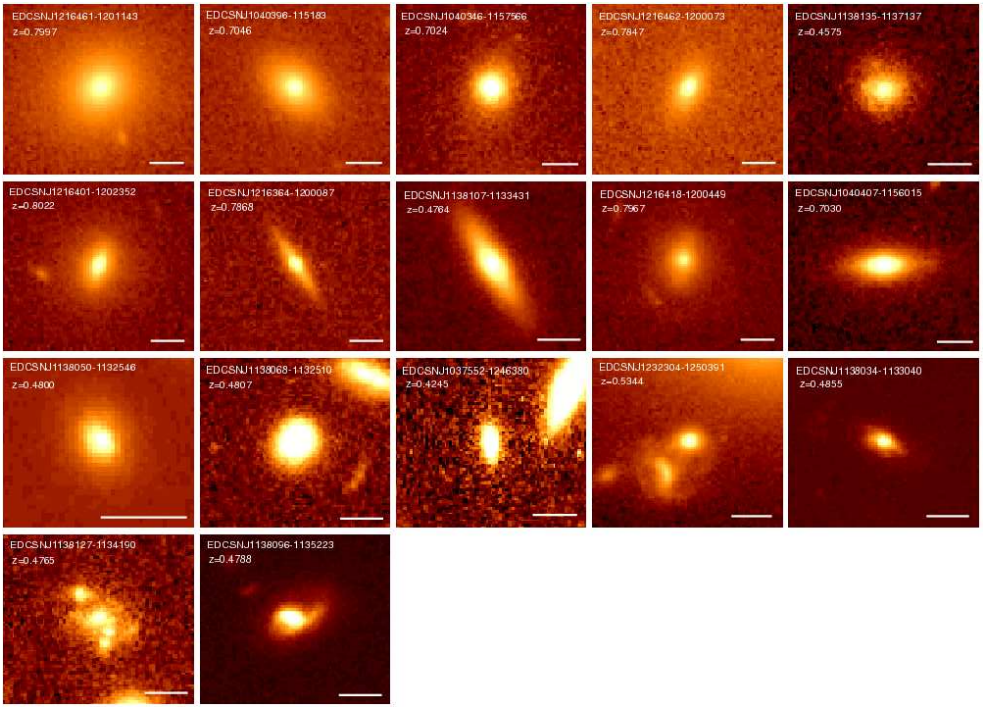

Figure 3.1: HST F814W images for a representative sample of ellipticals (top row), S0s (second row) and "blue tail" galaxies (third row). The last row shows the 2 galaxies that were excluded from our study due to morphological misclassification. The rightmost 2 galaxies in the third row (blue tail) exhibit some degree of perturbation in their morphologies (see text for further discussion). The horizontal white lines correspond to 5 kpc.

visual classification is, perforce, less reliable. These two misclassified galaxies were removed from our sample and will not be discussed further. We noticed that 6 out of the remaining 172 galaxies (3.5%) have signs of perturbation, although their early-type morphology is clear. Interestingly, 2 out of these 6 slightly perturbed galaxies are significantly bluer than the CMR. We will come back to this in section 3.4.

The cluster sample with the corresponding redshifts, line-of-sight velocity dispersions (σ_v) and number of early-type members is shown in table 3.1. The σ_v's are taken from Halliday *et al.* (2004) and Milvang-Jensen *et al.* (2008). The reliability of these velocity dispersions as mass estimators has been confirmed by weak lensing (Clowe *et al.*, 2006) and X-ray (Johnson *et al.*, 2006) estimates.

For consistency with previous work on the CMR of EDisCS cluster galaxies (De Lucia *et al.*, 2007), in the following we use magnitudes and colours measured in seeing-matched images with $FWHM = 0.8$ arcsec (the typical seeing in the optical images), using a fixed 1.0 arcsec radius circular aperture. This aperture represents a compromise between minimizing sky-subtraction and contamination errors and being as close

Table 3.1: Properties of the EDisCS cluster sample used in the analysis of this chapter. The columns correspond to: cluster ID, spectroscopic redshift, line-of-sight velocity dispersion, number (N) of early-type galaxies (E+S0), number ellipticals (N(E)) taken into account in the scatter calculation, and number of "blue tail" members ($N_{\rm blue}$). See text for details. Cluster redshifts and velocity dispersions were taken from Halliday *et al.* (2004) and Milvang-Jensen *et al.* (2008).

Cluster name	z	σ_v (km/s)	N(E+S0)	N(E)	$N_{\rm blue}$
Cl1037.9−1243a	0.4252	537^{+46}_{-48}	12	7	1
Cl1138.2−1133a	0.4548	542^{+63}_{-71}	9	7	1
Cl1138.2−1133	0.4796	732^{+72}_{-76}	16	11	3
Cl1232.5−1250	0.5414	1080^{+119}_{-89}	23	15	3
Cl1354.2−1230a	0.5952	433^{+95}_{-104}	4	4	0
Cl1103.7−1245a	0.6261	336^{+36}_{-40}	4	4	0
Cl1227.9−1138	0.6357	574^{+72}_{-75}	8	3	0
Cl1054.4−1146	0.6972	589^{+78}_{-70}	16	14	2
Cl1040.7−1155	0.7043	418^{+55}_{-46}	8	7	0
Cl1054.7−1245a	0.7305	182^{+58}_{-69}	6	5	0
Cl1054.7−1245	0.7498	504^{+113}_{-65}	18	13	0
Cl1354.2−1230	0.7620	648^{+105}_{-110}	5	4	2
Cl1216.8−1201	0.7943	1018^{+73}_{-77}	31	18	0

as possible to measuring global colours. We note that 1.0 arcsec corresponds to $\simeq 7$ kpc at $z \simeq 0.7$, and at these redshifts early-type galaxies in the luminosity range considered here have half-light radii ~ 3 kpc (Treu *et al.*, 2005; Trujillo *et al.*, 2007). The associated photometric errors were derived by placing empty apertures in regions of the image without detected objects to estimate accurately the sky contribution to the error budget. This is justified since the sky noise is the dominant source of error when measuring the aperture magnitudes of our faint galaxies (see White *et al.*, 2005, for details).

3.3 Method: the scatter-age test

The scatter-age test carried out in this thesis was developed by Bower, Lucey & Ellis (1992) as a reasonably simple, yet powerful method for constraining the formation history of early-type galaxies. They applied it at $z \sim 0$ to galaxies in the Virgo and Coma clusters. Ellis *et al.* (1997) applied the same test to galaxies in three $z \sim 0.54$

clusters. We apply it here to a much larger cluster sample, covering a significant cluster mass range. We have the added advantage that since 1997 the uncertainty in the cosmological parameters, and thus the transformation of redshift into look-back time, has decreased considerably. We also benefit from a large and homogeneous galaxy sample in a wide range of redshift and cluster velocity dispersion (or cluster mass). This method has been used by many authors in the past (e.g. van Dokkum *et al.*, 1998; Stanford, Eisenhardt & Dickinson, 1998; Blakeslee *et al.*, 2003, 2006; Mei *et al.*, 2006, 2009; Hilton *et al.*, 2009). A description of the specific steps we took to perform the scatter-age test follows.

We first constructed colour-magnitude diagrams (CMDs) of the early-type galaxies in each cluster using the photometric bands closest to rest-frame U and V. Rest-frame $U-V$ measures the strength of the 4000Å break and is therefore a very age-sensitive broadband colour (see section 3.3.1 for a detailed justification of our choice of observed colour). For most of the clusters this choice required CMDs of $R-I$ versus I, but for the three lowest redshift clusters we used $V-I$ versus I (see table 3.2). We then fitted a linear CMR for each cluster using a fixed slope of -0.09 [1] and setting the zeropoint to the median colour. This procedure is very robust, in particular for groups and clusters with small numbers of galaxies where the CMR slope cannot be determined to sufficient accuracy. Our results are not sensitive to the exact choice of slope since in general the CMR is reasonably flat and redshift-independent (Holden *et al.*, 2004). As an example, the CMD for the early-type galaxies in cluster CL1216.8−1201 is shown in figure 3.2. The full set of CMDs for our EDisCS cluster sample can be found in Appendix A.

For each cluster, the observed scatter in the galaxy colours about the CMR ($\sigma_{\rm obs}$) was computed as the r.m.s. of the residuals (in the colour direction) between the observed colours and the fitted CMR. We reject outliers in this process by imposing the condition that galaxy colours should be within ± 0.3 mag from the CMR. While other methods such as the biweight scatter estimator used by other authors (e.g. Mei *et al.*, 2009) reject outliers implicitly, we chose to do it explicitly. We discuss these outliers in some detail later.

[1] This value was previously used in De Lucia *et al.* (2007) to construct V-I CMRs for colour selected red-sequence galaxies from the EDisCS database

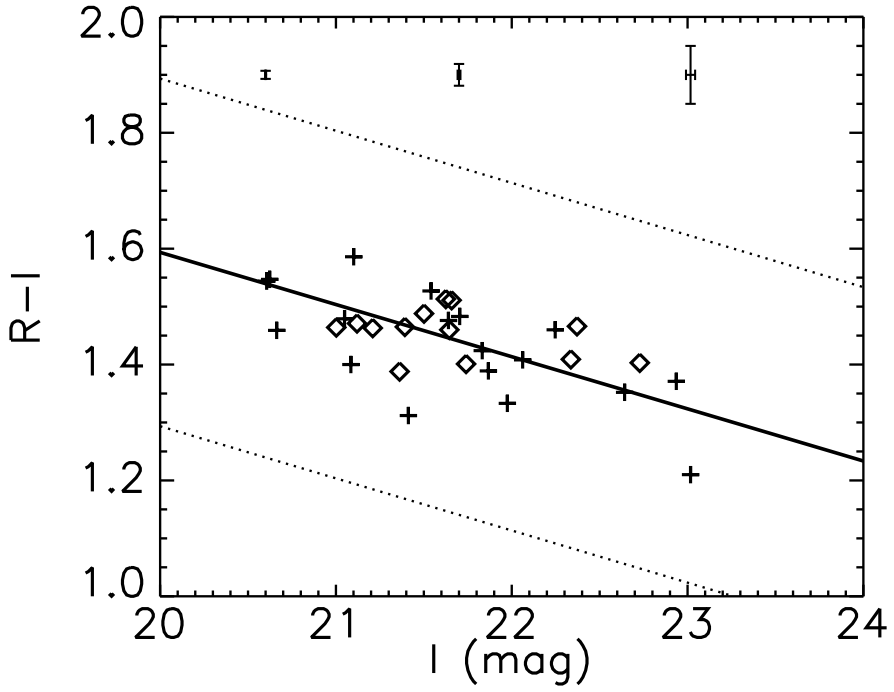

Figure 3.2: The $R-I$ vs. I colour-magnitude diagram for the early-type galaxies in cluster CL1216.8−1201 at $z = 0.79$ is shown here as an example. The full set of CMDs for our EDisCS clusters can be found in Appendix A. Elliptical galaxies are represented by "+" signs, and S0s by open diamonds. The solid line shows a linear fit to the colour-magnitude relation with the slope value determined by De Lucia *et al.* (2007). See text for details. The dotted lines correspond to ± 0.3 mag from the CMR. For reference, the typical sizes of the error bars are plotted on the top of the figure as a function of magnitude.

Following Bower, Lucey & Ellis (1992), the intrinsic scatter ($\sigma_{\rm int}$) was then obtained by subtracting, in quadrature, the mean value of the photometric colour uncertainty from the observed scatter. The colour uncertainties range from 0.012 to 0.021 (White *et al.*, 2005), and have therefore little effect on the observed scatter (see section 3.4).

Bower, Lucey & Ellis (1992) used $\sigma_{\rm int}$ to constrain the formation history of the galaxies by assuming the following relationship between the colour scatter and the colour evolution of the stellar population (Bower, Lucey & Ellis, 1992):

$$\delta(U-V)_0 = \frac{d(U-V)_0}{dt}(t_{\rm H} - t_{\rm F})\beta \leq \sigma_{\rm int}, \tag{3.1}$$

where $t_{\rm H}$ is the age of the Universe at the cluster redshift, $t_{\rm F}$ is the look-back time from then to the epoch at which star formation ended, and $d(U-V)_0/dt$ (where the subscript "0" denotes rest-frame) is derived from galaxy evolution models. This factor should be reasonably well understood as it is mainly governed by main-sequence evolution (for a given IMF). In this equation, β parametrizes the spread in formation time Δt as

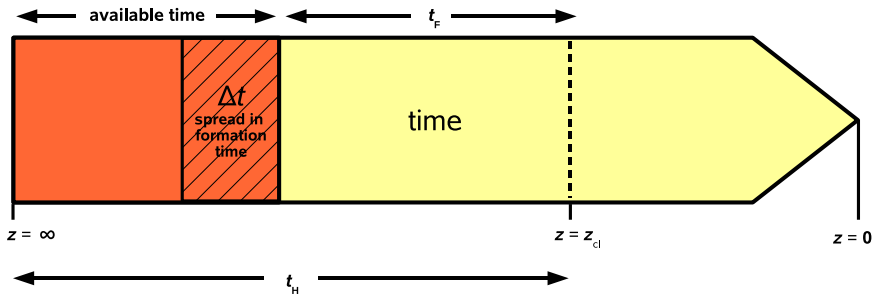

Figure 3.3: Time-line of the Universe illustrating the different parameters used in equations 3.1 and 3.2. The time arrow starts on the left at the beginning of the Universe ($z = \infty$). The orange region shows the total available time galaxies can use to form stars. Δt is the time galaxies actually spend forming stars. From then on, the cluster galaxies are assumed to evolve passively until the observed redshift (z_{cl}). We define $t_{\rm F}$ as the time elapsed from the epoch when star formation ended until the cosmic time corresponding to z_{cl}.

a fraction of the total available time:

$$\beta = \frac{\Delta t}{(t_{\rm H} - t_{\rm F})}. \tag{3.2}$$

Thus, $\beta = 1$ implies no synchronization, i.e. the galaxies in the sample formed using all the available time, while $\beta = 0.1$ would mean a high degree of synchronization, with all the galaxies forming in the last 10% of the available time. Figure 3.3 illustrates the time-line defined by equations 3.1 and 3.2.

We calculated the $d(U-V)_0/dt$ factor using Bruzual & Charlot (2003, hereafter BC03) models[2] for a passively-evolving stellar populations that formed in a single burst of 0.1 Gyr duration. The exact burst duration does not have a significant effect on our conclusions provided that it is much shorter than $t_{\rm F}$. Solar metallicity ($Z_{\odot} = 0.02$), a Chabrier (2003) initial mass function (IMF) and no dust attenuation were assumed. Using alternative IMFs (e.g. Salpeter, 1955) would not alter our conclusions because for the stellar masses of interest (given the range in $t_{\rm F}$), the relative differences in the IMFs are only minor (cf. Bower, Lucey & Ellis, 1992). The use of models with solar metallicity is partially motivated by the results presented in Sánchez-Blázquez *et al.* (2009), where ages and metallicities are derived for EDisCS red-sequence galaxies from their absorption line indices. Sánchez-Blázquez *et al.* (2009) found solar-metallicity mod-

[2]For the range of ages discussed in this chapter and the optical colours on which we base our conclusions, using alternative population synthesis models such as those of Maraston (2005) would not change our results.

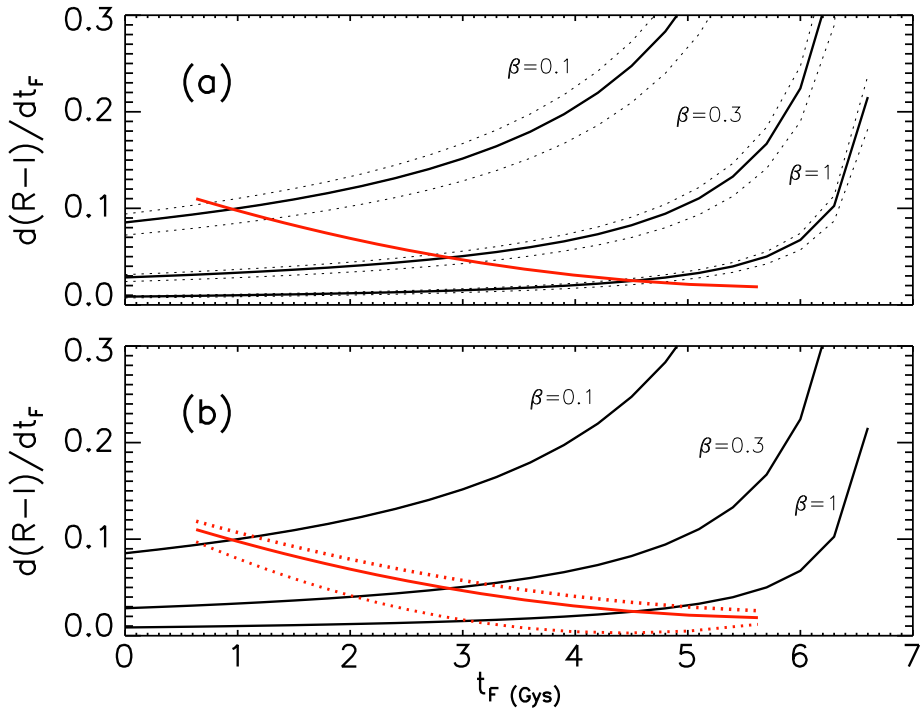

Figure 3.4: Illustration of the colour-scatter method and the associated random (a) and systematic (b) uncertainties for the cluster CL1216.8−1201 at $z = 0.79$. The rate of colour change ($d\mathrm{Colour}/dt$) as a function of $t_{\rm F}$ is shown by the identical solid red lines in panels (a) and (b). In this example we use the observed $(R-I)$, very close to rest-frame $(U-V)$ at the cluster redshift, computed using BC03 stellar population models for galaxies with solar metallicity and a single star formation burst of 0.1 Gyr duration (see text for details). The scatter about the CMR provides an upper limit to the allowed rate of colour evolution, parametrized by equation 3.3 for a given β (equation 3.2). This constraint is shown in both panels by the identical solid black lines, as derived from the intrinsic colour scatter for this cluster and assuming three different values of β. The intersection between the observational lines (solid black) and the model ones (solid red) constrains $t_{\rm F}$. The dotted black lines in panel (a) correspond to the $\pm 1\sigma$ random errors affecting the solid black line as a result of the observational uncertainty in the colour scatter. The red dotted lines in panel (b) illustrate the effects of systematic model uncertainties (e.g. metallicity) on $t_{\rm F}$. These lines correspond to models with the same star formation history as for the red solid line but different metallicities: the upper line has $Z_{\rm sub-solar} = 0.008$, whilst the lower line has $Z_{\rm super-solar} = 0.05$.

els agreed well with the observed galaxy spectra. We discuss the effect of assuming different metallicities later.

Figure 3.4 shows how equation 3.1 can be used to constrain the star-formation history of the galaxies from the colour scatter $\sigma_{\rm int}$ of our richest cluster. It also illustrates the effect of the relevant random and systematic uncertainties. In figure 3.4(a), the red solid line represents $d(R-I)/dt$ (very close to rest-frame $d(U-V)_0/dt$) as a function of $t_{\rm F}$, calculated from the BC03 models. The black solid lines are defined by the equation

$$\frac{d(R-I)}{dt} = \frac{\sigma_{\rm int}}{(t_{\rm H} - t_{\rm F})\beta} \tag{3.3}$$

for several values of β. Equation 3.1 implies that the allowed region lies below the black lines, and thus the intersection of the red and black lines provides a constraint (upper limit) on $t_{\rm F}$ for a given β. It is clear that the colour scatter alone cannot be used to constrain $t_{\rm F}$ and β simultaneously. The dotted black lines in figure 3.4(a) represent the $\pm1\sigma$ random errors[3] in the colour scatter, showing their effect on the $t_{\rm F}$ uncertainty. The effect of systematic uncertainties, such as changing the model chemical composition, are shown on panel (b). The dotted red lines correspond to stellar population models with non-solar metallicity ($Z_{\rm sub-solar} = 0.008$ and $Z_{\rm super-solar} = 0.05$). It is immediately apparent that the effect of systematic model uncertainties such as these in the calculation of $t_{\rm F}$ is, in general, significantly larger than that of photometric random errors. This implies that absolute values of $t_{\rm F}$ must be interpreted with great caution. However, it is not unreasonable to assume that these systematics would affect all the galaxies similarly, making any *differential* or *comparative* study precise and, hopefully, robust. Unless otherwise stated, we consider random uncertainties only when discussing $t_{\rm F}$ since our study is largely comparative, but it is important to bear in mind that substantial systematic uncertainties do exist.

3.3.1 Colour dependence of the derived $t_{\rm F}$

Previous studies have noted that colours which bracket the 4000Å break provide the most sensitive indicators of age changes, yet are the least affected by photometric errors (e.g. Blakeslee *et al.*, 2006). For this reason, and following Bower, Lucey & Ellis (1992), we decided to carry out the age-scatter test using observed colours close to rest-frame $U-V$. Nevertheless, it is instructive to study how the actual colour choice could affect our results. We used our richest cluster, CL1216.8−1201, as the ideal test bed for this purpose. Using the galaxy sample in this cluster, we carried out the scatter-age test with CMDs compiled for different sets of colours. Most colours straddle the 4000Å break at $z = 0.79$ (the cluster redshift), with the exceptions of $I-J$ and $I-K$. The values of $\sigma_{\rm int}$ and $t_{\rm F}$ derived for each colour are plotted in figure 3.5 for different values of β. It is clear that, at least for $\beta \geq 0.3$, all the colours provide a consistent

[3]The errors in the colour scatter were estimated from the 16% and 84% confidence levels in the χ^2 distribution of the measured $\sigma_{\rm int}$, which correspond to $\pm1\sigma$ uncertainties.

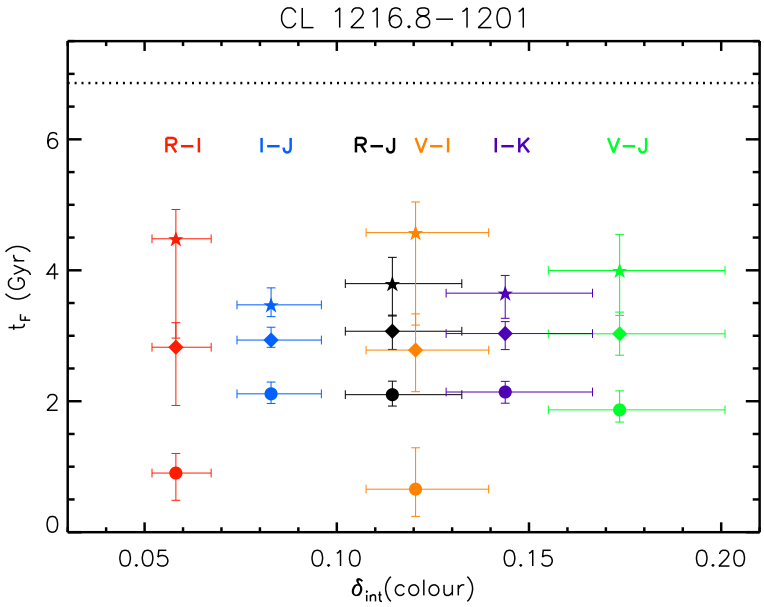

Figure 3.5: The derived formation times of the early-type galaxies in the cluster CL1216.9−1201 at $z = 0.79$ are plotted against the intrinsic CMR scatter measured for the different colours used in the scatter analysis. With the exception of $I - J$ and $I - K$ all colours straddle the 4000Å break at the cluster redshift. Filled stars correspond to $\beta = 1.0$, diamonds to $\beta = 0.3$ and circles to $\beta = 0.1$ (see equation 3.2). The black dotted line indicates the age of the Universe ($t_{\rm H}$) at the cluster redshift. In this figure the errors in $t_{\rm F}$ are calculated as the sum (in quadrature) of the random and systematic uncertainties discussed in the text. Within the errors, most colours yield consistent values of $t_{\rm F}$ (particularly for $\beta \geq 0.3$). However, for $\beta = 0.1$ the optical-optical and optical-infrared colours give discrepant results possibly due to the difficulty in modelling the contribution of asymptotic giant branch stars.

value of $t_{\rm F}$ within the combined random and systematic errors. However, for $\beta = 0.1$ the optical-optical and optical-infrared colours give discrepant results. This is probably because at the relevant stellar population ages (1–2 Gyr) asymptotic giant branch stars have a potentially large, and very uncertain, contribution to the near-infrared galaxy emission, making the model predictions very unreliable (Maraston, 2005; Conroy & Gunn, 2010). The colour with the smallest scatter and smallest scatter uncertainty is $R - I$, which is the closest to rest-frame $U - V$ at this redshift. This provides additional justification for the use of observed colours that are the closest match to rest-frame $U - V$ in our analysis.

Table 3.2: Values of the measured intrinsic scatter ($\sigma_{\rm int}$) and the calculated formation time ($t_{\rm F}$) and redshift ($z_{\rm F}$) for solar metallicity and $\beta = 0.1, 0.3$ and 1.0. The associated uncertainties correspond to the random errors (16% and 84% confidence levels in a χ^2 distribution). Recall that $t_{\rm F}$ is the lookback time, from the cluster redshift, since star formation ceased.

Cluster name	z	CMR colour	$\sigma_{\rm int}$	$t_{\rm F}(\beta=0.1)$ (Gyr)	$t_{\rm F}(\beta=0.3)$ (Gyr)	$t_{\rm F}(\beta=1.0)$ (Gyr)	$z_{\rm F}(\beta=0.1)$	$z_{\rm F}(\beta=0.3)$	$z_{\rm F}(\beta=1.0)$
Cl1037.9−1243a	0.4252	$V-I$	$0.09^{+0.03}_{-0.01}$	$2.3^{+0.4}_{-0.6}$	$4.4^{+0.3}_{-0.4}$	$6.0^{+0.2}_{-0.3}$	$0.76^{+0.08}_{-0.1}$	1.3 ± 0.1	$2.1^{+0.1}_{-0.2}$
Cl1138.2−1133a	0.4548	$V-I$	$0.10^{+0.03}_{-0.02}$	$2.4^{+0.2}_{-0.3}$	$3.34^{+0.1}_{-0.2}$	$4.0^{+0.1}_{-0.1}$	$0.82^{+0.04}_{-0.06}$	$1.03^{+0.03}_{-0.05}$	1.22 ± 0.03
Cl1138.2−1133	0.4796	$V-I$	$0.09^{+0.03}_{-0.01}$	$2.1^{+0.3}_{-0.4}$	$3.7^{+0.2}_{-0.3}$	$5.1^{+0.2}_{-0.3}$	$0.79^{+0.06}_{-0.07}$	$1.19^{+0.07}_{-0.09}$	1.8 ± 0.1
Cl1232.8−1201	0.5414	$R-I$	$0.08^{+0.02}_{-0.01}$	$1.8^{+0.3}_{-0.4}$	$3.8^{+0.2}_{-0.3}$	$5.1^{+0.2}_{-0.3}$	$0.82^{+0.06}_{-0.07}$	$1.40^{+0.008}_{-0.1}$	2.6 ± 0.2
Cl1354.2−1230a	0.5952	$R-I$	$0.04^{+0.03}_{-0.009}$	$2.2^{+0.5}_{-1}$	$4.2^{+0.4}_{-1}$	$5.7^{+0.3}_{-0.7}$	$1.0^{+0.1}_{-0.3}$	$1.7^{+0.2}_{-0.4}$	$2.8^{+0.3}_{-0.6}$
Cl1103.7−1245a	0.6261	$R-I$	$0.08^{+0.07}_{-0.02}$	$1.0^{+0.6}_{-0.9}$	$3.1^{+0.4}_{-1}$	$4.7^{+0.3}_{-0.8}$	$0.8^{+0.1}_{-0.2}$	$1.4^{+0.2}_{-0.4}$	$2.2^{+0.2}_{-0.5}$
Cl1227.9−1138	0.6357	$R-I$	$0.09^{+0.04}_{-0.02}$	$0.5^{+0.4}_{-0.4}$	$2.5^{+0.3}_{-0.6}$	$4.1^{+0.2}_{-0.4}$	$0.71^{+0.07}_{-0.06}$	$1.2^{+0.1}_{-0.2}$	$1.8^{+0.1}_{-0.2}$
Cl1054.4−1146	0.6972	$R-I$	$0.06^{+0.02}_{-0.01}$	$1.0^{+0.3}_{-0.5}$	$2.9^{+0.2}_{-0.3}$	$4.5^{+0.2}_{-0.3}$	$0.86^{+0.07}_{-0.1}$	$1.44^{+0.09}_{-0.1}$	2.4 ± 0.2
Cl1040.7−1155	0.7043	$R-I$	$0.05^{+0.02}_{-0.01}$	$1.1^{+0.4}_{-0.7}$	$3.2^{+0.3}_{-0.6}$	$4.9^{+0.2}_{-0.4}$	0.9 ± 0.1	1.6 ± 0.2	$2.7^{+0.2}_{-0.3}$
Cl1054.7−1245a	0.7305	$R-I$	$0.11^{+0.06}_{-0.02}$	$0.5^{+0.5}_{-0.4}$	$1.6^{+0.5}_{-1}$	$4.0^{+0.2}_{-0.5}$	$0.80^{+0.1}_{-0.07}$	$1.4^{+0.1}_{-0.2}$	$2.1^{+0.1}_{-0.3}$
Cl1054.7−1245	0.7498	$R-I$	$0.10^{+0.02}_{-0.01}$	$0.6^{+0.3}_{-0.4}$	$1.8^{+0.3}_{-0.4}$	$3.6^{+0.1}_{-0.2}$	$0.84^{+0.06}_{-0.08}$	$1.30^{+0.08}_{-0.11}$	$1.90^{+0.06}_{-0.1}$
Cl1354.2−1230	0.7620	$R-I$	$0.05^{+0.03}_{-0.01}$	$0.9^{+0.5}_{-0.8}$	$2.9^{+0.4}_{-0.9}$	$4.6^{+0.3}_{-0.7}$	$0.9^{+0.1}_{-0.2}$	$1.6^{+0.2}_{-0.4}$	$2.7^{+0.3}_{-0.5}$
Cl1216.8−1201	0.7943	$R-I$	$0.058^{+0.009}_{-0.006}$	$0.9^{+0.2}_{-0.3}$	$2.8^{+0.2}_{-0.2}$	$4.5^{+0.1}_{-0.2}$	$0.96^{+0.05}_{-0.07}$	1.6 ± 0.1	$2.75^{+0.09}_{-0.2}$

Table 3.3: Main characteristics of the comparison samples.

	Cluster name	z	$\sigma_{\rm int}$	Colour used in $\sigma_{\rm int}$	Ref. for $\sigma_{\rm int}$	σ_v (Km/s)	Ref. for σ_v	Symbol in Fig. 3.6
	Coma	0.0231	0.056 ± 0.01	$U-V$	1	821^{+49}_{-38}	8	⋇
	Virgo	0.0038	0.044 ± 0.01	$U-V$	1	632^{+41}_{-29}	8	⋇
	CL1358+62	0.3283	0.079 ± 0.01	$B-V$	2	1027^{+51}_{-45}	9	⋇
low-z	CL0412-65	0.510	0.131 ± 0.027	$(U-V)_{z=0}$	3	681^{+256}_{-185}	10	⋇
	CL0016+16	0.546	0.06 ± 0.01	$(U-V)_{z=0}$	3	1127^{+166}_{-112}	7	⋇
	CL0054-27	0.563	0.06 ± 0.01	$(U-V)_{z=0}$	3	742^{+599}_{-147}	10	⋇
	MS 1054-0321	0.831	0.070 ± 0.008	$(U-B)_{z=0}$	4	1156 ± 82	4	◊
	RX J0152.7-1357	0.834	0.050 ± 0.005	$(U-B)_{z=0}$	4	1203^{+96}_{-123}	4	◊
	CL1604+4304	0.897	0.031 ± 0.003	$(U-B)_{z=0}$	4	703 ± 110	4	◊
high-z	CL1604+4321	0.924	0.043 ± 0.006	$(U-B)_{z=0}$	4	582 ± 167	4	◊
	RDCS J0910+5422	1.106	0.060 ± 0.009	$(U-B)_{z=0}$	4	675 ± 190	4	◊
	RDCS J1252.9-2927	1.237	0.112 ± 0.022	$(U-B)_{z=0}$	4	747^{+74}_{-84}	4	◊
	RX J0849+4452	1.261	0.070 ± 0.014	$(U-B)_{z=0}$	4	740^{+113}_{-134}	4	◊
	RX J0848+4453	1.270	0.049 ± 0.027	$(U-B)_{z=0}$	4	650 ± 170	4	◊
very high-z	XMMU J2235.3-2557	1.39	0.055 ± 0.018	$J-Ks$	5	762 ± 265	11	□
	XMMXCS J2215.9-1738	1.46	0.12 ± 0.05	$z_{850}-J$	6	580 ± 140	11	△

Note: Following Blakeslee *et al.* (2006), the scatter in $(U-B)_{z=0}$ was transformed into $(U-V)_{z=0}$ scatter by adding 0.04.
References: (1) Bower, Lucey & Ellis (1992); (2) van Dokkum *et al.* (1998); (3) Ellis *et al.* (1997); (4) Mei *et al.* (2009) and references therein; (5) Lidman *et al.* (2008); (6) Hilton *et al.* (2009); (7) Borgani *et al.* (1999); (8) Fadda *et al.* (1996); (9) Fisher *et al.* (1998); (10) Girardi & Mezzetti (2001); (11) Mullis *et al.* (2005); (12) Hilton *et al.* (2007)

3.4 The scatter in the colour-magnitude relation

3.4.1 The CMR scatter for different clusters

For each cluster, we calculated the intrinsic colour scatter $\sigma_{\rm int}$ following the method described in section 3.3. The values of $\sigma_{\rm int}$ and the actual colours used for each cluster are listed in table 3.2. At this stage, we exclude from this calculation all galaxies whose colours are > 0.3 mag bluer than the fitted CMR. The number of galaxies excluded in each cluster is listed in table 3.1. In total, there are 12 (7%) of these blue early-type galaxies in our sample. We justify this approach and discuss these galaxies later.

The colour scatter shows no significant evolution with redshift for the clusters in the EDisCS sample (figure 3.6, top panel). To extend the redshift baseline and compare our results with previous studies, we plot in figure 3.6 similar colour scatter measurements from the sources listed in table 3.3. No redshift dependence is found even for this extended redshift range. The bottom panel of figure 3.6 further shows that the colour scatter does not correlate with cluster velocity dispersion (σ_v) either, implying that the scatter is not strongly affected by cluster mass. We note that the velocity dispersion range spanned by our sample is very broad ($200 \lesssim \sigma_v \lesssim 1200$ km/s). Adding the clusters in the comparison samples reinforces our result.

3.4.2 CMR scatter dependence on galaxy properties

To explore the overall behaviour of the galaxy colours around the CMR, figure 3.7 shows the distribution of the residuals for the complete galaxy sample as a function of the absolute rest-frame B magnitude M_B (for details of the calculation of M_B, see Rudnick *et al.*, 2009). By construction, the residuals are concentrated about their median value ($\simeq 0$; solid line in figure 3.7). The vast majority of the colour residuals follow a normal distribution reasonably well. The scatter is small, as discussed above. However, at faint magnitudes there is a clear "blue-tail" containing a few galaxies with significantly bluer colours (smaller blue symbols in figure 3.7). These results can also be seen in the upper histogram of figure 3.8, which shows the distribution of the colour residuals for the complete sample of early-type cluster galaxies. The

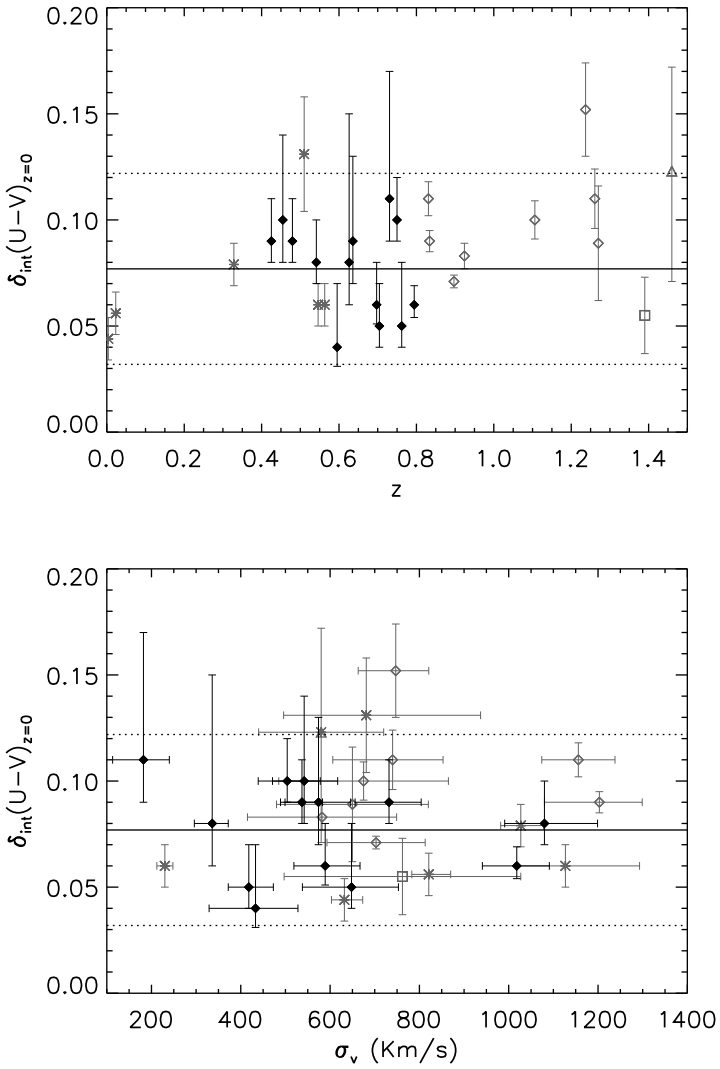

Figure 3.6: The upper panel shows the dependence of the intrinsic scatter in the observed colour closest to rest-frame $(U-V)_{z=0}$ for EDisCS clusters (filled black diamonds) and several comparison samples at lower and higher redshift (grey symbols). The low redshift cluster sample (asterisks) was compiled from the work of Bower, Lucey & Ellis (1992); van Dokkum *et al.* (1998) and Ellis *et al.* (1997). The higher redshift sample was taken from Mei *et al.* (2009) (open diamonds), Hilton *et al.* (2009) (open triangle) and Lidman *et al.* (2008) (open square). See table 3.3 for details about the comparison samples. This plot reveals there is no significant CMR scatter evolution with redshift up to $z < 1.5$. The lower panel shows the scatter as function of cluster velocity dispersion. In both panels, the solid line represents the median $\sigma_{\rm int}$ value for the EDisCS clusters and the dotted lines correspond to $\pm 2\sigma$. The CMR scatter does not correlate with cluster velocity dispersion.

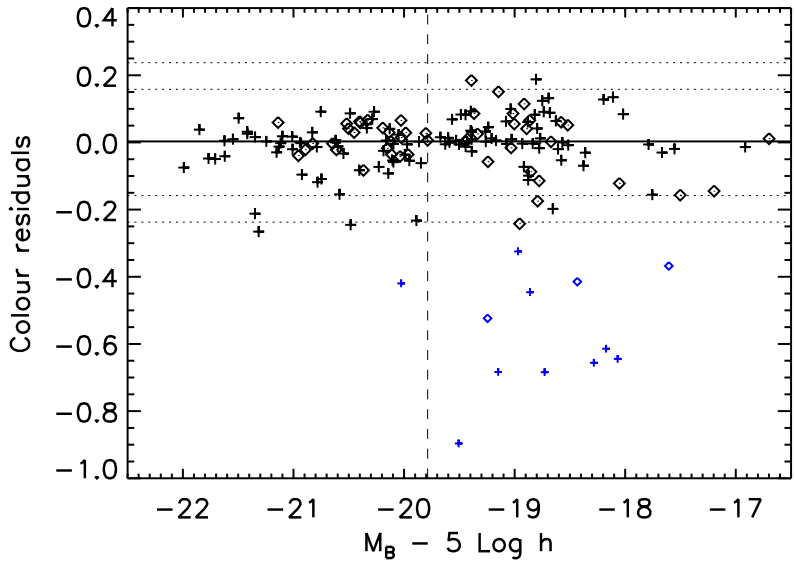

Figure 3.7: Observed colour residuals around the CMR as a function of M_B of all the galaxies in the sample. Note that we express the magnitude as $M_B - 5$ Log h, where $h = H_0/70$. Elliptical galaxies are represented with crosses and lenticulars with diamonds. The solid line indicates the location of the median, dotted lines correspond to 2σ and 3σ for the black data points, and the blue symbols represent the galaxies in the "blue tail" (see text for details). The median luminosity is also shown for reference (black dashed line).

measured scatter for the whole sample is small ($\sigma_{\rm obs} = 0.078$ when excluding the "blue-tail") and significantly larger than the scatter due to the photometric errors ($\simeq 0.017$). This implies that the intrinsic colour scatter for the complete sample is $\sigma_{\rm int} = 0.076^{+0.005}_{-0.004}$, very close to the average scatter for the individual clusters ($\langle\sigma_{\rm int}\rangle = 0.077$, cf. table 3.2).

There are 12 galaxies (7% of the total sample) with colours > 0.3 mag bluer than the CMR. The number of "blue" galaxies in each cluster is listed in table 3.1, while their individual IDs and some observed properties are presented in table 3.4. These galaxies were excluded from our scatter-age analysis (section 3.5) for consistency with previous studies (e.g. Mei *et al.*, 2009) where outliers are rejected implicitly. The choice was to exclude them explicitly, but we discuss the implications that their existence and properties have in our conclusion. Interestingly, 2 out of the 12 blue galaxies show a small degree of disruption in their morphologies, as found by visually inspecting their HST images (see comments in table 3.4 and figure 3.1). In section 3.2 6 galaxies (4%) were found in our full sample that, despite their clear early-type morphology, show some signs of disruption. Now we find that 2 of these disturbed galaxies have

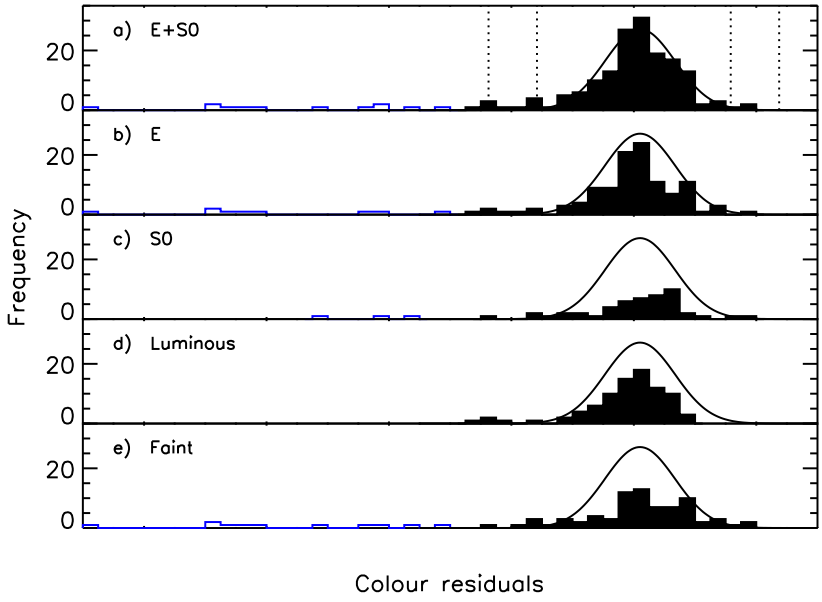

Figure 3.8: Histograms of the observed colour residuals around the CMR for the different galaxy sub-samples computed from figure 3.7: (a) the complete sample (Ellipticals and S0s); (b) Ellipticals only (c) S0s only; (d) luminous galaxies and (e) faint galaxies. The dotted lines in the top panel correspond to 2σ and 3σ for a Gaussian distribution with $\sigma_{\rm obs} = 0.078$. The solid lines in all panels show a gaussian fit to the complete sample (top) for comparison. The open blue part of each histogram corresponds to the "blue tail" (see text and figure 3.7 for details).

"blue" colours, indicating that among the blue galaxies, morphological disturbances are much more common than among the ones in the CMR. Nevertheless, the rest of the blue galaxies (10) do not show any clear sign of morphological disruption. We further discuss the implications of these faint blue galaxies (i.e. the "blue tail") in our conclusions.

Table 3.4: Properties of the "blue tail" galaxies. The "excluded" galaxies are also listed in the two bottom lines.

EDisCS galaxy ID	Type	Residual (mag)	M_B	Comments (from spectra; morphology)
EDCSNJ1054199−1146065	E	-0.32	-18.97	Several emission lines
EDCSNJ1054207−1148130	S0	-0.41	-18.43	Considerable [OII] emission
EDCSNJ1232307−1249573	E	-0.90	-19.51	Absorption-line spectra
EDCSNJ1232336−1252103	S0	-0.52	-19.24	Galaxy of spectral type k+a
EDCSNJ1232304−1250391	E	-0.42	-20.03	Considerable [OII] emission; Some sign of disturbance
EDCSNJ1138050−1132546	E	-0.60	-18.17	Strong [OII] emission
EDCSNJ1138068−1132510	E	-0.68	-18.73	Starburst?; High surface brightness
EDCSNJ1138034−1133049	E	-0.64	-18.07	Strong [OII] emission; Some sign of disturbance
EDCSNJ1354073−1233336	E	-0.45	-18.86	Strong [OII] emission
EDCSNJ1354022−1234283	E	-0.68	-19.15	Strong [OII] emission; Compact galaxy
EDCSNJ1037564−1245134	S0	-0.37	-17.61	Considerable [OII] emission
EDCSNJ1138135−1137137	E	-0.66	-18.28	Considerable [OII] emission
EDCSNJ1138096−1135223	*	-0.33	-19.00	Strong [OII] emission; Very disturbed/Merging
EDCSNJ1138127−1134190	*	-0.33	-17.88	Either HII regions or large merger

* These galaxies where misclassified as E in Desai *et al.* (2007). We excluded them from the sample since their HST images reveal that they are not early-type galaxies and they show strong signs of disruption (see section 3.2).

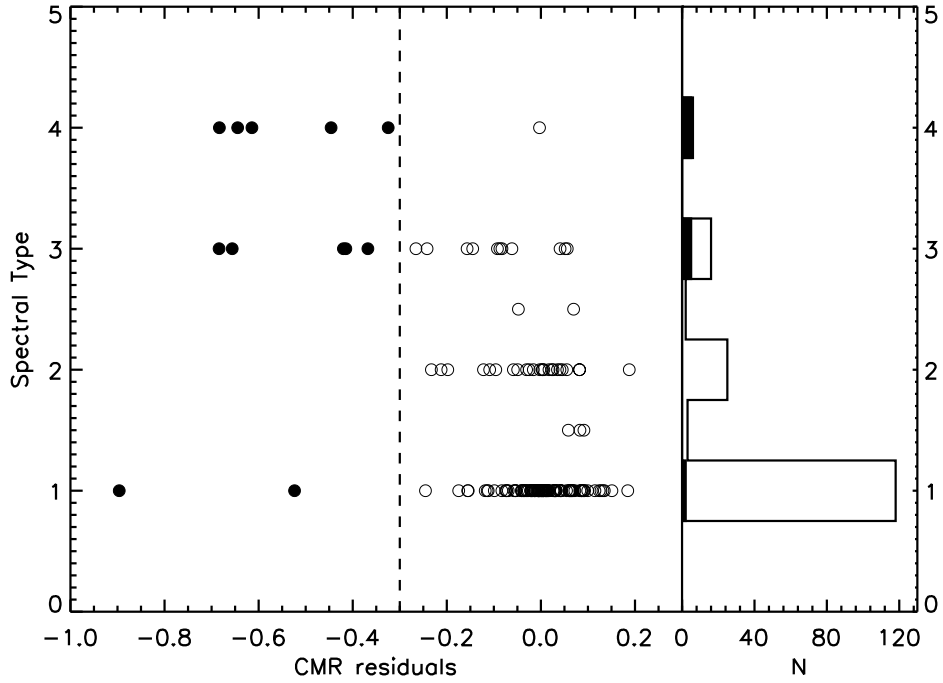

Figure 3.9: The left side of the figure shows the spectral type of our sample galaxies as a function of CMR residuals. The dotted line indicates the boundary between red-sequence galaxies and the "blue tail" (filled symbols). A vertical histogram on the right side of the figure shows the distribution of the spectral types. In the histogram, "blue tail" galaxies are highlighted in the shaded area. The spectral types range from 1 to 4, where 1 corresponds to absorption-line spectrum; 2 to absorption-line spectrum plus some very weak emission; 3 to emission-lines with EW[OII]$< 25\mathring{A}$ rf; and 4 to strong emission line spectrum (EW[OII]$> 25\mathring{A}$ rf).

Figure 3.9 shows the spectral type of the sample galaxies as a function of CMR residuals. Blue galaxies are represented with filled circles (and in the shaded histogram). The vast majority of the early-type galaxies in the red sequence (open symbols and open histogram) have absorption line spectra, while the "blue" tail galaxies show higher spectral types indicating they have emission lines in addition to their blue colour, which is likely a consequence of the presence of younger stellar populations. Indeed, all galaxies with spectral type of 4 (except one) are in the "blue tail".

In what follows, we concentrate on the remaining 160 galaxies whose colours are within ± 0.3mag from the CMR. From these, we constructed sub-samples according to different galaxy properties:

- Morphology (E vs. S0), as indicated by different symbols in figure 3.7.
- Luminosity (Luminous vs. Faint), divided at the median rest frame B absolute luminosity (corresponding to $M_B^{\rm med} = -19.8$; cf. vertical dashed line in figure 3.7).

The four bottom histograms of figure 3.8 show the distribution of the colour residuals for each one of these sub-samples. Within the errors, we find that both ellipticals and S0s show the same scatter. However, the luminous galaxies have a slightly smaller intrinsic scatter than the faint ones. The values of $\sigma_{\rm int}$ for each sub-sample are listed in table 3.5. In the next section, we interpret these scatters in terms of the star-formation history of the different galaxy samples.

3.5 Star formation histories

3.5.1 Star-formation histories of the early-type galaxies in each cluster

Using the method discussed in section 3.3 and the intrinsic colour scatter measured for the early-type galaxies, we computed, for three values of β, the formation times $t_{\rm F}$ and their respective errors for each individual cluster or group (see table 3.2). An inspection of this table immediately shows that, as expected, for higher values of β (less synchronous galaxy formation) older ages are required to explain the small colour scatter. A clear trend is also apparent: at a fixed β, higher redshift clusters have smaller $t_{\rm F}$. However, if we correct for the difference in look-back time using our adopted cosmology, these $t_{\rm F}$ can be translated into formation redshifts, $z_{\rm F}$, and the trend disappears. All the EDisCS clusters yield consistent formation redshifts for their early-type galaxy population ($z_{\rm F} \simeq 0.8$ for $\beta = 0.1$, $z_{\rm F} \simeq 1.4$ for $\beta = 0.3$ and $z_{\rm F} \simeq 2.4$ for $\beta = 1.0$). This is shown in figure 3.10, where $z_{\rm F}$ is plotted vs. cluster redshift for the different values on β. For comparison, we overplot the formation redshifts derived by Sánchez-Blázquez *et al.* (2009) using absorption-line indices in the spectra of EDisCS early-type red-sequence galaxies (blue and red diamonds). The blue points (corresponding to galaxies with velocity dispersions < 175km/s) agree very well with our formation redshifts for $\beta = 0.3$ (black diamonds), while the red points (galaxy velocity dispersions > 175km/s) agree with $\beta \geq 0.3$. Moreover, galaxy ages derived from the analysis of the Fundamental Plane of these galaxies (Saglia et al. in preparation) are also in agreement with our formation redshifts for $\beta \geq 0.3$.

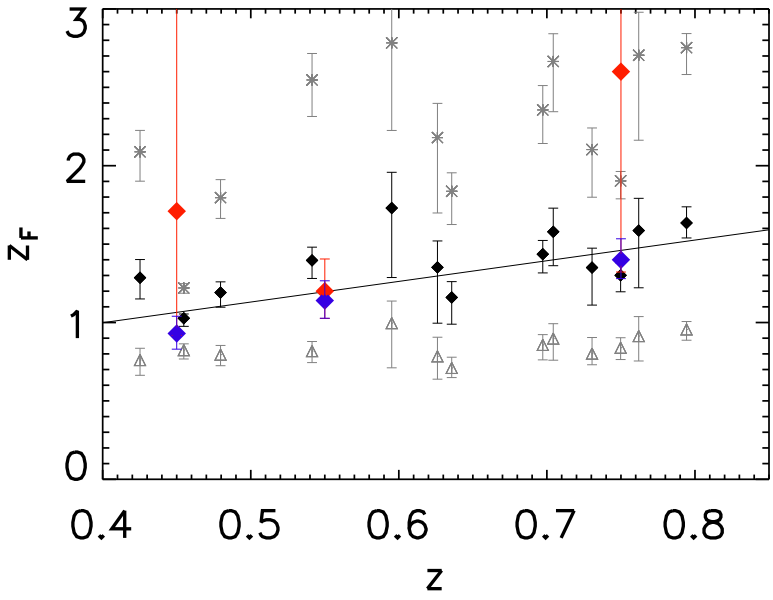

Figure 3.10: Galaxy formation redshift $z_{\rm F}$ vs. cluster redshift. Symbols correspond to the different values of β used: triangles for $\beta = 0.1$, filled diamonds for $\beta = 0.3$ and stars for $\beta = 1.0$. The solid line is a linear fit to the solid black diamonds. For comparison, the predicted $z_{\rm F}$ from Sánchez-Blázquez *et al.* (2009) are shown as larger coloured symbols. The blue diamonds correspond to the morphologically-selected sample of EDisCS early-type galaxies with galaxy velocity dispersions < 175km/s, while the red symbols correspond to the sample with galaxy velocity dispersions > 175 km/s. The blue points agree very well with our $z_{\rm F}$ for $\beta = 0.3$, whilst the red points are in agreement with our results if $\beta \geq 0.3$. We observe an increase of $z_{\rm F}$ with cluster redshift (see also figure 3.11).

Figure 3.10 also shows that $z_{\rm F}$ may be slightly higher for higher redshift EDisCS clusters (fitted line). Although this trend is not very significant, it would be desirable to extend the redshift baseline to test whether it continues at higher redshifts. We can do that by using the study published by Mei *et al.* (2009). These authors follow a very similar procedure to ours, and predict formation times based on a colour-scatter analysis for a value of $\beta \simeq 0.3$. Their galaxy samples also contain morphologically-classified ellipticals and S0s, and can therefore be compared to ours. Their results are plotted as open diamonds in figure 3.11, together with our results for $\beta = 0.3$. If we take these points at face value, the trend of increasing $z_{\rm F}$ with redshift becomes very significant. However, a word of caution is required. Although our study and that of Mei *et al.* (2009) are very similar, there are some differences. First, their photometry and the colours that they use are different because the higher redshift of their clusters. Second, they estimate the intrinsic colour scatter using biweight scale estimator

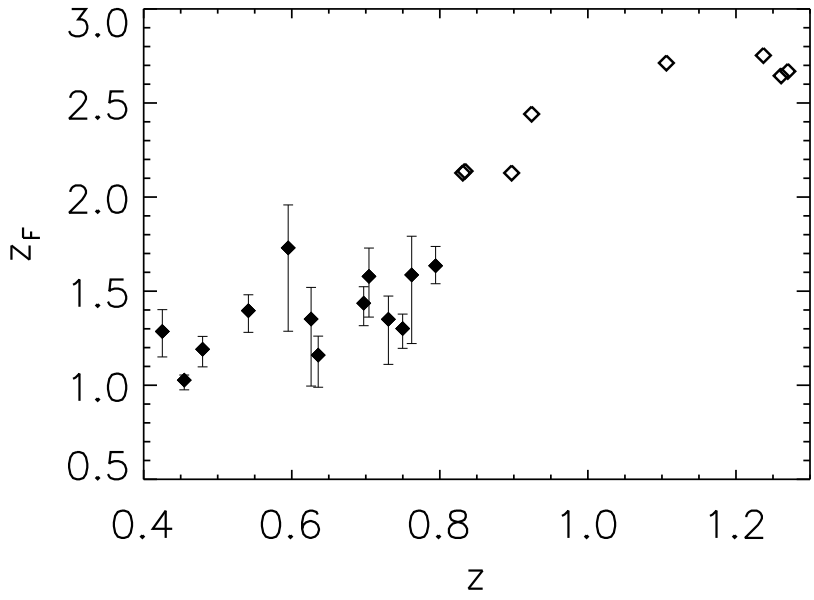

Figure 3.11: Galaxy formation redshift $z_{\rm F}$ (derived using $\beta = 0.3$) vs. cluster redshift for EDisCS clusters (solid diamonds) and for the clusters published by Mei *et al.* (2009) (open diamonds). We observe that $z_{\rm F}$ increases slightly with cluster redshift for the EDisCS sample (see also fitted line in figure 3.10). This trend becomes stronger when we include the higher redshift comparison sample.

(which implicitly excludes outliers). However, using their method with our data does not change our results since we exclude outliers explicitly, as discussed in section 3.3. Finally, their implementation of the scatter-age test differs in some minor details from ours, although they use the same Bruzual & Charlot (2003) models. We believe these differences are probably not important for this exercise, but we cannot be completely certain without re-analysing their data. With all these caveats, the trend observed in figure 3.11 would imply that morphologically-classified elliptical and S0 galaxies formed earlier in higher redshift clusters than in lower redshift ones.

Figure 3.12 shows $z_{\rm F}$ plotted against cluster velocity dispersion. Consistent with figure 3.6, no correlation is found between $z_{\rm F}$ and σ_v, implying that the formation time of morphologically-classified ellipticals and S0s does not depend strongly on cluster mass.

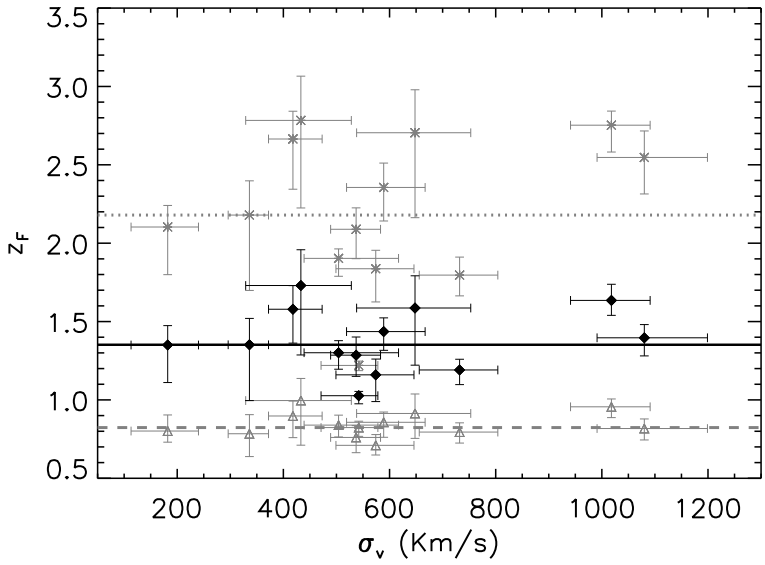

Figure 3.12: Galaxy formation redshift $z_{\rm F}$ vs. cluster velocity dispersion. As in figure 3.10, symbols correspond to the different values of β: triangles for $\beta = 0.1$, filled diamonds for $\beta = 0.3$ and stars for $\beta = 1.0$. The dashed, solid and dotted lines correspond to the median formation redshift for each value of β. We find that $z_{\rm F}$ does not depend on the cluster velocity dispersion.

3.5.2 Dependence of the star-formation histories on galaxy properties

In table 3.5, we show the colour scatter and derived formation redshift for the galaxy samples divided in terms of morphology and luminosity, as discussed in section 3.4.2. Within the errors, ellipticals and S0s show the same scatter. Since the E and S0 samples have very similar mean redshifts, similar colour scatters imply similar average formation redshift. However, the faint galaxies seem to exhibit a larger scatter than the bright ones. This, together with the fact that the luminous subsample has a higher average redshift than the faint one, suggests that the most luminous (massive) early-type galaxies formed earlier than the fainter (less massive) ones.

An identical conclusion is reached if the sample is split by stellar mass (derived following Bell & de Jong, 2001) instead of by luminosity, which is not surprising since homogeneous colours imply near-constant stellar mass-to-light ratios. When splitting the sample by galaxy velocity dispersion or dynamical mass (cf. Saglia et al. in preparation), similar trends are observed, albeit with smaller statistical significance since only half of the galaxies in our sample have measured velocity dispersions.

Table 3.5: Scatter analysis results for the morphology and luminosity-split sub-samples. The colour scatter and the derived formation times and redshifts are given for three values of β.

Sample	$\langle z \rangle$	$\sigma_{\rm int}$	$t_{\rm F}(\beta = 0.1)$	$t_{\rm F}(\beta = 0.3)$	$t_{\rm F}(\beta = 1.0)$	$z_{\rm F}(\beta = 0.1)$	$z_{\rm F}(\beta = 0.3)$	$z_{\rm F}(\beta = 1.0)$
All	0.6411	$0.077^{+0.005}_{-0.004}$	$2.64^{+0.07}_{-0.08}$	$4.04^{+0.06}_{-0.07}$	$5.45^{+0.06}_{-0.07}$	$1.22^{+0.3}_{-0.3}$	$1.85^{+0.04}_{-0.05}$	$2.88^{+0.07}_{-0.08}$
E	0.6443	$0.075^{+0.005}_{-0.004}$	$2.65^{+0.09}_{-0.1}$	$4.05^{+0.08}_{-0.09}$	$5.45^{+0.07}_{-0.09}$	$1.22^{+0.3}_{-0.3}$	$1.85^{+0.04}_{-0.05}$	$2.88^{+0.07}_{-0.08}$
S0	0.6589	$0.079^{+0.009}_{-0.007}$	$2.6^{+0.1}_{-0.2}$	$4.0^{+0.1}_{-0.1}$	$5.3^{+0.1}_{-0.1}$	$1.24^{+0.05}_{-0.05}$	$1.87^{+0.06}_{-0.07}$	$2.9^{+0.1}_{-0.1}$
Luminous	0.7016	$0.070^{+0.006}_{-0.005}$	2.636 ± 0.1	$4.00^{+0.08}_{-0.1}$	$5.33^{+0.08}_{-0.09}$	$1.34^{+0.04}_{-0.05}$	$2.03^{+0.08}_{-0.09}$	$3.1^{+0.2}_{-0.2}$
Faint	0.6071	$0.080^{+0.007}_{-0.006}$	$2.668^{+0.1}_{-0.1}$	$4.10^{+0.09}_{-0.1}$	$5.6^{+0.1}_{-0.1}$	$1.11^{+0.03}_{-0.04}$	$1.67^{+0.05}_{-0.05}$	$2.65^{+0.08}_{-0.09}$

3.6 The CMR zeropoint

Our CMR scatter analysis cannot constrain $t_{\rm F}$ and β simultaneously. Until now, we have not discussed the zero-point of the CMR because predicting absolute colours from stellar population models is, arguably, more uncertain than predicting differential colour changes (see, e.g., Aragón-Salamanca *et al.*, 1993). However, since accurate zero points are available, it is worthwhile checking whether consistent and, perhaps, additional constraints can be obtained from them. Figure 3.13 shows for each of the EDisCS clusters the CMR colour corresponding to the median absolute B magnitude of the whole sample, after correcting for luminosity evolution. Specifically, for each cluster we determine the colour of its CMR for $M_{\rm B} = M^*_{\rm B} + 1.15$, where $M^*_{\rm B}$ is empirically-determined (Crawford, Bershady & Hoessel, 2009; Rudnick *et al.*, 2009). These zero-points do not correlate with intrinsic cluster properties such as their velocity dispersions or masses.

The solid lines in the figure show the predictions of Bruzual & Charlot (2003) models

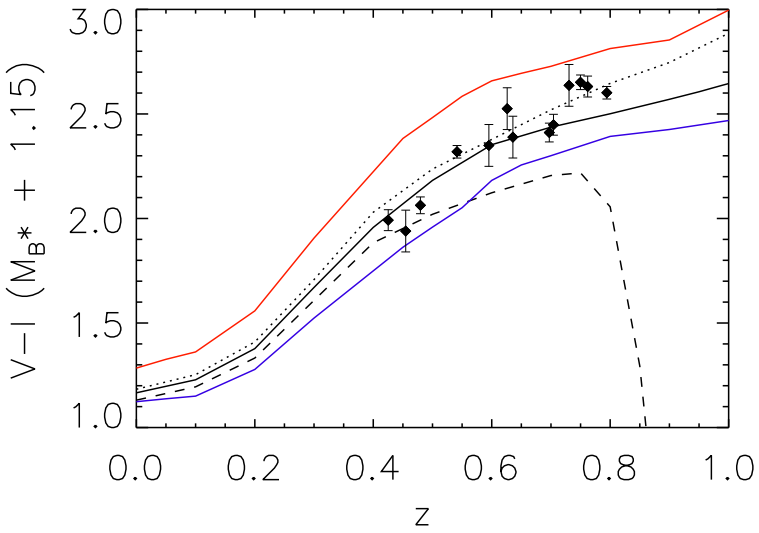

Figure 3.13: $V-I$ CMR zero-point vs. redshift for the EDisCS cluster galaxies (points) compared with population synthesis models from Bruzual & Charlot (2003). The black lines have been computed with $Z_{\rm solar} = 0.02$ metallicity, the blue one with $Z_{\rm sub-solar} = 0.008$, and the red one with $Z_{\rm super-solar} = 0.05$. The black dashed line corresponds to $\beta = 0.1$ ($z_{\rm F} \sim 0.9$), the black, blue and red solid lines to $\beta = 0.3$ ($z_{\rm F} \sim 1.5$) and the black dotted line to $\beta = 1.0$ ($z_{\rm F} \sim 2.5$). See text for details. The observed points clearly rule out a $\beta = 0.1$ scenario (i.e. very synchronized formation for all the galaxies). However, they are in agreement with $\beta \geq 0.3$.

for $z_{\rm F} \sim 1.5$ (corresponding to $\beta = 0.3$, cf. section 3.5.1) for $Z_{\rm sub-solar} = 0.008$ (blue), $Z_{\rm solar} = 0.02$ (black) and $Z_{\rm super-solar} = 0.05$ (red). It is clear that for median luminosity galaxies non-solar models do not provide an acceptable fit to the galaxy colours for any value of β.[4] However, solar-metallicity models do a reasonable job. This provides additional justification for the use of solar metallicity models in our analysis (cf. section 3.3).

Taking the solar models at face value, a constraint on β can be derived from figure 3.13. The black-dashed line corresponds to $\beta = 0.1$ ($z_{\rm F} \sim 0.9$), the black solid line to $\beta = 0.3$ ($z_{\rm F} \sim 1.5$) and the black dotted line to $\beta = 1.0$ ($z_{\rm F} \sim 2.5$). The observed points clearly rule out $\beta = 0.1$ (i.e. very synchronized formation for all the galaxies). They are in reasonably good agreement with $\beta = 1.0$, but $\beta = 0.3$ is not ruled out. Hence, it seems reasonably safe to conclude that $\beta \geq 0.3$ on the basis of this analysis. If we translate this into the time interval Δt over which all the galaxies "formed", the constraint translates to $\Delta t \gtrsim 1$ Gyr. Since $t_{\rm F}$ refers to the time at which star formation ceased, this implies that there was an extended epoch over which cluster galaxies had their star formation truncated/stopped. In other words, this cessation of star formation was not synchronized for all the cluster early-type galaxies.

3.7 Discussion

In this chapter, we have studied the colour-magnitude relation (CMR) for a sample of early-type galaxies from the ESO Distant Cluster Survey (EDisCS). Our sample consists of 172 strictly morphologically-classified ellipticals and S0 galaxies in 13 clusters and groups with redshifts $0.4 < z < 0.8$ and velocity dispersions $200 \lesssim \sigma_v \lesssim 1200$ km/s. All these galaxies are spectroscopically-confirmed cluster members, and their magnitudes span the range $-22 \lesssim M_B - 5\log h \lesssim -17.5$. We have analysed the colour scatter about the CMR and its zeropoint to derive meaningful constraints on the formation history of these galaxies. Assuming that the intrinsic colour scatter about the CMR is due to differences in stellar population ages, our main results are:

- In agreement with previous studies, the intrinsic colour scatter $\sigma_{\rm int}$ about the

[4] For clarity, we show the non-solar metallicity lines for $\beta = 0.3$ only.

CMR in rest-frame $U - V$ is small ($\langle\sigma_{\rm int}\rangle = 0.076$). However, there is a small minority of faint early-type galaxies (7%) that are significantly bluer than the CMR and these were excluded from the scatter analysis. These galaxies probably represent a population of young galaxies that have not yet joined the red-sequence population. Interestingly, only 2 out of the 12 blue galaxies show signs of morphological disturbances and/or interactions, while the rest are bona-fide ellipticals or S0s. However, the vast majority of the blue galaxies have emission lines in their spectra indicative of ongoing star formation (see table 3.4). Faint blue low-mass early-type galaxies have been reported in previous studies (e.g. Blakeslee *et al.*, 2006; Bamford *et al.*, 2009), preferentially in low density environments. To explain the existence of these low-mass blue early-type galaxies with normal E/S0 morphologies in the field Huertas-Company *et al.* (2010); Kannappan, Guie & Baker (2009) propose two possible explanations. First, they could be the result of minor mergers, which would trigger centrally-concentrated star-formation, helping to build a bulge, and eventually taking them to the red sequence. Alternatively, the disks in these galaxies are perhaps being (re)built from the surrounding gas, moving then back (or staying) in the blue-cloud. It is hard to see how this second possibility would work in the cluster environment, where it is more likely that gas is removed than allowed to fall onto these low mass galaxies. In clusters, minor mergers remain a possibility, in particular if they occur while these galaxies were in filaments and/or groups, but they need to be minor enough to avoid strong morphological disruption. It is also possible that these galaxies are just approaching the cluster for the first time, and will eventually stop forming stars due to gas removal by the cluster environment. This would take them to the red sequence without severely disrupting their morphologies.

- We observe no significant evolution of the intrinsic colour scatter to $z \simeq 0.8$ from the EDisCS clusters alone. This result is consistent with previous studies (e.g. Ellis *et al.*, 1997). After expanding our sample with higher redshift clusters from the literature, we have still found no significant evolution in $\sigma_{\rm int}$ up to $z \sim 1.5$. Moreover, in the wide range of cluster velocity dispersion (mass) of our sample ($100 \lesssim \sigma_v \lesssim 1300$) the scatter does not seem to show any trend. Because

our sample is strictly morphologically-selected, this implies that by the time cluster elliptical and S0 galaxies achieve their morphology, the vast majority have already joined the red sequence. The only exception seems to be the very small fraction ($\lesssim 7\%$) of faint blue early-types.

- Following the work of Bower, Lucey & Ellis (1992), we used the colour scatter to estimate the galaxies' formation time $t_{\rm F}$, defined as the time elapsed since the major episode of star formation. This allowed us to calculate the formation redshift $z_{\rm F}$ for the early-type galaxy population in each cluster. Yet again, we measured no significant dependency of $z_{\rm F}$ on the cluster velocity dispersion. However, we found that $z_{\rm F}$ increases weakly with cluster redshift within the EDisCS sample. This trend becomes very clear when the higher redshift clusters from Mei *et al.* (2009) are included. This implies that, at any given redshift, to have a population of fully-formed ellipticals and S0s they must have formed most of their stars $\simeq 2$–4 Gyr prior to observation. That does not mean that *all* early-type galaxies in *all* clusters formed at these high redshifts. It means that the ones that we observe to already have early-type morphologies also have reasonably old stellar populations. This is partly a manifestation of the "progenitor bias" (van Dokkum & Franx, 1996), but also a consequence of the vast majority of the early-type galaxies in clusters (in particular the massive ones) being already red (i.e., already having old stellar populations) by the time they achieved their morphology.

- Elliptical and S0 galaxies show very similar colour scatter, implying that they have similar stellar population ages. If we assume that their observed properties are representative of the early-type cluster galaxy population at these redshifts, the scarcity of blue S0s indicates that, if they are the descendants of spirals whose star formation has ceased (Aragón-Salamanca, Bedregal & Merrifield, 2006; Bedregal, Aragón-Salamanca & Merrifield, 2006; Barr *et al.*, 2007), the galaxies were already red when they became S0s, i.e. the parent spiral galaxies became red before loosing their spiral arms. The red spirals found preferentially in dense environments (Wolf *et al.*, 2009; Bamford *et al.*, 2009; Masters *et al.*, 2010) are the obvious candidate progenitors of these S0s.

- Dividing the sample in two halves by luminosity (or stellar mass), we find that the formation redshift $z_{\rm F}$ (derived from the CMR scatter in each sample) is smaller for fainter galaxies than for brighter ones. This indicates that fainter early-type galaxies finished forming their stars later. Our results are also consistent with the observation that the cluster red sequence built over time with the brightest galaxies reaching the sequence earlier than fainter ones (De Lucia *et al.*, 2004, 2007; Rudnick *et al.*, 2009).

- The CMR scatter analysis cannot constrain both the formation time $t_{\rm F}$ and formation interval Δt simultaneously. However, its combination with the observed evolution of the CMR zero point, enabled us to conclude that the early-type cluster galaxy population must have had their star formation truncated/stopped over an extended period $\Delta t \gtrsim 1\,$Gyr. Hence, the cessation of star formation was not synchronized for all the cluster early-type galaxies.

Chapter 4

The effect of the environment on the gas kinematics and stellar structure of distant galaxies

4.1 Introduction

In this chapter, and in chapter 5, the EDisCS dataset is used to make a statistically significant investigation of the environmental effects on galaxy evolution.

We focus our analysis on the physical mechanism(s) transforming star-forming spirals into passive S0s. So far, a number of plausible mechanisms have been proposed. We summarize the most important ones here:

(i) Ram-pressure stripping (Gunn & Gott, 1972): the pressure due to the passage of the galaxy through the intra-cluster medium removes the galaxy's gas in timescales comparable to their cluster crossing time (a few 10^9yr). The HI can be removed and/or its distribution could become very asymmetric, while cold molecular gas is of high enough surface density to prevent its disturbance even in the most massive clusters (Boselli & Gavazzi, 2006, and references therein). Simulations show that a mild starburst due to gas compression may or may not occur before the gas is stripped and star formation is eventually quenched (Fujita, 1998). Depending upon the model one assumes, the gas could be removed from the disk, the halo or both. Each case affects the

star formation of the galaxy differently, as illustrated in figure 4.1. One possibility, is that all the gas is removed from the disk and halo of the galaxy, rapidly truncating the star formation (Abadi, Moore & Bower, 1999; Quilis, Moore & Bower, 2000), alternatively, if only the gas in the halo is removed, the star formation declines gradually, until it eventually halts due to the consumption of the disk gas reservoir that is not replenished (Bekki, Couch & Shioya, 2002). A third possibility is that the interaction with the ICM removes the halo gas, but also the increased pressure in the disk gas may actually trigger an initial burst of star-formation, causing an enhancement in the SFR. The gas in the disk is used faster, due to the increased activity, producing a subsequent rapid decline of the SFR (Bekki & Couch, 2003). Recent high resolution hydrodynamic simulations (Tonnesen & Bryan, 2009) suggest that low ram pressure values compress the gas possibly enhancing the star formation, while high values create smaller amounts od high density gas. Other simulations (e.g. Kapferer *et al.*, 2009) claim a star formation enhancement of more than a magnitude under high ram pressure, in addition to complex structures in the gaseous wake. Furthermore, simulations by Roediger & Hensler (2005) show that gas disks of galaxies in high density environments are heavily truncated or completely stripped, whilst in lower density environments, the gas disks of galaxies are disturbed.

(ii) Mergers: simulations predict that a merger between unequal mass spirals can form an S0 galaxy (Bekki, 1998), while major mergers are very likely to produce giant ellipticals (Naab & Burkert, 2003). In cluster cores, the high relative speeds of galaxies prevent the formation of gravitationally bound pairs during close encounters. In cluster outskirts, the environment however is less dense in general and mergers are likely to take place (Mihos, 2003).

(iii) Galaxy harassment (Moore *et al.*, 1999): tidal forces due to close high-speed encounters with other, more massive, galaxies can cause disk thickening and gas fuelling of the central region (possibly resulting in star formation). As a consequence, the gas becomes exhausted and star formation is quenched. This mechanism is understood to be particularly important in dwarf or low-surface-brightness galaxies and is most efficient in the cluster periphery.

(iv) Tidal interactions between galaxies and the cluster potential, “strangulation”, or

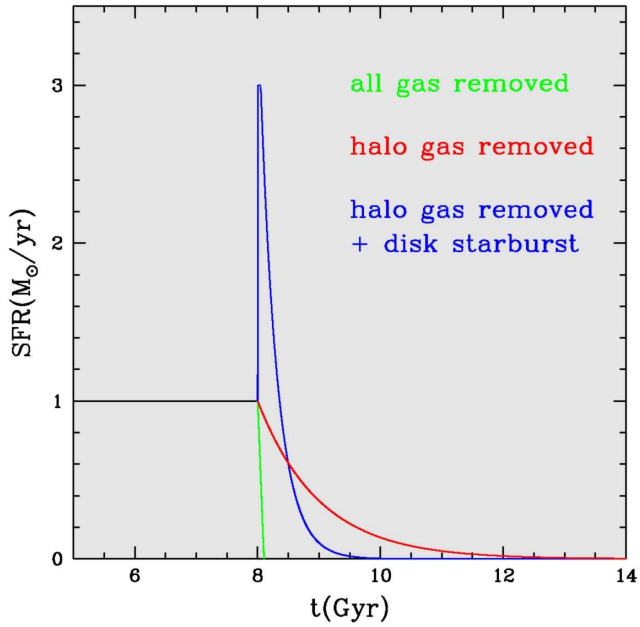

Figure 4.1: Illustration of the possible star formation histories that a galaxy falling into a cluster may experience. Initially the galaxy is forming stars at a constant rate (SFR$\sim 1\mathrm{M}_\odot/\mathrm{yr}$ in this example, like in the Milky Way). One possibility is that all the gas is removed from the galaxy (disk and halo), rapidly truncating the star formation (Abadi, Moore & Bower, 1999; Quilis, Moore & Bower, 2000, green line), alternatively, if only the gas in the halo is removed, the star formation declines gradually, until it eventually halts due to the consumption of the disk gas reservoir that is not replenished (Bekki, Couch & Shioya, 2002, red line). A third possibility is that the interaction with the ICM removes the halo gas, but also the increased pressure in the disk gas may actually trigger an initial burst of star-formation, causing an enhancement in the SFR. Because of the increased activity, the gas in the disk is used faster, producing a subsequent rapid decline of the SFR (Bekki & Couch, 2003, blue line). Figure taken from Bamford (2006).

"starvation" (Larson, Tinsley & Caldwell, 1980; Balogh, Navarro & Morris, 2000): the hot halo of a galaxy is stripped upon falling into a more massive halo. The tidal field of the cluster or group then removes the halo gas from the galaxy, halting its accretion onto the disk (Bekki, Couch & Shioya, 2001). Hence, this mechanism effectively truncates the galaxy star formation, in a simmilar manner to that illustrated by the red line in Figure 4.1. Although this mechanism is effective in low mass groups (McCarthy *et al.*, 2008; Kawata & Mulchaey, 2008), it is unclear whether it can account for the apparently strong effect of the cluster environment. It is possible however, that the extreme properties observed in galaxy clusters may be the result of some "preprocessing" of galaxies in groups before accretion into the cluster (e.g. Zabludoff & Mulchaey, 1998; McGee *et al.*, 2009).

Each one of these mechanisms is expected to be effective in different regions of the cluster environment. This is illustrated in figure 4.2, where the different ranges of

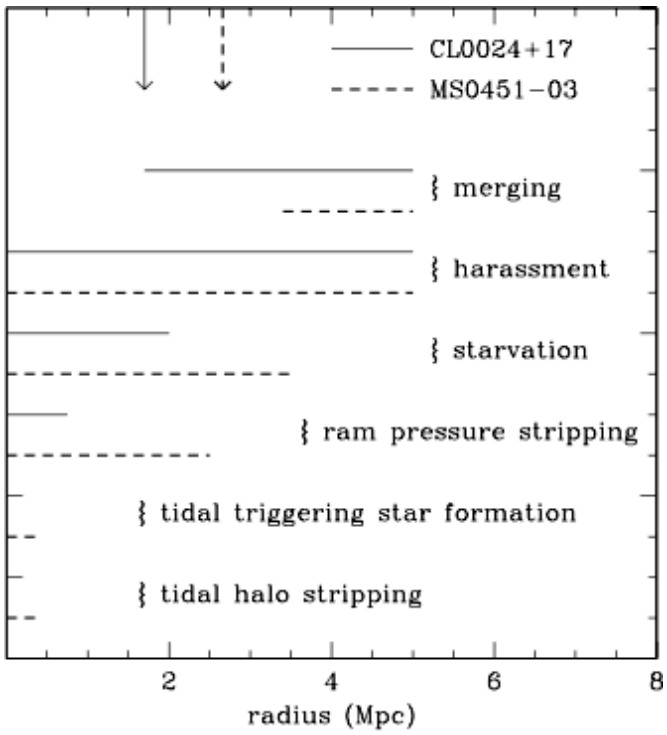

Figure 4.2: Schematic diagram indicating the clustercentric radius over which each of several listed physical mechanisms may be effective at fully halting star formation or transforming the visual morphology of a radially infalling galaxy. The ranges are indicated for two clusters: Cl 0024 (solid line) and MS 0451 (dashed line). The arrows indicate the virial radius of each cluster (i.e. the radius of a sphere centred on the galaxy cluster, within which virial equilibrium holds). The tidal processes in this diagram refer to interactions with the cluster potential, while tidal forces during galaxy-galaxy interactions are a component of the harassment mechanism. Figure taken from Moran *et al.* (2007a)

action of the proposed mechanisms are shown for two massive intermediate redshift clusters. From this figure, it is clear that tidal stripping is more effective towards the centre of clusters while ram pressure stripping, starvation and harassment are effective up to larger radii (in that order), and mergers dominate outside of the cluster centre. However, these regions can overlap, and hence the difficulty in separating the effects of the various physical processes with observations. The study by Moran *et al.* (2007a), has suggested that the transformation of spiral galaxies into S0s is a heterogeneous process that nevertheless proceeds robustly across a variety of different environments. Whilst ICM related processes mainly affect (suppress) the star formation, the morphological transformation is likely to be driven by tidal processes such as harassment. However, there is still much debate on the importance of each mechanism.

Numerous studies have been carried out to identify which one of these mechanisms is dominating galaxy transformation. A common approach to studying the physical

mechanisms driving galaxy evolution is to observe and compare the properties of well defined galaxy samples in different environments. Examples of these properties include gas and dust content, star formation rate, chemical composition, stellar populations, kinematics, luminosity, colour and many others. The combination of these observables (and the ability to reproduce them with models) is crucial for a complete understanding. In addition to the study of individual galaxy characteristics, understanding the effect of environment on scaling relations is a very useful way of addressing the problem.

This chapter investigates the effect of environment on the gas kinematics and the structure of the stars in distant galaxies, and chapter 5 further investigates environmental effects on the scaling relations and star formation of disk galaxies.

4.2 The sample

In the analysis of the present chapter and in that of chapter 5, we focus on a sub-sample of galaxies from the EDisCS dataset, consisting of galaxies with measurable emission in their spectra, as described in the following.

First, we rejected galaxies with emission-lines clearly affected by sky lines or without a discernible tilt (as judged by visual inspection). We then rejected galaxies with inclinations of less than 30° (inclination $= 0$ corresponding to face-on) to ensure that rotation could be measured[1]. Section 4.2.1 describes how the inclinations were computed. We also rejected observations affected by slit misalignment (misalignment with respect to the major axis of the galaxy $> 30^\circ$) to ensure secure rotational velocity measurements. After applying these conditions, there were 1038 emission lines, belonging to a total of 422 galaxies. Typically, we could detect 3 emission lines per galaxy. These were typically (in order of frequency), the [OII]3727Å doublet, Hβ, the [OIII] 5007 and 4959Å lines, Hγ, and Hδ.

The "true" parent emission-line galaxy distribution is well represented by our sample. The fraction of EDisCS galaxies with emission-line spectra for which we were able to model emission-lines and measure a rotation curve is fairly constant ($\simeq 35\%$) in the

[1]Rotation velocities are used in the construction of Tully-Fisher relations in Chaper 5

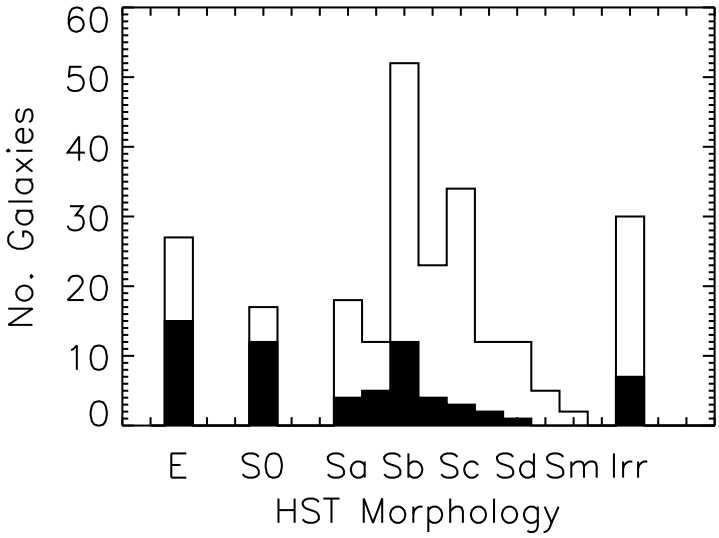

Figure 4.3: Histogram of the morphological types for those galaxies with HST observations in our parent emission-line galaxy sample. The open area represents the morphology distribution of the galaxy sample with HST observations. The shaded area will be discussed in section 4.3.1 and it corresponds to the galaxies (within the HST sample) with "bad" emission line fits (i.e. disturbed gas kinematics). The different morphologies are labelled in the plot. Whilst most of the galaxies have late-type morphologies, there is a small group of early-types in our emission-line galaxy sample.

magnitude range of our galaxies ($18 < I < 26$ mag).

In section 4.4, we impose additional constraints on the sample, in both M_B and redshift, to produce a luminosity-limited sample. This step is required in order to create matched cluster and field galaxy samples. Until then, all the sample described in this section is considered, unless otherwise stated.

As explained above, our sample selection was based on the presence of measurable emission lines (and not on galaxy morphology). It is therefore interesting to determine which galaxy morphologies passed our selection criteria. We have HST observations for 61% of our sample, hence reliable visual morphologies (Desai *et al.*, 2007). Figure 4.3 shows a histogram of the morphological types for the galaxies with HST observations. The open histogram contains all the fitted galaxies. The shaded area represents potential kinematically-disturbed galaxies, as explained later in section 4.3.1.

As expected, most of the emission-line galaxies in our sample are spirals, and the distribution peaks at Sb morphology types. However, somewhat unexpected, there is a significant population of early-type galaxies, 27 of which are ellipticals. We return to

Table 4.1: Number of galaxies per morphology type for the sub-set of galaxies with HST observations. This sample is drawn from the measurable-emission-line galaxy sample, where no redshift or magnitude cuts have been made. The columns correspond to: (1) the morphology type; (2) the total number of galaxies with that morphology; and (3) the number of galaxies within that morphology group for which none of the emission-line fits were "good", i.e. galaxies with disturbed gas kinematics. We refer to section 4.3.1 for the definitions of "good" and "bad" fits. These numbers are also represented in figures 4.3 and 4.8.

Morphology	No. galaxies	No. "Bad" galaxies
Elliptical (E)	27	15
Lenticular (S0)	17	12
Spiral (Sa to Sm)	169	31
Irregular (Irr)	30	7

this finding in section 4.3.1 after studying the gas kinematics of the galaxies. Table 4.1 quantifies the morphology distribution shown in figure 4.3.

Note that in a study of the star formation histories of EDisCS galaxies, Poggianti *et al.* (2009) found a few spiral galaxies with spectra showing no emission lines. Obviously, these passive spirals are not present in our sample.

We also note that we do not attempt to exclude galaxies hosting an AGN from our emission-line sample. We are unable to identify AGNs in our data, as the traditional optical diagnostics are based on emission lines that are not included in the spectral range covered by most of our spectra. In Poggianti *et al.* (2008) however, it was estimated that, the contamination from pure AGNs in EDisCS spectroscopic sample is at most 7%. Because the contamination is negligible, we conveniently refer to galaxies interchangeably as "emission-line" or "star-forming".

4.2.1 Structural parameters

Inclinations were derived by fitting a a 2-component 2D fit to F814W HST images when available, or I_{814}-band (VLT) images otherwise. The fit accounted for a bulge with a de Vaucouleurs profile and an exponential disk component, convolved to the PSF of the images. This was done using the GIM2D software (see Simard *et al.*, 2002, 2009, for a detailed description of the method used).

Inclinations are used to correct absolute magnitudes from internal extinction (sec-

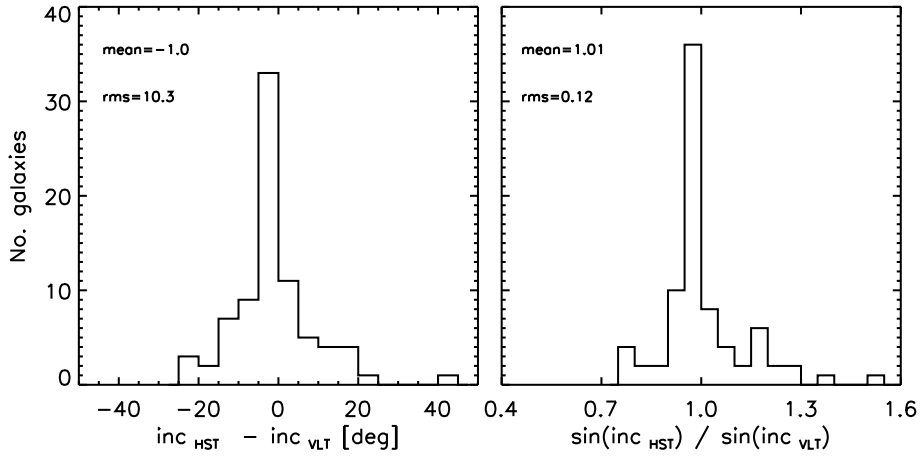

Figure 4.4: Inclinations derived from F814W HST images ($\mathrm{inc_{HST}}$) are compared with those computed from I-band VLT images ($\mathrm{inc_{VLT}}$) for galaxies within our (luminosity and redshift limited) matched samples A and B used in later in this work (see section 4.4). The left hand panel shows a histogram of the difference between both values. The right hand panel shows a histogram of the ratio of the sines of both inclinations. We plot these ratios to understand how much the Tully-Fisher relation (in particular, $\log V_{\mathrm{rot}}$, computed in chapter 5) would be affected . As is evident, the distribution in the right hand panel is very narrow and peaks at 1. In both panels, the mean value and rms of the distributions are shown for reference.

tion 4.2.2) and to compute rotation velocities (chapter 5). For this reason, we verified that the use of different image data sets (HST or VLT) does not bias our results. This is illustrated in figure 4.4, where HST inclinations are compared with those computed from VLT images. The figure contains two histograms. The one in the left hand panel shows the distribution of the difference between the two inclinations ($\mathrm{inc_{HST}} - \mathrm{inc_{VLT}}$). The distribution peaks very near zero and has a rms scatter of ~ 10 deg. The right hand panel shows the ratio of the sines of the two inclinations, $\sin(\mathrm{inc_{HST}})$ and $\sin(\mathrm{inc_{VLT}})$. This was done to quantify and understand how much the choice of one or the other value of inclination would affect the positioning of the data points on the TFR (i.e. the values of $\log V_{\mathrm{rot}}$). The distribution in the right hand panel is very narrow, with a clear peak at $\sin(\mathrm{inc_{HST}})/\sin(\mathrm{inc_{VLT}}) = 1$. Therefore, we can reliably use VLT-derived inclinations without biasing our results. This is also true for the less-demanding position angles.

We note that inclinations were derived from a 2D fit to the images, under the assumption that all galaxies had a "bulge" and a "disk" component (see Simard *et al.*, 2009). The presence of a "disk" component does not necessarily imply that there is an actual disk, because many dynamically hot systems have simple exponential profiles. We

know from our HST observations that not all the emission-line galaxies are disks (e.g. see figure 4.3), however, the vast majority are (96% within the luminosity and redshift matched samples defined in section 4.4). Potential biases introduced by the small fraction of non-disk galaxies included in our sample are discussed later.

4.2.2 Rest-frame magnitudes

The magnitudes used throughout this and the following chapter, were absolute B-band magnitudes, M_B. We chose M_B because it is a good tracer of recent star formation. Values of M_B were calculated from the observed SED of each galaxy, normalized to its total I-band flux, and the spectroscopic redshift (we refer to Rudnick *et al.*, 2009, 2003, for details of the calculation of M_B and luminosities).

The magnitudes were additionally corrected for internal extinction, following the prescription of Tully *et al.* (1998), to give the corrected absolute rest-frame B-band magnitudes, M_B, used in this chapter (and in chapter 5).

4.3 Emission-line fitting

In order to study the state of the gas kinematics in our galaxy sample (this chapter), as well as computing trustworthy rotational velocities to populate the Tully-Fisher diagram (chapter 5), we need a reliable method to compute the rotation velocity ($V_{\rm rot}$) of the galaxies under study. We use a synthetic rotation curve method based on ELFIT2D by Simard & Pritchet (1999), and dubbed ELFIT2PY by Bamford *et al.* (2005), which was designed to fit rotation curves to spatially resolved emission lines of distant galaxies. In this technique, a model emission line is created for a particular set of parameters, assuming a *Courteau* rotation curve (Courteau, 1997), and exponential surface-brightness profile. The galaxy inclination, seeing, and instrumental profile are provided as input and the fitting procedure also accounts for the galaxy size being comparable to the slit-width. A Metropolis algorithm (a Markov chain Monte Carlo proposed by Metropolis *et al.*, 1953) is used to search the parameter space to find those which best fit the data, and to determine the confidence intervals of these parameters.

For this work, ELFIT2PY was modified to best suit the characteristics of the EDisCS data used. The algorithm constructs a 2D model of each emission-line studied, which is used in this chapter to identify kinematical disturbances in the galaxies' gas. Additionally, ELFIT2PY computes the rotational velocity of each emission line ($V_{\rm rot,i}$), together with the best fit for the emission scale-length ($r_{\rm d,emission,i}$) of the line. These two quantities will be thoroughly described and used in chapter 5.

Many galaxies in our sample have more than one measurable emission line, and a fit was performed for each line independently. Final values of $V_{\rm rot}$ and $r_{\rm d,emission}$ are computed in section 5.3 by combining the individual measurements. The final errors in the measured parameters include the uncertainty caused by the multiplicity of chi-squared minima. All errors represent 68% confidence intervals (1σ errors).

4.3.1 Quality control

To determine the state of the gas in the galaxies (if the galaxy is kinematically disturbed or not) as well as ensure the use of secure rotational velocities, we visually examined a sub-set of emission line fits and investigated whether poor fits could be identified by their reduced χ^2 (output from ELFIT2PY), median and maximum signal-to-noise of the data, length of confidence intervals, and/or extent of the emission-line. We reached the conclusion that there was no efficient way of rejecting poorly fitted emission-lines without visually inspecting their quality. For this reason, two people independently (the author of this thesis and Alfonso Aragón-Salamanca) inspected the fits made to all the (1038) emission lines. We graded the fits according to their quality and created two groups: "good" and "bad". Both classifiers agreed in the vast majority of the cases (91%). In the few cases where we disagreed, we adopted the most pessimistic outcome. This classification yielded 527 "good" quality fits (i.e. reliable emission line fits) and 511 "bad" ones. The "bad" fits correspond to either lines with poor signal, artefacts in the postage stamps (e.g. a poorly subtracted overlapping sky line or cosmic rays), or more frequently, poor fits due to disturbed gas kinematics in the targeted galaxy (i.e. observed rotation curve that did not resemble a rotating disk). We note that generally, galaxies with kinematically "bad" fits consistently showed the same distorted features in all their visible emission lines. The "bad" fits were not used

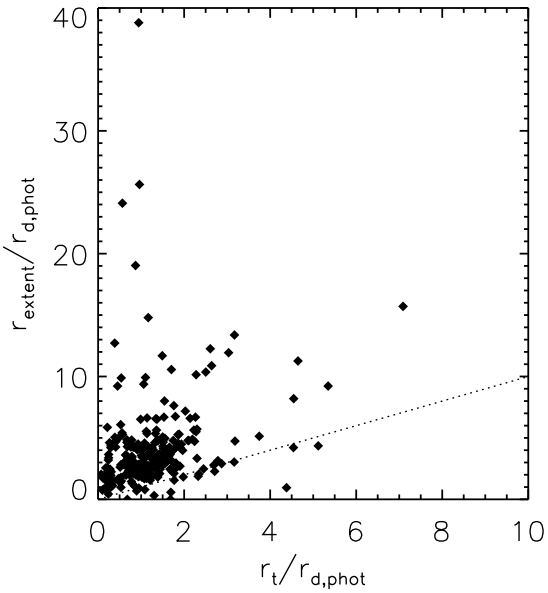

Figure 4.5: The extent of the fitted emission lines normalized to the photometric scalelength ($r_{\rm entent}/r_{\rm d,phot}$) is plotted versus the turnover radius normalized to the photometric scalelength ($r_{\rm t}/r_{\rm d,phot}$). The dotted lines simply shows the one-to-one relation for comparison. This plot shows how the emission lines of our "good" fit sample extend beyond the turnover radius, making our rotational velocity measures reliable.

in the Tully-Fisher analysis (section 5.4.1), as they could not yield reliable rotation velocities. However, we used the information that they provided in this chapter to study of the fraction of potential "kinematically disturbed" galaxies with luminosity, environment and morphology (cf. sections 4.5.1, 4.5.2 and 4.5.3).

Within the "good" fit sample of emission-lines, in almost all of the cases, the observed emission extended beyond turnover radius[2]. This is demonstrated in figure 4.5, where we compare the extension of the emission with the turnover radius. From this figure it is clear that most of the emission lines extend beyond the turnover radius. We note that in figure 4.5 we only plot the "good" emission-line fits because only in this sample we have reliable measures of $r_{\rm d,emission}$ and hence $r_{\rm t}$.

Figures 4.6 and 4.7 show examples of "good" and "bad" emission-line fits respectively. The complete set of emission line fits can be found in the EDisCS website at: *http://www.mpa-garching.mpg.de/ediscs/Papers/Jaffe_tfr_2011/RCfits.html*.

[2]The turnover radius $r_{\rm t}$, is the radius at which the rotation curve of a galaxy "turns" from diferential rotation to rigid. In ELFIT2PY, this radius has been set to be proportional to the disk scalelength of the emission ($r_{\rm d,emission}$).

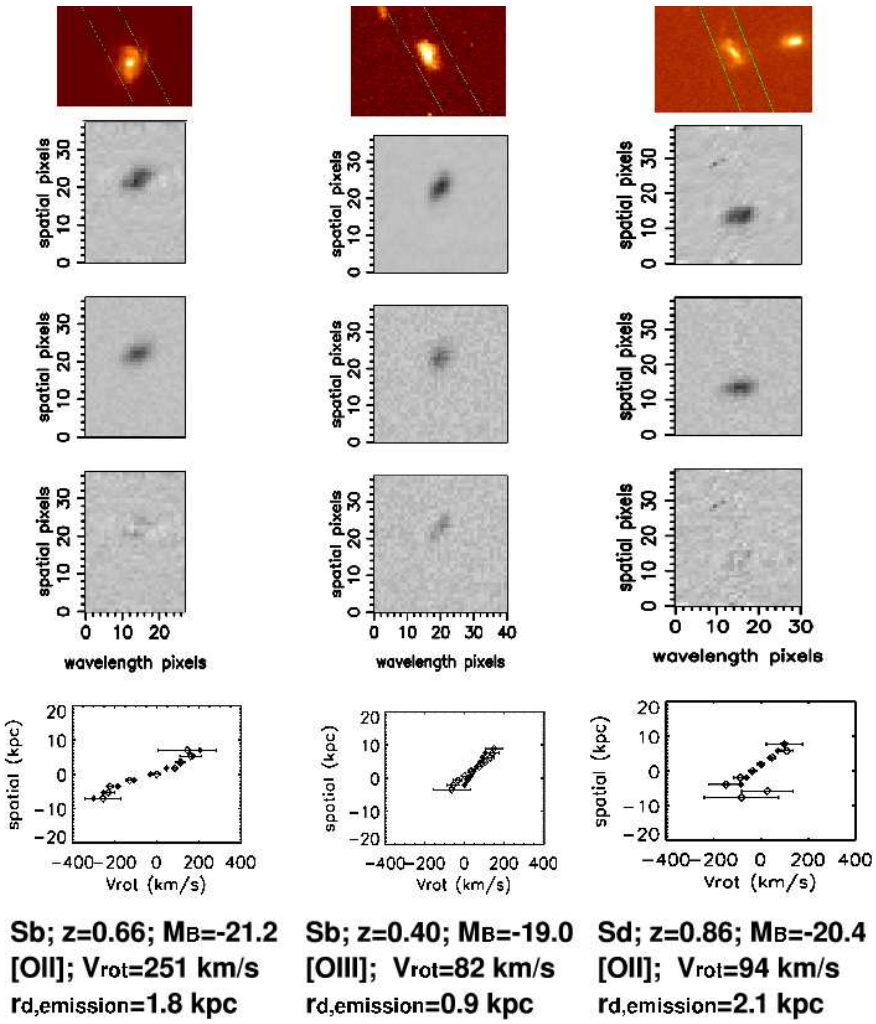

Figure 4.6: Representative examples of our HST images, emission line fits and rotation curves. 3 Galaxies are shown as means of illustrating the method and the quality of the fits. The first row shows the HST image of the galaxy with the slit position overlaid, the second row shows an extracted emission line from the 2D spectrum (postage stamp), the third row shows the best fitted model to that line, while the fourth row contains the residuals of the previous two. In addition, the traces or 1D rotation curves are shown in the bottom row in physical units. Open circles represent the data points, while the filled ones are the model points. At the bottom of each column the morphology, redshift, M_B, line plotted, $V_{\rm rot}$, and $r_{d,emission}$ are specified. This figure only shows "good" fits, while figure 4.7 shows "bad" fits. Note that the left most panel is a very good fit, whilst the other two good fits (more typical) are less good but still model the data reasonably well. Note that for example in the third column (from left to right), the emission line had a sky line subtracted. Although the subtraction is visible, this does not affect the fitting of the rotation curve significantly. There were cases however, where the sky subtraction was not as clean, making the fit a more difficult task.

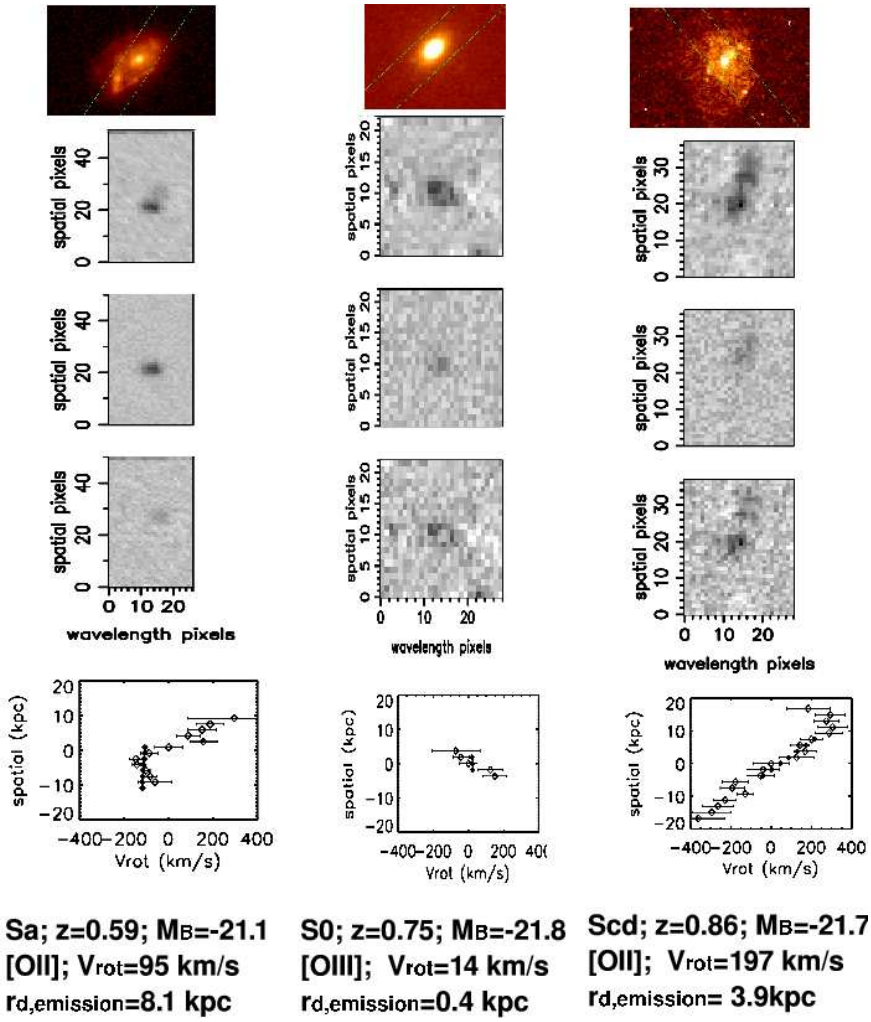

Figure 4.7: This figure similar to figure 4.6, but shows three example galaxies that had "bad" fits. These fits show clear signs of kinematical disturbance in the 2D spectra, and in the observed rotation curves. For this reason the model fails at reproducing a *Courteau* rotation curve.

In section 4.2, we showed that the parent emission-line sample spans a wide range of morphologies but is mostly composed of spirals. At this stage, it is interesting to see how the quality of the emission-line fits is correlated with morphology, especially if we assume that galaxies with "bad" fits are kinematically disturbed systems. The shaded area in the histogram of figure 4.3 shows the morphology distribution of the poorly fitted galaxies (galaxies for which all the emission-line fits available were flagged as "bad"). The open histogram draws the distribution of the full (good and bad) parent sample where HST images were available. The fraction of "bad" or kinematically-disturbed galaxies ($f_{\rm K}$) is plotted as a function of morphology in figure 4.8, and table 4.1 lists (in numbers) the amount of "bad" fits obtained for each morphology group. It is evident that the worst fitted group of galaxies (the ones showing the greatest deviations from a *Courteau* rotation curve) are the early types (E and S0s). Interestingly,

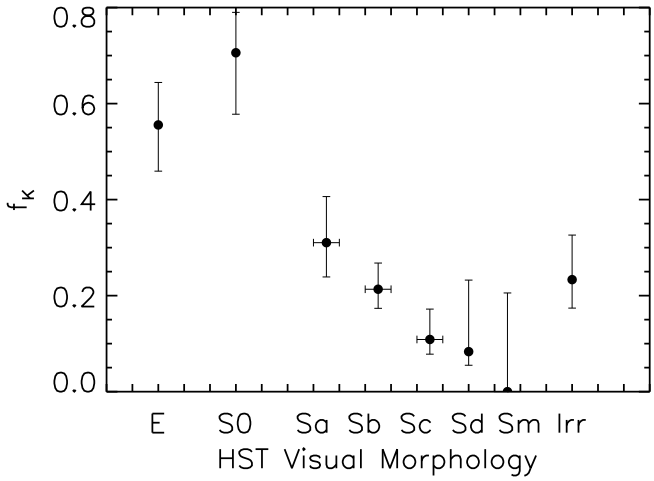

Figure 4.8: The fraction of galaxies with disturbed kinematics ($f_{\rm K}$) in the whole emission-line sample are shown for the different morphologies. Galaxies in cluster/group and the field are plotted. Horizontal error bars (when present) represent the grouping of adjacent morphology types, these cases are: Sa + Sab, Sb + Sbc, and Sc + Scd. This was done to increase the number of galaxies in these morphology bins. Error bars are the confidence intervals (c≈0.683) for binomial populations, from a beta distribution (see Cameron, 2010).

the worst fitted galaxies seem to be S0s and not the ellipticals nor the irregulars. However, as expected, the galaxies with the least amount of "bad" fits are the spirals. In the context of spiral-to-S0 transformation, this implies that galaxies already having S0 morphology have been subjected to strong disturbances in their gas content.

A very interesting finding is the discovery of 41 emission-line early-type galaxies, 17 of which have "good" rotation curve fits. These galaxies could be the first observational evidence of intermediate-redshift early-type galaxies with extended rotating gas disk. Although, these objects are not thoroughly studied in this thesis, we are currently carrying a separate investigation on this interesting group of galaxies (Jaffé et al., in preparation, see chapter 6), where we examine their formation scenario and possible evolutionary link to the $z \sim 0$ analogues found by (e.g.) the SAURON collaboration (see Emsellem *et al.*, 2007, and references therein).

4.4 Matched samples

Our emission-line galaxies (with fitted rotation curves) span a broad range of redshifts and rest-frame B-magnitudes, as figure 4.9 shows. Galaxies of all qualities are plotted.

The galaxies with "good" rotation curve fits are plotted in colours other than grey, depending on their environment: the blue open diamonds correspond to field galaxies, red filled diamonds to cluster galaxies, and black asterisks to group galaxies. The galaxies with "bad" rotation-curve fits are plotted in grey with the same symbols for environment. It is clear that there are more field than cluster/group galaxies (∼60% of the emission-line galaxies are in the field). Field galaxies are also more widely distributed in both redshift ($0 < z < 1.2$) and rest-frame B-magnitudes ($M_B < -14$) than the cluster/group population. The difference in redshift between the field and cluster sample is a direct result of the redshift of our clusters. The different ranges in M_B are a consequence of the different redshift ranges, as the observed I-band targeting limit was the same for both cluster and field galaxies.

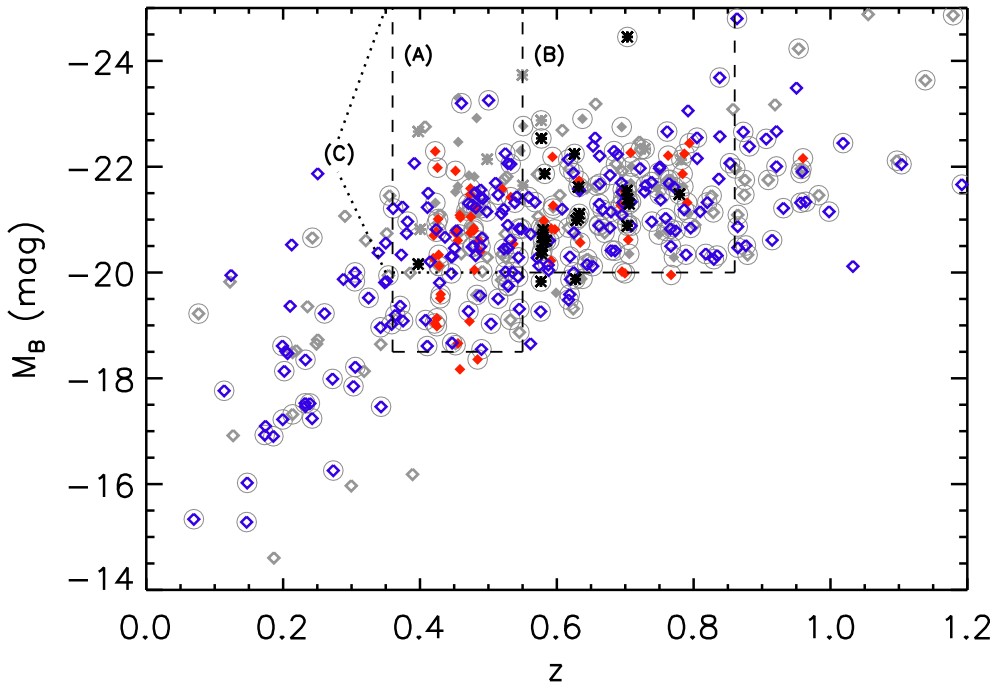

Figure 4.9: Distribution of M_B with redshift for the 422 galaxies of our measurable-emission-line sample. The cluster galaxies are plotted in filled diamonds, groups ($\sigma_{cl} < 400$km/s) are represented as asterisks and the field sample corresponds to the open diamonds. The red, black and blue colours (for cluster, group and field galaxies respectively) correspond to those galaxies with "good" rotation-curve fits, whilst the grey symbols represent the poorly-fitted galaxies. Three sub-samples are drawn from this plot: the lower redshift matched sample A (labelled dashed-line box), the higher redshift sample, B (again drawn within a dashed-line box), and an overall matched sample C that covers the redshift range $0.36 < z < 0.75$ and has the same magnitude limit as sample B (see dotted lines for guidance). For future reference, we have highlighted galaxies with HST observations with a surrounding grey circle.

In table B.1, all the emission-line galaxies used in this work are listed, along with some of their measured quantities such as kinematical disturbances, rotation velocity, emission disk scalelength, etc.

In order to investigate possible differences between cluster/group and field galaxies, we created field galaxy samples to match the cluster/group population. We did this by imposing cuts in redshift and M_B simultaneously. Three different cuts were made, producing three luminosity-limited or "matched" samples, represented (with boxes) in figure 4.9 and summarized in table 4.2.

The samples containing all ("good" and "bad") galaxies are used throughout this chapter, whilst in chapter 5 we focus mainly on the matched samples containing galaxies with good rotation-curve fits.

The redshift cuts for samples A and B were chosen so that each bin spans the same amount of cosmic time (~ 1.5 Gyr). Therefore, sample C spans ~ 3 Gyr of cosmic time. Throughout the rest of this thesis, we only consider galaxies within the limits of these 3 matched samples, unless otherwise stated. By doing this, we ensure a fair comparison between field and cluster galaxies (similar epochs and luminosities), which is the main goal of this investigation. In this chapter we will only consider the overall matched sample C. Samples A and B, although described here for simplicity, are not used until chapter 5.

We created matched samples in M_B rather than in stellar mass ($M_\star$), to keep the sample selection as close to the observables as possible. We note however that matching the samples in $M_\star$ does not make a significant difference since M_B and $M_\star$ are well correlated in our sample (see Figure 4.10). Our M_B-matched sample C is equivalent to a $M_\star$-matched sample of $M_\star \gtrsim 3 \times 10^9 \mathrm{M}_\odot$, in the same redshift range, with the exception of a few galaxies ($\sim 2\%$ of the galaxies in C). Figure 4.10 shows that, although there is some scatter, M_B and $M_\star$ are clearly correlated. In this plot, the M_B limit is shown as a vertical dashed line, and the $M_\star$ limit as a horizontal one. These lines delimit four regions in the plot: the upper-right region contains galaxies selected in both magnitude and mass (73.7%), the upper-left area contains those selected in mass but not in magnitude (9.7%), the lower-right region those selected in magnitude but not in mass (2.4%), and the lower-left those not selected in mass nor magnitude (14.2%).

Table 4.2: Characteristics of the matched samples A, B and C of cluster/group and field galaxies (see figure 4.9), as well as for the whole sample (without any M_B or z cuts). For each sample, the following information is given: the magnitude limit, redshift range, number of galaxies with "good" rotation-curve fits, and number of galaxies with poor or "bad" rotation-curve fits. The last two quantities are given for cluster/group galaxies (labelled "Cluster") as well as for galaxies in cluster/groups or the field (labelled "Total"). The number of field galaxies in each case can be calculated by simply subtracting the number of cluster/group galaxies from the total number. The table also gives the sample sizes for the sub-samples with HST observations, in the same format as explained above.

	Sample A		**Sample B**		**Sample C**		**No cuts**	
M_B (faint) limit	-18.5 mag		-20.0 mag		-20.0 mag		-	
redshift range	$0.36 \leq z \leq 0.55$		$0.55 < z \leq 0.86$		$0.36 \leq z \leq 0.86$		-	
All galaxies	Cluster	Total	Cluster	Total	Cluster	Total	Cluster	Total
Total No.	57	143	60	151	109	264	132	422
No. "good" galaxies	35	100	37	105	65	181	81	289
No. "bad" galaxies	22	43	23	46	44	83	51	133
Galaxies with HST observations:	Cluster	Total	Cluster	Total	Cluster	Total	Cluster	Total
Total No.	23	69	56	111	73	155	88	259
No. "good" galaxies	18	55	34	77	47	112	59	188
No. "bad" galaxies	5	14	22	34	26	43	29	72

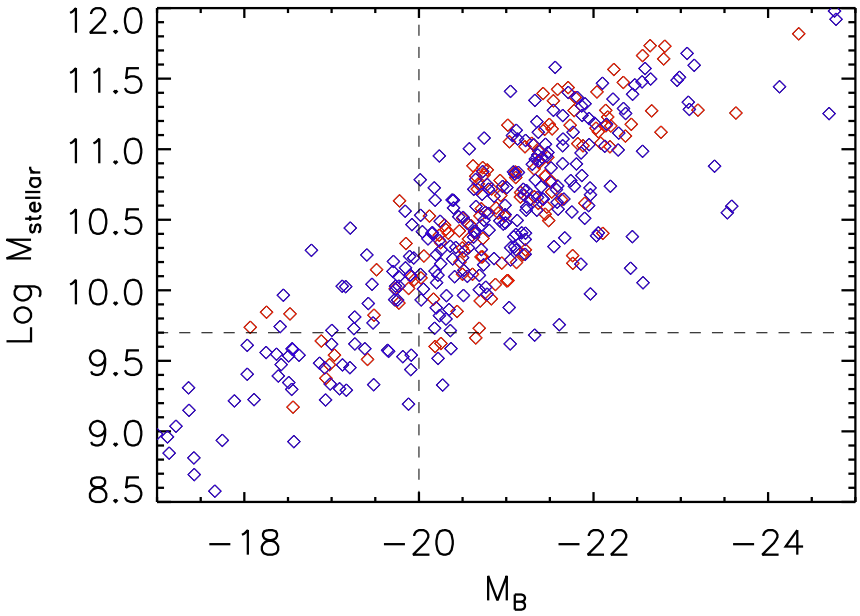

Figure 4.10: B-band magnitude is plotted against the logarithm of the stellar mass for those emission-line galaxies in the range $0.36 \leqslant z \leqslant 0.86$. This plot shows that because M_B and $M_\star$ are clearly correlated, a stallar mass selection would not difeer much from a magnitude selection. The $M_{\rm B}$ limit of sample C is shown in a vertical dashed line and a close-equivalent $M_\star$ limit is shown in a horizontal dashed line.

The morphologies of the cluster and field galaxies in the matched sample C are shown in figure 4.11 for galaxies with HST observations. The filled areas correspond to galaxies with "bad" rotation curve fits or disturbed gas kinematics in the field (upper panel) and cluster/group (lower panel) environments respectively. The overall distribution (of "good" plus "bad" galaxies) is shown by the solid lines (open histograms) in each case. Although the numbers are low (due to the sample being restricted to HST observations), the figure shows that there are more "bad" fits in cluster environments ($\sim 44\%$) than in the field ($\sim 25\%$). This effect is studied thoroughly in section 4.5.1 for the full sample C. Figure 4.11 also shows that while all of the cluster/group early-type galaxies had "bad" fits, 7 field early-types (6 ellipticals and 1 S0) in this "matched" sample survived the quality filters. We emphasize that in the morphology distribution shown previously in figure 4.3, the number counts are higher than in figure 4.11 because in figure 4.3, we did not restrict our emission-line sample in any way, whilst in figure 4.11 we imposed magnitude and redshift cuts to create a "matched" sample.

As mentioned in section 4.2.2 when describing the data, the rest-frame B-band magni-

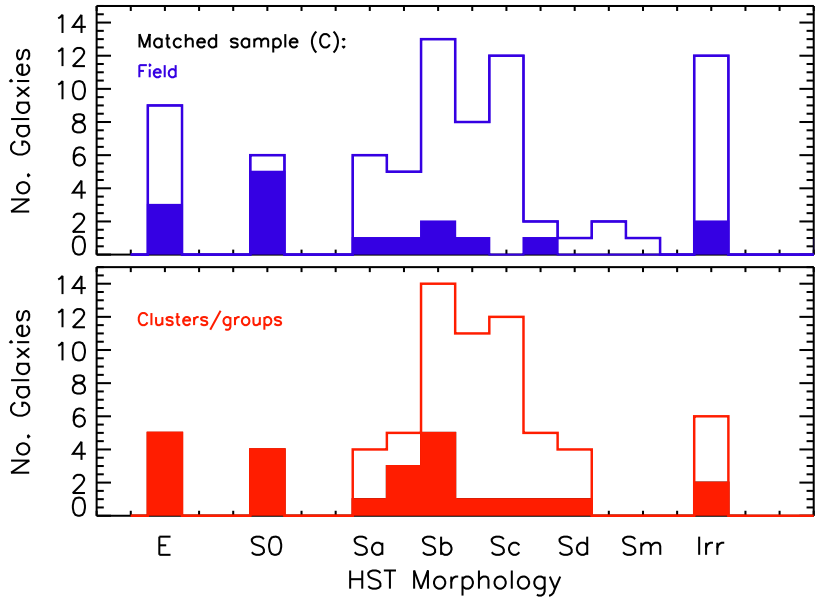

Figure 4.11: Histogram of the morphological types for the galaxies with HST observations that are in the C matched sample for cluster/groups (bottom panel) and the field (top panel). The filled areas (in both panels) represent the galaxies for which all rotation-curve fits were "bad". The different morphologies are labelled in the plot.

tudes were corrected for internal extinction. When accounting for this effect, we used the galaxy inclinations, which were calculated from the measured ellipticities, assuming all the galaxies to be disks. As figure 4.11 illustrates, not all of the galaxies in our matched sample are disks. We note however that the number of ellipticals is so small (6 in samples A and B, within sub-set of galaxies with HST observations) that the M_B correction applied to them does not alter our results. However, the inclination correction could potentially underestimate the luminosity and this may produce scatter in the Tully-Fisher relation (studied in section 5.4.1) since both M_B and the rotational velocity depend on the inclination. The typical M_B correction for these galaxies was very small (~ -0.3 mag), since their inclinations were all below $\sim 55°$. In section 5.4.3 however, we study the Tully-Fisher relation of (strictly) morphologically selected spirals, where the inclination correction is more reliable.

4.5 Results

4.5.1 Kinematically disturbed galaxies

As explained in section 4.3.1, a significant fraction of the fits made to the emission lines in our galaxy sample were classified as "bad" fits. Many of these lines showed evidence of disturbed gas kinematics in the galaxy, thus, a *Courteau* rotation curve could not provide a good fit. We use this information to investigate the fraction of galaxies with disturbed gas kinematics ("bad" galaxies) with environment. The left-hand panel of figure 4.12 shows the fraction of "bad" over total number of galaxies ($f_{\rm K} = \frac{N_{\rm bad}}{N_{tot}}$) in the matched sample C as a function of M_B (in bins that contain the same number of field galaxies). Although sample C spans a broad redshift range, in section 5.4.2 we show that the luminosity evolution is not significant in $0.3 < z < 0.9$ redshift interval.

The 1-σ uncertainties in the bad fractions were calculated from the confidence intervals (at confidence level, c≈0.683) derived from binomial population proportions using the beta distribution (see Cameron, 2010, for a description and justification of the method).

It is evident that the fraction of kinematically-disturbed galaxies in clusters is greater than in the field population, at least for $M_B < -20.5$. The percentage of "bad" over total number of galaxies in the whole M_B and redshift range (of sample C) is 44±5% for clusters and groups ($44 \pm 6\%$ in clusters, $31^{+10}_{-7}\%$ in groups), and $25^{+4}_{-3}\%$ in the field.

It is important to recall that not all galaxies that were categorized as "bad" are necessarily kinematically disturbed, but the majority of them are. As explained in section 4.3.1, some of them simply had poor quality spectra (e.g. badly subtracted sky lines near the studied galaxy emission line) but frequently, it is a difficult task to distinguish between these cases. Nonetheless, it is reasonable to argue that the results presented here are not biased because in principle, galaxies with bad spectra should appear in both field and cluster samples equally. However, to verify that this is true, we examined all galaxy spectra again to make a very conservative cut that distinguishes kinematically-disturbed galaxies from the others (all the doubtful cases were rejected). We repeated the exercise presented in the left hand panel of figure 4.12 but this time, we only con-

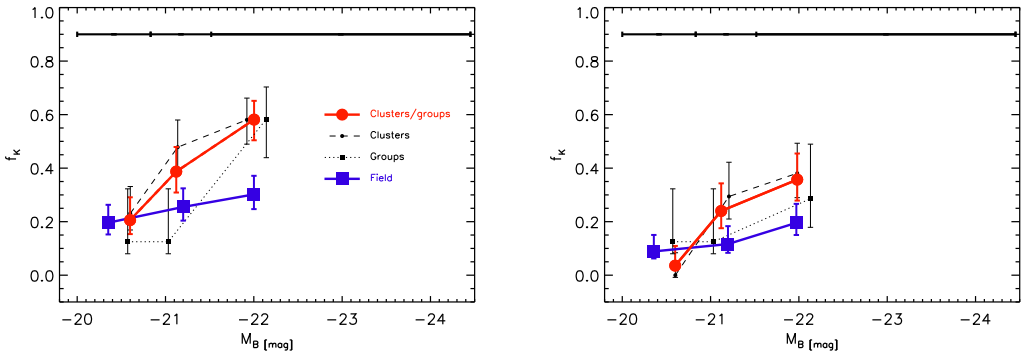

Figure 4.12: The fraction of galaxies with disturbed kinematics is shown for different environments as a function of M_B for the "matched" sample C (see figure 4.9 for the definition of the samples). In the left hand panel, all the "bad" rotation curve fits are considered. The right hand panel shows the same but with a more conservative cut in the definition of "bad". In this case, we have revised the "bad" emission-line fits to isolate galaxies with "secure" kinematical distortions (see text for details) and reject galaxies with spectra that are presumably affected by artefacts. The different environments are shown in the legend of the plot on the left and also apply for the right hand plot. The error bars in the abscissa correspond to confidence intervals for binomial populations (from a beta distribution, see Cameron, 2010) and the horizontal error bars (shown at the top of the plots) simply represent the bin size in M_B. These bins were chosen to contain similar number of field galaxies. The position of the points correspond to the median value of the galaxies within their magnitude bin. It is clear that the plot on the right agrees with the plot on the left, albeit with larger error bars due to the reduced sample size.

sidered as "bad", those galaxies with clear and strong signs of kinematical disturbance in their spectra. By making these conservative cuts, the sample reduced to about half of its size. This is shown in the right hand panel of figure 4.12, where we found similar trends as in the left hand panel, but for a smaller number of galaxies. Numerically, the percentage of (confirmed) kinematically disturbed over total number of galaxies in the whole M_B range is $22^{+6}_{-5}\%$ for clusters, $17^{+10}_{-5}\%$ for groups, $21^{+5}_{-4}\%$ for clusters and groups, and $13^{+3}_{-2}\%$ for field galaxies. Because of the difficulties in separating kinematically-disturbed galaxies from the rest, and having shown that the cut adopted does not bias the trends with magnitude and environment, we adopt the first cut (shown in the left panel of Figure 4.12) hereafter.

Figure 4.12 shows that, in clusters, the fraction of kinematically-disturbed galaxies is higher at brighter magnitudes. This does not happen in the field (or the effect is too mild to detect). It is not clear whether groups follow more closely the cluster or field behaviour (more detailed discussion in section 4.5.2). A possible interpretation is that the trend observed in clusters could be the result of fainter (less massive) cluster galaxies having already been stripped of their gas completely. This would cause

them to have no (or very little) emission in their spectra, and are hence excluded from our emission-line galaxy sample. Nonetheless, it is arguable whether this could be a consequence of a larger fraction of early-type galaxies, (which are more likely to have disturbed rotation curves, as shown in figure 4.8) at higher luminosities in clusters. We discarded this possibility by repeating the exercise shown in figure 4.12 with only the morphologically confirmed spirals. The results we obtain are compatible with our findings for the entire emission-line sample but are inevitably affected by larger uncertainties due to the reduced number of galaxies.

In addition to the above interpretation, it is arguable that the most luminous galaxies are those that were accreted more recently and therefore our results reflect the influence of the cluster environment at play. In a hierarchical Universe, one expects more massive systems to be accreted later, although there is some scatter (De Lucia et al., in preparation). In section 4.5.2 however, we show that the fraction of kinematically-disturbed galaxies decreases with distance from the cluster centre (see figure 4.14), hence the above interpretation is unlikely. The results of section 4.5.2 suggest another possibility: $f_{\rm K}$ may grow with luminosity because brighter (emission-line) galaxies may be more likely to reside in the cluster centres, where there is a higher incidence of kinematically-disturbed galaxies. We discard this possibility since we find no correlation between the luminosity of the cluster galaxies and their distance to the cluster centre.

4.5.2 Probing the environment

In section 4.5.1, we compared the gas kinematics of cluster, group and field galaxies. There are other ways however of studying environmental effects on the galaxy's gas state. In this section, we investigate the dependence of the fraction of kinematically-disturbed galaxies with (i) velocity dispersion of the galaxies' host cluster, (ii) projected distance from the galaxy to the cluster centre, and (iii) projected galaxy density.

A useful way to quantify the global environment in which a galaxy resides is in terms of the cluster velocity dispersion of the parent cluster ($\sigma_{\rm cluster}$), a good proxy for the cluster mass. The top panel of figure 4.13 shows the cluster velocity dispersion distribution of all the cluster emission-line galaxies (open histogram) in the matched sample

C, and highlights the distribution of galaxies with bad fits or kinematical disturbances (filled histogram). The cluster velocity dispersion range covered by EDisCS is very broad and thus is a good probe of environmental effects on galaxy properties. The bottom panel of figure 4.13 shows the fraction of kinematically-disturbed galaxies as a function of cluster velocity dispersion. This plot reinforces the results presented in section 4.5.1, showing that the fraction of kinematically-disturbed galaxies increases with $\sigma_{\rm cluster}$ by a factor of ~ 2 between $\sigma_{\rm cluster} \simeq 100 - 1200$ km/s. A non-parametric Spearman's rank correlation coefficient analysis of the trend shown in figure 4.13 indicates that the observed correlation is significant at the 83% level.

A frequently-used way to quantify the local environment of a galaxy is the distance from the cluster centre, which should be correlated with, among other things, the density of the intracluster medium (ICM) and the velocities of the galaxies inside that radius. To compare galaxies in all clusters, we normalize the distance from the galaxy to the centre of the cluster (r) by R_{200}[3], and study the ratio r/R_{200}. The values of r/R_{200} used here were computed in Poggianti *et al.* (2006) and are projected (2D) distances. Figure 4.14 shows the fraction of kinematically-disturbed galaxies as a function of r/R_{200}. The blue point corresponds to the field population and is plotted for reference at arbitrarily large radius. The figure shows a clear trend of increasing disturbance towards the cluster centre. This correlation is also significant at the 98% level.

We investigate how the fraction of kinematically-disturbed galaxies is affected by projected galaxy densities. The projected local galaxy densities used here are described in Poggianti *et al.* (2008). Briefly, densities were computed for each spectroscopically confirmed cluster member. They were derived from the circular area (A) that, in projection on the sky, encloses the N closest galaxies brighter than an absolute M_V limit. Hence, the projected density is $\Sigma = N/A$ and is given in number of galaxies per square megaparsec. The value of N used was 10, and the limiting magnitude was $M_V = -20$. In this chapter, we use the density computed from the "statistical subtraction method" described in Poggianti *et al.* (2008). In this method, all galaxies in the EDisCS photometric catalogues are used, and Σ is then corrected using a statistical background subtraction. We note that the calculations made in Poggianti *et al.* (2008) excluded two

[3]Where R_{200} is defined as the projected radius delimiting a sphere with interior mean density 200 times the critical density, commonly used as an equivalent of virial radius.

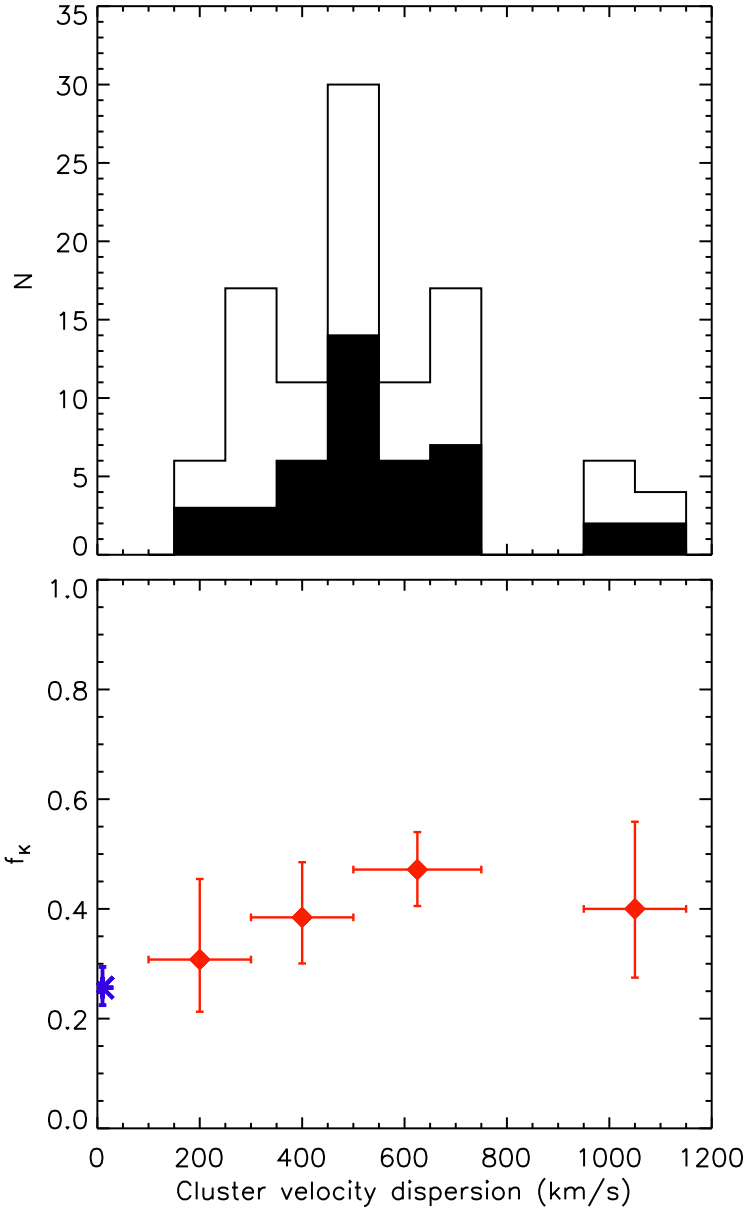

Figure 4.13: Top: The cluster velocity dispersion distribution of all galaxies in sample C (open histogram) and the distribution of those with "bad" fits (filled histogram) are plotted. Bottom: The fraction of "bad" galaxies (i.e. galaxies with disturbed kinematics) is shown as a function of cluster velocity dispersion for the matched sample C. The blue asterisk at $\sigma_{\rm cluster} \simeq 0$ km/s corresponds to the field population, shown for comparison. The values of $\sigma_{\rm cluster}$ were taken from Halliday *et al.* (2004), Milvang-Jensen *et al.* (2008), and Poggianti *et al.* (2009). A non-parametric Spearman's rank correlation coefficient analysis indicates that the correlation shown in this figure is significant at the 83% level.

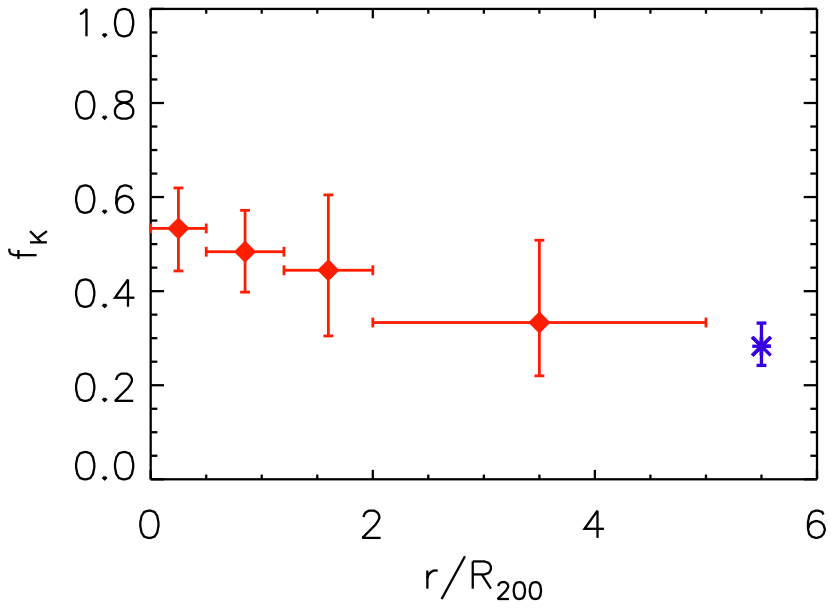

Figure 4.14: The fraction of galaxies with disturbed kinematics is shown as a function of r/R_{200} for the luminosity-limited sample C. All the "bad" rotation curve fits are considered. The data point for the field is plotted for comparison at arbitrarily high r/R_{200} as a blue asterisk. There seems to be significantly more galaxies with disturbed gas kinematics towards the cluster centre than in the field or high cluster-centric distances. A Spearman's rank correlation test indicates that the correlation shown in this figure is significant at the 98% level.

fields without deep spectroscopy, and two others that have a neighbouring rich structure at slightly different redshift, indistinguishable by photometric properties alone. For this reason, our Σ analysis contains only part of our matched sample C, but this fraction is nonetheless significant.

Figure 4.15 (bottom panel) shows the fraction of kinematically disturbed cluster/group galaxies in the luminosity-limited sample C as a function of projected densities. It is clear that the fraction of kinematically-disturbed galaxies remains constant with Σ, up to the highest densities.

To test that the trends seen in figures 4.15, 4.13, and 4.14 are not dominated by the inclusion of elliptical and S0 galaxies (which we know are more likely to be disturbed, see figure 4.8), we repeated each plot without the known E/S0s and obtained the same trends. In addition, we repeated them with only confirmed spirals. Because we only have visual (HST) morphologies for about half of the sample, the number of galaxies reduces significantly. The observed trends for the spiral galaxy sample remain

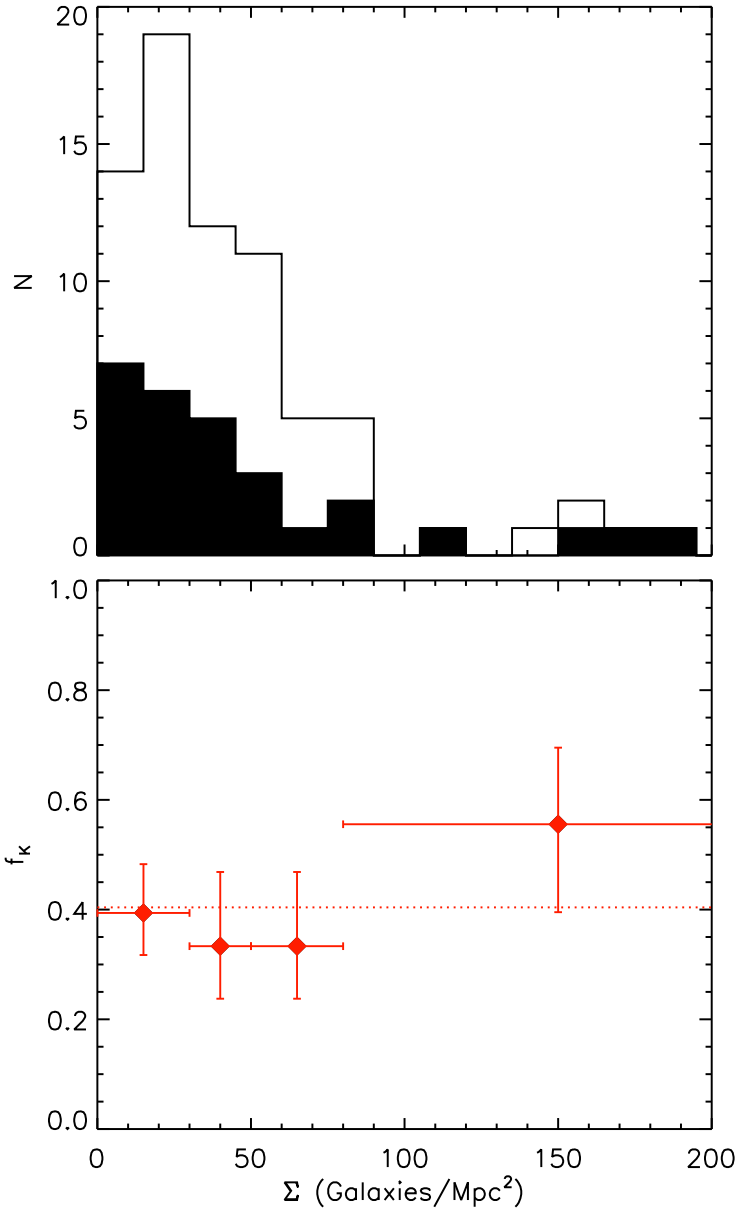

Figure 4.15: The top panel shows the distribution of the projected densities of the cluster emission-line galaxies in sample C. In the bottom panel, the fraction of galaxies with disturbed kinematics is shown as a function of projected density for cluster/group galaxies in the luminosity-limited sample C. The horizontal dotted line corresponds to the median value of $f_{\rm K}$ and is plotted to show that the fraction of kinematically-disturbed galaxies is consistent with that value at all densities.

unchanged, but inevitably suffer from greater uncertainty.

Because of the small number of galaxies in the bins of figures 4.13, 4.14 and 4.15, we adopted a conservative approach in estimating the confidence intervals (the one described in Cameron, 2010). However, the clear and smooth trends that we observe in figures 4.13 and 4.14 seem to suggest that we are overestimating the the errors somewhat.

When comparing the results obtained from figures 4.13, 4.14, and 4.15, it is clear that the gas kinematics is not affected by the local galaxy density, but significantly affected by the nature of the global environment itself (cluster mass and distance from centre). This strongly suggests that what affects most the properties of the gas in cluster galaxies has to be linked to the ICM and/or the gravitational potential of the cluster itself and not to galaxy interactions.

4.5.3 Morphologically disturbed galaxies

With the aim of comparing the state and distribution of the gas and the stars for galaxies in different environments, we performed an independent analysis of the morphological disturbances of the galaxies, as traced by optical (HST) imaging. The expectation is that our analysis of the 2D spectroscopy we have just described provides information on the gas structure and distribution, while the optical light traces the stellar structure. For the 126 (out of 224) galaxies with HST observations in the luminosity limited sample C, we fitted a smooth single-Sersic index model. We used the GALFIT code, described in Peng *et al.* (2002). The set-up with which GALFIT runs, named GALPHYT[4], is described in detail in Hoyos *et al.* (2011). Residual images were created by subtracting the model from the galaxy's HST image. These residuals highlight the presence of morphological distortions and contain valuable information about the interaction state.

Three people (the author of this thesis, Alfonso Aragón-Salamanca and Carlos Hoyos) independently examined the residual images and graded the level of morphological disturbance of the galaxies under study. We did this by looking for different fea-

[4]Developed in python by Carlos Hoyos

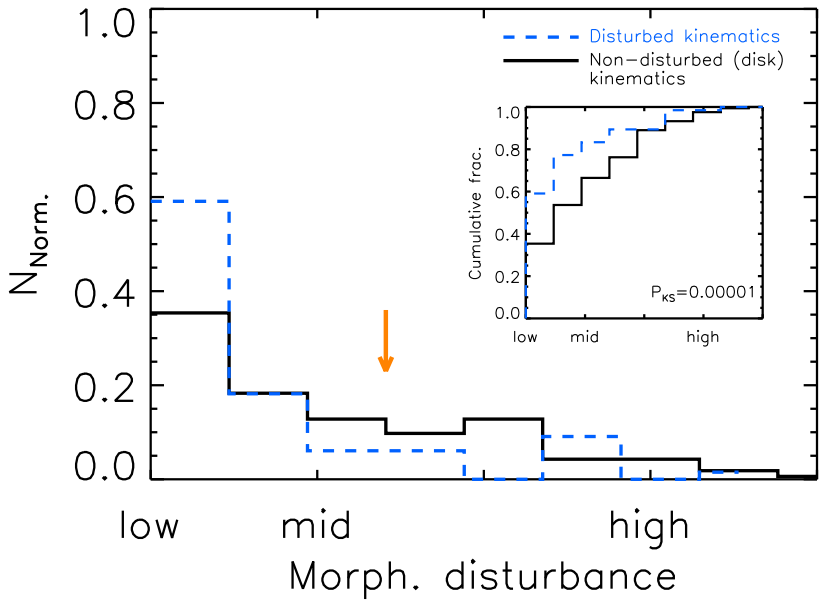

Figure 4.16: The distribution of the degree of morphological distortion is plotted in a histogram with normalized area (to unity) for: galaxies with good rotation curve fits (i.e. with normal disk kinematics, shown in a black solid line), and galaxies with disturbed disk kinematics (blue dashed line). The vertical (orange) arrow indicates the limit where we have separated non-disturbed from disturbed morphologies (definition used for figure 4.18). The sample plotted is the luminosity limited sample C that counts with HST observations (see circled symbols in figure 4.9). The inset panel shows the cumulative distributions of the morphological disturbance, as well as KS statistics, for the kinematically disturbed and undisturbed galaxies.

tures such as asymmetry, presence of tidal tails, nuclear components, mergers, and interactions. Each of these parameters were graded separately. By comparing the parameter space drawn by each examiner, we reached the conclusion that the most reliable (and consistent) way of determining the degree of morphological disturbance was the quantification of the asymmetry in the residual image. Hence, we defined a morphological disturbance index by combining the grades for the asymmetry parameter from the different examiners into an average grade. The disturbance index increases from 0 in the positive direction as the level of asymmetry becomes stronger. From the distribution of morphological distortion in our sample, we then defined two sub-samples of morphologically "good" and morphologically-disturbed galaxies by choosing a threshold value (see orange arrow in figure 4.16). Figure 4.17 shows a few examples of what we call morphologically disturbed and undisturbed galaxies. The complete set of HST images, single-Sersic fits and residuals images for the EDisCS galaxies treated in this chapter can be found at: *http://www.mpa-*

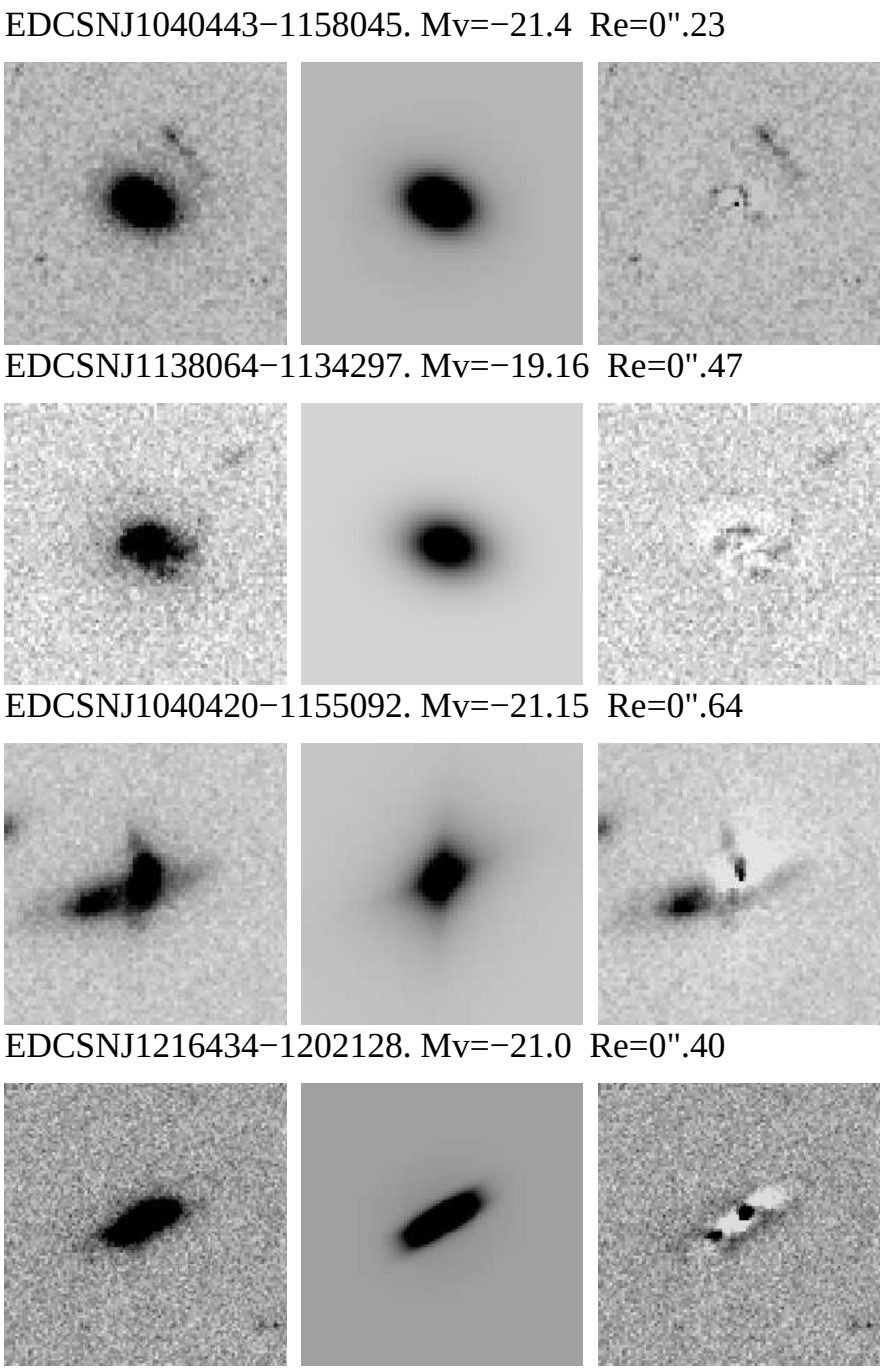

Figure 4.17: Representative examples of the method used to identify morphological disturbances in our galaxy sample. Our results are shown for four galaxies, the two on the top were considered "good fits" or morphologically undisturbed galaxies, while the other two were classified as "morphologically disturbed". The first column presents the HST cutout of the galaxies, the second column shows the best-fit model made to that image, and the third column exhibits the residual image between the model and the data. Galaxy names, M_V and effective radius are listed at the top of each galaxy.

garching.mpg.de/ediscs/Papers/Jaffe_tfr_2011/single_sersic_fits.html.

To understand how the morphological and kinematical disturbances are related, we compared the morphological disturbance index for both the kinematically "good" and "bad" samples. This is illustrated in figure 4.16, where we have plotted the morphological distortion index for the galaxies with disturbed gas kinematics (dashed blue line) and the galaxies with good rotation curve fits (solid black line). The figure also contains an inner plot showing the cumulative distributions and the resulting KS statistics. We find that although the distributions are statistically different ($P_{\rm KS}$ of only 0.15%), there does not seem to be a very clear difference between the morphological disturbance indices of galaxies with perturbed and unperturbed gas distributions. This suggests that the disturbance we observe in the gas is not directly linked to the galaxys morphological distortions.

Keeping in mind that early type galaxies are more likely to be kinematically disturbed (see figure 4.8), and that there are more kinematically-disturbed galaxies in clusters than in the field (see figure 4.12), we repeated the analysis shown in figure 4.16 with only morphologically-classified spiral galaxies, separating cluster and field ones. The results did not change significantly.

We also studied the fraction of morphologically disturbed galaxies, $f_{\rm M}$, as a function of M_B in the same manner of section 4.5.1. The result is shown in Figure 4.18 (plotted in the same way as Figure 4.12 for comparison). We observe that there is no significant difference between the morphologically disturbed galaxy fraction between cluster, group, and field environments in the M_B range studied. Our results are actually consistent with a constant morphologically disturbed fraction as a function of M_B in all environments. The total fraction of morphologically disturbed galaxies (over the full M_B and redshift range of sample C) is 47 ± 7% in clusters, 41^{+12}_{-10}% in groups, 45 ± 6% in cluster and groups, and 49 ± 6% in the field. It is important to point out that these fractions should only be compared internally within our study since the actual value of $f_{\rm M}$ will depend on the definition of "kinematically disturbed" or "morphologically disturbed". For instance, if we shift the vertical arrow in Figure 4.16 that defines the threshold between kinematical disturbed and non-disturbed galaxies, the fractions change in number. However, the lack of a trend seen in Figure 4.18 does not change.

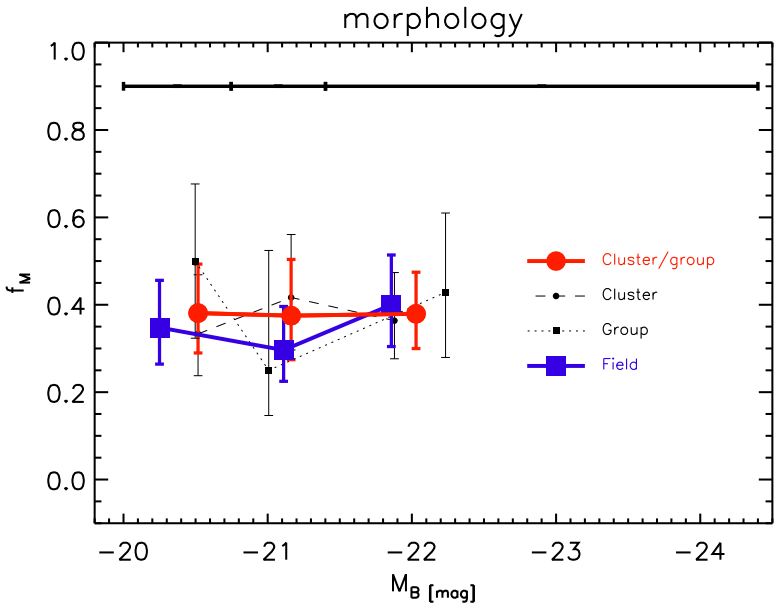

Figure 4.18: Fraction of morphologically-disturbed galaxies in different environments as a function of M_B, for galaxies with HST data in the matched sample C. This plot is analogous to the ones shown in figure 4.12, but instead of showing the disturbance in the gas kinematics with environment, it studies the disturbances in the stellar structure. The different symbols correspond to different environments, as shown in the legend. The error bars and M_B bins (shown at the top of the plot) are as in figure 4.12. We observe no dependence of morphological disturbance on environment.

We emphasize that the high fraction of disturbed galaxies (of $\sim 50\%$, cf. Figure 4.18) is a direct result of the threshold used to define morphological disturbances (the orange arrow in Figure 4.16 roughly divides the galaxy sample in half). Moreover, by subtracting a smooth model to the HST images, small morphological disturbances are enhanced (cf. Hoyos *et al.*, 2011), increasing the number of galaxies categorized as "morphologically disturbed".

We note that, our index for morphological disturbance (a visual index) is very similar to the asymmetry index in the CAS system (Conselice, 2003). Our threshold value for defining morphologically-disturbed galaxies is approximately equivalent to a CAS asymmetry index greater than 0.2. When using CAS asymmetry measurements and adopting this threshold value, we obtain the same trends observed in figures 4.16 and 4.18.

The results presented here for the disturbance of the structure of the galaxies' stellar component and those from section 4.5.1, show that the fraction of kinematically-disturbed galaxies is higher in clusters, whilst the fraction of morphologically-disturbed

galaxies does not change significantly with environment (see figures 4.12 and 4.18). This suggests that environmental effects are mild enough to not disturb the stellar structure in the galaxies significantly, but to strongly affect the gas in cluster environments. The implications of this result will be discussed in section 4.6.

4.6 Discussion

We have presented a detailed analysis of the effects of the environment on the gas and stars of distant galaxies. We have studied the gas kinematics, and stellar morphology of galaxies in various environments, which has provided us with important clues about the physical mechanisms transforming galaxies. We summarize and discuss our results in the following.

From the full EDisCS galaxy sample at $z \lesssim 1$, we selected all galaxies with measurable emission in their spectra, inclinations $> 30^{\circ}$ (to avoid face-on galaxies), and slit misalignment (with respect to the major axis of the galaxy) $< 30^{\circ}$. We then modelled the 2D emission lines and fitted a rotation curve to obtain rotational velocities. All the fits were individually inspected in a quality check procedure that separated our galaxy sample into two categories. The first one contains galaxies for which their emission lines yielded acceptable fits ("good" sample). The second one consists of galaxies for which no emission line could be fitted satisfactorily, and thus no reliable rotational velocity could be derived ("bad" sample). We then computed $V_{\rm rot}$ for each galaxy from the "good" emission-line fits.

Galaxy morphology was not taken into account in the sample selection. To investigate the morphology distribution of our emission-line sample, we studied the morphology distribution of the sub-sample of galaxies that have HST data (61% of our sample). We found that while most of the emission-line galaxies in our sample are spirals, 16% were classified as early-type galaxies (E or S0). Notably, the highest quality rotation-curve fits were obtained in the spiral sample, while the early-type galaxy group contained a significant fraction of "bad" galaxies. We nevertheless discovered 12 ellipticals and 5 S0s with clearly extended rotation curves in their emission. These interesting galaxies, although not studied in detail in this thesis, are currently being investigated (Jaffé et

al. in preparation).

We have shown that the galaxies with "bad" rotation curve fits represent a population of kinematically-disturbed galaxies. The fraction of kinematically-disturbed galaxies ($f_{\rm K}$) decreases significantly with morphological type (towards later types). Within the spiral sample, there is a difference of a factor of ~ 3 between Sa and Scd galaxies, and this difference is even higher if we include S0 galaxies. In the context of spiral-to-S0 transformation, this implies that galaxies already having S0 morphology have been subject of stronger gas disturbance.

By studying the fraction of kinematically-disturbed galaxies over the same M_B and redshift range in cluster, group, and field environments, we have found that $f_{\rm K}$ is clearly higher in cluster/group environments than in the field (for $M_B < -20.5$). The presence of kinematically-disturbed galaxies in clusters was first found by Rubin, Waterman & Kenney (1999) in the Virgo cluster, and has been confirmed by similar studies of the kinematical properties of galaxies in distant clusters (e.g. Ziegler *et al.*, 2003; Jäger *et al.*, 2004; Metevier *et al.*, 2006; Moran *et al.*, 2007b). The difference in the kinematics between cluster and field galaxies we find for EDisCS emission-line galaxies agrees with these previous results.

While the fraction of kinematically-disturbed galaxies in the field is roughly constant ($\cong 25\%$) throughout the M_B range, in clusters $f_{\rm K}$ is not only higher, but increases with luminosity. In other words, the most luminous (massive) galaxies exhibit more signs of gas disturbance. We interpret this trend as evidence that many of the fainter (less massive) galaxies have been completely stripped of their gas. This causes them to have no (or very little) emission in their spectra. For this reason, these galaxies are not selected in our emission-line galaxy sample. Moreover, we propose that if we were able to detect emission in these galaxies, the fraction of cluster galaxies with disturbed gas kinematics should be significantly higher than in the field at all luminosities, with a much smaller luminosity dependence. We have considered, but disfavour, two alternative explanations for the observed behaviour. First, the most luminous galaxies could be those that were accreted more recently and therefore their observed properties will reflect the recent influence of the cluster environment. This could be the result of the hierarchical cluster assembly, where more massive systems are accreted later (De Lu-

cia et al. in preparation). This interpretation is unlikely because we also find that the fraction of kinematically-disturbed galaxies decreases with distance from the cluster centre (see below). Second, it could be that $f_{\rm K}$ grows with luminosity because brighter emission line galaxies may reside at the centre of the clusters, where we find higher incidence of kinematically-disturbed galaxies. We discard this possibility because we find no correlation between the luminosity of our cluster emission-line galaxies and their distance to the cluster centre.

To ascertain which physical mechanisms are affecting the gas kinematics, we studied how $f_{\rm K}$ varies with different proxies for environment. We found that, although $f_{\rm K}$ increases with cluster velocity dispersion (by a factor of ~ 2) and decreases with distance from the cluster centre (by the same factor), it remains constant with projected galaxy density. Although our results suffer from considerable uncertainty, they are self-consistent, and suggest that the physical mechanism acting on cluster galaxies is probably related to the ICM or the cluster potential itself and not to galaxy interactions.

We also tested whether there is any correlation between the degree of kinematical disturbance in the galaxies' gas and the amount of disturbance in their morphologies. We did this by fitting a smooth single-Sersic index model to each galaxy (with available HST data) and subtracted it from the original HST image. The corresponding residual images thus highlighted morphological distortions. By inspecting them carefully, we found that $\sim 50\%$ of the galaxies show significant signs of asymmetry that we have interpreted as the possible result of a recent interaction. We hote however that the method we use highlights small assymetries and hence we do not claim that 50% of the galaxies have recently experienced a merger event. More likely, a few of these galaxies are mergers and most are only experiencing less violent interactions. We did not find a clear direct link between the kinematic disturbance in the galaxies' gas and their morphological disturbance, indicating that the physical mechanisms and/or timescales involved are different.

In sum, our results suggest the physical mechanism responsible for the transformation of star-forming spirals into passive S0s in clusters efficiently disturbs the galaxies' star-forming gas and reduces their star-formation activity, but leaves their stellar disks largely undisturbed. In particular, our findings support a mechanism that is related to

the intra-cluster medium, with galaxy-galaxy interactions and mergers playing only a limited role.

Chapter 5

The effect of the environment on the Tully-Fisher Relation and star formation of distant galaxies

5.1 Introduction

In addition to the study of the state of the gas and the stars in a homogeneous galaxy sample (chapter 4), understanding the effect of environment on scaling relations is a very useful way of identifying the physical mechanism(s) driving galaxy evolution. In particular, the relation between disk luminosity and maximum rotational velocity, i.e. the Tully-Fisher relation (TFR, Tully & Fisher, 1977) has proven to be one of the fundamental empirical clues to the physics of galaxy formation, in particular, to the relation between dark and luminous matter in galaxies. By comparing the TFR of cluster versus (vs.) field galaxies it is possible to spot potential environmental effects that ultimately transform spirals into S0s. Whilst the internal kinematics of galaxies reflect the overall gravitational potential (providing a proxy for the total mass), the luminosity can be used as a proxy for both luminous mass and star formation, if the right photometric band is chosen (the rest-frame B-band luminosity is particularly sensitive to star formation).

Much effort has been made in understanding the local TFR, and its redshift evolution

(e.g. Tully & Fisher 1977; Cole *et al.* 1994; Vogt *et al.* 1996; Ziegler *et al.* 2002; Kannappan, Fabricant & Franx 2002; Milvang-Jensen *et al.* 2003; Böhm *et al.* 2004; Bamford, Aragón-Salamanca & Milvang-Jensen 2006; Nakamura *et al.* 2006; Weiner *et al.* 2006; Pizagno *et al.* 2007; Kutdemir *et al.* 2010, and references therein). Kassin *et al.* (2007) developed a revised TFR with the aim of understanding the scatter about the stellar-mass TFR. This new relation replaced rotation velocity ($V_{\rm rot}$) with a revised kinematic estimator ($S_{0.5}$) that accounts for disordered or non-circular motions through the gas velocity dispersion σ_{gal}: $S_{0.5}^2 = 0.5V_{\rm rot}^2 + \sigma_{gal}^2$. This new relation between stellar mass and $S_{0.5}$ is remarkably tight for their Keck/DEIMOS spectroscopic sample over $0.1 < z < 1.2$ with no detectable evolution in slope or intercept with redshift. They conclude from this that the galaxies are perhaps virialized over this 8 billion year period. Furthermore, they find that the $S_{0.5}$ stellar-mass TFR is consistent with the absorption-line-based stellar-mass Faber-Jackson relation for nearby elliptical galaxies in terms of slope and intercept, suggesting a physical connection between them. This has also been seen locally (over a larger mass range) by Zaritsky, Zabludoff & Gonzalez (2008).

A few studies of the effect of the environment on the TFR have also been made. For instance, Milvang-Jensen *et al.* (2003) found, in a rather small sample (containing 8 cluster spirals at $z = 0.83$ and additional field galaxies), that cluster spirals were brighter than the field ones by $\sim 0.5-1$ mag at a fixed rotation velocity (1.5-2σ result). Bamford *et al.* (2005) found the same behavior with a significantly larger sample (111 galaxies in total at $0 < z < 1$). They conclude that this effect could be caused by an initial interaction with the intra-cluster medium. Conversely, Ziegler *et al.* (2003) and Nakamura *et al.* (2006) found no difference between the cluster and field TFR of galaxies. Work by Ziegler *et al.* (2003); Jäger *et al.* (2004); Metevier *et al.* (2006) have further discussed the effect of environment in the internal gas kinematics of galaxies, beyond the TFR. They have found that in cluster environment many galaxies show unusual kinematic signatures such as noncircular motions.

Undoubtedly, larger and more homogeneous studies that search for relations with respect to cluster properties, redshift, etc. are still needed.

In addition to the TFR and the global star formation in galaxies, an important aspect

presumably affected by environment is the concentration of the star formation within the disk. In fact, a potential difference between the different mechanisms is their predictions on the star formation within the affected galaxies. In some ram-pressure stripping models (e.g. Bekki & Couch, 2003) it is possible that the star formation is enhanced across the disk, while in a merger or tidal stripping scenario, a centrally concentrated starburst is likely to occur (Mihos & Hernquist, 1994). But before we can distinguish these differences, we must establish that a starburst or star formation suppression is present.

In this chapter, we use the EDisCS dataset to study the effect of the environment on the TFR, star formation, and location of the star formation within the discs of distant galaxies. Unfortunately, because of the relatively low spectral resolution of our data we are not able to make a comparative study of the $S_{0.5}$ stellar-mass TFR of Kassin *et al.* (2007) (see chapter 2 for details on our dataset). Our aim is to understand which physical processes are primarily responsible for the transformation of spiral galaxies into S0s in clusters. In particular, we are interested in addressing the following questions. How is the star formation of a galaxy falling onto a cluster affected? Does it decline immediately, or does it go through a period of enhancement? If so, is there a significant offset between the cluster and field TFR? Is this last episode of star formation centrally concentrated, leading to an enhanced bulge-to-disk that would occur during a spiral-to-S0 transformation? Do these processes depend on the galaxy location within the cluster, or on cluster properties such as their mass or concentration?

5.2 The sample

In this analysis, we use the same EDisCS emission-line galaxies described in section 4.2. The only additional constrain we place in this chapter (except for section 5.4.4) is that the quality of the rotation-curve fits had to be good.

In section 4.3, the method used for fitting rotation curves to the emission-line galaxy sample was described. In short, this process yielded a rotation velocity and emission disk scale-length for each fitted emission line. After careful quality checks, we divided our sample in two groups, in accordance with the quality of the fits: "'good" or "bad".

In general, poor or "bad" fits were caused by kinematical disturbances in the gas disk, and hence a reliable measure of the rotational velocity or emission disk scale-length was not obtained. For the construction of a TFR, we need reliable rotation velocity measurements. For this reason, we only considered "good" emission-line fits. After rejecting the "bad" fits, our sample decreased in size to 527 lines belonging to 292 galaxies. By performing such sample cleaning, we are able to ensure that all the fits used have reliable rotation curves, hence reliable measurements of $V_{\rm rot}$. Most galaxies (55%) had more than one "good" emission line. The remaining galaxies had only one measurable emission line from which a final rotational velocity could be computed.

5.2.1 Star formation rates

In addition to the rotation velocities, emission disk scale-lengths, and rest-frame magnitudes, this chapter makes use of star formation rates to analyse possible environmental effects on galaxy evolution.

The star formation rates (SFRs, not corrected for dust) used in this chapter were derived from the observed [OII]3727Å fluxes following Poggianti *et al.* (2008). These fluxes were obtained by multiplying the observed [OII] equivalent width by the continuum flux, estimated from the broadband photometry using total galaxy magnitudes. We derived specific star formation rates (SSFRs) by simply dividing the SFRs by the stellar mass.

Stellar masses ($M_{\star}$) were computed by John Moustakas (see Vulcani *et al.*, 2011) using the *kcorrect* tool (Blanton & Roweis, 2007), which models the observed broad-band photometry, fitting templates obtained with spectrophotometric models.

We used a Kroupa (2001) IMF covering the $0.1\,{\rm M}_{\odot}$–$100\,{\rm M}_{\odot}$ mass range.

5.3 Unique measurements of $V_{\rm rot}$ and $r_{\rm d,emission}$

Our 2D emission-line fitting procedure (ELFIT2DPY, described in section 4.3) yielded measurements of the rotation velocity ($r_{\rm d,emission,i}$) and the emission scale-length ($r_{\rm d,emission,i}$) of individual emission-lines in our galaxy sample. Because many galaxies have more

than one measurable emission line, a fit was performed for each line independently. We label each line with the index i, which goes from 1 to the total number of emission lines available in the galaxy under study (N). The complete fitting procedure yielded N values of $V_{\rm rot,i}$ and $r_{\rm d,emission,i}$ (as well as their uncertainties) for each galaxy.

We combined the individual rotational velocity measurements in each galaxy into a unique $V_{\rm rot}$ value taking only "good" quality fits into account. We were then left with $N_{\rm good}$ values of $V_{\rm rot,i}\pm^{\sigma_i^+}_{\sigma_i^-}$ per galaxy, where the index i represents the individual lines and σ_i^- and σ_i^+ are the left- and right-hand side errors in $V_{\rm rot,i}$. These (asymmetric) errors come from the best-fit model's confidence intervals. We then combined the $V_{\rm rot,i}$'s by taking the weighted average, given by

$$V_{\rm rot} = \frac{\sum_{i=0}^{N_{\rm good}} \omega_i V_{\rm rot,i}}{\omega_i}, \tag{5.1}$$

where $\omega_i = 1/\sigma_{tot,i}^2$, and $\sigma_{tot,i}^2 = [(\sigma_i^+)^2 + (\sigma_i^-)^2]/2$, i.e. the average variance. The upper and lower errors ($\sigma^+_{V_{\rm rot}}$ and $\sigma^-_{V_{\rm rot}}$, or just $\sigma^\pm_{V_{\rm rot}}$) in the unique $V_{\rm rot}$ were also evaluated by combining the individual errors in each galaxy. These unique error values were determined as the maximum value of the following two quantities:
(i) A weighted combination of the standard errors ($\sigma_i^\pm$) estimated by the best-fit model

$$\sigma^\pm_{V_{\rm rot,com}} = \sum_{i=0}^{N_{\rm good}} \sigma_i^\pm \left(\frac{\omega_i}{\sum_{i=0}^{N_{\rm good}} \omega_i} \right)^2; \tag{5.2}$$

(ii) The standard error in the weighted mean, determined from the individual measurements

$$(s_{V_{\rm rot}})^2 = \frac{\sum_{i=0}^{N_{\rm good}} (V_{\rm rot,i} - V_{\rm rot})^2}{N_{\rm good} - 1}. \tag{5.3}$$

In other words, the $+$ and $-$ errors in $V_{\rm rot}$ are given by

$$(\sigma^\pm_{V_{\rm rot}})^2 = Max \begin{pmatrix} (\sigma^\pm_{V_{\rm rot,com}})^2 \\ (s_{V_{\rm rot}})^2 \end{pmatrix}. \tag{5.4}$$

In this way, we take into account the cases for which there were inconsistent velocity measurements within galaxies with more than one emission line. In these cases, equation 5.2 would underestimate the true uncertainty, while equation 5.3 provides a more realistic error. The only problem in using the described Max function (equation 5.4)

arises for galaxies with only one measured emission line for which equation 5.3 has no meaning. However, we consider this to be a minor problem compared to the possibility of seriously underestimating the uncertainties. In most cases (66% of the time), equation 5.4 yielded $(s_{V_{\rm rot}})^2 = (\sigma^{\pm}_{V_{\rm rot,com}})^2$.

To test the reliability of the measured errors we also computed a χ_i for each value of $V_{\rm rot,i}$ by calculating the quantity

$$\chi_i = \frac{V_{\rm rot,i} - V_{\rm rot}}{\sqrt{\frac{(\sigma_{\rm i}^{+})^2+(\sigma_{\rm i}^{-})^2}{2} + \frac{(\sigma^{+}_{V_{\rm rot}})^2+(\sigma^{-}_{V_{\rm rot}})^2}{2}}}, \tag{5.5}$$

which has a physical meaning only for galaxies with more than one velocity measurement. Figure 5.1 shows a histogram of the χ_i values obtained. As is clearly evident, the χ_i distribution is very Gaussian and has a standard deviation remarkably close to 1, giving a high degree of confidence in the total errors used in this work and confirming that our errors are internally consistent.

A complete table with the final $V_{\rm rot}$, $r_{\rm d,emission}$, and other characteristics of our full sample can be found in Appendix B. In this table, we have flagged the galaxies for which we had good or bad emission-line fits. We note that the galaxies that did not have a meaningful fit because they only had "bad" emission-line fits still have listed values of $V_{\rm rot}$ and $r_{\rm d,emission}$ and special care should be taken in using this numbers.

Final values of the emission scale-length, $r_{\rm d,emission}$, were computed in a similar manner as $V_{\rm rot}$. This quantity will be useful in the study of the concentration of star formation with environment, carried in section 5.4.5.

5.4 Results

5.4.1 The Tully-Fisher Relation of cluster and field galaxies

One of the principal aims of this chapter is to study possible variations with environment of the TFR to help us understand what happens when field galaxies fall into a cluster. Having created matched cluster and field galaxy samples (section 4.4), we proceed to construct Tully-Fisher diagrams and compare the distribution of cluster and field galaxies in them. For this study, we only use galaxies with good rotation-

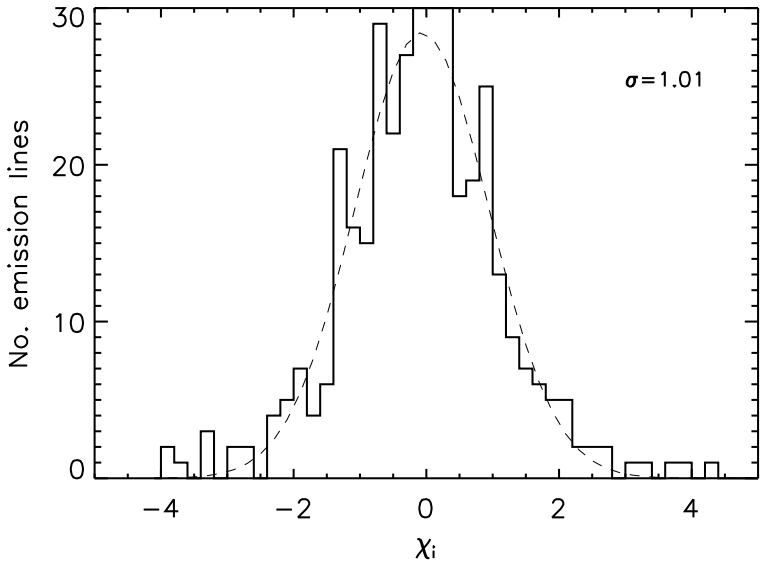

Figure 5.1: A histogram of the computed χ_i (see equation 5.5) for the independent velocity measurements in the galaxies with more than one good emission line available. The Gaussianity of the χ_i-distribution and its unity standard deviation provides a high degree of confidence in the total errors in the rotational velocities used in this work.

curve fits. To ensure these galaxies are supported by rotation, we checked that their computed velocities were consistent with non-zero rotation by rejecting galaxies with $V_{\rm rot} < 2\sigma^{-}_{V_{\rm rot}}$, where $\sigma^{-}_{V_{\rm rot}}$ is the left-hand side error on $V_{\rm rot}$. Forty-five of our "good" galaxies were consistent with no rotation. Typically, these galaxies have $V_{\rm rot} \sim 15$ km/s and $\sigma^{-}_{V_{\rm rot}} \sim 20$ km/s. Their morphology distribution is as broad as the parent sample, with a higher number of irregular galaxies, and their M_B mimics the sample of "good" galaxies, peaking at ~ -20.3 mag.

The top panels in figure 5.2 shows our TFRs. The absolute rest frame B-magnitude is plotted against the $\log V_{\rm rot}$ for cluster/group galaxies (red symbols) and field galaxies (blue symbols) for the low and mid-z matched samples (sample A in the left hand panel and sample B in the right hand panel). The fiducial local TFR of Tully *et al.* (1998, from now on T98) is shown as a dotted-dashed line in both panels for reference. A relation can be seen in both samples, although the M_B limit of sample B confines the TFR to a range of a few magnitudes. The observed scatter in the TFR is 0.233 dex in $V_{\rm rot}$. This scatter is not dominated by the errors in $V_{\rm rot}$, which are typically ~ 0.07 dex. The intrinsic scatter we measure is thus 0.230 dex. Our scatter is larger than local studies of the TFR but smaller than similar studies at high redshift. For example, the

TFR presented here has lower scatter than that of Kassin *et al.* (2007). As mentioned above, they are able to reduce it significantly by replacing rotation velocity with a kinematic estimator, which accounts for non-circular motions through the gas velocity dispersion. In this chapter, owing to our poor spectral resolution, we are unable to measure velocity dispersions, and hence apply their method. In section 5.4.3 however, we show that the scatter is reduced if we limit our sample to spiral galaxies only.

To compare the cluster and field TFRs, we define the quantity ΔM_B as the vertical difference in M_B between our data points and the local relation plotted. The middle and bottom panels in figure 5.2 show the ΔM_B distributions and cumulative distributions respectively, again for the two redshift ranges of our A and B matched samples. The fact that the ΔM_B distribution peaks at ~ -1 mag is probably due to some evolution with redshift of the TFR (Vogt *et al.*, 1996; Bamford *et al.*, 2005; Bamford, Aragón-Salamanca & Milvang-Jensen, 2006; Weiner *et al.*, 2006). However, since it is extremely difficult to make direct reliable comparisons between TFRs at $z \sim 0$ and at intermediate z (see, e.g. Weiner *et al.*, 2006), we will not attempt to quantify this evolution here and only make comparisons internally within our sample for which the selection effects and measurement biases are the same. From these plots, we can see that cluster/group and field galaxies have a remarkably similar distributions of ΔM_B, implying that they follow the same TFR. When applying a KS test to the matched sample A (left hand panels), we obtained a probability that the 2 samples are drawn from the same distribution of $P_{\rm KS} = 0.99$. In sample B (right hand panels), $P_{\rm KS} = 0.74$. These numbers are also shown in the bottom panel of figure 5.2.

Although no difference is observed between cluster/group and field TFR in M_B (for a fixed $V_{\rm rot}$), it is still possible that a difference could arise in their $V_{\rm rot}$ for a fixed M_B. To test whether this hypothesis is true, we computed the horizontal (velocity) difference between the data points and the local TFR ($\Delta V_{\rm rot}$). Again, no difference between cluster/group and field galaxies is observed.

The lack of evidence for environmental effects on the TFR could be caused by the fact that we cannot plot the kinematically-disturbed galaxies on our Tully-Fisher diagrams, as their rotational velocities cannot be reliably measured. If there were an enhancement/suppression of the star formation in galaxies falling into clusters (hence

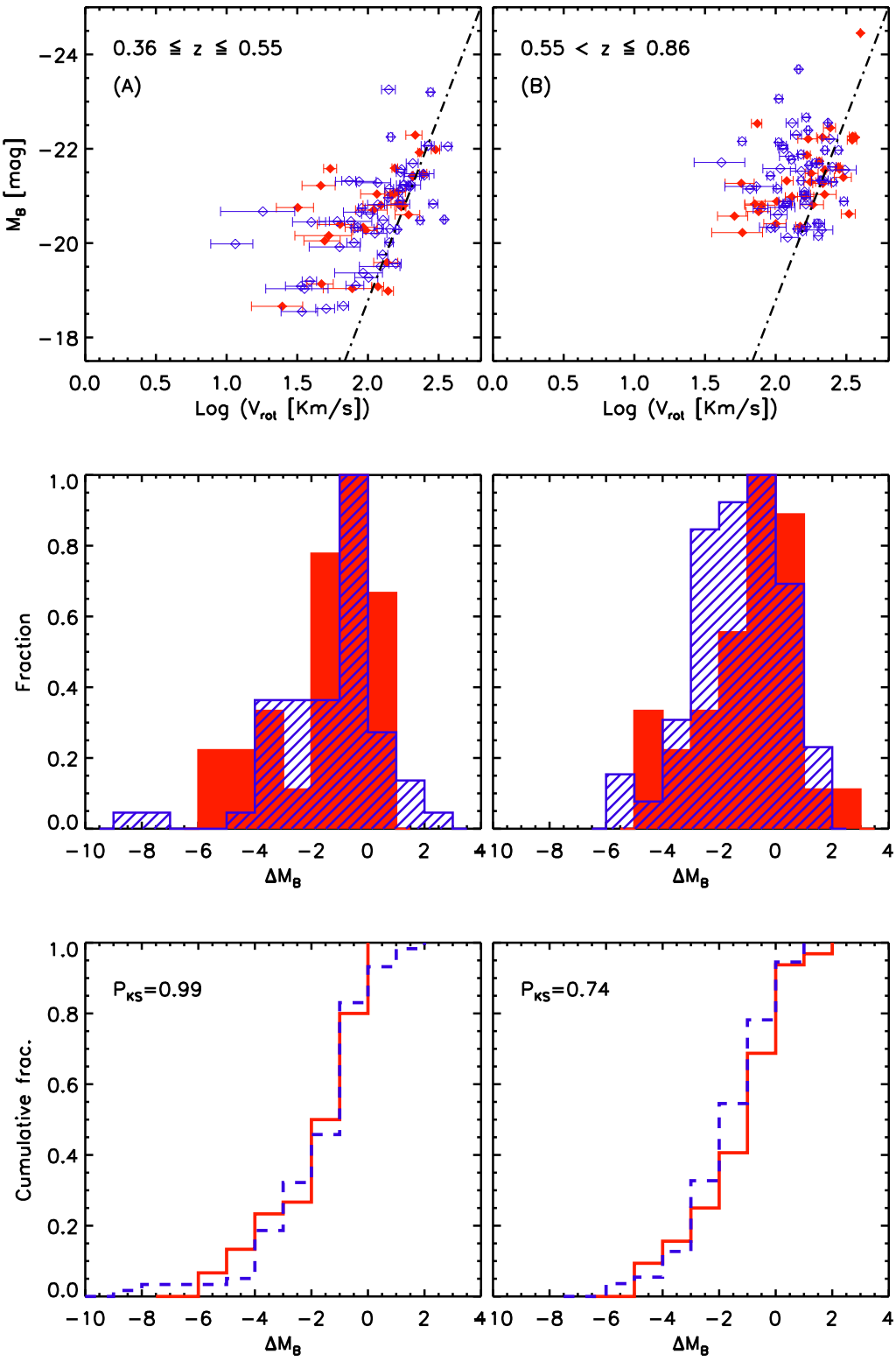

Figure 5.2: M_B vs. $\log V_{\rm rot}$ is plotted in the two upper panels for the low and mid-z samples (A and B, respectively, as labelled). As in figure 4.9, the cluster/group galaxies are plotted as red filled diamonds, and the matched field sample corresponds to the blue open diamonds. The fiducial TFR of Tully *et al.* (1998) is marked by the dotted-dashed line in both panels. The middle panels show the distribution of the vertical difference between the points and the plotted line (ΔM_B) for cluster/group (red) and field (blue) galaxies for each sub-sample. The bottom panels show the cumulative distributions of ΔM_B in each case. The Kolmogorov-Smirnov (KS) probability that the two samples follow the same distribution, $P_{\rm KS}$, is shown in a corner.

an increased B-band luminosity), this should be more easily seen in the galaxies that already show signs of gas disturbance. However, it is precisely these galaxies (flagged as kinematically "bad") we rejected because of our inability to fit a robust rotation curve (from which we could measure $V_{\rm rot}$). Nevertheless, if we take the observed lack of differences between the field and cluster TFRs at face value, we would conclude that there is no significant enhancement in the star formation of the infalling galaxies (which presumably could have been caused by environmental effects such as mergers in the cluster outskirts or compression of the interstellar medium by interaction with the clusters' dense intergalactic medium). However, it is clear that additional independent evidence is needed to draw definitive conclusions. To achieve this we will combine the TFR results shown here with a study of the star formation activity of the galaxies in section 5.4.4.

The lack of significant differences between the TFRs of field and cluster galaxies that we find here agrees with the work of Nakamura *et al.* (2006), but disagrees with the 3σ difference found by Bamford *et al.* (2005). While Nakamura et al. carried out rotation curve quality controls similar to the ones performed here, Bamford et al. accepted fits of lower quality. To test whether this is the cause of the discrepant results we repeated our TFR analysis accepting the $V_{\rm rot}$ values derived from all the fits, including those from bad quality ones. We find that even when including the "bad" fits, we found no significant difference between the TFRs of cluster/groups and the field. We thus conclude that differences in the quality of the accepted fits are not responsible for the discrepant results obtained by Bamford et al. and ourselves. We offer no convincing explanation for this discrepancy, but since our sample is significantly larger than theirs and the quality of our data is at least as good (and often better), we trust that our result is more robust.

5.4.2 The difference between cluster and group galaxies in the TFR

Cluster cores can have severe effects on galaxies residing near it. Galaxies however, are thought to interact with harsh environments well before reaching the centre of a cluster. (Kodama *et al.*, 2001; Treu *et al.*, 2003). In the hierarchical scenario of structure formation, infalling groups of galaxies build the rich galaxy clusters we observe

today. Galaxy groups are thus likely to represent a natural environment for galaxy *pre-processing* (e.g. Fujita, 2004) through tidal interactions that would not be as effective in higher velocity dispersion environments.

In this section, we distinguish galaxies in clusters and groups in the quest for evidence of more refined environmental effects. We compare galaxies in clusters, groups, and the field with each other in the Tully-Fisher diagram in a similar manner to section 5.4.1.

When distinguishing group from cluster galaxies our number counts inevitably drop. We therefore consider in this section the matched sample C that spans the redshift range $0.36 \leqslant z \leqslant 0.86$ and is limited by $M_B = -20$ mag. In this way, we improve the quality of our statistics. Because the redshift range of the full matched sample C is large, we first test whether evolutionary effects would bias this study in the following. We do not attempt however to perform an accurate TFR evolution study since it is very difficult to properly fit a TFR to high redshift galaxy samples (given the magnitude cuts and the amount of scatter present). For this reason, we only quantify evolutionary trends by comparing our data points with the local TFR, assuming the slope is constant across the entire redshift range.

The middle panels of figure 5.2 showed that our matched samples have a brighter TFR than the local relation. We represent this with the quantity ΔM_B, which equals the vertical difference between the galaxy's M_B and the local TFR. By comparing the same galaxy population (e.g. only field galaxies) in sub-samples A and B (at low and mid-z, respectively) against the local relation, we are able to quantify the TFR evolution from $z = 0$ to the mean redshifts of samples A and B. The field galaxies of sample A, show a median Δ_{M_B} of $= -0.93$ mag ($\langle \Delta M_B \rangle = -1.39$ mag), while, in the higher redshift sample B, they show median $\Delta_{M_B} = -1.34$ mag ($\langle \Delta M_B \rangle = -1.35$ mag). We emphasize that we do not attempt to make a detailed study of the TFR evolution here. Formally, this simple test suggests that there is a ~ 1 mag evolution in the TFR's M_B, from $z = 0$ to $z \sim 0.5$, in agreement with previous studies (Vogt *et al.*, 1996; Bamford *et al.*, 2005; Bamford, Aragón-Salamanca & Milvang-Jensen, 2006; Weiner *et al.*, 2006).

We then looked for any evidence for evolution in M_B in the range $0.3 < z < 0.9$ by

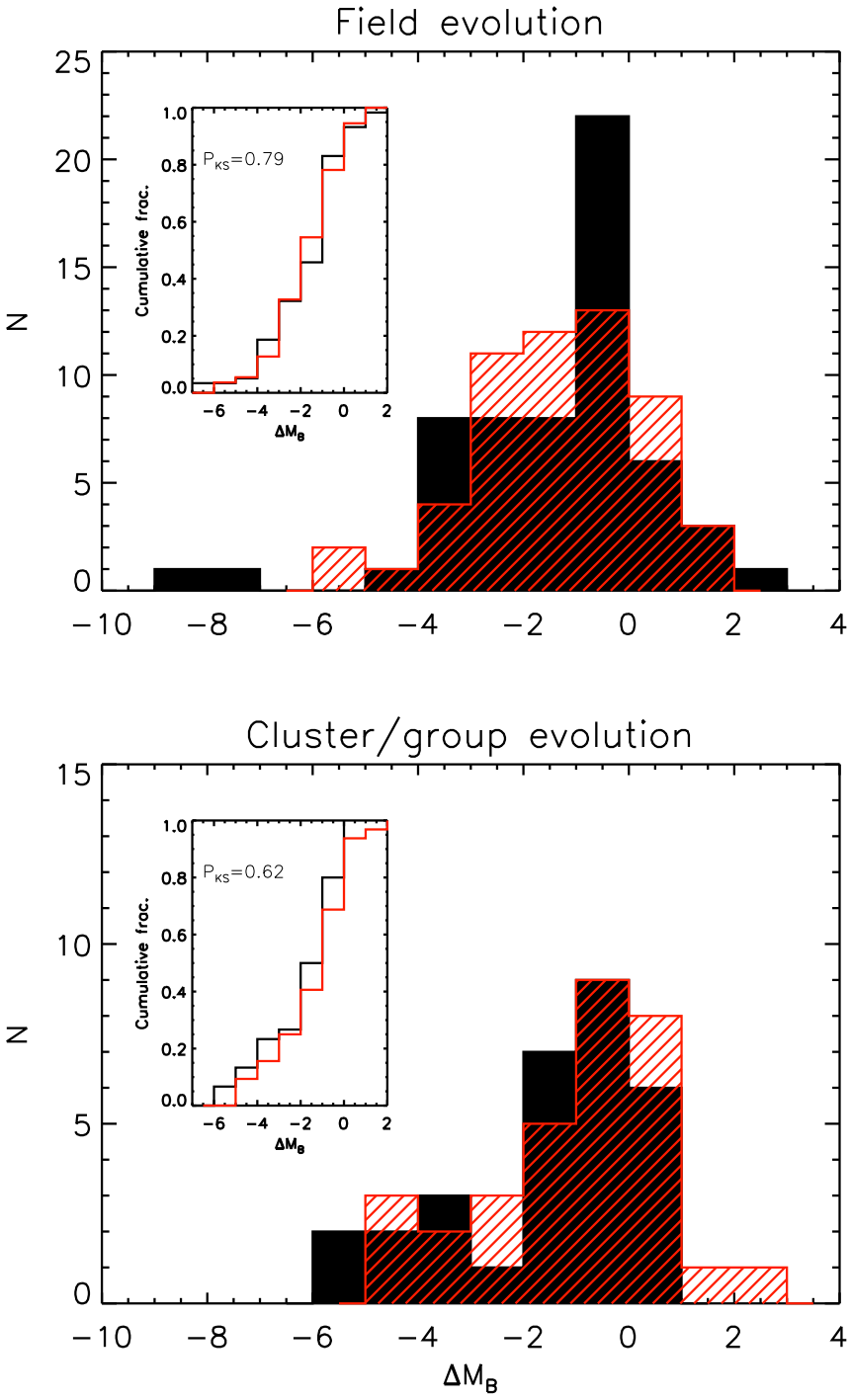

Figure 5.3: The distribution of ΔM_B for the field galaxies (upper panel) and cluster/group galaxies (lower panel). The black solid histogram in both panels corresponds to the lower redshift galaxies in the matched sample A, while the red, dashed histogram traces the higher redshift matched sample B (see section 4.4 for the definition of these samples). In addition, each panel shows a smaller inner plot containing the cumulative distributions of samples **A** and **B** for each case. These smaller plots also show the resulting KS statistics.

comparing sub-samples A and B against each other. We did this separately for the field and cluster/group populations. Figure 5.3 shows the ΔM_B distribution for the field (upper panel) and the cluster/group galaxies (lower panel). The black solid histogram corresponds to the lower redshift galaxies in sample A, while the red, dashed histogram traces the higher redshift sample B. In each panel, a smaller inner plot shows the cumulative distributions of samples A and B, in addition to the KS statistics. From these plots, we see that although there is a significant offset in M_B from the local relation, there is no evident evolution within the redshift range of our matched sample. In other words, we find weak or no evolution of the TFR in either field or cluster/group galaxies at $0.3 < z < 0.9$. This result allows us to compare different galaxy populations (cluster, group, and field galaxies) across the full redshift range of the matched sample C expecting redshift-dependent effects to be small.

The left hand side of figure 5.4 shows the absolute rest-frame B-magnitude plotted against $\log V_{\rm rot}$ for sample C. As in figure 5.2, the fiducial local TFR is again plotted (dotted-dashed line) for reference. The middle panel presents histograms of ΔM_B for cluster (solid red), group (open black), and field (dashed blue), while the bottom panel contains the cumulative distributions of ΔM_B for cluster (solid red line), group (dotted black line), and field (dashed blue line) galaxies. In addition, KS statistics are shown in the left hand side of this plot.

We find that by making the distinction between group and cluster galaxies in the TFR, no significant differences arise. This can also be seen in the lower-left panel of figure 5.4, where the cumulative fractions and KS statistics are shown. We still find no significant differences, suggesting again a lack of environmental effects on the TFR, at least when selecting emission-line galaxies that are not kinematically disturbed.

5.4.3 The TFR of morphologically classified spirals

It is well known that the TFR scatter is related to galaxy morphology (e.g. Kannappan, Fabricant & Franx, 2002) and it is arguable whether S0 and spiral galaxies, for example, should follow the same relation. Recent studies (Bedregal, Aragón-Salamanca & Merrifield, 2006; Williams, Bureau & Cappellari, 2010) showed that S0 galaxies have the same TFR slope as the spirals, but are on average fainter at a given rotational

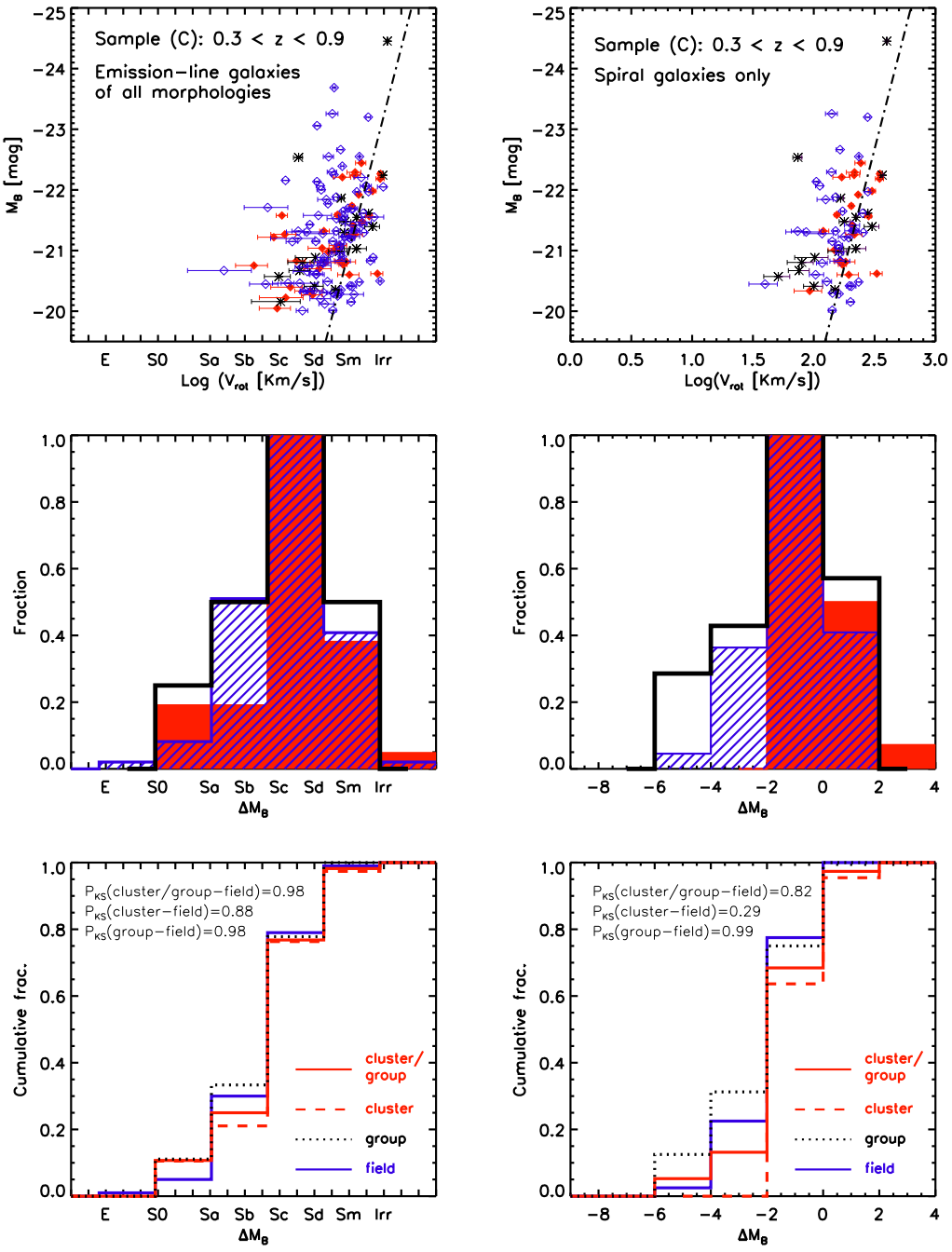

Figure 5.4: As in figure 5.2, M_B vs. $\log V_{\rm rot}$ for the galaxies in the matched sample C are plotted in the upper panel. Cluster galaxies are plotted as red filled diamonds, groups are represented as black asterisks, and the matched field sample corresponds to the blue open diamonds. The fiducial TFR of Tully *et al.* (1998) is marked by the dotted-dashed line. The middle panel shows the ΔM_B distribution for cluster (red, solid), groups (black, open), and field (blue, shaded) galaxies. The bottom panels show the cumulative distributions of ΔM_B for cluster (solid red line), group (dotted black line), and field (dashed blue line) galaxies. KS statistics are shown in the left hand side of the plot. The **left** hand panels consider all emission-line galaxies in sample C, whilst in the **right** hand panel, only morphologically classified spirals are plotted.

velocity.

The TFR sample we have studied so far contains galaxies with unknown morphology and a few known not to be spirals. To study the effect of environment on the spiral-TFR, we extract the morphologically classified spirals from our matched sample C to construct a TFR of spirals only. Out of the 151 "good" emission-line galaxies in this sample (88 of which have HST observations, see circled symbols in figure 4.9), only 66 have a confirmed HST spiral morphology and velocities consistent with non-zero rotation. The top-right panel of figure 5.4 shows the spiral TFR at $0.3 < z < 0.8$. The distribution of galaxies in the TFR is tighter than that seen when plotting all the emission-line galaxy sample (left hand side of figure 5.4). The intrinsic scatter in the spiral-TFR is 0.18 dex in $\log V_{\rm rot}$ (compared with 0.23 dex if we consider all emission-line galaxies in the luminosity-limited sample). When comparing the distributions of the TFR residuals for the emission-line sample (left hand side of figure 5.4) and morphologically classified spirals (right hand side of the figure) for each environment, we find that the distributions of group and field galaxies are remarkably similar, whilst the cluster galaxies show some deviation. In numbers, we obtained the following KS probabilities: $P_{\rm KS} = 0.23$ for cluster members, $P_{\rm KS} = 1.00$ for galaxies in groups, and $P_{\rm KS} = 0.97$ in the field sample.

When studying the environmental effects on the spiral-TFR, we again observe no difference between the TFR residuals of field and cluster/group galaxies (see solid blue and solid red lines in the bottom-right panel of figure 5.4), but this time, a small difference between cluster ($\sigma_{cl} > 400$ km/s structures; dashed, red line) and field galaxies seems to appear. However, its significance is too small ($P_{\rm KS} = 0.29$, see cumulative fractions and KS statistics in the bottom-right panel of figure 5.4) to consider it too seriously. When combining cluster and group galaxies into one (more numerous) sample, and comparing with the field, this difference becomes negligible ($P_{\rm KS} = 0.82$).

Complementary to the results found in this section, and in sections 5.4.2 and 5.4.1, we investigated possible correlations between TFR residuals (ΔM$_B$) with cluster velocity dispersion, distance from the cluster centre and projected galaxy density, and found that there are no obvious trends with environment.

5.4.4 Star formation

In sections 5.4.1 and 5.4.2, we found that the TFR of "good" galaxies (i.e. galaxies with no sign of kinematical distortion) is not significantly affected by environment. To test the effect that environment may have on the the kinematically-disturbed galaxies, which cannot be placed on the TFR, we take a more direct route by comparing the specific star formation rates (SSFRs, see section 5.2.1) of the kinematically-disturbed galaxies with the rest. We find that kinematically-disturbed galaxies show lower SSFRs than their non-disturbed counterparts in all environments. This is shown in the top row of figure 5.5. The KS statistics yield a very small probability that the two samples (kinematically disturbed and undisturbed) follow the same distribution ($P_{\rm KS}$ of the order of 10^{-14}), which means that these distributions are certainly not the same. Our sample exhibits a lower SSFR for the kinematically-disturbed galaxies, particularly in cluster environments.

In section 4.5.1, we showed that there are more kinematically disturbed galaxies in clusters and groups than in the field, and therefore our finding is consistent with that of Poggianti *et al.* (2008), who showed that cluster galaxies have slightly lower average SSFR than field ones. The suppressed SSFR for the kinematically-disturbed galaxies is also seen in the field, so it is not exclusively a cluster phenomenon. However, since there are more disturbed galaxies in clusters than in the field, the average SSFR of star-forming cluster galaxies is smaller than that of field ones, in agreement with Poggianti *et al.* (2008) results.

Although the difference in the SSFR distributions of disturbed and undisturbed galaxies is very clear, there is a potential caveat. If a galaxy has a low SSFR it will have a low [OII] emission line equivalent width (EW). This will make fitting the rotation curve more difficult, lowering the quality of the fits, and increasing the probability that the galaxy is classified as kinematically disturbed. In the middle and bottom panels of figure 5.5 we compare the EW and flux of the [OII] doublet for the "good" and "bad" galaxies in clusters and in the field separately. We find that "bad" or kinematically-disturbed galaxies have lower EW[OII] and lower [OII] flux in all environments. The problem arises when trying to decide which is the cause and which the effect. The perturbed gas kinematics could be related to a process that also suppresses the SFR,

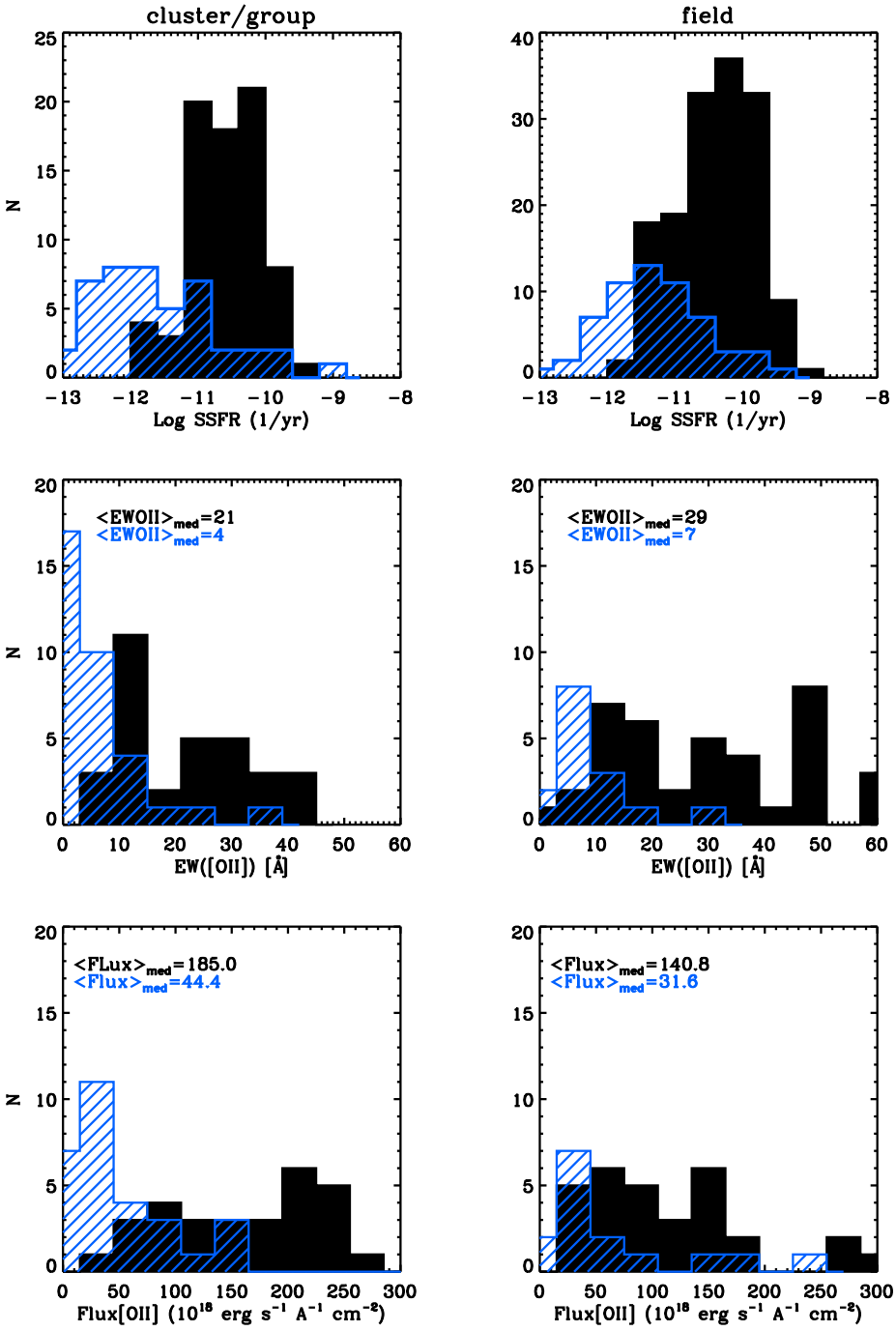

Figure 5.5: A comparison between the star formation of the kinematically-disturbed galaxies (shaded blue histograms) and the undisturbed ones (solid black histograms). Cluster galaxies are shown in the left hand panels and field galaxies in the right. The top row shows the specific star formation rates, the middle the equivalent width of the [OII] emission, and the bottom row compares the flux in OII. Median values are shown inside the plots.

providing a real physical link between both observations. However, it could also be that low SSFR galaxies have lower [OII] fluxes and EWs, making their rotation curves more difficult to fit well, and thus the apparent link is purely observational and not physical. Using only the information presented in this chapter so far it is very difficult to know which one of these possibilities is the true one. However the additional independent evidence indicating that star formation is suppressed in cluster starforming galaxies (Poggianti *et al.*, 2008; Vulcani *et al.*, 2010; Finn *et al.*, 2010) suggests that the observed connection between disturbed kinematics and suppressed SSFR is a physical one. The results of section 5.4.5 will also support this conclusion.

5.4.5 Concentration of the emission

To examine the location of the star formation within the disks of our emission-line galaxies, and its dependence on environment, we compared the size of the stellar disk, as traced by the photometric scale-length ($r_{\rm d,phot}$), with the size of the gas disk, i.e. the scale-length of the emission lines in the spectra ($r_{\rm d,emission}$). Emission scale-lengths were output from ELFIT2PY, while photometric scale-lengths were derived by fitting a 2-component 2D model that accounted for a bulge with a de Vaucouleurs profile and an exponential disk component, convolved with the PSF of the images. This was done using the GIM2D software (see Simard *et al.*, 2002, 2009, for a detailed description of the method used). The values of $r_{\rm d,phot}$ used here were computed from the HST F814W images, because of the higher quality of the data. We note however that if we used the scale-lengths measured from I-band VLT photometry, the results presented here would not change. We note that many dynamically hot systems have simple exponential profiles, hence the presence of a "disk" component does not necessarily imply the presence of an actual disk. For this reason, in this section we only considered galaxies that have been visually classified as disks (S0s and spirals only).

In figure 5.6, we compare both (photometric and emission) scale-lengths. The top panels show the ratio $r_{\rm d,emission}/r_{\rm d,phot}$ plotted against $r_{\rm d,phot}$ in the mid- and high-redshift samples (A and B, respectively) for cluster/group and field galaxies in different symbols. The median values of this scale length ratio are the same (within the errors) for cluster/group and field galaxies in both samples. This suggests that the environment

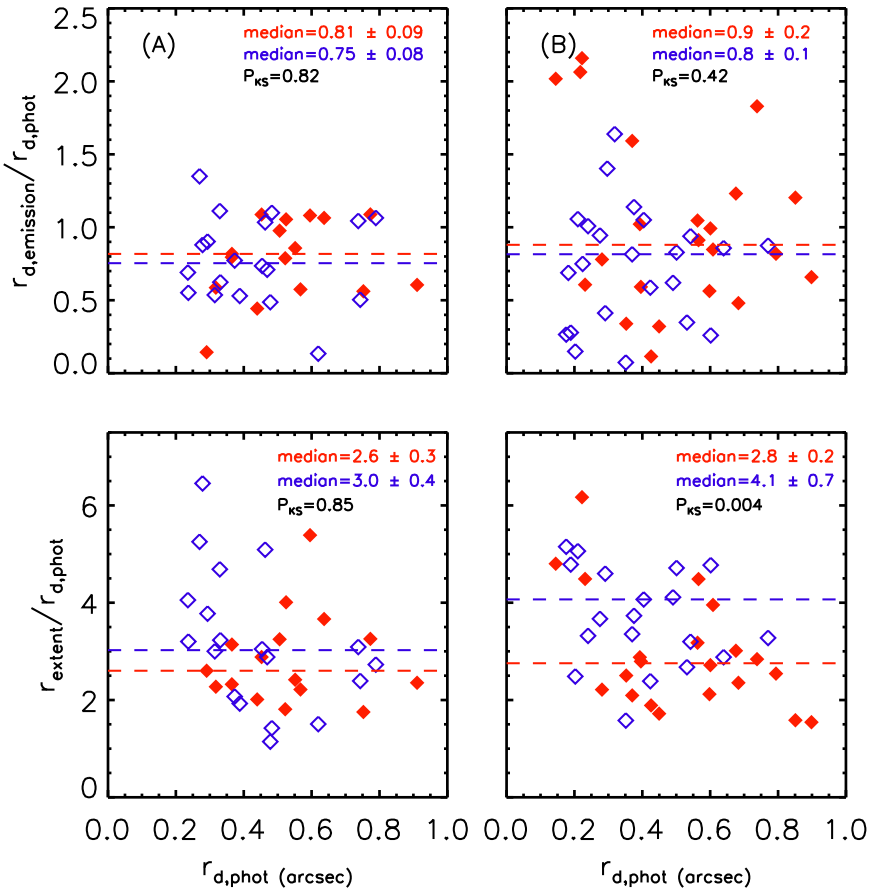

Figure 5.6: A comparison of the scale-lengths measured in the emission-lines ($r_{\rm d,emission}$, top panel) and the emission-line extent($r_{\rm extent}$, bottom panel) versus those obtained from the photometry ($r_{\rm d,phot}$) in different environments. Only kinematically "good" galaxies with disk morphology (S0s and spirals) in the matched samples A (left) and B (right) were taken into account. Cluster/group galaxies are plotted in filled red symbols, whilst field galaxies correspond to the open blue diamonds. The red and blue dashed lines show respectively the median deviation from a flat distribution, for the cluster/group and field galaxies, respectively. This plots show that whilst there is no difference in the location of the star formation within the stellar disks of cluster/group and field galaxies (top), there seems to be a truncation of the gas disks in cluster/group galaxies with respect to the field (bottom).

is not significantly affecting the gas concentration in emission-line galaxies that show no evidence of kinematical distortions.

In contrast with this result, Bamford, Milvang-Jensen & Aragón-Salamanca (2007) found that the emission (and thus the star formation) of cluster spirals seems to be more concentrated than that of field ones. Since these authors did not separate kinematically undisturbed and disturbed galaxies we repeated the test using all our fits, "good" and "bad". In this case we did find some weak evidence suggesting a more concentrated star formation in cluster galaxies than in field ones, but the large scatter introduced

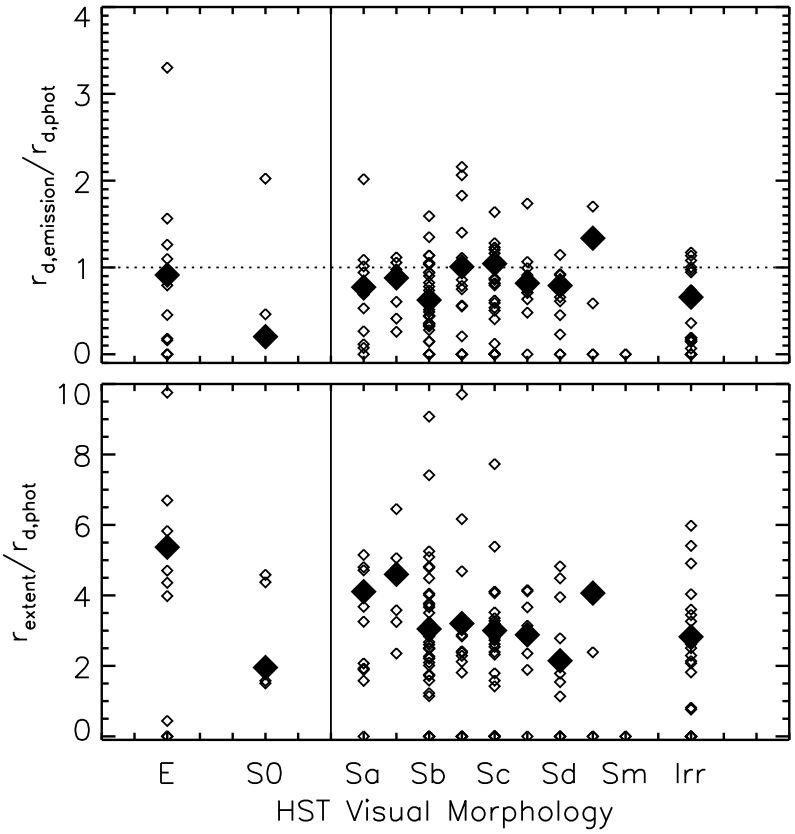

Figure 5.7: A comparison of $r_{\rm d,emission}/r_{\rm d,phot}$ (top) and $r_{\rm extent}/r_{\rm d,phot}$ with the different morphologies, for all the emission-line sample with HST observations. The horizontal dotted line in the top panel just guides the eye to where $r_{\rm d,emission} = r_{\rm d,phot}$ and the vertical solid line (both panels) divides early- from late-type galaxies. The larger solid symbols highlight the median values for each morphology type.

by the unreliable values of $r_{\rm d,emission}$ derived from the "bad" fits prevented us from reaching any definitive conclusion.

When fitting the emission lines with ELFIT2PY (section 4.3), the extent of the line, $r_{\rm extent}$, is also computed. This quantity is defined as the distance from the continuum centre to where the line could no longer be reliably detected above the noise. Although $r_{\rm extent}$ depends on properties of the data (e.g. seeing, pixel size) and is thus not suitable for comparison with other studies, it is useful for the internal comparison of our own dataset. We use this quantity to investigate whether the extent of the gas disk is affected by cluster environment.

The bottom row of figure 5.6 shows how the extent of the emission compares to the size of the stellar disk in a similar manner as figure 5.6. Despite the scatter, the plots exhibit a $\sim 1-2\sigma$ difference between field and cluster/group galaxies. This is more ev-

ident in the higher redshift sample (B). Cluster/group galaxies show smaller emission extents than field galaxies, implying that the cluster environment effectively truncates the gas disks. This is consistent with the results of Koopmann & Kenney (2004), who, found that $\sim 50\%$ of spiral galaxies in the Virgo cluster have their Hα disks truncated, whereas field galaxies do not show such evidence as frequently. Additionally, they find that most of the galaxies that exhibit truncated gas disks have relatively undisturbed stellar disks. From their results, they conclude that the reduced SFRs of Virgo spiral galaxies must be mainly caused by ICM gas stripping, which is also the scenario that our results favour.

In the top panel of figure 5.7, we plot the ratio $r_{\rm d,emission}/r_{\rm d,phot}$ as a function of morphology, for all the emission-line galaxies. We find that $r_{\rm d,emission}/r_{\rm d,phot}$ is roughly constant (with some scatter) throughout all the morphology types. The bottom panel shows $r_{\rm extent}/r_{\rm d,phot}$ for the different morphology types. A small decrease in $r_{\rm extent}/r_{\rm d,phot}$ is observed towards later morphological types. This is consistent with the results shown in figure 4.8 and a scenario in which star forming spiral galaxies are transformed into passive S0s via stripping of their gas.

5.5 Discussion

This chapter has presented a detailed analysis of the effects of the environment on the Tully-Fisher relation, star formation, and concentration of the emission of galaxies in various environments, which has provided us with further clues about the physical mechanisms transforming galaxies. We summarize and discuss our results in the following.

As in chapter 4, we focused on EDisCS galaxies with measurable emission lines in their spectra. After modelling the 2D emission lines and rejecting poor fits (mainly due to disturbed gas kinematics), we computed rotation velocities ($V_{\rm rot}$) and emission-line disk scalelengths ($r_{\rm d,emission}$). We then searched for environmental effects on the galaxies' scaling relations, by studying the Tully-Fisher relation (TFR) of cluster, group and field galaxies in matched samples (in M_B and z). We found that there is no difference between the distribution of cluster, group and field galaxies in the Tully-Fisher

diagram up to $z < 1$. The distributions are strikingly similar (the KS probability that the cluster/group and field TFR are drawn from the same distribution is $P_{\rm KS} \sim 0.98$). This result agrees with Nakamura *et al.* (2006) and Ziegler *et al.* (2003) but contradicts the findings of Bamford *et al.* (2005), who found a brighter TFR for cluster galaxies. Because our sample is larger and more homogeneous than the one published by these authors, and our quality control more robust we are confident on the reliability of our findings. Taken at face value this result suggests that the cluster environment does not induce a strong enhancement on the star-formation activity of spiral galaxies entering it.

In an attempt to reduce the scatter about the TFR, we have performed the above-mentioned analysis with only morphologically confirmed spirals. This reduced the number of galaxies significantly (by half) since we do not have HST observations for all the emission-line sample. Nevertheless, we obtained a tighter TFR (as expected, e.g. Kannappan, Fabricant & Franx, 2002) and were able to make comparisons between the different environments. Our results show that, for the spiral sample, the cluster/group TFR again does not differ significantly from the field relation. No statistically-significant difference is found either when comparing the TFRs of galaxies in the field and in clusters with $\sigma_{cl} > 400$km/s (i.e., when excluding group galaxies).

To further confirm that the TFR is not significantly affected by environment, we studied the TFR residuals as a function of cluster velocity dispersion, distance from the cluster centre and projected galaxy density, and found no evidence for a correlation between environment and TFR residuals.

At face value, the fact that we find no significant environmental effects on the TFR seems to suggest that there is no strong enhancement or suppression of the star formation activity in cluster spiral galaxies. However this cannot be the whole story, since the TFR analysis can only be properly done for galaxies with reasonably regular rotation curves (and thus galaxies without strong distortions in their gas structure and kinematics). If the main environmental effects on spirals manifest themselves as disturbances in the galaxies' gas, the kinematically-disturbed galaxies are a key component of the whole picture. Because these galaxies cannot be reliably placed on the TFR we need to use other tests to assess the effect of the environment on their star formation activity.

Using the [OII] emission line as an estimator of the galaxies' current star formation we find that kinematically-disturbed galaxies exhibit lower specific star formation rates (SSFR, i.e., star formation rate per unit stellar mass) in all environments. Although some observational biases may be at play, using independent evidence from previous EDisCS studies we argue that this effect is probably real. If so, this suggests that there may be a physical connection between the disturbance in the galaxies' gas and their reduction in star-formation activity.

Further support to this interpretation comes from our study of the spatial distribution of the line emission, taken as a tracer of star formation. The concentration of the star formation, parametrised as the ratio of the exponential scale length of the line emission divided by the exponential scale length of the stellar disk, seems to be unaffected by the environment for the galaxies with undisturbed gas. However, although the exponential scale lengths of the line emission do not seem to be affected, the actual extent of the emission appears to be. The radial extent of the galaxies' emission (in units of their stellar disk scale length) is smaller in cluster environments than in the field. In other words, the star formation seems to be more concentrated (or truncated) in cluster galaxies. This means that the cluster environment not only reduces the galaxy's star formation activity but also makes what star formation remains more concentrated. This has been independently observed in clusters at lower redshifts (Wolf *et al.*, 2009).

Chapter 6

Conclusions and further work

6.1 Conclusions

In this thesis, we have investigated the rôle of environment on galaxy formation and evolution, giving particular focus to the transformation of star forming spirals into passive S0s. We utilized photometric and spectroscopic observations of galaxies at $0 < z < 1$ in a wide range of environments from the ESO Distant Cluster Survey.

6.1.1 Formation of early-type galaxies

In chapter 3, we constrained the star formation histories of early-type galaxies in clusters. We did this by studying the colour-magnitude relation (CMR) for a sample of 172 morphologically-classified elliptical and S0 cluster galaxies. The following conclusions are drawn:

(i) The intrinsic colour scatter about the CMR is very small ($\langle\sigma_{\rm int}\rangle = 0.076$) in rest-frame $U - V$. However, there is a small minority of faint early-type galaxies (7%) that are significantly bluer than the CMR. The small scatter indicates that either all the early-type galaxies in the clusters formed at the same time or that they all have old stellar populations.

(ii) We observe no significant dependence of $\sigma_{\rm int}$ with redshift or cluster velocity dispersion. Because our sample is strictly morphologically-selected, this implies that by

the time cluster elliptical and S0 galaxies achieve their morphology, the vast majority have already joined the red sequence. The only exception seems to be the very small fraction of faint blue early-types.

(iii) Assuming that the intrinsic colour scatter is due to differences in stellar population ages, we estimate the galaxy formation redshift $z_{\rm F}$ of each cluster. We find that $z_{\rm F}$ does not depend on the cluster velocity dispersion. However, $z_{\rm F}$ increases weakly with cluster redshift within the EDisCS sample. This trend becomes very clear when higher redshift clusters from the literature are included. This suggests that, at any given redshift, in order to have a population of fully-formed ellipticals and S0s they needed to have formed most of their stars $\simeq 2$–$4\,$Gyr prior to observation. That does not mean that *all* early-type galaxies in *all* clusters formed at these high redshifts. It means that the ones we see already having early-type morphologies also have reasonably-old stellar populations. This is partly a manifestation of the "progenitor bias", but also a consequence of the fact that the vast majority of the early-type galaxies in clusters (in particular the massive galaxies) were already red (i.e., already had old stellar populations) by the time they achieved their morphology.

(iv) Elliptical and S0 galaxies exhibit very similar colour scatter, implying similar stellar population ages.

(v) The scarcity of blue S0s indicates that, if they are the descendants of spirals whose star-formation has ceased, the parent galaxies were already red when they became S0s. This suggests the red spirals found preferentially in dense environments could be the progenitors of these S0s.

(vi) Fainter early-type galaxies finished forming their stars later (i.e., have smaller $z_{\rm F}$), consistent with the cluster red sequence being built over time and the brightest galaxies reaching the red sequence earlier than fainter ones.

(vii) Combining the CMR scatter analysis with the observed evolution in the CMR zero point we find that the early-type cluster galaxy population must have had their star formation truncated/stopped over an extended period $\Delta t \gtrsim 1\,$Gyr.

6.1.2 Evolution of star-forming galaxies as a function of environment

In chapters 4 and 5, we studied the properties of the gas and the stars in a sample of 418 EDisCS emission-line galaxies.Our principal aim was to try to understand the main physical mechanisms acting on galaxies when they fall into clusters. Our main findings are:

(i) The fraction of galaxies with kinematically-disturbed gas disks is higher in galaxy clusters than in the field. While this fraction does not change with luminosity in the field, in clusters it increases significantly with increasing luminosity. We can explain this trend a the consequence of gas being more easily removed from lower mass (fainter) galaxies, taking them out from the emission-line galaxy sample.

(ii) The fraction of kinematically-disturbed galaxies increases with cluster velocity dispersion and decreases with distance from the cluster centre, which is indicative of strong environmental effects on the galaxies' gas. However, we found no correlation between the fraction of kinematically-disturbed galaxies and the projected galaxy density. We interpret this as a strong indication that what is causing disturbances in the galaxies gas is likely related to the intracluster medium (ICM) and not due to galaxy-galaxy interactions.

(iii) The fraction of galaxies with disturbed optical morphologies in our emission-line sample is luminosity independent and similar in clusters, groups, and the field. Indeed, there is little correlation between the presence of kinematically-disturbed gas and morphological distortions. These results, combined with (i) and (ii) above, suggest that environmental effects are mild enough to ensure that, whilst they do not disturb the stellar disks, they do strongly affect the gas in cluster galaxies.

(iv) No environmental effects on the Tully-Fisher relation are found for the emission-line galaxy sample nor for the morphologically-classified spirals.

(v) Result (iv) is inevitably limited to the galaxies with undisturbed kinematics. Since reliable rotation velocities cannot be determined for kinematically-disturbed galaxies, these cannot be placed on the Tully-Fisher relation. For this reason we explored the possibility that signatures of enhanced or suppressed star formation could be present

in the kinematically-disturbed galaxies. Indeed, we find that kinematically-disturbed galaxies have lower specific star formation rates.

(vi) Cluster galaxies display truncated star-forming disks relatively to similarly-selected field galaxies.

(vii) There are several elliptical and S0 galaxies with extended gas disks, which will be discussed in a forthcoming paper.

Previous studies have shown that, statistically, spiral galaxies transform into S0s in cluster environments (e.g. Desai *et al.*, 2007, and references therein). This fact, together with the results presented here, lead to the following conclusions: if infalling spirals are the progenitors of cluster S0s, the physical mechanism responsible for this transformation is such that it efficiently disturbs the galaxies' star-forming gas and reduces their star-formation activity, but leaves their stellar disks largely undisturbed. Moreover, the star-forming gas is either removed more efficiently from the outskirts of the galaxies, or it is driven towards the centre (or both). In any case, this makes any remaining star formation more centrally concentrated, helping to build the bulges of S0s. We conclude that the physical mechanism responsible for the spiral-to-S0 transformation in clusters is related to the ICM, with galaxy-galaxy interactions and mergers playing only a limited role. Of course, this does not imply that S0s in lower-density environments cannot form via different mechanism(s).

6.1.3 Reconstructing the whole story

From this thesis, we have learned about the histories of the oldest and the youngest galaxies in the universe separately. It is therefore appropriate to link their evolutionary paths to reconstruct the complete galaxy formation and evolution picture.

On the one hand, elliptical and S0 galaxies in clusters are very old stellar systems which populate the red-sequence throughout cosmic time, with the most massive ones reaching the red-sequence first. On the other hand, the star formation in young galaxies is significantly affected by the cluster environment, while their morphologies are less easily disturbed. If passive S0s are the descendants of star-forming spirals, our results are consistent with a mechanism that strips, disturbs and concentrates the gas in

galaxies through interaction with the ICM. Once they have stopped forming stars and their morphologies have changed, possibly aided by secondary effects such as minor mergers and galaxy-galaxy interactions, they evolve passively, becoming redder and redder. However, the picture is not as simple as that, since there are always exceptions. We find that not all early-type galaxies are red and that not all star-forming galaxies are spirals.

Overall, our results are consistent with a scenario in which the massive early-type galaxies we see in clusters today were formed first, either via wet mergers between smaller gas rich disk spirals that would help build up their mass, or from already-massive spirals that transformed into S0s by the effect of cluster environment. Alternatively, it is also possible that less massive spirals in clusters transformed into S0s and later gained some mass via dry minor mergers. The red-sequence in clusters kept being built over time, particularly at its faint end, most likely from spirals being stripped of their gas by their interaction with the ICM. In this scenario, the faint blue E/S0 galaxies we find in clusters represent a transition population. However, the evolution in the field could be slower, and driven by different mechanisms. In fact, we find star-forming E/S0 galaxies with extended and undisturbed gas disks in the field.

6.2 Further work

6.2.1 Origin of gas disks in distant early-type galaxies

In chapter 4 we found 17 early-type galaxies with evidence of extended gas disks in their emission. These are very interesting objects, because they are in contrast with what is typically thought of E/S0 galaxies (i.e. that they are red and dead objects). The author of this thesis is currently leading an investigation on these objects to understand the origin of their gas and to test if these are the high redshift analogues of the early-type galaxies found by in the local Universe (the fast and slow rotators in Emsellem *et al.*, 2007, and references therein). This work is being carried out in direct collaboration with Harald Kuntscher (from the SAURON collaboration), Alfonso-Aragón-Salamanca, and the EDisCS collaboration.

6.2.2 Kinematical properties of backsplash galaxies

The work carried for this thesis also let to a project, currently being led by Rhys Rhodes (University of Nottingham), that investigates the properties of the backsplash galaxy population through the comparison of our observations with large scale structure simulations (Millenium, Springel *et al.*, 2005) and galaxy evolution models (De Lucia *et al.*, 2006). The aim is to identify and characterize backsplash galaxies within EDisCS. We want to understand how and when galaxy properties are affected as they infall in the cluster and thereafter. For example, is the gas in a galaxy affected soon after the galaxy falls into the cluster?, or do gas disturbances require longer timescales (i.e. more orbits)?. To do this, we are combining the information from the simulations with the results presented in chapters 4 and 5.

6.2.3 Galaxy evolution: nature and nurture

So far, we have obtained important clues about the mechanisms that quench the star formation and transform the morphologies of massive galaxies in clusters, but high redshift studies, like the one presented in this thesis, are biased towards high galaxy mass. Low redshift surveys such as the Sloan Digital Sky Survey are able to probe galaxy properties in a wider mass range. They have indeed found that galaxies divide into two distinct families at a stellar mass $M_\star \sim 3 \times 10 M_\odot$ (e.g. Kauffmann *et al.*, 2003). Studying galaxies of all masses in lower redshift clusters is thus key in understanding galaxy evolution, in particular, understanding the reason behind the characteristic $M_\star$ scale where galaxies transition from young to old. For this reason, pursuing a holistic study of galaxies at lower redshift in different environments is ideal.

Adopting this approach, the author of this thesis will work on a project led by Bianca Poggianti on "Star Formation in Clusters and Superclusters". The project consists of a broad set of data in low redshift clusters, from which we can learn important clues about galaxy evolution. The clusters we will be studying are Abell 2192 and Abell 963. They are not only at low enough redshift to probe the low-$M_\star$ end, but are also very different in their dynamical state and star formation properties. This makes them excellent laboratories for galaxy evolution. We will combine HI information

with stellar masses, morphology and environment to build a complete picture of the formation and evolution for these two clusters. Cold HI gas is the source material for star formation, and is also key in understanding environmental processes such as ram-pressure stripping (e.g. Kenney, van Gorkom & Vollmer, 2004; Chung *et al.*, 2007). Studying it is thus essential for understanding galaxy transitions.

Appendices

Appendix A

Colour-magnitude diagrams of EDisCS cluster early-type galaxies

The colour-magnitude diagram for the early-type galaxies in the EDisCS clusters listed in Table 3.1 are shown in Figures A.1 and A.2. Elliptical galaxies are represented by "+" signs, and S0s by open diamonds. The solid line shows a linear fit to the colour-magnitude relation with the slope value determined by De Lucia *et al.* (2007). See Chapter 3 for details. The dotted lines correspond to ± 0.3 mag from the CMR. Blue symbols highlight blue-tail galaxies (outside $\pm$0.3 mag of the CMR). The plots in the figures are ordered with ascending redshift, in the same way as Table 3.1.

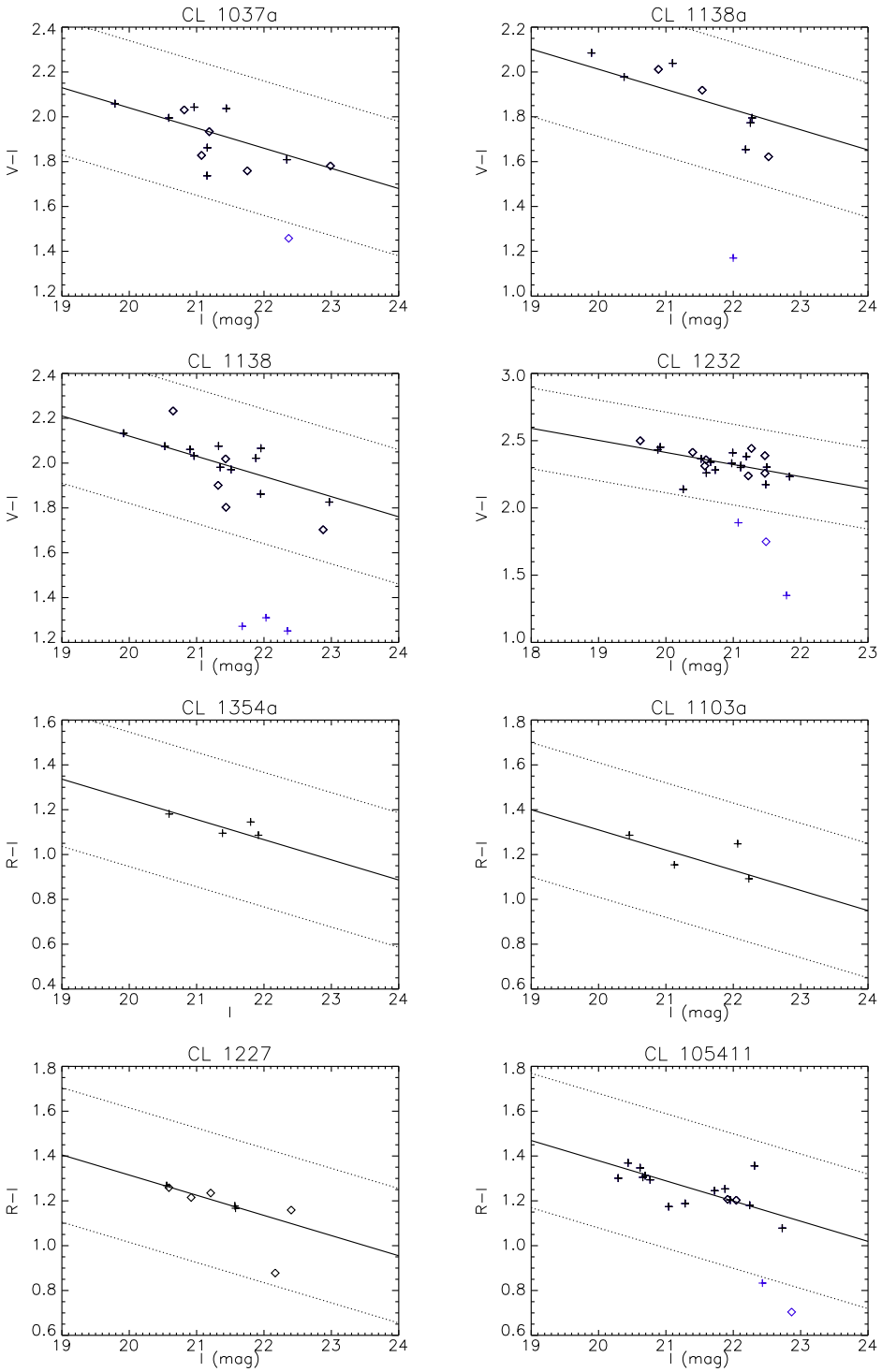

Figure A.1: CMRs of EDisCS early-type cluster galaxies (continued in Figure A.2).

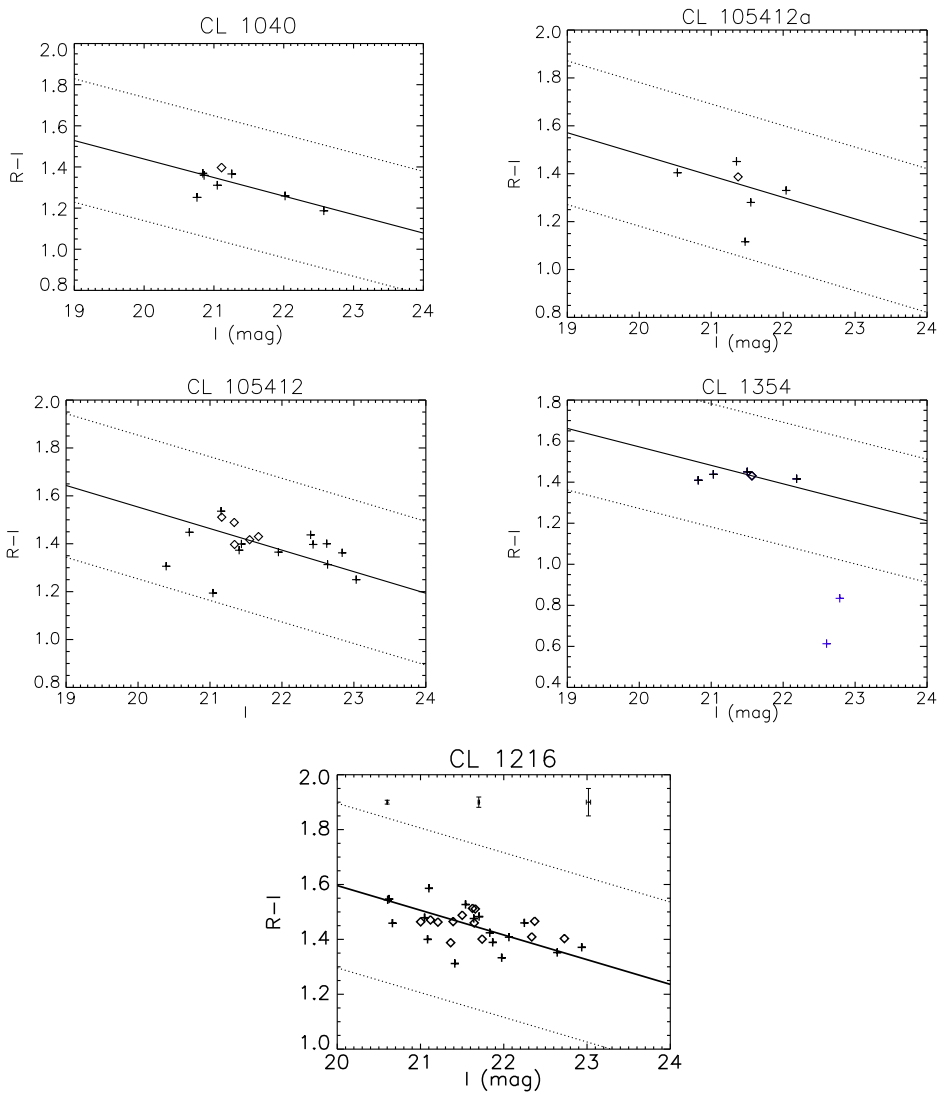

Figure A.2: CMRs of EDisCS early-type cluster galaxies (continuation of Figure A.1).

Appendix B

Measured rotation velocities and emission scale-lengths

In Table B.1 we present our measurements of rotation velocity, kinematical disturbance, and emission disk scalelengths, output from our 2D emission-line fitting procedure (Section 4.3), as well as the morphological disturbances found from the single-Sersic fits to the HST data (Section 4.5.3). We also included other characteristics of the data for completeness. The columns in the table contain:

1. name of galaxy in the EDisCS catalogue
2. galaxy environment: "f" stands for for field, "c" for cluster ($\sigma_{cl} \gtrsim 400$km/s) and "g" for group ($\sigma_{cl} \lesssim 400$km/s)
3. redshift
4. B-band magnitude corrected for internal extinction
5. logarithm of the rotation velocity (derived from ELFIT2PY), and associated confidence error
6. inclination used (from HST photometry if available, otherwise computed from I-band VLT images)
7. flag for kinematical disturbances ("good" or "bad" for undisturbed and disturbed, respectively) as judged from the emission lines in the 2D spectra.

8. Hubble T morphology type, obtained by visual inspection of the HST images. The numbers correspond to the following types: star=-7, X=-6, E=-5, S0=-2, Sa=1, Sb=3, Sbc=4, Sc=5, Scd=6, Sd=7, Sdm=8, Sm=9, Im=10, Irr=11, ?=66, and "-" is placed whenever there is no HST data available

9. flag for morphological disturbances ("good" or "bad" for undisturbed and disturbed, respectively) as detected from the single-sersic fits made to the HST images. We note that these flags must be interpreted with care as they do not necessarily represent mayor morphological disturbances (cf. Section 5.3).

10. extent of the line as measured by ELFIT2PY (only usable within our data since it depends on e.g. seeing)

11. the emission-line (exponential) disk scalelenght

12. the photometric disk scalelengths, obtained from HST data, plus their uncertainties

13. the photometric disk scalelengths, obtained from VLT data, plus their uncertainties

We note that the values of $\log V_{\rm rot}$, $r_{\rm d,emission}$, and $r_{\rm extent}$ are not listed for kinematically disturbed galaxies (intead a "–" is placed), as these values are not physically correct and can thus be missleading.

Table B.1: This table contains many of the quantities calculated and used throughout the thesis. The columns are: (1) name of galaxy in the catalogue, (2) environment ("f" for field, "c" for cluster and "g" for group), (3) redshift, (4) B-band magnitude corrected for internal extinction, (5) logarithm of the rotation velocity (from ELFIT2PY) and associated confidence error, (6) inclination used (from HST photometry if available, otherwise computed from I-band VLT images), (7) flag for kinematically disturbed ("bad") or undisturbed ("good") galaxies as judged by their emission-line fits, (8) Hubble T morphology type, obtained by visual inspection of the HST images (star=-7, X=-6, E=-5, S0=-2, Sa=1, Sb=3, Sbc=4, Sc=5, Scd=6, Sd=7, Sdm=8, Sm=9, Im=10, Irr=11, ?=66, and "-" is placed whenever there is no HST data available), (9) flag for morphological disturbances ("good" or "bad") as detected from the single-sersic fits made to the HST images, (10) extent of the line as measured by ELFIT2PY (only usable within our data since it depends on e.g. seeing), (11) the emission-line (exponential) disk scalelenght, and (12 and 13) the photometric disk scalelengths (for HST and VLT data), plus their uncertainties.

Object ID [EDCSNJ*] (1)	envi-. ronment (2)	z (3)	M_B (mag) (4)	$\log V_{\rm rot}$ (km/s) (5)	inc (°) (6)	kinem. dist. (7)	Huble T morph. (8)	morph. dist. (9)	$r_{\rm d,emission}$ ($''$) (10)	$r_{\rm extent}$ ($''$) (11)	$r^{\rm HST}_{\rm d,phot}$ ($''$) (12)	$r^{\rm VLT}_{\rm d,phot}$ ($''$) (13)
1018364-1208375	c	0.4736	-20.75	$1.50^{+0.11}_{-0.15}$	71	good	–	–	$0.23^{+0.03}_{-0.03}$	1.65	–	$0.40^{+0.04}_{-0.03}$
1018383-1212119	f	0.6335	-21.55	$2.49^{+0.08}_{-0.11}$	31	good	–	–	$0.23^{+0.07}_{-0.06}$	1.07	–	$1.20^{+0.25}_{-0.18}$
1018407-1209413	f	0.2904	-21.07	–	82	bad	–	–	–	–	–	$0.88^{+0.01}_{-0.01}$
1018417-1212331	f	0.2356	-19.36	–	71	bad	–	–	–	–	–	$1.01^{+0.03}_{-0.04}$
1018421-1209540	f	0.5234	-21.76	–	80	bad	–	–	–	–	–	$1.41^{+0.21}_{-0.20}$
1018430-1212568	c	0.4744	-21.05	$2.18^{+0.01}_{-0.02}$	73	good	–	–	$0.40^{+0.02}_{-0.02}$	1.36	–	$0.78^{+0.03}_{-0.03}$
1018437-1214144	f	0.2103	-19.37	$1.13^{+0.26}_{-0.89}$	71	good	–	–	$0.49^{+0.09}_{-0.09}$	2.92	–	$1.05^{+0.02}_{-0.03}$
1018471-1210513	c	0.4716	-21.83	–	60	bad	–	–	–	–	–	$1.08^{+0.04}_{-0.05}$
1018473-1213164	c	0.4756	-20.83	–	40	bad	–	–	–	–	–	$0.34^{+0.02}_{-0.02}$
1018475-1212446_A	f	0.6966	–	$2.06^{+0.02}_{-0.03}$	74	good	–	–	$0.35^{+0.15}_{-0.15}$	0.86	–	$0.74^{+0.08}_{-0.08}$
1018475-1212446_B	c	0.4767	–	$1.87^{+0.15}_{-0.23}$	74	good	–	–	$0.21^{+0.04}_{-0.04}$	1.89	–	$0.74^{+0.08}_{-0.08}$

table continues in next page...

Object ID	env.	z	M_B	$\log V_{\rm rot}$	inc	kin. dist.	T-type	mor. dist.	$r_{\rm d,emission}$	$r_{\rm extent}$	$r^{\rm HST}_{\rm d,phot}$	$r^{\rm VLT}_{\rm d,phot}$
1018475-1213456	f	0.4879	-21.44	–	79	bad	–	–	–	–	–	$0.89^{+0.04}_{-0.04}$
1018481-1208151	f	0.6251	-20.76	$2.05^{+0.08}_{-0.11}$	69	good	–	–	$0.11^{+0.03}_{-0.03}$	1.46	–	$0.35^{+0.02}_{-0.02}$
1018490-1212553	c	0.4733	-21.47	$2.39^{+0.03}_{-0.03}$	34	good	–	–	$0.60^{+0.04}_{-0.04}$	1.47	–	$0.70^{+0.01}_{-0.01}$
1018507-1208362	f	0.4454	-20.30	$2.16^{+0.04}_{-0.06}$	50	good	–	–	$0.35^{+0.06}_{-0.06}$	1.99	–	$0.57^{+0.01}_{-0.02}$
1018513-1209019_A	f	0.1529	–	$1.00^{+0.30}_{-0.84}$	74	good	–	–	$0.05^{+0.01}_{-0.01}$	2.53	–	$0.93^{+0.06}_{-0.03}$
1018513-1209019_B	f	1.1009	–	$2.11^{+0.01}_{-0.02}$	74	good	–	–	$0.34^{+0.01}_{-0.01}$	1.01	–	$0.93^{+0.06}_{-0.03}$
1018516-1213162	c	0.4724	-19.08	$2.07^{+0.04}_{-0.04}$	38	good	–	–	$0.55^{+0.13}_{-0.13}$	0.57	–	$0.44^{+0.06}_{-0.04}$
1018548-1210359	f	0.5105	-21.69	$2.32^{+0.04}_{-0.05}$	73	good	–	–	$0.37^{+0.06}_{-0.05}$	1.43	–	$0.65^{+0.02}_{-0.02}$
1018555-1209321	f	0.5284	-20.90	$2.23^{+0.02}_{-0.02}$	60	good	–	–	$0.32^{+0.04}_{-0.04}$	0.87	–	$0.43^{+0.02}_{-0.01}$
1037428-1245573	c	0.4225	-21.32	–	64	bad	2	bad	–	–	$0.69^{+0.01}_{-0.02}$	$2.28^{+0.20}_{-0.18}$
1037450-1244475	c	0.4215	-19.04	$1.89^{+0.14}_{-0.21}$	76	good	3	bad	$0.20^{+0.04}_{-0.03}$	0.88	$0.44^{+0.01}_{-0.01}$	$0.48^{+0.06}_{-0.04}$
1037455-1245227	c	0.4265	-21.01	$2.17^{+0.05}_{-0.05}$	59	good	3	bad	$0.66^{+0.08}_{-0.08}$	2.10	$0.52^{+0.01}_{-0.00}$	$0.68^{+0.02}_{-0.02}$
1037459-1241531	c	0.4256	-21.98	$2.48^{+0.03}_{-0.03}$	69	good	5	bad	$2.21^{+0.29}_{-0.29}$	4.01	$1.14^{+0.02}_{-0.01}$	$1.42^{+0.01}_{-0.02}$
1037463-1244588	f	0.6443	-20.15	$2.30^{+0.03}_{-0.03}$	36	good	2	good	$0.22^{+0.01}_{-0.02}$	1.06	$0.21^{+0.00}_{-0.00}$	$0.26^{+0.03}_{-0.02}$
1037465-1246590	c	0.4239	-20.77	$2.24^{+0.03}_{-0.03}$	49	good	4	good	$0.34^{+0.04}_{-0.04}$	0.95	$0.52^{+0.01}_{-0.01}$	$0.66^{+0.02}_{-0.01}$
1037472-1246088	f	0.5322	-19.11	–	64	bad	66	bad	–	–	$0.48^{+0.04}_{-0.03}$	$0.49^{+0.07}_{-0.06}$
1037475-1246030	c	0.4247	-19.13	$1.67^{+0.08}_{-0.10}$	66	good	3	bad	$0.15^{+0.02}_{-0.02}$	0.72	$0.32^{+0.02}_{-0.02}$	$0.36^{+0.05}_{-0.05}$
1037478-1246542	c	0.4274	-20.33	$1.97^{+0.10}_{-0.13}$	55	good	4	good	$0.48^{+0.04}_{-0.04}$	1.33	$0.55^{+0.01}_{-0.01}$	$0.64^{+0.02}_{-0.02}$
1037489-1247071	f	0.8531	-22.07	$2.05^{+0.03}_{-0.04}$	74	good	3	good	$0.18^{+0.01}_{-0.01}$	1.42	$0.53^{+0.03}_{-0.03}$	$0.35^{+0.03}_{-0.03}$
1037494-1243270	g	0.5799	-20.57	$1.71^{+0.09}_{-0.12}$	56	good	3	good	$0.12^{+0.04}_{-0.04}$	0.88	$0.35^{+0.01}_{-0.01}$	$0.36^{+0.02}_{-0.03}$
1037495-1246452	f	0.5327	-22.05	$2.57^{+0.03}_{-0.05}$	68	good	-2	bad	$0.08^{+0.01}_{-0.01}$	0.93	$0.62^{+0.00}_{-0.00}$	$0.78^{+0.01}_{-0.02}$
1037501-1246582	c	0.4280	-20.12	$1.82^{+0.21}_{-0.40}$	40	good	3	good	$0.43^{+0.04}_{-0.03}$	1.32	$0.75^{+0.03}_{-0.03}$	$0.84^{+0.02}_{-0.03}$
1037502-1244098	g	0.5800	-20.80	$1.90^{+0.09}_{-0.12}$	46	good	3	good	$0.65^{+0.15}_{-0.15}$	1.79	$0.56^{+0.01}_{-0.01}$	$0.65^{+0.02}_{-0.02}$
1037525-1243541	g	0.5772	-22.88	–	80	bad	2	bad	–	–	$0.33^{+0.00}_{-0.00}$	$0.63^{+0.06}_{-0.12}$
1037526-1243306	f	0.4709	-19.27	$2.00^{+0.06}_{-0.10}$	57	good	3	bad	$0.33^{+0.02}_{-0.02}$	1.38	$0.45^{+0.02}_{-0.01}$	$0.60^{+0.08}_{-0.06}$

table continues in next page...

Object ID	env.	z	M_B	$\log V_{\rm rot}$	inc	kin. dist.	T-type	mor. dist.	$r_{\rm d,emission}$	$r_{\rm extent}$	$r^{\rm HST}_{\rm d,phot}$	$r^{\rm VLT}_{\rm d,phot}$
1037527-1244485	c	0.4223	-22.29	$2.33^{+0.05}_{-0.07}$	78	good	2	bad	$0.55^{+0.06}_{-0.06}$	2.14	$0.91^{+0.01}_{-0.01}$	$0.90^{+0.13}_{-0.13}$
1037528-1243508	g	0.5770	-20.85	–	43	bad	3	bad	–	–	$0.41^{+0.01}_{-0.00}$	$3.26^{+0.29}_{-0.34}$
1037528-1244192	c	0.4303	-19.59	$2.13^{+0.08}_{-0.09}$	71	good	3	bad	$0.32^{+0.02}_{-0.02}$	1.26	$0.57^{+0.02}_{-0.02}$	$0.69^{+0.07}_{-0.08}$
1037531-1243551	g	0.5788	-20.41	$2.00^{+0.07}_{-0.09}$	57	good	3	good	$0.17^{+0.03}_{-0.03}$	0.62	$0.28^{+0.00}_{-0.00}$	$0.36^{+0.03}_{-0.02}$
1037532-1247270	f	0.9979	-21.15	$2.60^{+0.00}_{-0.01}$	36	good	8	bad	$0.50^{+0.03}_{-0.02}$	3.08	$0.29^{+0.07}_{-0.05}$	$0.48^{+0.02}_{-0.03}$
1037535-1244006	g	0.5775	-22.53	$1.87^{+0.03}_{-0.04}$	69	good	4	good	$1.35^{+0.07}_{-0.09}$	2.10	$0.74^{+0.02}_{-0.03}$	$1.27^{+0.02}_{-0.03}$
1037539-1243326	f	0.4912	-20.02	–	46	bad	3	bad	–	–	$0.29^{+0.00}_{-0.00}$	$0.34^{+0.02}_{-0.02}$
1037539-1247248	f	1.0328	-20.12	$2.03^{+0.12}_{-0.27}$	34	good	–	–	$0.09^{+0.02}_{-0.02}$	2.03	–	$0.34^{+0.06}_{-0.04}$
1037541-1246241	f	0.6461	–	$2.09^{+0.03}_{-0.04}$	85	good	7	good	$0.31^{+0.02}_{-0.02}$	1.53	$1.34^{+0.07}_{-0.05}$	$0.86^{+0.04}_{-0.04}$
1037542-1241391	f	0.4708	-21.31	$1.94^{+0.12}_{-0.17}$	61	good	1	bad	$0.19^{+0.04}_{-0.04}$	0.75	$0.39^{+0.02}_{-0.02}$	$2.65^{+0.09}_{-0.10}$
1037542-1244395	g	0.5790	-20.67	$1.88^{+0.08}_{-0.09}$	73	good	3	bad	$0.14^{+0.05}_{-0.03}$	0.77	$0.45^{+0.01}_{-0.01}$	$0.52^{+0.03}_{-0.02}$
1037543-1243020	c	0.4247	-18.98	$2.14^{+0.04}_{-0.04}$	51	good	5	good	$0.30^{+0.04}_{-0.04}$	0.85	$0.37^{+0.01}_{-0.01}$	$0.41^{+0.02}_{-0.02}$
1037547-1246322	f	0.4470	-18.67	$1.83^{+0.04}_{-0.04}$	71	good	11	bad	$0.15^{+0.02}_{-0.02}$	0.91	$0.22^{+0.01}_{-0.01}$	$0.25^{+0.05}_{-0.04}$
1037552-1246368	c	0.4245	-20.93	–	75	bad	-2	bad	–	–	$0.34^{+0.01}_{-0.01}$	$0.32^{+0.02}_{-0.01}$
1037553-1246380	g	0.5768	-19.83	$1.58^{+0.17}_{-0.27}$	67	good	-2	bad	$0.10^{+0.11}_{-0.11}$	0.73	$0.16^{+0.01}_{-0.01}$	$0.15^{+0.03}_{-0.04}$
1037555-1247123	f	0.4606	-23.20	$2.44^{+0.02}_{-0.02}$	78	good	4	bad	$1.22^{+0.04}_{-0.05}$	3.01	$1.27^{+0.01}_{-0.01}$	$1.62^{+0.02}_{-0.02}$
1037556-1243133	f	1.1385	-23.63	–	79	bad	66	good	–	–	$0.34^{+0.03}_{-0.03}$	$0.81^{+0.12}_{-0.10}$
1037558-1246327	f	0.8763	-20.51	$1.37^{+0.25}_{-0.64}$	48	good	11	bad	$0.02^{+0.01}_{-0.01}$	0.76	$0.13^{+0.00}_{-0.00}$	$0.14^{+0.02}_{-0.02}$
1037577-1244094	c	0.4295	-19.51	$1.13^{+0.39}_{-\infty}$	51	good	3	good	$0.04^{+0.03}_{-0.02}$	0.76	$0.29^{+0.01}_{-0.00}$	$0.24^{+0.04}_{-0.04}$
1037579-1244340	f	0.4764	-21.28	$2.07^{+0.09}_{-0.15}$	78	good	5	good	$0.37^{+0.08}_{-0.07}$	1.78	$0.74^{+0.01}_{-0.01}$	$0.83^{+0.02}_{-0.02}$
1037580-1241553	f	0.6836	-22.30	$2.15^{+0.04}_{-0.04}$	63	good	4	good	$0.28^{+0.07}_{-0.07}$	0.80	$0.24^{+0.02}_{-0.01}$	$6.51^{+0.20}_{-0.16}$
1037587-1245140	f	0.9564	-21.32	$2.30^{+0.01}_{-0.02}$	62	good	8	good	$0.48^{+0.01}_{-0.01}$	1.46	$0.36^{+0.04}_{-0.04}$	$0.59^{+0.04}_{-0.04}$
1037588-1245566	f	0.7733	-20.79	$2.07^{+0.04}_{-0.05}$	71	good	1	bad	$0.14^{+0.01}_{-0.01}$	2.38	$0.18^{+0.01}_{-0.01}$	$0.57^{+0.46}_{-0.17}$
1037593-1245431	f	0.4977	-21.15	$2.15^{+0.03}_{-0.03}$	47	good	2	good	$0.25^{+0.01}_{-0.01}$	1.80	$0.28^{+0.01}_{-0.01}$	$0.31^{+0.01}_{-0.02}$
1037594-1246209	f	0.8741	-21.47	–	70	bad	11	good	–	–	$0.53^{+0.04}_{-0.03}$	$0.60^{+0.04}_{-0.03}$

table continues in next page...

Object ID	env.	z	M_B	$\log V_{\rm rot}$	inc	kin. dist.	T-type	mor. dist.	$r_{\rm d,emission}$	$r_{\rm extent}$	$r^{\rm HST}_{\rm d,phot}$	$r^{\rm VLT}_{\rm d,phot}$
1037598-1245433	g	0.5774	-20.35	$2.17^{+0.03}_{-0.03}$	77	good	7	–	$0.62^{+0.21}_{-0.21}$	2.54	$0.57^{+0.05}_{-0.04}$	$0.60^{+0.08}_{-0.04}$
1038019-1246556	f	0.3028	-17.85	$1.91^{+0.10}_{-0.13}$	63	good	66	bad	$0.49^{+0.07}_{-0.05}$	1.04	$0.40^{+0.03}_{-0.03}$	$0.49^{+0.04}_{-0.04}$
1038038-1243164	f	0.4923	-21.40	$2.04^{+0.14}_{-\infty}$	74	good	–	–	$0.02^{+0.01}_{-0.01}$	0.83	–	$0.59^{+0.21}_{-0.14}$
1040320-1152401	f	0.5387	-21.32	$1.87^{+0.05}_{-0.05}$	48	good	4	good	$0.41^{+0.02}_{-0.02}$	1.54	$0.33^{+0.00}_{-0.00}$	$1.38^{+0.08}_{-0.08}$
1040346-1155511	c	0.7088	-22.00	–	81	bad	7	bad	–	–	$0.41^{+0.01}_{-0.01}$	$0.35^{+0.02}_{-0.02}$
1040350-1157594	c	0.7043	-20.62	$2.52^{+0.04}_{-0.05}$	60	good	3	bad	$0.59^{+0.05}_{-0.05}$	0.77	$0.37^{+0.02}_{-0.03}$	$0.36^{+0.04}_{-0.03}$
1040356-1156026	c	0.7081	-21.69	–	34	bad	-5	bad	–	–	$0.24^{+0.00}_{-0.00}$	$0.71^{+0.15}_{-0.12}$
1040386-1153055	f	0.7957	-20.84	$2.08^{+0.02}_{-0.03}$	74	good	66	bad	$0.27^{+0.01}_{-0.01}$	1.27	$0.47^{+0.03}_{-0.02}$	$0.48^{+0.04}_{-0.04}$
1040388-1154195	f	0.8646	-20.47	$1.97^{+0.05}_{-0.06}$	63	good	7	good	$0.27^{+0.03}_{-0.02}$	1.43	$0.30^{+0.01}_{-0.02}$	$0.32^{+0.08}_{-0.04}$
1040399-1153543	c	0.7059	-20.35	–	60	bad	6	bad	–	–	$0.36^{+0.01}_{-0.02}$	$0.33^{+0.04}_{-0.04}$
1040401-1157507	f	0.6243	-21.88	$2.18^{+0.02}_{-0.02}$	50	good	3	bad	$0.51^{+0.01}_{-0.01}$	1.73	$0.54^{+0.01}_{-0.01}$	$0.52^{+0.01}_{-0.01}$
1040402-1154295	f	0.9637	-21.34	$2.22^{+0.02}_{-0.02}$	53	good	1	good	$0.27^{+0.01}_{-0.01}$	3.20	$0.27^{+0.01}_{-0.01}$	$0.33^{+0.02}_{-0.03}$
1040409-1155272	f	0.6247	-20.00	$0.35^{+1.44}_{-\infty}$	74	good	3	bad	$0.03^{+0.03}_{-0.02}$	0.50	$0.20^{+0.01}_{-0.01}$	$0.19^{+0.05}_{-0.07}$
1040409-1157230	g	0.6316	-21.62	$2.44^{+0.01}_{-0.02}$	61	good	5	bad	$0.83^{+0.03}_{-0.03}$	2.04	$0.68^{+0.01}_{-0.01}$	$0.86^{+0.02}_{-0.02}$
1040410-1152550	f	0.9575	-21.96	–	74	bad	5	bad	–	–	$0.69^{+0.18}_{-0.12}$	$0.34^{+0.04}_{-0.04}$
1040410-1155590	c	0.7079	-22.26	$2.54^{+0.02}_{-0.02}$	58	good	5	good	$1.44^{+0.05}_{-0.04}$	4.80	$0.30^{+0.02}_{-0.02}$	$0.93^{+0.02}_{-0.02}$
1040410-1156345	c	0.7009	-21.54	–	55	bad	4	good	–	–	$0.40^{+0.00}_{-0.00}$	$0.45^{+0.02}_{-0.02}$
1040415-1156207	f	0.6240	-19.32	–	39	bad	-2	bad	–	–	$0.20^{+0.02}_{-0.01}$	$1.70^{+0.64}_{-0.34}$
1040419-1155198	f	0.7388	-20.96	$2.21^{+0.03}_{-0.03}$	71	good	5	good	$0.32^{+0.01}_{-0.02}$	1.24	$0.37^{+0.01}_{-0.01}$	$0.45^{+0.05}_{-0.03}$
1040420-1155092	f	0.5875	-20.14	$0.68^{+0.41}_{-\infty}$	57	good	1	good	$0.02^{+0.01}_{-0.01}$	0.55	$0.35^{+0.01}_{-0.03}$	$0.31^{+0.04}_{-0.02}$
1040443-1158045	g	0.6317	-21.03	$2.35^{+0.08}_{-0.10}$	54	good	1	bad	$0.15^{+0.10}_{-0.10}$	0.70	$0.14^{+0.00}_{-0.00}$	$0.22^{+0.06}_{-0.04}$
1040449-1152360	f	0.8645	-21.09	–	47	bad	5	–	–	–	$-4.90^{+-4.90}_{--4.90}$	$0.34^{+0.02}_{-0.02}$
1040467-1154041	g	0.7821	-22.13	–	72	bad	3	bad	–	–	$0.34^{+0.01}_{-0.01}$	$0.31^{+0.07}_{-0.05}$
1040471-1153262	g	0.7792	-21.48	$2.25^{+0.05}_{-0.04}$	52	good	5	good	$0.23^{+0.03}_{-0.03}$	1.11	$0.40^{+0.01}_{-0.01}$	$0.37^{+0.01}_{-0.01}$
1040476-1158184	f	0.6171	-20.85	–	36	bad	-2	bad	–	–	$0.29^{+0.01}_{-0.01}$	$0.31^{+0.05}_{-0.04}$

table continues in next page...

Object ID	env.	z	M_B	$\log V_{\rm rot}$	inc	kin. dist.	T-type	mor. dist.	$r_{\rm d,emission}$	$r_{\rm extent}$	$r^{\rm HST}_{\rm d,phot}$	$r^{\rm VLT}_{\rm d,phot}$
1040480-1152408	f	0.5354	-20.01	$1.90^{+0.05}_{-0.05}$	64	good	11	good	$0.16^{+0.00}_{-0.00}$	2.36	$0.23^{+0.01}_{-0.01}$	$0.27^{+0.02}_{-0.03}$
1040483-1156427	g	0.6329	-21.11	$1.53^{+0.33}_{-\infty}$	83	good	11	bad	$0.08^{+0.05}_{-0.05}$	0.90	$1.18^{+0.09}_{-0.07}$	$0.67^{+0.05}_{-0.04}$
1040492-1156399	f	0.5193	-19.86	–	79	bad	1	bad	–	–	$0.20^{+0.01}_{-0.01}$	$0.23^{+0.07}_{-0.08}$
1040493-1152154	f	0.6560	-22.55	$2.12^{+0.04}_{-0.04}$	71	good	–	–	$0.71^{+0.04}_{-0.04}$	3.59	–	$2.19^{+0.15}_{-0.13}$
1040517-1153222	f	0.9147	-20.61	$2.06^{+0.04}_{-0.03}$	50	good	3	bad	$0.17^{+0.01}_{-0.01}$	1.11	$0.38^{+0.09}_{-0.09}$	$0.25^{+0.40}_{-0.25}$
1054194-1147007	f	0.0764	-19.22	–	38	bad	3	good	–	–	$1.23^{+0.00}_{-0.00}$	$1.71^{+0.01}_{-0.01}$
1054198-1146337	c	0.6972	-21.42	–	50	bad	11	good	–	–	$0.26^{+0.01}_{-0.01}$	$0.49^{+0.02}_{-0.02}$
1054207-1148130	c	0.6996	-19.98	$1.00^{+0.66}_{-\infty}$	67	good	-2	bad	$0.04^{+0.05}_{-0.03}$	0.41	$0.21^{+0.01}_{-0.01}$	$0.25^{+0.12}_{-0.11}$
1054223-1147460	f	0.8634	-24.80	$1.13^{+0.87}_{-\infty}$	84	good	3	bad	$0.04^{+0.03}_{-0.02}$	0.97	$0.11^{+0.00}_{-0.00}$	$0.02^{+0.03}_{-0.02}$
1054236-1149453	f	0.6629	-21.68	$0.87^{+0.76}_{-\infty}$	61	good	1	good	$0.05^{+0.04}_{-0.03}$	0.90	$0.18^{+0.01}_{-0.01}$	$0.06^{+0.01}_{-0.01}$
1054264-1147207	c	0.6963	-21.57	$2.45^{+0.02}_{-0.03}$	81	good	7	good	$0.59^{+0.03}_{-0.04}$	1.39	$0.90^{+0.02}_{-0.02}$	$0.60^{+0.04}_{-0.04}$
1054277-1149315	f	0.7623	-21.75	–	62	bad	11	good	–	–	$0.44^{+0.01}_{-0.01}$	$0.70^{+0.02}_{-0.02}$
1054278-1149580	c	0.6949	-22.75	–	56	bad	3	bad	–	–	$0.25^{+0.02}_{-0.01}$	$2.04^{+0.14}_{-0.12}$
1054292-1149028	c	0.7030	-20.93	–	69	bad	-6	bad	–	–	$0.92^{+0.15}_{-0.07}$	$0.40^{+0.08}_{-0.05}$
1054303-1148158	c	0.6952	-20.02	$2.00^{+0.16}_{-0.38}$	47	good	66	good	$0.13^{+0.08}_{-0.06}$	0.32	$0.25^{+0.01}_{-0.01}$	$0.32^{+0.06}_{-0.03}$
1054338-1146388	f	0.7613	-22.66	$2.22^{+0.02}_{-0.03}$	78	good	5	bad	$0.67^{+0.02}_{-0.02}$	2.52	$0.77^{+0.08}_{-0.08}$	$1.16^{+0.07}_{-0.09}$
1054339-1147352	f	0.8608	-21.97	–	53	bad	-5	bad	–	–	$0.27^{+0.01}_{-0.01}$	$0.19^{+0.02}_{-0.02}$
1054343-1147004	c	0.6935	-21.27	$1.76^{+0.09}_{-0.11}$	50	good	11	good	$0.22^{+0.04}_{-0.04}$	1.60	$0.30^{+0.01}_{-0.01}$	$0.23^{+0.03}_{-0.03}$
1054356-1245264	c	0.7493	-21.89	–	52	bad	-2	bad	–	–	$0.37^{+0.01}_{-0.01}$	$1.25^{+0.08}_{-0.07}$
1054358-1243099	f	0.2424	-17.24	$1.80^{+0.07}_{-0.08}$	79	good	3	bad	$0.20^{+0.02}_{-0.02}$	0.89	$0.31^{+0.01}_{-0.01}$	$0.34^{+0.02}_{-0.02}$
1054389-1243521	f	0.2428	-20.66	–	76	bad	4	bad	–	–	$0.89^{+0.01}_{-0.01}$	$1.02^{+0.01}_{-0.01}$
1054392-1243462	f	0.5250	-20.01	$2.15^{+0.03}_{-0.03}$	45	good	3	good	$0.35^{+0.01}_{-0.01}$	1.42	$0.27^{+0.01}_{-0.01}$	$0.45^{+0.02}_{-0.02}$
1054414-1245384	c	0.7504	-21.47	–	76	bad	-6	good	–	–	$0.31^{+0.01}_{-0.01}$	$0.38^{+0.03}_{-0.02}$
1054436-1244401	f	0.5228	-20.45	$1.60^{+0.10}_{-0.13}$	66	good	3	good	$0.18^{+0.03}_{-0.03}$	1.07	$0.33^{+0.01}_{-0.00}$	$0.41^{+0.01}_{-0.01}$
1054441-1246036	f	0.2322	-17.53	$1.63^{+0.05}_{-0.06}$	78	good	7	good	$0.20^{+0.01}_{-0.01}$	0.95	$0.44^{+0.01}_{-0.01}$	$0.52^{+0.03}_{-0.02}$

table continues in next page...

Object ID	env.	z	M_B	$\log V_{\rm rot}$	inc	kin. dist.	T-type	mor. dist.	$r_{\rm d,emission}$	$r_{\rm extent}$	$r^{\rm HST}_{\rm d,phot}$	$r^{\rm VLT}_{\rm d,phot}$
1054457-1244068	f	0.5891	-20.60	$2.02^{+0.07}_{-0.05}$	65	good	5	good	$0.30^{+0.03}_{-0.03}$	2.02	$0.49^{+0.01}_{-0.01}$	–
1054486-1243269	c	0.7491	-20.72	–	41	bad	2	bad	–	–	$0.26^{+0.01}_{-0.01}$	$0.35^{+0.02}_{-0.01}$
1054494-1247066	f	1.0184	-22.45	$2.52^{+0.02}_{-0.02}$	57	good	6	bad	$0.53^{+0.05}_{-0.05}$	1.61	$0.58^{+0.03}_{-0.02}$	$0.77^{+0.03}_{-0.03}$
1054498-1245499	f	0.2017	-18.14	$1.62^{+0.06}_{-0.07}$	65	good	3	good	$0.10^{+0.02}_{-0.02}$	0.89	$0.25^{+0.00}_{-0.00}$	$0.30^{+0.01}_{-0.01}$
1054512-1242223	f	0.2326	-17.47	$1.76^{+0.13}_{-0.18}$	44	good	–	–	$0.29^{+0.03}_{-0.03}$	1.22	–	$0.35^{+0.03}_{-0.03}$
1054515-1244509	f	0.6446	-20.26	–	55	bad	2	bad	–	–	$0.23^{+0.01}_{-0.02}$	$0.24^{+0.02}_{-0.03}$
1054525-1244189	g	0.7283	-22.34	–	41	bad	-5	good	–	–	$0.38^{+0.01}_{-0.00}$	$0.32^{+0.02}_{-0.02}$
1059031-1254292	c	0.4561	-23.30	–	78	bad	–	–	–	–	–	$1.46^{+0.05}_{-0.05}$
1059052-1254215	c	0.4547	-20.80	$2.09^{+0.10}_{-0.13}$	55	good	–	–	$0.44^{+0.07}_{-0.07}$	1.17	–	$0.96^{+0.04}_{-0.03}$
1059058-1255024	f	0.6626	-22.20	$2.39^{+0.05}_{-0.06}$	53	good	–	–	$0.32^{+0.00}_{-0.00}$	4.64	–	$2.29^{+0.16}_{-0.14}$
1059061-1252541	f	0.5190	-21.11	$2.23^{+0.01}_{-0.01}$	42	good	–	–	$0.29^{+0.04}_{-0.04}$	1.95	–	$0.40^{+0.01}_{-0.01}$
1059063-1249405	f	0.6956	-21.92	–	44	bad	–	–	–	–	–	$0.52^{+0.04}_{-0.06}$
1059065-1252425	c	0.4592	-21.04	$2.06^{+0.09}_{-0.12}$	52	good	–	–	$0.11^{+0.04}_{-0.04}$	1.08	–	$0.20^{+0.01}_{-0.01}$
1059085-1252506	c	0.4584	-18.17	$1.84^{+0.15}_{-0.23}$	80	good	–	–	$0.13^{+0.04}_{-0.04}$	0.71	–	$0.42^{+0.16}_{-0.13}$
1059086-1255576	c	0.4515	-20.75	$0.68^{+1.10}_{-\infty}$	40	good	–	–	$0.02^{+0.01}_{-0.01}$	0.53	–	$0.69^{+0.09}_{-0.10}$
1059089-1252444	f	0.4120	-21.50	$2.23^{+0.03}_{-0.03}$	59	good	–	–	$0.51^{+0.03}_{-0.03}$	3.61	–	$0.58^{+0.01}_{-0.01}$
1059100-1251390	c	0.4517	-21.52	–	33	bad	–	–	–	–	–	$2.00^{+0.13}_{-0.08}$
1059100-1252337	f	0.4150	-20.21	$2.05^{+0.08}_{-0.09}$	65	good	–	–	$0.29^{+0.04}_{-0.03}$	1.03	–	$0.49^{+0.02}_{-0.02}$
1059104-1253211	c	0.4553	-21.63	–	58	bad	–	–	–	–	–	$1.61^{+0.05}_{-0.04}$
1059105-1249497	f	0.5729	-21.06	–	63	bad	–	–	–	–	–	$0.43^{+0.02}_{-0.02}$
1059121-1250330	c	0.4556	-18.66	$1.39^{+0.14}_{-0.22}$	77	good	–	–	$0.13^{+0.03}_{-0.03}$	2.29	–	$0.19^{+0.08}_{-0.08}$
1059135-1254337	c	0.4559	-22.47	–	79	bad	–	–	–	–	–	$0.95^{+0.07}_{-0.04}$
1059156-1250183	f	0.5200	-20.35	–	70	bad	–	–	–	–	–	$0.44^{+0.33}_{-0.37}$
1059156-1254404	c	0.4592	-21.14	–	59	bad	–	–	–	–	–	$0.45^{+0.03}_{-0.03}$
1059169-1255242	f	0.3515	-20.74	–	55	bad	–	–	–	–	–	$0.83^{+0.03}_{-0.03}$

table continues in next page...

Object ID	env.	z	M_B	$\log V_{\rm rot}$	inc	kin. dist.	T-type	mor. dist.	$r_{\rm d,emission}$	$r_{\rm extent}$	$r^{\rm HST}_{\rm d,phot}$	$r^{\rm VLT}_{\rm d,phot}$
1059176-1255154	f	0.2191	-18.52	–	59	bad	–	–	–	–	–	$1.07^{+0.04}_{-0.03}$
1059198-1251424	c	0.4553	-20.61	$1.76^{+0.41}_{-\infty}$	64	good	–	–	$0.04^{+0.06}_{-0.06}$	0.58	–	$0.42^{+0.31}_{-0.10}$
1103322-1243181	f	0.6044	-21.46	–	71	bad	–	–	–	–	–	$0.47^{+0.02}_{-0.02}$
1103323-1243143	f	0.4109	-21.23	$2.30^{+0.07}_{-0.08}$	61	good	–	–	$0.41^{+0.06}_{-0.06}$	1.81	–	$0.72^{+0.02}_{-0.02}$
1103336-1249004	f	0.6966	-21.32	$2.18^{+0.02}_{-0.02}$	75	good	7	–	$0.60^{+0.01}_{-0.02}$	1.28	–	$0.76^{+0.04}_{-0.03}$
1103346-1244269	f	0.4106	-18.61	$1.70^{+0.06}_{-0.07}$	71	good	5	–	$0.16^{+0.02}_{-0.02}$	0.94	$0.31^{+0.02}_{-0.02}$	$0.39^{+0.03}_{-0.02}$
1103348-1244157	f	0.3556	-21.45	–	84	bad	4	good	–	–	$1.32^{+0.04}_{-0.03}$	$1.04^{+0.02}_{-0.02}$
1103355-1244515	g	0.6259	-22.24	$2.56^{+0.01}_{-0.01}$	35	good	5	–	$1.35^{+0.02}_{-0.02}$	3.15	–	$0.80^{+0.01}_{-0.01}$
1103365-1244223	g	0.7031	-24.45	$2.60^{+0.00}_{-0.00}$	77	good	3	good	$1.35^{+0.05}_{-0.04}$	2.60	$1.64^{+0.02}_{-0.02}$	$1.80^{+0.06}_{-0.07}$
1103368-1248298	f	0.5484	-20.83	$2.22^{+0.07}_{-0.09}$	44	good	4	–	$0.51^{+0.08}_{-0.08}$	0.91	–	$0.56^{+0.02}_{-0.01}$
1103370-1247124	f	0.3051	-20.00	$2.05^{+0.03}_{-0.04}$	81	good	5	–	$0.51^{+0.05}_{-0.05}$	1.32	–	$0.84^{+0.02}_{-0.02}$
1103374-1244072	g	0.7058	-21.30	$2.25^{+0.04}_{-0.05}$	78	good	11	bad	$0.61^{+0.04}_{-0.05}$	1.34	$0.63^{+0.02}_{-0.02}$	$0.64^{+0.03}_{-0.03}$
1103393-1246119	f	0.1475	-16.02	$2.00^{+0.06}_{-0.05}$	73	good	11	–	$0.21^{+0.03}_{-0.03}$	1.07	$0.59^{+0.02}_{-0.02}$	$0.78^{+0.08}_{-0.06}$
1103395-1244537	f	0.7217	-21.97	$2.44^{+0.02}_{-0.03}$	64	good	2	–	$0.16^{+0.01}_{-0.01}$	2.87	$0.60^{+0.03}_{-0.04}$	$1.53^{+0.61}_{-0.48}$
1103398-1246578	g	0.7022	-21.55	$2.35^{+0.01}_{-0.01}$	66	good	6	–	$0.60^{+0.01}_{-0.01}$	1.63	$0.60^{+0.01}_{-0.02}$	$0.63^{+0.02}_{-0.02}$
1103398-1247485	f	0.3424	-18.96	$1.81^{+0.13}_{-0.19}$	66	good	11	–	$0.20^{+0.03}_{-0.03}$	0.88	–	$0.37^{+0.03}_{-0.02}$
1103401-1244377	g	0.7032	-20.88	$2.01^{+0.11}_{-0.17}$	35	good	4	–	$0.45^{+0.03}_{-0.02}$	2.65	$0.22^{+0.00}_{-0.00}$	$0.24^{+0.02}_{-0.01}$
1103401-1244530	f	0.7228	-22.33	–	67	bad	3	good	–	–	$0.56^{+0.02}_{-0.02}$	$1.38^{+0.06}_{-0.06}$
1103404-1247358	f	0.8049	-22.55	$2.37^{+0.00}_{-0.00}$	46	good	5	–	$0.56^{+0.01}_{-0.01}$	2.16	–	$0.57^{+0.04}_{-0.02}$
1103418-1244344	f	0.3539	-19.94	–	65	bad	-2	bad	–	–	$0.28^{+0.00}_{-0.01}$	$0.35^{+0.03}_{-0.04}$
1103424-1245086	f	0.1990	-18.61	$1.71^{+0.01}_{-0.01}$	64	good	5	bad	$0.42^{+0.03}_{-0.03}$	1.75	$0.98^{+0.02}_{-0.02}$	$1.12^{+0.02}_{-0.02}$
1103430-1245370	f	0.6584	-21.64	–	55	bad	-2	bad	$0.12^{+0.11}_{-0.08}$	–	$0.50^{+0.01}_{-0.01}$	$1.55^{+0.16}_{-0.13}$
1103435-1248339	f	0.8788	-20.34	–	60	bad	11	–	$0.07^{+0.06}_{-0.04}$	–	–	$0.37^{+0.02}_{-0.03}$
1103446-1249085	c	0.9598	-22.16	$2.50^{+0.02}_{-0.03}$	66	good	7	–	$0.71^{+0.04}_{-0.03}$	3.57	–	$0.44^{+0.04}_{-0.03}$
1103447-1245597	c	0.9588	–	$1.86^{+0.12}_{-0.22}$	63	good	3	–	$0.10^{+0.02}_{-0.03}$	0.76	$0.26^{+0.01}_{-0.01}$	$1.24^{+0.15}_{-0.08}$

table continues in next page...

Object ID	env.	z	M_B	$\log V_{\rm rot}$	inc	kin. dist.	T-type	mor. dist.	$r_{\rm d,emission}$	$r_{\rm extent}$	$r^{\rm HST}_{\rm d,phot}$	$r^{\rm VLT}_{\rm d,phot}$
1103457-1245397	c	0.9562	-21.88	–	54	bad	2	bad	–	–	$0.28^{+0.01}_{-0.01}$	$0.68^{+0.09}_{-0.06}$
1103458-1243353	f	0.4275	-20.12	–	31	bad	-5	bad	–	–	–	$0.43^{+0.03}_{-0.03}$
1103462-1247552	f	0.5003	-23.26	$2.15^{+0.05}_{-0.05}$	66	good	5	–	$0.75^{+0.03}_{-0.03}$	2.28	$0.74^{+0.01}_{-0.02}$	$6.70^{+0.07}_{-0.08}$
1103463-1246578	g	0.6284	-20.99	$2.21^{+0.06}_{-0.09}$	78	good	4	–	$0.34^{+0.05}_{-0.05}$	1.27	$0.60^{+0.03}_{-0.03}$	$0.64^{+0.02}_{-0.03}$
1103477-1247428	f	0.7657	-21.75	–	45	bad	6	bad	–	–	$0.63^{+0.03}_{-0.02}$	$0.88^{+0.02}_{-0.02}$
1103485-1247452	f	0.7668	-20.50	$1.19^{+0.54}_{-\infty}$	52	good	-5	–	$0.03^{+0.02}_{-0.02}$	0.76	$0.16^{+0.01}_{-0.02}$	$2.71^{+0.87}_{-0.54}$
1103495-1248506	f	1.1920	-21.66	$1.23^{+0.12}_{-0.20}$	49	good	7	–	$0.20^{+0.01}_{-0.01}$	0.00	$0.17^{+0.01}_{-0.01}$	$0.22^{+0.02}_{-0.02}$
1103504-1247559	g	0.6273	-19.87	$1.78^{+0.05}_{-0.06}$	64	good	66	–	$0.10^{+0.04}_{-0.04}$	0.96	$0.20^{+0.01}_{-0.01}$	$0.21^{+0.03}_{-0.02}$
1103508-1247279	f	0.6953	-21.09	$2.20^{+0.03}_{-0.04}$	48	good	5	–	$0.57^{+0.00}_{-0.00}$	1.84	$0.64^{+0.03}_{-0.03}$	$0.67^{+0.02}_{-0.02}$
1103531-1243096	g	0.7033	-21.39	$2.48^{+0.06}_{-0.06}$	30	good	4	–	$0.52^{+0.12}_{-0.12}$	1.37	$0.22^{+0.01}_{-0.00}$	$0.22^{+0.02}_{-0.02}$
1103540-1245259	f	0.9210	-22.00	$1.50^{+0.11}_{-0.14}$	37	good	5	–	$0.69^{+0.02}_{-0.02}$	1.90	$0.59^{+0.02}_{-0.02}$	$0.59^{+0.02}_{-0.02}$
1103543-1248403	f	0.7661	-20.82	$2.21^{+0.04}_{-0.04}$	62	good	8	–	$0.25^{+0.01}_{-0.01}$	1.01	$0.42^{+0.01}_{-0.02}$	$0.48^{+0.02}_{-0.02}$
1119111-1128458	f	0.4536	-20.79	$1.31^{+0.23}_{-0.37}$	57	good	–	–	$0.44^{+0.02}_{-0.02}$	1.77	–	$0.56^{+0.01}_{-0.02}$
1119112-1133186	f	0.2507	-18.73	–	73	bad	–	–	–	–	–	$0.24^{+0.02}_{-0.02}$
1119138-1129498	f	0.3485	-19.81	$1.98^{+0.11}_{-0.10}$	48	good	–	–	$1.12^{+0.08}_{-0.69}$	0.71	–	$0.37^{+0.01}_{-0.01}$
1119151-1133077	f	0.2506	-21.87	$2.34^{+0.02}_{-0.02}$	64	good	–	–	$0.15^{+0.02}_{-0.02}$	1.07	–	$1.48^{+0.01}_{-0.01}$
1119163-1127282_A	f	1.0241	–	$2.18^{+0.02}_{-0.02}$	61	good	–	–	$0.27^{+0.01}_{-0.01}$	2.63	–	$0.87^{+0.02}_{-0.02}$
1119163-1127282_B	f	0.9671	–	$1.95^{+0.05}_{-0.07}$	61	good	–	–	$0.16^{+0.01}_{-0.02}$	1.05	–	$0.87^{+0.02}_{-0.02}$
1119165-1131400	f	0.6953	-21.52	$0.13^{+0.87}_{-\infty}$	53	good	–	–	$0.73^{+0.03}_{-0.02}$	1.75	–	$0.80^{+0.04}_{-0.04}$
1119168-1129376	g	0.5496	-23.73	–	52	bad	–	–	–	–	–	$2.41^{+0.27}_{-0.37}$
1119169-1128380	f	0.7918	-23.06	$2.02^{+0.03}_{-0.02}$	52	good	–	–	$0.49^{+0.01}_{-0.02}$	1.96	–	$3.56^{+0.23}_{-0.23}$
1119173-1129425	g	0.5503	-21.64	–	40	bad	–	–	–	–	–	$1.16^{+0.05}_{-0.04}$
1119181-1132049	f	0.1239	-19.95	$1.47^{+0.19}_{-0.35}$	33	good	–	–	$0.65^{+0.09}_{-0.09}$	1.85	–	$1.11^{+0.01}_{-0.01}$
1119184-1128134	f	0.3391	-20.37	$1.94^{+0.01}_{-0.01}$	68	good	–	–	$0.35^{+0.01}_{-0.01}$	1.36	–	$0.29^{+0.02}_{-0.02}$
1119204-1127409	f	0.5286	-20.46	$1.78^{+0.05}_{-0.06}$	58	good	–	–	$0.15^{+0.01}_{-0.01}$	1.06	–	$0.34^{+0.12}_{-0.09}$

table continues in next page...

Object ID	env.	z	M_B	$\log V_{\rm rot}$	inc	kin. dist.	T-type	mor. dist.	$r_{\rm d,emission}$	$r_{\rm extent}$	$r^{\rm HST}_{\rm d,phot}$	$r^{\rm VLT}_{\rm d,phot}$
1119215-1129103	f	0.5284	-22.06	$2.42^{+0.04}_{-0.05}$	68	good	–	–	$0.45^{+0.07}_{-0.07}$	1.70	–	$0.75^{+0.01}_{-0.02}$
1119216-1131053	f	0.9587	-21.91	$1.66^{+0.09}_{-0.08}$	53	good	–	–	$0.19^{+0.01}_{-0.01}$	1.27	–	$0.26^{+0.03}_{-0.02}$
1119216-1132421	f	0.4746	-20.86	–	69	bad	–	–	–	–	–	$1.06^{+0.07}_{-0.04}$
1119216-1132475	f	0.4764	-21.43	–	46	bad	–	–	–	–	–	$0.88^{+0.03}_{-0.02}$
1119222-1129055	f	0.3727	-20.34	$1.93^{+0.02}_{-0.02}$	74	good	–	–	$0.22^{+0.01}_{-0.01}$	0.97	–	$0.36^{+0.02}_{-0.03}$
1119226-1128488	f	0.5269	-21.81	–	39	bad	–	–	–	–	–	$0.41^{+0.09}_{-0.09}$
1119235-1130144	f	0.6777	-20.85	$1.39^{+0.23}_{-0.33}$	43	good	–	–	$0.94^{+0.34}_{-0.36}$	1.14	–	$0.38^{+0.02}_{-0.02}$
1119243-1131232	f	0.2125	-20.52	$2.17^{+0.02}_{-0.02}$	59	good	–	–	$0.61^{+0.10}_{-0.10}$	2.67	–	$1.05^{+0.01}_{-0.01}$
1138034-1132394	f	0.6199	-19.87	$1.16^{+0.47}_{-\infty}$	58	good	3	bad	$0.09^{+0.03}_{-0.03}$	3.40	$0.13^{+0.01}_{-0.00}$	$2.06^{+0.13}_{-0.24}$
1138035-1132254	c	0.4785	-20.83	$2.22^{+0.05}_{-0.05}$	66	good	5	good	$0.47^{+0.05}_{-0.05}$	1.30	$0.45^{+0.00}_{-0.00}$	$0.54^{+0.01}_{-0.01}$
1138037-1137275	f	0.7384	-21.71	$1.62^{+0.17}_{-0.19}$	82	good	11	good	$0.21^{+0.03}_{-0.03}$	1.03	$1.27^{+0.17}_{-0.35}$	$0.54^{+0.06}_{-0.07}$
1138057-1131517	f	0.3586	-19.02	$1.76^{+0.13}_{-0.26}$	43	good	6	bad	$0.22^{+0.03}_{-0.04}$	1.30	$0.31^{+0.01}_{-0.01}$	$0.34^{+0.01}_{-0.01}$
1138064-1134252	f	0.6192	-20.30	$2.15^{+0.03}_{-0.02}$	36	good	3	bad	$0.43^{+0.01}_{-0.01}$	1.40	$0.38^{+0.00}_{-0.01}$	$0.43^{+0.02}_{-0.01}$
1138064-1134297	f	0.5452	-19.31	$1.41^{+0.22}_{-0.55}$	46	good	11	bad	$0.24^{+0.01}_{-0.01}$	1.27	$0.26^{+0.01}_{-0.01}$	$0.31^{+0.03}_{-0.04}$
1138069-1136160	c	0.4520	-18.62	–	51	bad	-2	bad	–	–	$0.25^{+0.01}_{-0.01}$	$0.24^{+0.02}_{-0.02}$
1138073-1132356	f	0.3711	-19.37	$1.97^{+0.14}_{-0.20}$	72	good	3	bad	$0.27^{+0.02}_{-0.02}$	1.11	$0.29^{+0.00}_{-0.00}$	$0.36^{+0.01}_{-0.01}$
1138076-1136272	f	0.6188	-19.58	$2.12^{+0.04}_{-0.03}$	67	good	7	bad	$0.29^{+0.02}_{-0.01}$	1.31	$0.47^{+0.05}_{-0.06}$	$0.44^{+0.13}_{-0.07}$
1138086-1131416	f	0.5039	-19.03	$1.55^{+0.17}_{-0.27}$	49	good	-5	good	$0.13^{+0.02}_{-0.02}$	0.98	$0.25^{+0.01}_{-0.02}$	$0.31^{+0.02}_{-0.02}$
1138086-1136549	c	0.4519	-21.92	$2.36^{+0.01}_{-0.01}$	54	good	2	good	$0.48^{+0.04}_{-0.04}$	1.64	$0.51^{+0.01}_{-0.00}$	$0.77^{+0.02}_{-0.02}$
1138094-1134286	f	0.5291	-19.74	$1.16^{+0.38}_{-\infty}$	55	good	6	good	$0.33^{+0.03}_{-0.04}$	1.35	$0.47^{+0.02}_{-0.01}$	$0.51^{+0.02}_{-0.02}$
1138097-1136571	f	0.8287	-21.14	–	69	bad	11	bad	–	–	$0.42^{+0.02}_{-0.02}$	$0.42^{+0.03}_{-0.03}$
1138099-1132035	c	0.4738	-21.59	$2.19^{+0.02}_{-0.02}$	75	good	1	good	$0.84^{+0.04}_{-0.04}$	2.52	$0.77^{+0.05}_{-0.04}$	$1.28^{+0.03}_{-0.04}$
1138104-1134064	c	0.4786	-20.79	$2.25^{+0.01}_{-0.01}$	81	good	6	bad	$0.74^{+0.07}_{-0.07}$	2.33	$0.64^{+0.03}_{-0.05}$	$0.93^{+0.06}_{-0.04}$
1138112-1135117	c	0.4842	-18.36	$0.88^{+0.53}_{-\infty}$	57	good	-2	bad	$0.03^{+0.01}_{-0.01}$	0.34	$0.22^{+0.02}_{-0.01}$	$0.35^{+0.10}_{-0.09}$
1138115-1135008	f	0.1857	-16.90	$2.02^{+0.04}_{-0.05}$	53	good	-5	bad	$0.16^{+0.02}_{-0.02}$	0.87	$0.20^{+0.01}_{-0.01}$	$0.18^{+0.02}_{-0.02}$

table continues in next page...

Object ID	env.	z	M_B	$\log V_{\rm rot}$	inc	kin. dist.	T-type	mor. dist.	$r_{\rm d,emission}$	$r_{\rm extent}$	$r^{\rm HST}_{\rm d,phot}$	$r^{\rm VLT}_{\rm d,phot}$
1138116-1134448	c	0.4571	-20.72	–	46	bad	-5	bad	–	–	$0.28^{+0.00}_{-0.00}$	$0.39^{+0.11}_{-0.08}$
1138117-1137542	f	0.5740	-20.13	$0.98^{+0.20}_{-0.39}$	49	good	–	–	$0.57^{+0.07}_{-0.07}$	1.51	–	$0.66^{+0.03}_{-0.02}$
1138127-1133524	c	0.4863	-20.60	$2.29^{+0.08}_{-0.10}$	49	good	6	good	$0.29^{+0.02}_{-0.02}$	1.15	$0.37^{+0.00}_{-0.00}$	$0.44^{+0.01}_{-0.01}$
1138139-1133090	f	0.3055	-18.21	$0.79^{+0.78}_{-\infty}$	47	good	11	good	$0.06^{+0.05}_{-0.03}$	0.80	$0.32^{+0.00}_{-0.00}$	$0.41^{+0.04}_{-0.03}$
1138170-1131411	f	0.2605	-19.23	$1.87^{+0.08}_{-0.10}$	47	good	-5	good	$0.21^{+0.06}_{-0.06}$	0.99	$0.18^{+0.00}_{-0.00}$	$0.19^{+0.10}_{-0.04}$
1138176-1133209	f	0.5286	-19.75	$2.10^{+0.04}_{-0.04}$	66	good	1	bad	$0.30^{+0.04}_{-0.04}$	0.77	$0.37^{+0.02}_{-0.02}$	$0.43^{+0.05}_{-0.05}$
1138177-1136332	f	0.3049	-19.83	$2.29^{+0.03}_{-0.04}$	40	good	6	bad	$1.22^{+0.18}_{-0.18}$	2.97	$0.72^{+0.02}_{-0.01}$	$1.17^{+0.02}_{-0.01}$
1138183-1135486	f	0.6525	-20.12	$2.09^{+0.07}_{-0.05}$	60	good	11	good	$0.33^{+0.05}_{-0.04}$	0.65	$0.29^{+0.01}_{-0.01}$	$0.31^{+0.04}_{-0.03}$
1138204-1131417	f	0.9090	-21.75	–	53	bad	-5	bad	–	–	$0.36^{+0.06}_{-0.04}$	$1.09^{+0.24}_{-0.14}$
1202370-1226079	f	0.4603	-20.36	–	52	bad	–	–	–	–	–	$0.65^{+0.02}_{-0.02}$
1202393-1222096	f	0.3858	-20.00	–	76	bad	–	–	–	–	–	$0.41^{+0.02}_{-0.02}$
1202398-1226154	f	0.7284	-21.53	$2.18^{+0.05}_{-0.08}$	72	good	–	–	$0.22^{+0.03}_{-0.02}$	1.15	–	$0.46^{+0.03}_{-0.04}$
1202400-1223011	c	0.4194	-20.27	$1.99^{+0.08}_{-0.09}$	79	good	–	–	$0.22^{+0.03}_{-0.04}$	0.98	–	$0.42^{+0.04}_{-0.04}$
1202406-1221340	f	0.4074	-22.76	–	54	bad	–	–	–	–	–	$1.83^{+0.03}_{-0.03}$
1202417-1221467	f	0.1269	-16.92	–	63	bad	–	–	–	–	–	$0.33^{+0.03}_{-0.03}$
1202428-1224401	c	0.4201	-20.70	$2.04^{+0.10}_{-0.13}$	59	good	–	–	$0.23^{+0.01}_{-0.02}$	1.01	–	$0.62^{+0.01}_{-0.01}$
1202435-1222204	f	0.3805	-20.74	$1.96^{+0.02}_{-0.02}$	51	good	–	–	$0.43^{+0.07}_{-0.07}$	1.68	–	$1.05^{+0.03}_{-0.03}$
1202462-1227018	f	0.1865	-14.61	–	83	bad	–	–	–	–	–	$0.01^{+0.42}_{-0.01}$
1202471-1226537	f	0.5224	-21.20	$2.30^{+0.03}_{-0.03}$	71	good	–	–	$0.44^{+0.04}_{-0.03}$	1.33	–	$0.67^{+0.02}_{-0.02}$
1202473-1221101	f	0.3511	-19.83	$2.08^{+0.07}_{-0.09}$	36	good	–	–	$0.41^{+0.07}_{-0.08}$	1.27	–	$0.79^{+0.04}_{-0.03}$
1202474-1221438	f	0.6944	-21.70	$2.28^{+0.01}_{-0.02}$	67	good	–	–	$0.62^{+0.10}_{-0.10}$	1.95	–	$0.56^{+0.04}_{-0.03}$
1202476-1221272	f	0.1742	-17.10	$1.60^{+0.12}_{-0.16}$	56	good	–	–	$0.23^{+0.03}_{-0.03}$	0.96	–	$0.43^{+0.02}_{-0.02}$
1202484-1222416	f	0.4814	-20.32	$1.91^{+0.02}_{-0.03}$	77	good	–	–	$0.12^{+0.01}_{-0.01}$	1.05	–	$0.36^{+0.22}_{-0.23}$
1202495-1225219	f	0.4811	-21.52	$1.95^{+0.25}_{-0.51}$	66	good	–	–	$0.14^{+0.07}_{-0.07}$	1.07	–	$0.61^{+0.02}_{-0.02}$
1216358-1203164	c	0.7850	-21.62	–	69	bad	11	good	–	–	$0.47^{+0.02}_{-0.01}$	$0.62^{+0.05}_{-0.05}$

table continues in next page...

Object ID	env.	z	M_B	$\log V_{\rm rot}$	inc	kin. dist.	T-type	mor. dist.	$r_{\rm d,emission}$	$r_{\rm extent}$	$r^{\rm HST}_{\rm d,phot}$	$r^{\rm VLT}_{\rm d,phot}$
1216361-1159014	f	0.4816	-21.23	$2.25^{+0.04}_{-0.05}$	72	good	5	bad	$0.89^{+0.06}_{-0.06}$	2.15	$0.79^{+0.02}_{-0.02}$	$0.93^{+0.02}_{-0.02}$
1216381-1203266	c	0.7939	-22.44	$2.39^{+0.04}_{-0.05}$	62	good	1	bad	$0.05^{+0.01}_{-0.01}$	0.80	$0.43^{+0.02}_{-0.02}$	$1.93^{+0.23}_{-0.40}$
1216403-1158254	f	0.2733	-16.26	$1.29^{+0.15}_{-0.27}$	67	good	3	bad	$0.20^{+0.10}_{-0.10}$	0.65	$0.53^{+0.07}_{-0.06}$	$0.49^{+0.07}_{-0.07}$
1216416-1158464	f	0.8644	-20.87	$1.22^{+0.39}_{-\infty}$	71	good	66	bad	$0.06^{+0.03}_{-0.02}$	0.80	$0.15^{+0.01}_{-0.01}$	$0.15^{+0.03}_{-0.04}$
1216434-1202128	c	0.7839	-21.86	$1.35^{+0.27}_{-0.73}$	74	good	11	good	$0.05^{+0.02}_{-0.01}$	0.97	$0.28^{+0.00}_{-0.00}$	$0.26^{+0.01}_{-0.01}$
1216440-1157516	c	0.7917	-21.12	–	41	bad	5	good	–	–	$0.37^{+0.02}_{-0.02}$	$0.33^{+0.01}_{-0.01}$
1216446-1202358	f	0.6698	-20.75	–	67	bad	-2	bad	–	–	$0.16^{+0.01}_{-0.01}$	$1.59^{+0.00}_{-0.07}$
1216447-1201282	c	0.7865	-22.24	$2.33^{+0.05}_{-0.04}$	44	good	6	good	$0.33^{+0.04}_{-0.03}$	1.61	$0.68^{+0.02}_{-0.02}$	$0.69^{+0.01}_{-0.01}$
1216452-1158200	f	0.2327	-18.35	$1.55^{+0.16}_{-0.25}$	73	good	3	bad	$0.10^{+0.02}_{-0.02}$	1.56	$0.21^{+0.00}_{-0.00}$	$0.21^{+0.01}_{-0.01}$
1216467-1159378	f	0.6669	-21.18	$1.69^{+0.27}_{-\infty}$	54	good	3	good	$0.05^{+0.04}_{-0.03}$	0.90	$0.19^{+0.00}_{-0.00}$	$1.27^{+0.11}_{-0.10}$
1216494-1159165	f	0.4082	-19.10	$1.91^{+0.06}_{-0.07}$	69	good	3	good	$0.16^{+0.02}_{-0.03}$	0.95	$0.24^{+0.01}_{-0.01}$	$0.18^{+0.01}_{-0.02}$
1216503-1159594	c	0.7906	-21.32	$2.08^{+0.05}_{-0.03}$	61	good	3	bad	$0.14^{+0.01}_{-0.01}$	1.04	$0.23^{+0.02}_{-0.01}$	$4.27^{+0.27}_{-0.27}$
1216504-1200120	f	0.9312	-21.22	$-0.32^{+1.94}_{-\infty}$	37	good	5	good	$0.03^{+0.03}_{-0.02}$	0.71	$0.27^{+0.01}_{-0.01}$	$0.21^{+0.02}_{-0.03}$
1216527-1202553	f	0.8263	-21.45	–	37	bad	-5	bad	–	–	$0.22^{+0.03}_{-0.02}$	$2.13^{+0.16}_{-0.42}$
1216533-1158540	f	0.4763	-20.48	$2.37^{+0.02}_{-0.02}$	49	good	5	good	$0.46^{+0.10}_{-0.10}$	0.69	$0.48^{+0.01}_{-0.01}$	$0.55^{+0.01}_{-0.01}$
1216537-1159276	f	0.2723	-17.99	$1.76^{+0.07}_{-0.09}$	53	good	3	bad	$0.32^{+0.02}_{-0.02}$	0.70	$0.28^{+0.02}_{-0.02}$	$0.32^{+0.02}_{-0.02}$
1216541-1157559	f	0.8748	-21.75	–	71	bad	-5	bad	–	–	$0.32^{+0.03}_{-0.03}$	$1.00^{+0.18}_{-0.14}$
1216548-1158039	f	0.9827	-21.46	–	36	bad	-5	–	–	–	$0.13^{+0.12}_{-0.05}$	$0.00^{+0.05}_{-0.00}$
1227440-1138591	f	0.5764	-19.26	$2.12^{+0.10}_{-0.12}$	33	good	1	bad	$0.30^{+0.02}_{-0.02}$	0.72	–	$1.98^{+0.26}_{-0.31}$
1227449-1138539	f	0.1731	-16.93	$1.05^{+0.36}_{-0.63}$	72	good	3	bad	$0.31^{+0.09}_{-0.09}$	1.94	–	$0.54^{+0.03}_{-0.05}$
1227462-1140319	g	0.5842	-20.60	$0.92^{+0.15}_{-0.30}$	30	good	4	bad	$0.64^{+0.02}_{-0.01}$	1.63	–	$0.50^{+0.02}_{-0.02}$
1227469-1139483	f	0.8342	-20.32	$1.97^{+0.03}_{-0.03}$	69	good	11	bad	$0.12^{+0.01}_{-0.01}$	1.82	–	$0.07^{+0.03}_{-0.02}$
1227475-1135475	g	0.5825	-21.87	$2.22^{+0.02}_{-0.02}$	81	good	5	bad	$0.75^{+0.04}_{-0.04}$	1.90	–	$0.89^{+0.04}_{-0.04}$
1227477-1136322	f	0.5588	-21.43	$1.96^{+0.02}_{-0.02}$	83	good	11	good	$0.35^{+0.03}_{-0.03}$	2.35	–	$0.42^{+0.03}_{-0.02}$
1227479-1140495	f	0.2137	-17.32	–	65	bad	3	bad	–	–	–	$0.71^{+0.04}_{-0.04}$

table continues in next page...

Object ID	env.	z	M_B	$\log V_{\rm rot}$	inc	kin. dist.	T-type	mor. dist.	$r_{\rm d,emission}$	$r_{\rm extent}$	$r_{\rm d,phot}^{\rm HST}$	$r_{\rm d,phot}^{\rm VLT}$
1227500-1136351	f	0.6796	-20.42	$2.29^{+0.01}_{-0.02}$	46	good	8	bad	$0.40^{+0.02}_{-0.01}$	1.70	–	$0.58^{+0.04}_{-0.03}$
1227503-1137253	f	0.2391	-17.52	$1.73^{+0.11}_{-0.13}$	35	good	3	bad	$0.14^{+0.05}_{-0.05}$	2.64	–	$0.87^{+0.13}_{-0.17}$
1227507-1139384	f	0.8725	-22.66	$1.58^{+0.39}_{-\infty}$	63	good	-5	bad	$0.02^{+0.02}_{-0.01}$	1.04	–	$1.66^{+0.12}_{-0.12}$
1227509-1135349	f	0.4899	-18.55	$1.53^{+0.11}_{-0.15}$	82	good	66	bad	$0.04^{+0.01}_{-0.01}$	0.70	–	$0.75^{+0.21}_{-0.19}$
1227524-1139108	f	1.0971	-22.11	–	36	bad	3	bad	–	–	–	$0.33^{+0.02}_{-0.02}$
1227531-1136325	f	0.5440	-20.29	$2.21^{+0.01}_{-0.01}$	63	good	9	good	$0.41^{+0.06}_{-0.06}$	3.37	–	$0.57^{+0.02}_{-0.02}$
1227537-1137447	f	0.7591	-21.03	$2.20^{+0.01}_{-0.02}$	42	good	6	good	$0.34^{+0.00}_{-0.00}$	1.53	–	$0.42^{+0.02}_{-0.02}$
1227539-1138211	f	0.4885	-20.49	$2.11^{+0.04}_{-0.04}$	44	good	5	good	$0.72^{+0.02}_{-0.02}$	1.70	–	$1.11^{+0.07}_{-0.04}$
1227546-1140238	f	0.6172	-19.48	$1.40^{+0.07}_{-0.07}$	78	good	9	bad	$0.22^{+0.02}_{-0.02}$	0.93	–	$0.89^{+0.20}_{-0.30}$
1227552-1137559	f	0.4893	-21.22	–	33	bad	-2	bad	–	–	–	$0.56^{+0.04}_{-0.05}$
1227554-1139178	c	0.6342	-20.56	$0.95^{+0.16}_{-0.33}$	56	good	4	good	$0.02^{+0.01}_{-0.01}$	0.76	–	$1.45^{+0.26}_{-0.52}$
1227558-1139556	f	0.4885	-21.42	$2.32^{+0.06}_{-0.06}$	51	good	3	bad	$0.49^{+0.06}_{-0.06}$	2.78	–	$1.22^{+0.03}_{-0.03}$
1227563-1137159	f	0.4460	-19.98	$1.06^{+0.12}_{-0.17}$	83	good	5	good	$0.20^{+0.01}_{-0.01}$	1.16	–	$0.37^{+0.03}_{-0.03}$
1227575-1137133	f	0.5453	-18.87	–	69	bad	3	bad	–	–	–	$2.76^{+0.18}_{-0.38}$
1227577-1137211	f	0.5451	-20.83	$2.46^{+0.03}_{-0.03}$	32	good	-5	bad	$0.51^{+0.04}_{-0.04}$	1.64	–	$1.97^{+0.09}_{-0.06}$
1227578-1136570	f	0.4679	-21.17	–	44	bad	1	good	–	–	–	$2.28^{+0.25}_{-0.16}$
1227582-1140248	f	0.5682	-21.33	$2.32^{+0.01}_{-0.01}$	49	good	3	bad	$0.70^{+0.04}_{-0.04}$	2.17	–	$0.73^{+0.02}_{-0.02}$
1227583-1140580	f	0.3427	-18.64	–	76	bad	–	–	–	–	–	$0.34^{+0.03}_{-0.02}$
1227585-1135120	f	0.8381	-23.69	$2.16^{+0.01}_{-0.01}$	80	good	11	good	$0.42^{+0.01}_{-0.01}$	1.64	–	$1.21^{+0.12}_{-0.11}$
1227586-1138496	f	0.8295	-20.25	$2.19^{+0.03}_{-0.03}$	57	good	66	good	$0.17^{+0.02}_{-0.02}$	1.02	–	$0.33^{+0.03}_{-0.03}$
1227589-1135135	c	0.6375	-22.91	–	60	bad	-5	bad	–	–	–	$1.89^{+0.06}_{-0.11}$
1227599-1139341	f	0.3640	-19.19	$1.59^{+0.05}_{-0.05}$	33	good	11	good	$0.36^{+0.08}_{-0.08}$	2.47	–	$0.67^{+0.02}_{-0.02}$
1228001-1136095	c	0.6325	-21.74	$2.31^{+0.02}_{-0.02}$	51	good	5	good	$0.86^{+0.07}_{-0.07}$	1.84	–	$0.82^{+0.02}_{-0.01}$
1228003-1135243	c	0.6376	-19.88	–	55	bad	1	–	–	–	–	$3.62^{+0.08}_{-0.18}$
1228006-1139294	f	0.8377	–	$1.89^{+0.03}_{-0.03}$	84	good	66	good	$0.34^{+0.04}_{-0.04}$	0.95	–	$0.74^{+0.04}_{-0.04}$

table continues in next page...

Object ID	env.	z	M_B	$\log V_{\rm rot}$	inc	kin. dist.	T-type	mor. dist.	$r_{\rm d,emission}$	$r_{\rm extent}$	$r^{\rm HST}_{\rm d,phot}$	$r^{\rm VLT}_{\rm d,phot}$
1228011-1138547	f	0.8814	-22.38	$2.38^{+0.02}_{-0.01}$	73	good	5	bad	$0.52^{+0.02}_{-0.02}$	1.51	–	$0.65^{+0.03}_{-0.04}$
1228021-1135252	f	0.5434	-19.92	$1.80^{+0.14}_{-0.22}$	73	good	8	bad	$0.44^{+0.03}_{-0.02}$	1.05	–	$0.57^{+0.07}_{-0.06}$
1228026-1139163	f	0.3431	-17.46	$1.05^{+0.30}_{-\infty}$	43	good	-5	bad	$0.02^{+0.01}_{-0.01}$	1.39	–	$0.02^{+0.04}_{-0.02}$
1228031-1140406	f	0.7712	-21.62	$2.40^{+0.03}_{-0.03}$	32	good	4	bad	$0.75^{+0.04}_{-0.04}$	1.77	–	$0.59^{+0.01}_{-0.01}$
1228034-1136367	f	0.6792	-21.15	$1.82^{+0.05}_{-0.05}$	76	good	66	good	$0.43^{+0.04}_{-0.04}$	1.37	–	$0.56^{+0.03}_{-0.02}$
1232274-1251372	f	0.1467	-15.28	$1.52^{+0.12}_{-0.13}$	40	good	-2	bad	$0.12^{+0.01}_{-0.02}$	1.11	$0.25^{+0.01}_{-0.01}$	$1.23^{+0.16}_{-0.41}$
1232288-1250490	c	0.5470	-22.30	–	71	bad	-2	bad	–	–	$0.44^{+0.01}_{-0.02}$	$1.45^{+0.08}_{-0.06}$
1232291-1253326	f	0.0695	-15.34	$1.71^{+0.10}_{-0.22}$	79	good	7	bad	$0.49^{+0.05}_{-0.05}$	1.11	$0.62^{+0.02}_{-0.01}$	$0.57^{+0.02}_{-0.02}$
1232296-1250119	c	0.5509	-22.77	–	73	bad	3	bad	–	–	$0.69^{+0.01}_{-0.01}$	$3.55^{+0.83}_{-1.16}$
1232308-1250297	f	0.9534	-24.23	–	70	bad	11	good	–	–	$0.45^{+0.02}_{-0.02}$	$5.84^{+0.26}_{-0.31}$
1232310-1252396	f	0.1138	-17.76	$1.73^{+0.03}_{-0.03}$	77	good	3	bad	$0.23^{+0.01}_{-0.01}$	1.58	$0.33^{+0.00}_{-0.00}$	$0.96^{+0.02}_{-0.04}$
1232327-1249057	c	0.5327	-21.42	$2.32^{+0.01}_{-0.00}$	66	good	5	good	$0.63^{+0.05}_{-0.05}$	3.21	$0.60^{+0.01}_{-0.01}$	$0.76^{+0.02}_{-0.01}$
1232352-1253514	f	0.7861	-21.19	$1.30^{+0.63}_{-\infty}$	58	good	11	good	$0.04^{+0.03}_{-0.03}$	0.80	$0.31^{+0.01}_{-0.02}$	$0.27^{+0.01}_{-0.01}$
1232365-1253142	f	0.5616	-18.65	$1.48^{+0.31}_{-\infty}$	70	good	–	–	$0.09^{+0.04}_{-0.04}$	2.39	$0.11^{+0.01}_{-0.01}$	$2.04^{+0.71}_{-1.00}$
1232373-1249247	f	0.6778	-21.84	$2.10^{+0.06}_{-0.07}$	67	good	2	good	$0.12^{+0.01}_{-0.01}$	1.34	$0.29^{+0.06}_{-0.05}$	$0.54^{+0.02}_{-0.02}$
1232393-1253463	c	0.5364	-20.54	$0.94^{+0.36}_{-\infty}$	37	good	4	good	$0.60^{+0.10}_{-0.10}$	1.21	–	$0.70^{+0.02}_{-0.03}$
1232401-1253286	f	0.3818	-20.96	$2.14^{+0.00}_{-0.01}$	59	good	11	good	$0.44^{+0.01}_{-0.01}$	1.36	$0.38^{+0.00}_{-0.00}$	$0.55^{+0.01}_{-0.01}$
1238335-1145205	c	0.4581	-21.08	$2.21^{+0.06}_{-0.09}$	68	good	–	–	$0.23^{+0.07}_{-0.07}$	1.42	–	$0.40^{+0.02}_{-0.02}$
1238389-1142283	f	0.5717	-21.85	–	72	bad	–	–	–	–	–	$0.70^{+0.02}_{-0.01}$
1238389-1142581	f	1.0551	-24.88	–	82	bad	–	–	–	–	–	$0.29^{+0.04}_{-0.03}$
1301302-1138187	c	0.4856	-21.12	–	62	bad	–	–	–	–	–	$0.83^{+0.23}_{-0.14}$
1301331-1142531	f	0.5321	-20.62	$2.01^{+0.05}_{-0.06}$	36	good	–	–	$0.19^{+0.04}_{-0.04}$	1.14	–	$0.39^{+0.02}_{-0.02}$
1301334-1142027	c	0.4796	-20.05	$1.69^{+0.11}_{-0.15}$	50	good	–	–	$0.20^{+0.06}_{-0.06}$	1.09	–	$0.46^{+0.02}_{-0.01}$
1301342-1141340	c	0.4819	-21.22	$1.67^{+0.10}_{-0.13}$	80	good	–	–	$0.26^{+0.05}_{-0.05}$	1.23	–	$0.64^{+0.03}_{-0.03}$
1301346-1139174	g	0.3974	-20.16	$1.72^{+0.16}_{-0.24}$	78	good	–	–	$0.11^{+0.04}_{-0.03}$	0.52	–	$0.43^{+0.02}_{-0.02}$

table continues in next page...

Object ID	env.	z	M_B	$\log V_{\rm rot}$	inc	kin. dist.	T-type	mor. dist.	$r_{\rm d,emission}$	$r_{\rm extent}$	$r^{\rm HST}_{\rm d,phot}$	$r^{\rm VLT}_{\rm d,phot}$
1301351-1138356	g	0.3976	-22.66	–	52	bad	–	–	–	–	–	$2.93^{+0.03}_{-0.04}$
1301354-1138499	f	0.5246	-20.73	–	39	bad	–	–	–	–	–	$2.38^{+0.41}_{-0.14}$
1301358-1138292	g	0.4004	-20.82	–	57	bad	–	–	–	–	–	$0.80^{+0.01}_{-0.01}$
1301363-1138494	c	0.4787	-21.21	–	73	bad	–	–	–	–	–	$1.04^{+0.10}_{-0.12}$
1301365-1142453	f	0.1224	-19.82	–	77	bad	–	–	–	–	–	$1.23^{+0.01}_{-0.01}$
1301375-1138121	c	0.4882	-20.40	$1.80^{+0.10}_{-0.16}$	46	good	–	–	$0.36^{+0.05}_{-0.05}$	0.97	–	$0.74^{+0.03}_{-0.02}$
1301376-1141351	f	0.9503	-23.49	$2.03^{+0.05}_{-0.05}$	76	good	–	–	$0.39^{+0.02}_{-0.02}$	1.18	–	$0.60^{+0.02}_{-0.02}$
1301396-1139493_A	g	0.3971	–	–	83	bad	–	–	–	–	–	$1.32^{+0.04}_{-0.03}$
1301396-1139493_B	g	0.3984	–	–	83	bad	–	–	–	–	–	$1.32^{+0.04}_{-0.03}$
1301397-1139048	c	0.4795	-21.81	–	42	bad	–	–	–	–	–	$0.30^{+0.09}_{-0.29}$
1301402-1139229	c	0.4828	-22.92	–	54	bad	–	–	–	–	–	$3.11^{+0.03}_{-0.03}$
1301433-1142540	f	0.2038	-18.51	$1.83^{+0.05}_{-0.05}$	56	good	–	–	$0.30^{+0.02}_{-0.02}$	1.01	–	$0.33^{+0.01}_{-0.01}$
1301437-1142174	f	0.6568	-23.19	–	80	bad	–	–	–	–	–	$1.43^{+0.03}_{-0.04}$
1301443-1137153	f	0.6530	-22.39	$2.23^{+0.01}_{-0.01}$	41	good	–	–	$0.96^{+0.07}_{-0.07}$	2.14	–	$0.91^{+0.01}_{-0.01}$
1301445-1137184	f	0.4982	-20.29	–	58	bad	–	–	–	–	–	$0.25^{+0.03}_{-0.05}$
1301451-1140490	f	0.5881	-20.04	$1.79^{+0.27}_{-\infty}$	57	good	–	–	$0.16^{+0.04}_{-0.06}$	0.89	–	$0.38^{+0.02}_{-0.02}$
1352525-1135470	f	0.7518	-21.37	$1.32^{+0.26}_{-\infty}$	46	good	–	–	$0.33^{+0.02}_{-0.02}$	1.07	–	$0.43^{+0.02}_{-0.02}$
1352526-1135242	f	0.2138	-18.49	–	49	bad	–	–	–	–	–	$1.09^{+0.03}_{-0.03}$
1352567-1137080	f	0.6292	-20.68	–	72	bad	–	–	–	–	–	$1.79^{+0.40}_{-0.21}$
1352588-1136193	f	0.7507	-22.00	$2.06^{+0.03}_{-0.03}$	73	good	–	–	$0.37^{+0.01}_{-0.01}$	1.47	–	$0.50^{+0.02}_{-0.02}$
1352599-1136503	f	0.8368	-21.77	$2.11^{+0.02}_{-0.02}$	61	good	–	–	$0.21^{+0.01}_{-0.01}$	1.47	–	$0.34^{+0.02}_{-0.02}$
1353007-1137288	f	0.2064	-18.47	$1.69^{+0.10}_{-0.19}$	70	good	–	–	$0.26^{+0.04}_{-0.05}$	1.60	–	$0.68^{+0.02}_{-0.01}$
1353012-1137400	c	0.5811	-20.98	$2.11^{+0.04}_{-0.05}$	72	good	–	–	$0.31^{+0.01}_{-0.01}$	1.67	–	$0.39^{+0.02}_{-0.02}$
1353014-1139521	f	0.4238	-20.82	$2.07^{+0.05}_{-0.07}$	74	good	–	–	$0.30^{+0.04}_{-0.04}$	1.16	–	$0.39^{+0.01}_{-0.01}$
1353019-1136413	f	0.7501	-21.97	$2.35^{+0.02}_{-0.01}$	68	good	–	–	$0.33^{+0.02}_{-0.01}$	1.25	–	$0.42^{+0.02}_{-0.01}$

table continues in next page...

Object ID	env.	z	M_B	$\log V_{\rm rot}$	inc	kin. dist.	T-type	mor. dist.	$r_{\rm d,emission}$	$r_{\rm extent}$	$r^{\rm HST}_{\rm d,phot}$	$r^{\rm VLT}_{\rm d,phot}$
1353026-1139464	f	0.6439	-21.61	–	71	bad	–	–	–	–	–	$0.68^{+0.02}_{-0.01}$
1353027-1138441	f	0.5619	-20.73	$1.90^{+0.05}_{-0.06}$	64	good	–	–	$0.50^{+0.06}_{-0.06}$	1.33	–	$0.79^{+0.04}_{-0.04}$
1353032-1137207	c	0.5920	-20.83	$1.85^{+0.07}_{-0.07}$	69	good	–	–	$0.14^{+0.03}_{-0.03}$	0.82	–	$0.34^{+0.02}_{-0.02}$
1353054-1139222	f	0.4504	-20.46	$1.88^{+0.15}_{-0.22}$	42	good	–	–	$0.35^{+0.05}_{-0.05}$	1.58	–	$1.70^{+0.50}_{-0.25}$
1353060-1141006	f	0.8095	-21.15	$2.01^{+0.03}_{-0.03}$	53	good	–	–	$0.22^{+0.01}_{-0.01}$	1.53	–	$0.45^{+0.03}_{-0.02}$
1353123-1138095	c	0.5916	-20.22	$1.76^{+0.14}_{-0.22}$	58	good	–	–	$0.14^{+0.07}_{-0.04}$	0.43	–	$0.28^{+0.01}_{-0.02}$
1353591-1231311	c	0.5989	-19.62	–	53	bad	–	–	–	–	–	$0.30^{+0.02}_{-0.02}$
1354003-1230138	f	0.6616	-20.91	–	72	bad	4	bad	–	–	$0.38^{+0.01}_{-0.02}$	$0.50^{+0.03}_{-0.03}$
1354009-1233233	f	0.6622	-21.30	$2.41^{+0.02}_{-0.02}$	41	good	3	bad	$0.26^{+0.01}_{-0.00}$	1.01	$0.28^{+0.00}_{-0.00}$	$0.30^{+0.01}_{-0.01}$
1354016-1232406	f	0.5247	-22.25	$2.16^{+0.01}_{-0.02}$	57	good	66	good	$0.25^{+0.01}_{-0.01}$	1.91	$0.54^{+0.01}_{-0.02}$	$1.44^{+0.02}_{-0.03}$
1354022-1234283	c	0.7711	-20.29	–	44	bad	-5	bad	–	–	$0.08^{+0.01}_{-0.01}$	$0.03^{+0.02}_{-0.03}$
1354030-1229397	f	0.2996	-15.97	–	43	bad	–	–	–	–	–	$0.00^{+0.19}_{-0.00}$
1354049-1234087	f	0.6617	-20.89	$2.48^{+0.03}_{-0.03}$	47	good	-5	bad	$0.36^{+0.02}_{-0.04}$	1.35	$0.23^{+0.01}_{-0.01}$	$2.39^{+0.54}_{-0.42}$
1354052-1233490	f	0.5142	-19.51	$2.09^{+0.14}_{-0.15}$	32	good	4	good	$0.13^{+0.05}_{-0.05}$	0.76	$0.24^{+0.01}_{-0.01}$	$0.24^{+0.01}_{-0.01}$
1354055-1234136	f	0.5142	-21.47	$2.39^{+0.07}_{-0.13}$	54	good	-5	bad	$0.10^{+0.03}_{-0.03}$	0.28	$0.64^{+0.01}_{-0.02}$	$1.48^{+0.04}_{-0.07}$
1354057-1235043	f	0.3892	-16.18	–	40	bad	–	–	–	–	–	$0.85^{+0.85}_{-0.85}$
1354073-1233336	c	0.7670	-19.95	$2.17^{+0.02}_{-0.04}$	42	good	-5	bad	$0.22^{+0.01}_{-0.01}$	0.94	$0.17^{+0.01}_{-0.01}$	$0.21^{+0.07}_{-0.02}$
1354074-1233206	f	0.8177	-20.35	$2.22^{+0.01}_{-0.01}$	46	good	-5	bad	$0.12^{+0.00}_{-0.00}$	0.86	$0.13^{+0.01}_{-0.01}$	$0.00^{+0.05}_{-0.00}$
1354095-1229021	f	0.7085	-20.88	$2.08^{+0.05}_{-0.06}$	65	good	11	good	$0.33^{+0.04}_{-0.04}$	1.15	$0.41^{+0.03}_{-0.02}$	$0.43^{+0.03}_{-0.03}$
1354095-1233132	f	0.6167	-22.14	$2.02^{+0.02}_{-0.02}$	64	good	5	bad	$0.60^{+0.06}_{-0.06}$	2.46	$0.32^{+0.08}_{-0.05}$	$9.22^{+0.44}_{-0.63}$
1354104-1230539	c	0.7601	-20.78	–	55	bad	3	bad	–	–	$0.27^{+0.01}_{-0.02}$	$0.23^{+0.04}_{-0.05}$
1354107-1231236	f	0.6183	-21.96	–	77	bad	-2	bad	–	–	$0.19^{+0.00}_{-0.00}$	$0.07^{+0.05}_{-0.01}$
1354111-1230243	f	0.7085	-21.33	$2.34^{+0.03}_{-0.04}$	58	good	1	good	$0.34^{+0.03}_{-0.03}$	2.36	$0.50^{+0.01}_{-0.01}$	$0.55^{+0.02}_{-0.02}$
1354118-1232499	c	0.5946	-21.26	$2.33^{+0.06}_{-0.07}$	57	good	4	bad	$0.37^{+0.03}_{-0.03}$	1.13	$0.39^{+0.00}_{-0.00}$	$0.47^{+0.02}_{-0.01}$
1354119-1234485	f	0.7302	-21.65	$2.24^{+0.02}_{-0.02}$	33	good	4	good	$0.32^{+0.03}_{-0.03}$	2.88	$0.30^{+0.00}_{-0.00}$	$0.34^{+0.01}_{-0.01}$

table continues in next page...

Object ID	env.	z	M_B	$\log V_{\rm rot}$	inc	kin. dist.	T-type	mor. dist.	$r_{\rm d,emission}$	$r_{\rm extent}$	$r^{\rm HST}_{\rm d,phot}$	$r^{\rm VLT}_{\rm d,phot}$
1354127-1233241	c	0.7627	-22.21	$2.23^{+0.07}_{-0.07}$	82	good	5	good	$0.65^{+0.08}_{-0.07}$	2.02	$0.79^{+0.06}_{-0.19}$	$0.76^{+0.03}_{-0.04}$
1354129-1229280	f	0.1995	-17.22	$2.16^{+0.03}_{-0.03}$	72	good	2	bad	$0.44^{+0.03}_{-0.03}$	1.42	$0.40^{+0.01}_{-0.01}$	$0.47^{+0.04}_{-0.03}$
1354139-1229474	f	0.6865	-22.05	–	74	bad	-5	bad	–	–	$0.88^{+0.04}_{-0.08}$	$0.05^{+0.00}_{-0.01}$
1354140-1233159	c	0.5971	-20.81	$2.26^{+0.08}_{-0.09}$	68	good	7	bad	$0.52^{+0.20}_{-0.20}$	2.41	$0.61^{+0.02}_{-0.03}$	$0.71^{+0.04}_{-0.03}$
1354142-1229132	f	0.3249	-19.52	$1.96^{+0.07}_{-0.09}$	60	good	1	good	$0.33^{+0.02}_{-0.02}$	1.35	$0.33^{+0.00}_{-0.00}$	$0.43^{+0.02}_{-0.02}$
1354144-1228536_A	f	0.8245	–	–	36	bad	-5	–	–	–	$0.47^{+0.02}_{-0.02}$	$0.60^{+0.03}_{-0.04}$
1354144-1228536_B	f	0.8243	–	–	36	bad	-5	–	–	–	$0.47^{+0.02}_{-0.02}$	$0.60^{+0.03}_{-0.04}$
1354144-1231514	c	0.5946	-21.21	–	47	bad	1	good	–	–	$0.49^{+0.01}_{-0.01}$	$0.67^{+0.02}_{-0.01}$
1354145-1229101	f	1.1038	-22.05	$1.80^{+0.08}_{-0.08}$	55	good	1	bad	$0.17^{+0.01}_{-0.00}$	0.81	$0.22^{+0.01}_{-0.01}$	$0.18^{+0.06}_{-0.07}$
1354148-1228392_A	f	0.3647	–	$0.98^{+0.11}_{-0.15}$	43	good	11	–	$0.09^{+0.00}_{-0.00}$	1.39	$0.42^{+0.10}_{-0.07}$	$0.97^{+0.03}_{-0.04}$
1354148-1228392_B	f	0.3643	–	$-0.18^{+1.05}_{-\infty}$	43	good	11	–	$0.08^{+0.02}_{-0.02}$	0.88	$0.42^{+0.10}_{-0.07}$	$0.97^{+0.03}_{-0.04}$
1354164-1231599	c	0.5937	-22.18	$2.54^{+0.03}_{-0.03}$	77	good	5	bad	$1.02^{+0.10}_{-0.07}$	1.35	$0.85^{+0.03}_{-0.03}$	$1.25^{+0.04}_{-0.03}$
1354169-1230098	f	0.8199	-21.32	$2.33^{+0.04}_{-0.07}$	50	good	4	good	$0.17^{+0.02}_{-0.03}$	2.27	$0.22^{+0.02}_{-0.03}$	$0.55^{+0.04}_{-0.05}$
1354173-1233490	f	0.9061	-22.53	$2.26^{+0.02}_{-0.02}$	82	good	6	bad	$0.48^{+0.03}_{-0.02}$	1.43	$0.75^{+0.11}_{-0.07}$	$0.68^{+0.05}_{-0.05}$
1354176-1232261	f	0.4779	-20.50	$2.54^{+0.01}_{-0.01}$	36	good	-5	bad	$0.40^{+0.01}_{-0.01}$	1.25	$0.13^{+0.00}_{-0.00}$	$0.33^{+0.02}_{-0.02}$
1354180-1232048	f	1.1792	-24.86	–	65	bad	66	bad	–	–	$0.35^{+0.09}_{-0.09}$	$3.29^{+0.14}_{-0.12}$
1354180-1232242	f	0.7888	-20.34	$2.00^{+0.08}_{-0.11}$	46	good	11	bad	$0.24^{+0.03}_{-0.03}$	0.67	$0.24^{+0.01}_{-0.01}$	$0.30^{+0.03}_{-0.03}$
1354183-1231396	f	0.3753	-19.09	$1.53^{+0.08}_{-0.11}$	67	good	3	bad	$0.24^{+0.02}_{-0.01}$	0.55	$0.48^{+0.02}_{-0.02}$	$0.55^{+0.03}_{-0.02}$
1354184-1233370	f	0.6851	-20.41	$2.31^{+0.04}_{-0.04}$	65	good	5	bad	$0.46^{+0.03}_{-0.03}$	1.64	$0.40^{+0.03}_{-0.04}$	$0.47^{+0.04}_{-0.05}$
1354185-1234431	f	0.9092	–	–	85	bad	-5	bad	–	–	$1.01^{+0.15}_{-0.23}$	$0.12^{+0.07}_{-0.07}$
1354189-1233335	f	0.5252	-20.28	–	63	bad	66	bad	–	–	$0.40^{+0.21}_{-0.29}$	$0.56^{+0.02}_{-0.03}$
1354190-1234440	f	0.7298	–	$2.20^{+0.13}_{-0.19}$	43	good	4	bad	$0.09^{+0.04}_{-0.04}$	1.03	$0.45^{+0.02}_{-0.02}$	$1.71^{+0.15}_{-0.10}$
1354194-1233588	f	0.3608	-21.21	$2.29^{+0.02}_{-0.02}$	69	good	3	good	$0.49^{+0.01}_{-0.01}$	2.36	$0.46^{+0.01}_{-0.01}$	$1.25^{+0.10}_{-0.15}$
1410579-1147529	f	0.9296	–	$1.30^{+0.06}_{-0.09}$	74	good	–	–	$0.19^{+0.00}_{-0.00}$	1.39	–	$1.14^{+0.06}_{-0.06}$
1410587-1147390	f	0.3208	-20.61	–	75	bad	–	–	–	–	–	$0.64^{+0.01}_{-0.02}$

table continues in next page...

Object ID	env.	z	M_B	$\log V_{\rm rot}$	inc	kin. dist.	T-type	mor. dist.	$r_{\rm d,emission}$	$r_{\rm extent}$	$r^{\rm HST}_{\rm d,phot}$	$r^{\rm VLT}_{\rm d,phot}$
1411021-1147061	c	0.5239	-20.44	–	79	bad	–	–	–	–	–	$0.36^{+0.04}_{-0.03}$
1411025-1148084	f	0.8051	-22.16	$1.76^{+0.02}_{-0.02}$	54	good	–	–	$0.38^{+0.00}_{-0.00}$	1.75	–	$0.43^{+0.03}_{-0.03}$
1411028-1147006	c	0.5202	-21.58	$1.73^{+0.05}_{-0.05}$	32	good	–	–	$0.55^{+0.02}_{-0.02}$	1.65	–	$0.46^{+0.01}_{-0.01}$
1411043-1151253	c	0.5209	–	–	67	bad	–	–	–	–	–	$0.59^{+0.01}_{-0.01}$
1411055-1150350	f	0.7642	-21.68	$2.31^{+0.03}_{-0.02}$	62	good	–	–	$0.20^{+0.01}_{-0.01}$	1.02	–	$0.23^{+0.05}_{-0.02}$
1411058-1148128	f	0.4474	-20.30	$2.08^{+0.03}_{-0.04}$	74	good	–	–	$0.33^{+0.01}_{-0.01}$	1.23	–	$0.46^{+0.04}_{-0.07}$
1411062-1149068	f	0.3500	-20.56	$2.38^{+0.02}_{-0.02}$	53	good	–	–	$0.64^{+0.04}_{-0.04}$	1.58	–	$0.69^{+0.02}_{-0.02}$
1411063-1152001	f	0.3183	-18.13	–	51	bad	–	–	–	–	–	$0.17^{+0.06}_{-0.04}$
1411064-1150009	c	0.5209	-21.55	–	74	bad	–	–	–	–	–	$0.73^{+0.06}_{-0.05}$
1411066-1150498	f	0.4907	-20.66	$1.94^{+0.09}_{-0.12}$	54	good	–	–	$0.14^{+0.08}_{-0.08}$	0.97	–	$2.81^{+0.31}_{-0.36}$
1411084-1151070	f	0.4886	-21.56	$2.24^{+0.04}_{-0.04}$	72	good	–	–	$0.29^{+0.04}_{-0.04}$	0.63	–	$0.85^{+0.04}_{-0.05}$
1411091-1150276	f	0.2487	-18.65	–	81	bad	–	–	–	–	–	$0.59^{+0.02}_{-0.02}$
1411097-1147469	f	0.3918	-22.07	$2.42^{+0.03}_{-0.02}$	84	good	–	–	$0.51^{+0.08}_{-0.07}$	1.57	–	$1.37^{+0.05}_{-0.05}$
1411121-1146450	f	0.8383	-22.57	$1.58^{+0.50}_{-\infty}$	49	good	–	–	$0.06^{+0.04}_{-0.03}$	0.85	–	$1.50^{+0.13}_{-0.17}$
1411123-1149223	f	0.5714	-20.28	$2.33^{+0.08}_{-0.15}$	51	good	–	–	$0.57^{+0.12}_{-0.13}$	0.55	–	$0.29^{+0.02}_{-0.02}$
1411143-1149091	f	0.4287	-19.81	$0.22^{+0.63}_{-\infty}$	48	good	–	–	$0.03^{+0.01}_{-0.01}$	0.55	–	$0.29^{+0.04}_{-0.04}$
1411143-1149241	f	0.4291	-21.09	–	52	bad	–	–	–	–	–	$0.93^{+0.02}_{-0.02}$
1411149-1151143	f	0.4878	-19.56	$2.20^{+0.04}_{-0.05}$	33	good	–	–	$0.22^{+0.03}_{-0.04}$	1.00	–	$0.34^{+0.01}_{-0.02}$
1420094-1235510	f	0.6081	-22.69	–	38	bad	–	–	–	–	–	$3.48^{+0.11}_{-0.11}$
1420098-1235111	f	0.6078	-21.20	$1.86^{+0.14}_{-0.22}$	44	good	–	–	$0.18^{+0.06}_{-0.06}$	1.25	–	$0.39^{+0.03}_{-0.02}$
1420110-1235169	f	0.3745	-21.24	$2.26^{+0.03}_{-0.03}$	59	good	–	–	$0.39^{+0.03}_{-0.03}$	1.16	–	$0.81^{+0.01}_{-0.01}$
1420112-1234124	f	0.9189	-23.17	–	60	bad	–	–	–	–	–	$1.51^{+0.19}_{-0.14}$
1420115-1234206_A	f	0.6089	–	$2.41^{+0.05}_{-0.06}$	47	good	–	–	$0.86^{+0.09}_{-0.08}$	1.90	–	$1.08^{+0.02}_{-0.02}$
1420115-1234206_B	f	0.6079	–	$2.37^{+0.05}_{-0.05}$	47	good	–	–	$0.81^{+0.10}_{-0.09}$	2.40	–	$1.08^{+0.02}_{-0.02}$
1420118-1234482	f	0.4366	-20.67	$1.26^{+0.23}_{-0.30}$	75	good	–	–	$0.07^{+0.03}_{-0.03}$	0.61	–	$0.55^{+0.02}_{-0.01}$

table continues in next page...

Object ID	env.	z	M_B	$\log V_{\rm rot}$	inc	kin. dist.	T-type	mor. dist.	$r_{\rm d,emission}$	$r_{\rm extent}$	$r^{\rm HST}_{\rm d,phot}$	$r^{\rm VLT}_{\rm d,phot}$
1420120-1234427	f	0.9210	-22.67	$2.05^{+0.14}_{-0.25}$	83	good	–	–	$0.09^{+0.04}_{-0.03}$	0.99	–	$5.33^{+0.08}_{-0.39}$
1420124-1233148	f	0.2881	-19.87	$2.08^{+0.04}_{-0.04}$	71	good	–	–	$0.41^{+0.02}_{-0.02}$	2.42	–	$0.60^{+0.02}_{-0.02}$
1420133-1234428	f	0.5416	-21.44	$2.40^{+0.03}_{-0.03}$	73	good	–	–	$0.33^{+0.04}_{-0.04}$	1.39	–	$0.46^{+0.02}_{-0.02}$
1420163-1237563	f	0.6886	-22.23	$1.09^{+0.87}_{-\infty}$	39	good	–	–	$0.07^{+0.06}_{-0.05}$	0.25	–	$0.03^{+0.02}_{-0.03}$
1420173-1233083	f	0.6315	-21.58	$2.03^{+0.11}_{-0.12}$	52	good	–	–	$0.47^{+0.08}_{-0.11}$	1.52	–	$0.71^{+0.01}_{-0.02}$
1420175-1233271	g	0.4982	-22.14	–	56	bad	–	–	–	–	–	$0.86^{+0.03}_{-0.04}$
1420185-1238207	f	0.8576	-23.09	–	76	bad	–	–	–	–	–	$0.89^{+0.06}_{-0.07}$
1420240-1235589	f	0.7207	-22.47	–	58	bad	–	–	–	–	–	$0.96^{+0.06}_{-0.05}$

Bibliography

Abadi M. G., Moore B., Bower R. G., 1999. MNRAS, **308**, 947.

Aragón-Salamanca A., Ellis R. S., Couch W. J., Carter D., 1993. MNRAS, **262**, 764.

Aragón-Salamanca A., Bedregal A. G., Merrifield M. R., 2006. A&A, **458**, 101.

Arimoto N., Yoshii Y., 1987. A&A, **173**, 23.

Böhm A. *et al.*, 2004. A&A, **420**, 97.

Baldry I. K., Balogh M. L., Bower R. G., Glazebrook K., Nichol R. C., Bamford S. P., Budavari T., 2006. MNRAS, **373**, 469.

Balogh M. L., Navarro J. F., Morris S. L., 2000. ApJ, **540**, 113.

Bamford S. P., Aragón-Salamanca A., Milvang-Jensen B., 2006. MNRAS, **366**, 308.

Bamford S. P., Milvang-Jensen B., Aragón-Salamanca A., Simard L., 2005. MNRAS, **361**, 109.

Bamford S. P., Nichol R. C., Baldry I. K., Land K., Lintott C. J., Schawinski K., Slosar A., Szalay A. S., Thomas D., Torki M., Andreescu D., Edmondson E. M., Miller C. J., Murray P., Raddick M. J., Vandenberg J., 2009. MNRAS, **393**, 1324.

Bamford S. P., Milvang-Jensen B., Aragón-Salamanca A., 2007. MNRAS, **378**, L6.

Bamford S. P., 2006. *PhD thesis*, School of Physics and Astronomy, University of Nottingham, Nottingham, NG7 2RD, UK.

Barr J. M., Bedregal A. G., Aragón-Salamanca A., Merrifield M. R., Bamford S. P., 2007. A&A, **470**, 173.

Baum W. A., 1959. PASP, **71**, 106.

Bedregal A. G., Aragón-Salamanca A., Merrifield M. R., 2006. MNRAS, **373**, 1125.

Bekki K., Couch W. J., 2003. ApJ, **596**, L13.

Bekki K., Couch W. J., Shioya Y., 2001. PASJ, **53**, 395.

Bekki K., Couch W. J., Shioya Y., 2002. ApJ, **577**, 651.

Bekki K., 1998. ApJ, **502**, L133.

Bell E. F., de Jong R. S., 2001. ApJ, **550**, 212.

Bell E. F. *et al.*, 2005. ApJ, **625**, 23.

Bernardi M., Sheth R. K., Nichol R. C., Schneider D. P., Brinkmann J., 2005. AJ, **129**, 61.

Blakeslee J. P., Franx M., Postman M., Rosati P., Holden B. P., Illingworth G. D., Ford H. C., Cross N. J. G., Gronwall C., Benítez N., Bouwens R. J., Broadhurst T. J., Clampin M., Demarco R., Golimowski D. A., Hartig G. F., Infante L., Martel A. R., Miley G. K., Menanteau F., Meurer G. R., Sirianni M., White R. L., 2003. ApJ, **596**, L143.

Blakeslee J. P., Holden B. P., Franx M., Rosati P., Bouwens R. J., Demarco R., Ford H. C., Homeier N. L., Illingworth G. D., Jee M. J., Mei S., Menanteau F., Meurer G. R., Postman M., Tran K., 2006. ApJ, **644**, 30.

Blanton M. R., Roweis S., 2007. AJ, **133**, 734.

Bolzonella M., Kovač K., Pozzetti L., Zucca E., Cucciati O., Lilly S. J., Peng Y., Iovino A., Zamorani G., Vergani D., Tasca L. A. M., Lamareille F., Oesch P., Caputi K., Kampczyk P., Bardelli S., Maier C., Abbas U., Knobel C., Scodeggio M., Carollo C. M., Contini T., Kneib J., Le Fèvre O., Mainieri V., Renzini A., Bongiorno A., Coppa G., de la Torre S., de Ravel L., Franzetti P., Garilli B., Le Borgne J., Le Brun V., Mignoli M., Pelló R., Perez-Montero E., Ricciardelli E., Silverman J. D., Tanaka M., Tresse L., Bottini D., Cappi A., Cassata P., Cimatti A., Guzzo L., Koekemoer A. M., Leauthaud A., Maccagni D., Marinoni C., McCracken H. J., Memeo P., Meneux B., Porciani C., Scaramella R., Aussel H., Capak P., Halliday C., Ilbert O., Kartaltepe J., Salvato M., Sanders D., Scarlata C., Scoville N., Taniguchi Y., Thompson D., 2010. A&A, **524**, A76+.

Borch A., Meisenheimer K., Bell E. F., Rix H., Wolf C., Dye S., Kleinheinrich M., Kovacs Z., Wisotzki L., 2006. A&A, **453**, 869.

Borgani S., Girardi M., Carlberg R. G., Yee H. K. C., Ellingson E., 1999. ApJ, **527**, 561.

Boselli A., Gavazzi G., 2006. PASP, **118**, 517.

Bower R. G., Lucey J. R., Ellis R. S., 1992. MNRAS, **254**, 601.

Bruzual G., Charlot S., 2003. MNRAS, **344**, 1000.

Bundy K., Ellis R. S., Conselice C. J., 2005. ApJ, **625**, 621.

Bundy K., Ellis R. S., Conselice C. J., Taylor J. E., Cooper M. C., Willmer C. N. A., Weiner B. J., Coil A. L., Noeske K. G., Eisenhardt P. R. M., 2006. ApJ, **651**, 120.

Butcher H., Oemler, Jr. A., 1984. ApJ, **285**, 426.

Caldwell N., Rose J. A., Franx M., Leonardi A. J., 1996. AJ, **111**, 78.

Caldwell N., 1983. AJ, **88**, 804.

Cameron E., 2010. *ArXiv e-prints*.

Chabrier G., 2003. PASP, **115**, 763.

Chung A., van Gorkom J. H., Kenney J. D. P., Vollmer B., 2007. ApJ, **659**, L115.

Clowe D., Schneider P., Aragón-Salamanca A., Bremer M., De Lucia G., Halliday C., Jablonka P., Milvang-Jensen B., Pelló R., Poggianti B., Rudnick G., Saglia R., Simard L., White S., Zaritsky D., 2006. A&A, **451**, 395.

Cole S., Aragon-Salamanca A., Frenk C. S., Navarro J. F., Zepf S. E., 1994. MNRAS, **271**, 781.

Conroy C., Gunn J. E., 2010. ApJ, **712**, 833.

Conselice C. J., 2003. ApJS, **147**, 1.

Conselice C. J., 2006. MNRAS, **373**, 1389.

Couch W. J., Sharples R. M., 1987. MNRAS, **229**, 423.

Couch W. J., Ellis R. S., Sharples R. M., Smail I., 1994. ApJ, **430**, 121.

Courteau S., 1997. AJ, **114**, 2402.

Cowie L. L., Hu E. M., Songaila A., Egami E., 1997. ApJ, **481**, L9.

Crawford S. M., Bershady M. A., Hoessel J. G., 2009. ApJ, **690**, 1158.

De Lucia G., Poggianti B. M., Aragón-Salamanca A., Clowe D., Halliday C., Jablonka P., Milvang-Jensen B., Pelló R., Poirier S., Rudnick G., Saglia R., Simard L., White S. D. M., 2004. ApJ, **610**, L77.

De Lucia G., Springel V., White S. D. M., Croton D., Kauffmann G., 2006. MNRAS, **366**, 499.

De Lucia G., Poggianti B. M., Aragón-Salamanca A., White S. D. M., Zaritsky D., Clowe D., Halliday C., Jablonka P., von der Linden A., Milvang-Jensen B., Pelló R., Rudnick G., Saglia R. P., Simard L., 2007. MNRAS, **374**, 809.

De Lucia G., Poggianti B. M., Halliday C., Milvang-Jensen B., Noll S., Smail I., Zaritsky D., 2009. MNRAS.

De Lucia G., Kauffmann G., White S. D. M., 2004. MNRAS, **349**, 1101.

Dekel A., Silk J., 1986. ApJ, **303**, 39.

Desai V., Dalcanton J. J., Aragón-Salamanca A., Jablonka P., Poggianti B., Gogarten S. M., Simard L., Milvang-Jensen B., Rudnick G., Zaritsky D., Clowe D., Halliday C., Pelló R., Saglia R., White S., 2007. ApJ, **660**, 1151.

Dressler A., Gunn J. E., 1983. ApJ, **270**, 7.

Dressler A., Oemler, Jr. A., Butcher H. R., Gunn J. E., 1994. ApJ, **430**, 107.

Dressler A., Oemler, Jr. A., Couch W. J., Smail I., Ellis R. S., Barger A., Butcher H., Poggianti B. M., Sharples R. M., 1997. ApJ, **490**, 577.

Dressler A., 1980. ApJ, **236**, 351.

Eggen O. J., Lynden-Bell D., Sandage A. R., 1962. ApJ, **136**, 748.

Ellingson E., Lin H., Yee H. K. C., Carlberg R. G., 2001. ApJ, **547**, 609.

Ellis R. S., Smail I., Dressler A., Couch W. J., Oemler A. J., Butcher H., Sharples R. M., 1997. ApJ, **483**, 582.

Emsellem E., Cappellari M., Krajnović D., van de Ven G., Bacon R., Bureau M., Davies R. L., de Zeeuw P. T., Falcón-Barroso J., Kuntschner H., McDermid R., Peletier R. F., Sarzi M., 2007. MNRAS, **379**, 401.

Faber S. M., Willmer C. N. A., Wolf C., Koo D. C., Weiner B. J., Newman J. A., Im M., Coil A. L., Conroy C., Cooper M. C., Davis M., Finkbeiner D. P., Gerke B. F., Gebhardt K., Groth E. J., Guhathakurta P., Harker J., Kaiser N., Kassin S., Kleinheinrich M., Konidaris N. P., Kron R. G., Lin L., Luppino G., Madgwick D. S., Meisenheimer K., Noeske K. G., Phillips A. C., Sarajedini V. L., Schiavon R. P., Simard L., Szalay A. S., Vogt N. P., Yan R., 2007. ApJ, **665**, 265.

Faber S. M., 1973. ApJ, **179**, 731.

Fadda D., Girardi M., Giuricin G., Mardirossian F., Mezzetti M., 1996. ApJ, **473**, 670.

Fasano G., Poggianti B. M., Couch W. J., Bettoni D., Kjærgaard P., Moles M., 2000. ApJ, **542**, 673.

Ferreras I., Charlot S., Silk J., 1999. ApJ, **521**, 81.

Finlator K., Davé R., 2008. MNRAS, **385**, 2181.

Finn R. A., Zaritsky D., McCarthy D. W., Poggianti B., Rudnick G., Halliday C., Milvang-Jensen B., Pelló R., Simard L., 2005. ApJ, **630**, 206.

Finn R. A., Desai V., Rudnick G., Poggianti B., Bell E. F., Hinz J., Jablonka P., Milvang-Jensen B., Moustakas J., Rines K., Zaritsky D., 2010. ApJ, **720**, 87.

Fisher D., Fabricant D., Franx M., van Dokkum P., 1998. ApJ, **498**, 195.

Fritz A., Böhm A., Ziegler B. L., 2009. MNRAS, **393**, 1467.

Fujita Y., 1998. ApJ, **509**, 587.

Fujita Y., 2004. PASJ, **56**, 29.

Gallazzi A., Charlot S., Brinchmann J., White S. D. M., 2006. MNRAS, **370**, 1106.

Girardi M., Mezzetti M., 2001. ApJ, **548**, 79.

Gonzalez A. H., Zaritsky D., Dalcanton J. J., Nelson A., 2001. ApJS, **137**, 117.

Gonzalez A. H., Zaritsky D., Simard L., Clowe D., White S. D. M., 2002. ApJ, **579**, 577.

Gunn J. E., Gott J. R. I., 1972. ApJ, **176**, 1.

Halliday C., Milvang-Jensen B., Poirier S., Poggianti B. M., Jablonka P., Aragón-Salamanca A., Saglia R. P., De Lucia G., Pelló R., Simard L., Clowe D. I., Rudnick G., Dalcanton J. J., White S. D. M., Zaritsky D., 2004. A&A, **427**, 397.

Hilton M., Collins C. A., Stanford S. A., Lidman C., Dawson K. S., Davidson M., Kay S. T., Liddle A. R., Mann R. G., Miller C. J., Nichol R. C., Romer A. K., Sabirli K., Viana P. T. P., West M. J., 2007. ApJ, **670**, 1000.

Hilton M., Stanford S. A., Stott J. P., Collins C. A., Hoyle B., Davidson M., Hosmer M., Kay S. T., Liddle A. R., Lloyd-Davies E., Mann R. G., Mehrtens N., Miller C. J., Nichol R. C., Romer A. K., Sabirli K., Sahlén M., Viana P. T. P., West M. J., Barbary K., Dawson K. S., Meyers J., Perlmutter S., Rubin D., Suzuki N., 2009. ApJ, **697**, 436.

Holden B. P., Stanford S. A., Eisenhardt P., Dickinson M., 2004. AJ, **127**, 2484.

Hoyos C., den Brok M., Kleijn G. V., Carter D., Balcells M., Guzmán R., Peletier R., Ferguson H. C., Goudfrooij P., Graham A. W., Hammer D., Karick A. M., Lucey J. R., Matković A., Merritt D., Mouhcine M., Valentijn E., 2011. MNRAS, **411**, 2439.

Hubble E. P., 1926. ApJ, **64**, 321.

Huertas-Company M., Aguerri J. A. L., Tresse L., Bolzonella M., Koekemoer A. M., Maier C., 2010. A&A, **515**, A3+.

Ibata R. A., Gilmore G., Irwin M. J., 1994. Nature, **370**, 194.

Jäger K., Ziegler B. L., Böhm A., Heidt J., Möllenhoff C., Hopp U., Mendez R. H., Wagner S., 2004. A&A, **422**, 907.

Jarosik N., Bennett C. L., Dunkley J., Gold B., Greason M. R., Halpern M., Hill R. S., Hinshaw G., Kogut A., Komatsu E., Larson D., Limon M., Meyer S. S., Nolta M. R., Odegard N., Page L., Smith K. M., Spergel D. N., Tucker G. S., Weiland J. L., Wollack E., Wright E. L., 2011. ApJS, **192**, 14.

Johnson O., Best P., Zaritsky D., Clowe D., Aragón-Salamanca A., Halliday C., Jablonka P., Milvang-Jensen B., Pelló R., Poggianti B. M., Rudnick G., Saglia R., Simard L., White S., 2006. MNRAS, **371**, 1777.

Kannappan S. J., Fabricant D. G., Franx M., 2002. AJ, **123**, 2358.

Kannappan S. J., Guie J. M., Baker A. J., 2009. AJ, **138**, 579.

Kapferer W., Sluka C., Schindler S., Ferrari C., Ziegler B., 2009. A&A, **499**, 87.

Kassin S. A., Weiner B. J., Faber S. M., Koo D. C., Lotz J. M., Diemand J., Harker J. J., Bundy K., Metevier A. J., Phillips A. C., Cooper M. C., Croton D. J., Konidaris N., Noeske K. G., Willmer C. N. A., 2007. ApJ, **660**, L35.

Kauffmann G., Charlot S., 1998. MNRAS, **294**, 705.

Kauffmann G., Heckman T. M., White S. D. M., Charlot S., Tremonti C., Peng E. W., Seibert M., Brinkmann J., Nichol R. C., SubbaRao M., York D., 2003. MNRAS, **341**, 54.

Kauffmann G., White S. D. M., Guiderdoni B., 1993. MNRAS, **264**, 201.

Kawata D., Mulchaey J. S., 2008. ApJ, **672**, L103.

Kenney J. D. P., van Gorkom J. H., Vollmer B., 2004. AJ, **127**, 3361.

Kobayashi C., Springel V., White S. D. M., 2007. MNRAS, **376**, 1465.

Kodama T., Arimoto N., 1997. A&A, **320**, 41.

Kodama T., Arimoto N., Barger A. J., Arag'on-Salamanca A., 1998. A&A, **334**, 99.

Kodama T., Smail I., Nakata F., Okamura S., Bower R. G., 2001. ApJ, **562**, L9.

Koopmann R. A., Kenney J. D. P., 2004. ApJ, **613**, 866.

Kroupa P., 2001. MNRAS, **322**, 231.

Kutdemir E., Ziegler B. L., Peletier R. F., Da Rocha C., Böhm A., Verdugo M., 2010. A&A, **520**, A109+.

Larson R. B., Tinsley B. M., Caldwell C. N., 1980. ApJ, **237**, 692.

Larson R. B., 1974. MNRAS, **169**, 229.

Lidman C., Rosati P., Tanaka M., Strazzullo V., Demarco R., Mullis C., Ageorges N., Kissler-Patig M., Petr-Gotzens M. G., Selman F., 2008. A&A, **489**, 981.

Maraston C., 2005. MNRAS, **362**, 799.

Marinoni C., Monaco P., Giuricin G., Costantini B., 1999. ApJ, **521**, 50.

Masters K. L., Mosleh M., Romer A. K., Nichol R. C., Bamford S. P., Schawinski K., Lintott C. J., Andreescu D., Campbell H. C., Crowcroft B., Doyle I., Edmondson E. M., Murray P., Raddick M. J., Slosar A., Szalay A. S., Vandenberg J., 2010. MNRAS, **405**, 783.

McCarthy I. G., Frenk C. S., Font A. S., Lacey C. G., Bower R. G., Mitchell N. L., Balogh M. L., Theuns T., 2008. MNRAS, **383**, 593.

McGee S. L., Balogh M. L., Bower R. G., Font A. S., McCarthy I. G., 2009. MNRAS, **400**, 937.

Mei S., Holden B. P., Blakeslee J. P., Rosati P., Postman M., Jee M. J., Rettura A., Sirianni M., Demarco R., Ford H. C., Franx M., Homeier N., Illingworth G. D., 2006. ApJ, **644**, 759.

Mei S., Holden B. P., Blakeslee J. P., Ford H. C., Franx M., Homeier N. L., Illingworth G. D., Jee M. J., Overzier R., Postman M., Rosati P., Van der Wel A., Bartlett J. G., 2009. ApJ, **690**, 42.

Metevier A. J., Koo D. C., Simard L., Phillips A. C., 2006. ApJ, **643**, 764.

Metropolis N., Rosenbluth A., Rosenbluth M., Teller A., Teller E., 1953. *J. Chem. Phys.*, **21**, 1087.

Mihos J. C., Hernquist L., 1994. ApJ, **425**, L13.

Mihos C., 2003. *ArXiv Astrophysics e-prints*.

Milvang-Jensen B., Aragón-Salamanca A., Hau G. K. T., Jørgensen I., Hjorth J., 2003. MNRAS, **339**, L1.

Milvang-Jensen B., Noll S., Halliday C., Poggianti B. M., Jablonka P., Aragón-Salamanca A., Saglia R. P., Nowak N., von der Linden A., De Lucia G., Pelló R., Moustakas J., Poirier S., Bamford S. P., Clowe D. I., Dalcanton J. J., Rudnick G. H., Simard L., White S. D. M., Zaritsky D., 2008. A&A, **482**, 419.

Moore B., Lake G., Quinn T., Stadel J., 1999. MNRAS, **304**, 465.

Moran S. M., Ellis R. S., Treu T., Smith G. P., Rich R. M., Smail I., 2007a. ApJ, **671**, 1503.

Moran S. M., Miller N., Treu T., Ellis R. S., Smith G. P., 2007b. ApJ, **659**, 1138.

Mullis C. R., Rosati P., Lamer G., Böhringer H., Schwope A., Schuecker P., Fassbender R., 2005. ApJ, **623**, L85.

Naab T., Burkert A., 2003. ApJ, **597**, 893.

Nakamura O., Aragón-Salamanca A., Milvang-Jensen B., Arimoto N., Ikuta C., Bamford S. P., 2006. MNRAS, **366**, 144.

Nelan J. E., Smith R. J., Hudson M. J., Wegner G. A., Lucey J. R., Moore S. A. W., Quinney S. J., Suntzeff N. B., 2005. ApJ, **632**, 137.

Pelló R., Rudnick G., De Lucia G., Simard L., Clowe D. I., Jablonka P., Milvang-Jensen B., Saglia R. P., White S. D. M., Aragón-Salamanca A., Halliday C., Poggianti B., Best P., Dalcanton J., Dantel-Fort M., Fort B., von der Linden A., Mellier Y., Rottgering H., Zaritsky D., 2009. A&A, **508**, 1173.

Peng C. Y., Ho L. C., Impey C. D., Rix H., 2002. AJ, **124**, 266.

Peng Y., Lilly S. J., Kovač K., Bolzonella M., Pozzetti L., Renzini A., Zamorani G., Ilbert O., Knobel C., Iovino A., Maier C., Cucciati O., Tasca L., Carollo C. M., Silverman J., Kampczyk P., de Ravel L., Sanders D., Scoville N., Contini T., Mainieri V., Scodeggio M., Kneib J., Le Fèvre O., Bardelli S., Bongiorno A., Caputi K., Coppa G., de la Torre S., Franzetti P., Garilli B., Lamareille F., Le Borgne J., Le Brun V., Mignoli M., Perez Montero E., Pello R., Ricciardelli E., Tanaka M., Tresse L., Vergani D., Welikala N., Zucca E., Oesch P., Abbas U., Barnes L., Bordoloi R., Bottini

D., Cappi A., Cassata P., Cimatti A., Fumana M., Hasinger G., Koekemoer A., Leauthaud A., Maccagni D., Marinoni C., McCracken H., Memeo P., Meneux B., Nair P., Porciani C., Presotto V., Scaramella R., 2010. ApJ, **721**, 193.

Pizagno J., Prada F., Weinberg D. H., Rix H., Pogge R. W., Grebel E. K., Harbeck D., Blanton M., Brinkmann J., Gunn J. E., 2007. AJ, **134**, 945.

Poggianti B. M., Smail I., Dressler A., Couch W. J., Barger A. J., Butcher H., Ellis R. S., Oemler A. J., 1999. ApJ, **518**, 576.

Poggianti B. M., Bridges T. J., Carter D., Mobasher B., Doi M., Iye M., Kashikawa N., Komiyama Y., Okamura S., Sekiguchi M., Shimasaku K., Yagi M., Yasuda N., 2001. ApJ, **563**, 118.

Poggianti B. M. *et al.*, 2006. ApJ, **642**, 188.

Poggianti B. M., Desai V., Finn R., Bamford S., De Lucia G., Varela J., Aragón-Salamanca A., Halliday C., Noll S., Saglia R., Zaritsky D., Best P., Clowe D., Milvang-Jensen B., Jablonka P., Pelló R., Rudnick G., Simard L., von der Linden A., White S., 2008. ApJ, **684**, 888.

Poggianti B. M., Fasano G., Bettoni D., Cava A., Dressler A., Vanzella E., Varela J., Couch W. J., D'Onofrio M., Fritz J., Kjaergaard P., Moles M., Valentinuzzi T., 2009. ApJ, **697**, L137.

Postman M., Geller M. J., 1984. ApJ, **281**, 95.

Press W. H., Schechter P., 1974. ApJ, **187**, 425.

Quilis V., Moore B., Bower R., 2000. *Science*, **288**, 1617.

Roediger E., Hensler G., 2005. A&A, **433**, 875.

Rubin V. C., Waterman A. H., Kenney J. D. P., 1999. AJ, **118**, 236.

Rudnick G., Rix H., Franx M., Labbé I., Blanton M., Daddi E., Förster Schreiber N. M., Moorwood A., Röttgering H., Trujillo I., van der Wel A., van der Werf P., van Dokkum P. G., van Starkenburg L., 2003. ApJ, **599**, 847.

Rudnick G., von der Linden A., Pelló R., Aragón-Salamanca A., Marchesini D., Clowe D., De Lucia G., Halliday C., Jablonka P., Milvang-Jensen B., Poggianti B., Saglia R., Simard L., White S., Zaritsky D., 2009. ApJ, **700**, 1559.

Salpeter E. E., 1955. ApJ, **121**, 161.

Sánchez-Blázquez P., Jablonka P., Noll S., Poggianti B. M., Moustakas J., Milvang-Jensen B., Halliday C., Aragón-Salamanca A., Saglia R. P., Desai V., De Lucia G., Clowe D. I., Pelló R., Rudnick G., Simard L., White S. D. M., Zaritsky D., 2009. A&A, **499**, 47.

Sandage A., Visvanathan N., 1978a. ApJ, **223**, 707.

Sandage A., Visvanathan N., 1978b. ApJ, **225**, 742.

Simard L., Pritchet C. J., 1999. PASP, **111**, 453.

Simard L. *et al.*, 2002. ApJS, **142**, 1.

Simard L., Clowe D., Desai V., Dalcanton J. J., von der Linden A., Poggianti B. M., White S. D. M., Aragón-Salamanca A., De Lucia G., Halliday C., Jablonka P., Milvang-Jensen B., Saglia R. P., Pelló R., Rudnick G. H., Zaritsky D., 2009. A&A, **508**, 1141.

Springel V. *et al.*, 2005. Nature, **435**, 629.

Springel V., Frenk C. S., White S. D. M., 2006. Nature, **440**, 1137.

Stanford S. A., Eisenhardt P. R., Dickinson M., 1998. ApJ, **492**, 461.

Tanaka M., Finoguenov A., Kodama T., Morokuma T., Rosati P., Stanford S. A., Eisenhardt P., Holden B., Mei S., 2008. A&A, **489**, 571.

Thomas D., Maraston C., Bender R., Mendes de Oliveira C., 2005. ApJ, **621**, 673.

Tonnesen S., Bryan G. L., 2009. ApJ, **694**, 789.

Toomre A., Toomre J., 1972. ApJ, **178**, 623.

Trager S. C., Worthey G., Faber S. M., Burstein D., Gonzalez J. J., 1998. ApJS, **116**, 1.

Trager S. C., Faber S. M., Dressler A., 2008. MNRAS, **386**, 715.

Tremonti C. A. *et al.*, 2004. ApJ, **613**, 898.

Treu T., Ellis R. S., Kneib J., Dressler A., Smail I., Czoske O., Oemler A., Natarajan P., 2003. ApJ, **591**, 53.

Treu T., Ellis R. S., Liao T. X., van Dokkum P. G., Tozzi P., Coil A., Newman J., Cooper M. C., Davis M., 2005. ApJ, **633**, 174.

Trujillo I., Conselice C. J., Bundy K., Cooper M. C., Eisenhardt P., Ellis R. S., 2007. MNRAS, **382**, 109.

Tully R. B., Fisher J. R., 1977. A&A, **54**, 661.

Tully R. B., Pierce M. J., Huang J., Saunders W., Verheijen M. A. W., Witchalls P. L., 1998. AJ, **115**, 2264.

van Dokkum P. G., Franx M., 1996. MNRAS, **281**, 985.

van Dokkum P. G., Franx M., Kelson D. D., Illingworth G. D., Fisher D., Fabricant D., 1998. ApJ, **500**, 714.

van Dokkum P. G., Franx M., Fabricant D., Illingworth G. D., Kelson D. D., 2000. ApJ, **541**, 95.

van Dokkum P. G., Stanford S. A., Holden B. P., Eisenhardt P. R., Dickinson M., Elston R., 2001. ApJ, **552**, L101.

Vergani D., Scodeggio M., Pozzetti L., Iovino A., Franzetti P., Garilli B., Zamorani G., Maccagni D., Lamareille F., Le Fèvre O., Charlot S., Contini T., Guzzo L., Bottini D., Le Brun V., Picat J. P., Scaramella R., Tresse L., Vettolani G., Zanichelli A., Adami C., Arnouts S., Bardelli S., Bolzonella M., Cappi A., Ciliegi P., Foucaud S., Gavignaud I., Ilbert O., McCracken H. J., Marano B., Marinoni C., Mazure A., Meneux B., Merighi R., Paltani S., Pellò R., Pollo A., Radovich M., Zucca E., Bondi M., Bongiorno A., Brinchmann J., Cucciati O., de la Torre S., Gregorini L., Perez-Montero E., Mellier Y., Merluzzi P., Temporin S., 2008. A&A, **487**, 89.

Visvanathan N., Sandage A., 1977. ApJ, **216**, 214.

Vivas A. K., Zinn R., Andrews P., Bailyn C., Baltay C., Coppi P., Ellman N., Girard T., Rabinowitz D., Schaefer B., Shin J., Snyder J., Sofia S., van Altena W., Abad C., Bongiovanni A., Briceño C., Bruzual G., Della Prugna F., Herrera D., Magris G., Mateu J., Pacheco R., Sánchez G., Sánchez G., Schenner H., Stock J., Vicente B., Vieira K., Ferrín I., Hernandez J., Gebhard M., Honeycutt R., Mufson S., Musser J., Rengstorf A., 2001. ApJ, **554**, L33.

Vivas A. K., Jaffé Y. L., Zinn R., Winnick R., Duffau S., Mateu C., 2008. AJ, **136**, 1645.

Vogt N. P., Forbes D. A., Phillips A. C., Gronwall C., Faber S. M., Illingworth G. D., Koo D. C., 1996. ApJ, **465**, L15.

Vulcani B., Poggianti B. M., Finn R. A., Rudnick G., Desai V., Bamford S., 2010. ApJ, **710**, L1.

Vulcani B., Poggianti B. M., Aragón-Salamanca A., Fasano G., Rudnick G., Valentinuzzi T., Dressler A., Bettoni D., Cava A., D'Onofrio M., Fritz J., Moretti A., Omizzolo A., Varela J., 2011. MNRAS, **412**, 246.

Wang Y., Yang X., Mo H. J., van den Bosch F. C., 2007. ApJ, **664**, 608.

Weiner B. J., Willmer C. N. A., Faber S. M., Harker J., Kassin S. A., Phillips A. C., Melbourne J., Metevier A. J., Vogt N. P., Koo D. C., 2006. ApJ, **653**, 1049.

White S. D. M., Clowe D. I., Simard L., Rudnick G., De Lucia G., Aragón-Salamanca A., Bender R., Best P., Bremer M., Charlot S., Dalcanton J., Dantel M., Desai V., Fort B., Halliday C., Jablonka P., Kauffmann G., Mellier Y., Milvang-Jensen B., Pelló R., Poggianti B., Poirier S., Rottgering H., Saglia R., Schneider P., Zaritsky D., 2005. A&A, **444**, 365.

Williams M. J., Bureau M., Cappellari M., 2010. MNRAS, **409**, 1330.

Wolf C., Aragón-Salamanca A., Balogh M., Barden M., Bell E. F., Gray M. E., Peng C. Y., Bacon D., Barazza F. D., Böhm A., Caldwell J. A. R., Gallazzi A., Häußler B., Heymans C., Jahnke K., Jogee S., van Kampen E., Lane K., McIntosh D. H., Meisenheimer K., Papovich C., Sánchez S. F., Taylor A., Wisotzki L., Zheng X., 2009. MNRAS, **393**, 1302.

Worthey G., 1994. ApJS, **95**, 107.

Yang Y., Zabludoff A. I., Zaritsky D., Lauer T. R., Mihos J. C., 2004. ApJ, **607**, 258.

Yang Y., Zabludoff A. I., Zaritsky D., Mihos J. C., 2008. ApJ, **688**, 945.

Zabludoff A. I., Mulchaey J. S., 1998. ApJ, **496**, 39.

Zabludoff A. I., Zaritsky D., Lin H., Tucker D., Hashimoto Y., Shectman S. A., Oemler A., Kirshner R. P., 1996. ApJ, **466**, 104.

Zaritsky D., Zabludoff A. I., Gonzalez A. H., 2008. ApJ, **682**, 68.

Ziegler B. L., Bower R. G., Smail I., Davies R. L., Lee D., 2001. MNRAS, **325**, 1571.

Ziegler B. L., Böhm A., Fricke K. J., Jäger K., Nicklas H., Bender R., Drory N., Gabasch A., Saglia R. P., Seitz S., Heidt J., Mehlert D., Möllenhoff C., Noll S., Sutorius E., 2002. ApJ, **564**, L69.

Ziegler B. L., Böhm A., Jäger K., Heidt J., Möllenhoff C., 2003. ApJ, **598**, L87.